DSE Group 07 - Design of a VTOL Business Aircraft

Final Report

Group 7 - DSE Fall 2013

Delft University of Technology

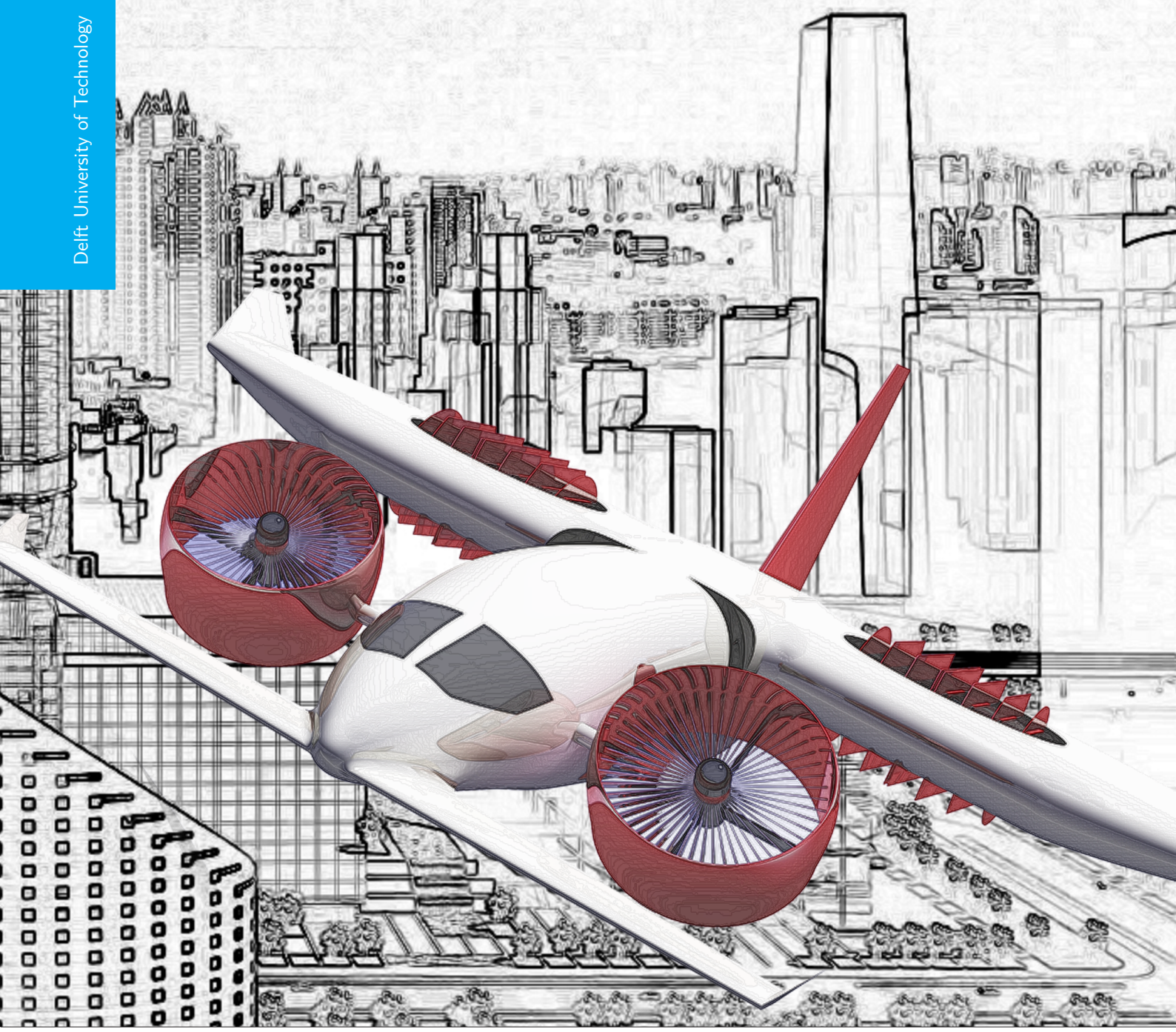

TU Delft Delft University of Technology

Challenge the future

DSE GROUP 07 - DESIGN OF A VTOL BUSINESS AIRCRAFT

FINAL REPORT

by

Group 7 - DSE Fall 2013

V. Bontempi De Marchi	1397117
R. Dekker	4065077
H. Jaberi	1384457
R.M. Koch	4108388
J. L'Ortye	4091604
J. van Manen	4001729
S.A. van der Meijden	4029917
Q. Payanda	1561936
B.J. Pijnacker Hordijk	4079817
C. Ravesteijn	4095189

January 28, 2014

Project duration:	November 11, 2013 – January 30, 2014	
Supervisor:	S. Shroff	TU Delft
Coaches:	M. Gallo	TU Delft
	V.P. Brugemann	TU Delft

TU Delft Delft University of Technology

PREFACE

This Final Report is the last in a series of reports on the 'Design of a Vertical Take-Off and Landing (VTOL) Business Aircraft'. As a part of the Design Synthesis Exercise, 10 students have worked hard over a time span of 10 weeks to deliver an Innovative VTOL Aircraft Design (InVADe).

The InVADe team would like to thank our tutor and coaches, S. Shroff, MSc, Ir. V.P. Brugemann and Dr. M. Gallo for their guidance and assistance throughout the span of the project.

Also a word of thanks goes out to Dott. Ing. Luigi U. Ricci Moretti (AgustaWestland), Ir. H. Benedictus, Prof. dr. D.G. Simons, Dr. M.D. Pavel, Ir. A.C. in 't Veld, Ir. W.A. Timmer, Dr. ir. R. Vos, Dr. ir. M. Voskuijl, Dr. C. Kassapoglou, Dr. ir. G.N. Saunders, Dr. ir. L.L.M. Veldhuis, Ir. D. Steenhuizen , Dr. A.G. Rao, Ir. Evert Jesse (ADSE) and Ir. Leonid Pavlov for their help on various occasions.

Group 7 - DSE Fall 2013
Delft, January 2014

SUMMARY

Innovative Vertical Take-off and Landing Aircraft Design (InVADe) was developed as a Design Synthesis Exercise (DSE) project. This environmentally friendly aircraft will be capable of operating in densely populated areas and will offer swift, point to point transportation. InVADe is designed to transport 10 people 2000 km at 600 km/h, while employing VTOL capabilities. It is expected to be flying by 2030.

Studies have shown that a large potential corporate market exists for such an aircraft. Alternative markets include medical rescue operations, military, and offshore engineering. Assuming a market share of 1.9%, 500 units will be sold over 20 years. The associated unit cost are calculated to be 6.55 million EUR. This unit cost uses a conservative estimate of the achievable market share. A still realistic market share of around 10% would result in a significant drop in the unit cost. With a sales price of 10.0 million EUR, a yearly return of investment of 9.1% can be achieved. An operating cost of 1,374 EUR per hour, enables a lower price per passenger than regular business class tickets, as long as InVADe carries four passengers or more.

The configuration of InVADe is chosen in such a way that a higher lift-to-drag ratio is attained in comparison to other VTOL aircraft. The design of InVADe consist of a 14 m fuselage, canard, two tilting ducting fans and main wing placed at 9.4 m from the root with a span 13.3 m. The main wing houses two ducted fans which are used during VTOL manoeuvres. During cruise the fans are closed off using a shutter mechanism to reduce drag. InVADe employs four lift-generating components. During VTOL operations, the four ducted fans provide the lift. During conventional flight the wing, canard, fuselage and two front ducts generate lift. The shape of the main wing consists of a squared part, housing the ducted fans, and a tapered outer wing section. The aspect ratio of the main wing is 6.19. During transition high lift devices enable InVADe to safely perform transition at a speed of 60 m/s.

Two turboshaft engines, housed in the fuselage, provide 3.5 MW of power to four electric generators, which in turn transmit power, via electric cables, to electric motors mounted in each duct. The motors then each power individual fans inside the ducts, which, together deliver enough thrust to lift the aircraft vertically off the ground. After take-off - in transition - while the front ducted fans tilt to provide thrust, shutters close off the ends of the aft duct, inside the wing. The rate of climb reaches a maximum of 19.8 m/s at sea level and the cruise speed of 600 km/h is reached at 75% power. The range varies depending on the payload from 1,082 km to 2,986 km.

Three different structural sections of the aircraft were designed: the wing structure, canard, and front ducts. The outer section of the wing features a wing box, whereas the inner section is outfitted with two main spars and a load carrying structure for the duct. In total, this structure has a weight of 191 kg per wing. For all structural elements, Aluminium 2024-T4 was used for its high endurance limit, good manufacturability and low embodied energy. The design is outfitted with a canard and a single vertical tail, sized for stability and control during flight. During hover and transition, stability augmentation systems are employed.

A sharp focus on sustainability, especially on noise and CO_2 emissions, motivated the design team to come up with innovative solutions and push the boundaries of the design to meet the needs of a future aerospace industry with lower environmental impact. With a CO_2 emission rate of 2.04 kg/km, comparable with other modern, small business aircraft, InVADe offers a significantly lower environmental impact, particularly for short flights, since it practically eliminates the need for getting to/from the airport. In the vertical take-off and landing phases, the total noise Sound Pressure Level (SPL) produced, after abatement measures, is as low as 80.7 dB at 100 m distance. This is comparable to the noise of a passenger car as heard from alongside a highway.

The resulting design is an innovative aircraft that will compete with existing modes of business air travel, while offering a significant advantage over the aforementioned. Its aircraft performance characteristics, such as cruise speed, range, rate of climb, and emissions are on par with some of the most modern business jets. Its VTOL capabilities, low noise levels, and swift, versatile, point to point transport options will make InVADe a smart choice for the future business traveller.

The scope of this design project includes the preliminary design of InVADe. A more detailed look into the subsystems, followed by flight testing and manufacturing, are to be performed after this report. Specific recommendations for further development include, among others: a more detailed ducted fan design, a study on the feasibility of active winglets, and a deeper investigation on the electric propulsion system, including alternative methods of energy storage.

CONTENTS

LIST OF SYMBOLS

A_a	Fan annulus area [m^2]
A_E	Fan exit area [m^2]
A_{encl}	Enclosed area by a thin-walled cross-section [m^2]
A_i	Series coefficient of element i [-]
A_R	Fan area [m^2]
AR	Aspect ratio [-]
B	Boom area [m^2]
b	Wing span [m]
b_{canard}	Canard span [m]
C_1, C_2	Regression coefficients [-]
C_D	Drag coefficient [-]
C_d	Airfoil drag coefficient [-]
C_{D_0}	Zero-lift drag coefficient [-]
C_f	Skin friction coefficient [-]
$\bar{C}_i$	Mean geometric chord length [m]
C_{L_α}	dC_L/d_α, derivative of lift coefficient with respect to α [1/rad]
C_L	Lift coefficient [-]
C_l	Airfoil lift coefficient [-]
C_m	Moment coefficient [-]
C_{X_u}	$\partial C_X/\partial u$. Stability derivative notation, in this case of force in X-direction with respect to u [-]
c	Local chord length [m]
c'	Chord length when extending flaps [m]
$\bar{c}$	Mean aerodynamic chord length [m]
c_b	Blade chord length [m]
c_f	Flap chord length, unextended [m]
c_r	Root chord length [m]
c_t	Tip chord length [m]
D	Drag force [N]
$\bar{D}$	Average drag during landing [N]
DI	Directivity index [-]
D_{duct}	Duct diameter [m]
D_F	Fan diameter [m]
D_f	Fuselage diameter [m]
D_H	Fan hub diameter [m]
dV/dH	Speed increase per m altitude during unsteady climb [1/s]
E	Young's modulus [N/m^2]
En	Endurance [s]
e	Oswald factor, indicates efficiency of lift distribution [-]
FF	Fuel fraction [-]
FM	Figure of merit [-]
F_S	Shear force [N]
f	Friction parameter in drag coefficient estimate [-]
$\bar{f}$	Frequency [Hz]
g	Gravitational acceleration [m/s^2]
H_T	Total enthalpy [J]
h	Height of a part [m]
$\bar{h}_x, \bar{h}_z$	Angular momentum components around the x- and z-axes [kg m^2/s]
I_{wire}	Electrical current running through a wire [A]
I_{xx}, I_{yy}, I_{zz}	Second moments of inertia about the x-, y- and z-axes [m^4]
I_{xy}	Product second moment of inertia of the x- and y-axes [m^4]
i	Element index in a sum [-]
J_{xx}, J_{yy}, J_{zz}	Mass moments of inertia about the x-, y- and z-axes [kg m^2]
J_{xz}	Mass product of inertia in the xz-plane [kg m^2]
K_b, K_c, K_s	Bending, compression and shear buckling coefficients [-]
K_g	Gust alleviation factor [-]
${K_X}^2, {K_Y}^2, {K_Z}^2$	Nondimensional mass moments of inertia about the x-, y- and z-axes [-]

K_{XZ}	Nondimensional mass product of inertia in the xz-plane [-]
k	Constant or parameter [-]
k_c	Parameter indicating the part of total lift generated by the main wing [-]
L	Lift force [N]
$\bar{L}$	Average lift force during landing [N]
l_{duct}	Duct length [m]
l_f	Fuselage length [m]
l_h	Distance between the aerodynamic center of the canard and that of the wing [m]
l_v	Distance between the aerodynamic center of the vertical tail and that of the wing [m]
M_{ac}	Pitching moment around the aerodynamic center [Nm]
MN	Mach number [-]
MoS	Margin of Safety [-]
M_T	Torsional moment [Nm]
M_x, M_y, M_z	Moments about the x-, y- and z-axes [Nm]
$\dot{m}$	Mass flow [kg/s]
N	Number of elements in a sum [-]
N_b	Number of blades [-]
N_p	Number of poles in electric motor [-]
n_L	Load factor [-]
n_{st}	Number of stringers
OPL	Overall power level [dB]
P_A	Available power [W]
P_{eq}	Maximum power produced by one front duct [W]
P_h	Hover power [W]
P_i	Ideal induced power [W]
P_{max}	Max rated power [W]
P_R	Power required [W]
PWL	Sound power level [dB]
p	Roll rate [rad/s]
q	Pitch rate [rad/s]
$\bar{q}$	Dynamic pressure [Pa]
q_s	Shear flow in a structure [N/m]
R	Distance to sound source [m]
R_b	Radius of the blade [m]
Ra	Range [m]
Re	Reynolds number [-]
ROC	Unsteady rate of climb [m/s]
R_{wire}	Electrical resistance of a wire [Ω]
$\bar{R}_x, \bar{R}_y, \bar{R}_z$	Reference normalized radii of gyration from the x-, y- and z-axes [-]
r	Yaw rate [rad/s]
S	Wing area [m^2]
S_{duct}	Duct lift generating area [m^2]
SFC	Specific fuel consumption [kg/J]
S_h	Canard surface area [m^2]
$S.M.$	Stability margin [-]
SPL	Sound pressure level [dB]
S_v	Vertical tail area [m^2]
S_{wet}	Wetted surface area [m^2]
S_{wf}	Flapped wing area [m^2]
s	Runway length required for landing [m]
T	Thrust force [N]
T_{av}	Average thrust force [N]
T_i	Static Thrust [N]
T_{por}	Portion of total thrust [N]
T_{shr}	Shrouded Thrust [N]
t	Thickness of a part [m]
$\bar{t}$	Time until failure [s]
$(t/c)_{max}$	Maximum airfoil thickness ratio [-]
U_{de}	Gust velocity [ft/s]
$\bar{u}$	Velocity component in longitudinal (forward) direction [m/s]
$\hat{u}$	Linearised nondimensional longitudinal velocity [-]
V	Total airspeed [m/s]
V_A	Approach velocity [m/s]

V_c	Climb velocity [m/s]
V_{cruise}	Cruise velocity [m/s]
V_e	Air velocity at duct exit [m/s]
V_h/V	Ratio between air velocities experienced by the canard and the main wing [-]
V_i	Induced velocity [m/s]
V_T	Touchdown velocity [m/s]
V_{tr}	Transition velocity [m/s]
$\bar{V}_V$	Vertical tail volume coefficient [-]
V_v/V	Ratio between air velocities experienced by the vertical tail and the main wing [-]
$\bar{v}$	Velocity component in lateral (spanwise) direction [m/s]
W	Weight [N]
w	Width of a part [m]
$\bar{w}$	Velocity component in vertical direction [m/s]
x	Longitudinal position [m]
$\bar{x}_{ac}$	Longitudinal aerodynamic center location, divided by Mean aerodynamic chord [-]
$\bar{x}_{cg}$	Longitudinal center of gravity position, divided by Mean aerodynamic chord [-]
$\bar{Y}$	Spanwise location of the mean aerodynamic chord [m]
y	Lateral (spanwise) position [m]
$\bar{y}$	Location of centroid in cross-section [m]
z	Vertical position [m]
α	Angle of attack [°]
$\alpha_{L=0}$	Zero lift angle of attack [°]
α_s	Stall angle of attack [°]
α_T	Front fan angle of attack [°]
β	Sideslip angle [°]
β_M	Parameter representing Mach number influence on C_{L_α} [-]
Γ	Circulation [m^2/s]
γ	Flight path angle of the aircraft [°]
ΔV_{canard}	Velocity increase at the main wing as a result of the canard [m/s]
δ_a	Flaperon deflection angle [°]
δ_e	Elevator deflection angle [°]
δ_f	Deflection angle of the flaps [°]
δ_r	Rudder deflection angle [°]
η	Airfoil efficiency parameter [-]
η_{prop}	Propulsive efficiency [-]
θ	Pitch angle [°]
θ_{duct}	Angle of the duct generating lift [°]
Λ	Sweep angle [°]
$\Lambda_{hingeline}$	Sweep of the flap hinge line [°]
λ	Taper ratio [-]
λ_t	Failure rate [-]
μ	Dynamic viscosity [Pa s]
μ_b	Nondimensional mass for asymmetric equations of motion [-]
μ_{br}	Friction coefficient at maximum brake power [-]
μ_c	Nondimensional mass for symmetric equations of motion [-]
μ_g	Gust parameter [-]
μ_L	Lift distribution parameter [-]
μ_t	Repair rate [-]
ν_e	Poisson's ratio [-]
ξ	Vorticity of a flow [1/s]
ρ	Air density [kg/m^3]
ρ_{SL}	Air density at an altitude [kg/m^3]
σ	Normal stress in a structure [N/m^2]
σ_v	Von Mises stress [N/m^2]
ς	Ratio of fan area to exit area [-]
τ	Shear stress in a structure [N/m^2]
Φ_E	Energy Flux [W/m^2]
ϕ	Roll angle [°]
ϕ_t	Inflow angle at the tip [°]
χ	Angle indicating spanwise position [°]
Ω	Rotational speed of fan [RPM]
ω	Angular velocity [rad/s]
∇	Differential operator [-]

LIST OF ABBREVIATIONS

AC	Alternating Current
APU	Auxiliary Power Unit
ATC	Air Traffic Control
AWG	American Wire Gauge
BEM	Beam Element Method
BWB	Blended Wing Body
CFD	Computational Fluid Dynamics
c.g.	Center of Gravity
CO_2	Carbon Dioxide
CS	Certification Specifications
CTOL	Conventional Take-Off and Landing
DC	Direct Current
DOC	Direct Operating Cost
DoD	Department of Defense
DSE	Design Synthesis Exercise
EMI	Electro Magnetic Interference
EOL	End-of-Life
EUR	Euro
FAA	Federal Aviation Administration
FAR	Federal Aviation Regulations
FBD	Free Body Diagram
FCU	Flight Computer Unit
FL	Flight Level
FMC	Flight Management Computer
GPS	Global Positioning System
GPWS	Ground Proximity Warning System
HLD	High Lift Device
HTS	High Temperature Superconductor
IATA	International Air Transport Association
IFR	Instrument Flight Rules
ILS	Instrument Landing System
ISA	International Standard Atmosphere
InVADe	Innovative VTOL Aircraft Design
ISA	International Standard Atmosphere
JIT	Just-In-Time
KIAS	Knots Indicated Air Speed
kts	Knots
L/D	Lift over Drag
LEMAC	Leading Edge Mean Aerodynamic Chord
MAC	Mean Aerodynamic Chord
MCDU	Multi-purpose Control Display Unit
MFD	Multi Function Display
MFHBA	Mean Flight Hours Between Abort
MFHBF	Mean Flight Hours Between Failure
MIT	Massachusetts Institute of Technology
MNS	Mission Needs Statement
MR	Mission Reliability
MTOW	Maximum Take-Off Weight
MTTR	Mean Time Till Repair
NACA	National Advisory Committee for Aeronautics
NASA	National Aeronautics and Space Administration
NDB	Non-Directional (Radio) Beacon
NO_X	Nitrous Oxides
OBS	Organisational Breakdown Structure
OC	Operations Center
OEW	Operational Empty Weight
OPEVAL	Operational Evaluation
PAMELA	Process for Advanced Management of EOL
PFD	Primary Flight Display
PIO	Pilot Induced Oscillation
POS	Project Objective Statement
QDF	Quantity Discount Factor
RAMS	Reliability, Availability, Maintainability and Safety
RoI	Return on Investment
SFC	Specific Fuel Consumption
S.M.	Stability Margin
SPL	Sound Pressure Level
STOL	Short Take-off and Landing
TCAS	Traffic Colliding Avoidance System
TO	Take-Off
TRAC	Telescoping Rotor Aircraft
TRL	Technology Readiness Level
TRU	Transformer Regulator Unit
USD	U.S. Dollar
VAC	Volt Alternating Current
VDC	Volt Direct Current
VHF	Very High Frequency
VFR	Visual Flight Rules
VOR	VHF Omni Directional Radio Range
VTOL	Vertical Take-off and Landing
WBS	Work Breakdown Structure
WCED	World Commission on Environment & Development
WFD	Work Flow Diagram
WIP	Work In Progress

1

INTRODUCTION

In today's world, fast, point to point transport is in high demand. High speed air travel is often only possible in between airports, which requires additional transport to and from the airports. Existing helicopters do enable point to point air travel, but can only fly at a limited maximum speed. Hence, a more time efficient method of air travel for the business market is worth investigating. Fast, inter-city, direct air travel can be achieved if an aircraft is able to take-off and land vertically, and, in addition, achieve high speeds during cruise. The preliminary design of such an aircraft is the challenge of a team consisting of ten students throughout the course of the Design Synthesis Exercise (DSE). The Project Objective Statement (POS) defined as: *"Impress the DSE tutor and coaches by designing an innovative & quiet VTOL business aircraft in 10 weeks with 10 students"*, describes the project definition. Following the POS, the Mission Needs Statement (MNS) was defined as: *"Transport 10 people 2000 km point to point at 600 km/h employing VTOL capabilities with 100 m noise level of at most 70 dB, flying by 2030"*. Finally, the working title for the project and the design was established: **InVADe** (Innovative VTOL Aircraft Design).

This Final Report covers the progress of the preliminary design phase of the InVADe four ducted fan aircraft. The aim of this report is to elaborate on the final state of the design resulting from this phase. The design is supported by technical work in the fields of propulsion, aerodynamics, stability and control, structures and performance.

First the reader is given insight into the background of the project. Therefore, Chapter 2 recaps the mission requirements and profile, which were set in the Mid-Term Report [29]. The market analysis, performed to research the marked needs, is described. A summary is given of the concept selection process that took place before the preliminary design phase. Chapter 3 contains the overall picture of the design, giving insight in the exterior and interior design, lift distribution and a current weight estimation of the aircraft.
Then, Chapters 4 to 8 delve into the technical aspects of the design. Chapter 4 describes the aerodynamic parameters and calculations relating to the design. The design of the propulsion system is found in Chapter 5, which includes calculations on engine power and noise. Chapter 6 begins by laying out the structural design framework, and describes the structural design of specific parts in the aircraft. Next, Chapter 7 elaborates on stability and control aspects of the aircraft during each phase of flight. Then, Chapter 8 discusses the overall performance of the aircraft.

Chapter 9 elaborates on the development analysis including operations, logistics and manufacturing. In addition, the chapter contains the risk assessment, as well as a Reliability, Availability, Maintainability and Safety (RAMS) analysis. Chapters 10 and 11 include analyses on the costs and sustainability of the aircraft. Next, in Chapter 12, compliance of the aircraft with respect to the given requirements is checked. Finally, the report is concluded in Chapters 13 and 14.

2

BACKGROUND

This report is the fourth and final report for the 'Design of an innovative VTOL business aircraft'. This chapter summarizes what has been done in the previous reports so far in order to reach the final design. First, the mission requirements for InVADe are introduced and the mission profile associated with the aircraft is described. Then, a brief introduction into the market needs is made and finally the process up until this final report is described.

2.1. MISSION REQUIREMENTS

This section presents all client and team requirements for the InVADe project. Table 2.1 contains all client requirements and Table 2.2 contains all team requirements, identified according to the following scheme:

$$XX-YYYY-\#\#$$

XX is 'Ct' for client requirements and 'Tm' for team requirements. YYYY is 'cons' for constraints and 'tech' for technical requirements. ## is the requirement ID number following its subdivision. The requirements are split up into into killer, driving, and secondary requirements.

Table 2.1: Client constraints and technical requirements

Req. ID	Description	Type		
		Killer	Driving	Secondary
Ct-cons-01	Range of 2000 km with 1000 kg payload after a VTOL take off from sea level/ ISA+15 °C ambient conditions, including a landing and take-off halfway		✈	
Ct-cons-02	Payload 10(+2) passengers (100 kg+15 kg per person)		✈	
Ct-cons-03	Cockpit crew 1 (2 optional)		✈	
Ct-cons-04	Design cruise speed 600 km/h at 75% maximum cruise rating	✈		
Ct-cons-05	Service ceiling 7000 m		✈	
Ct-cons-06	Achieve a rate of climb 9 m/s		✈	
Ct-cons-07	Very low noise levels (urban area operations) equal or less than 70 dB within a 100 m distance during take-off and landing	✈		
Ct-cons-08	Unit cost below 8 000 000 EUR		✈	
Ct-cons-09	Average unit cost according to the expected production of 500 units over 20 years		✈	
Ct-cons-10	First flight in 2030		✈	
Ct-cons-11	Design for 20000 flight hours		✈	
Ct-cons-12	CO_2 emissions lower than 2.5 kg/km		✈	
Ct-cons-13	Comply with corresponding CS23 or CS29 regulations		✈	
Ct-tech-01	VTOL capability		✈	
Ct-tech-02	End-of-life disposal plan		✈	
Ct-tech-03	Investigation into production facilities and their possible locations		✈	

2.2. MISSION PROFILE DIAGRAM

The following section summarises the mission profile and its different phases, according to Requirements Ct-cons-01, Ct-cons-06, and Ct-cons-05.

Table 2.2: Team constraints and technical requirements

Req. ID	Description	Type		
		Killer	Driving	Secondary
Tm-cons-01	Take-off and land from 15x15 m helipad		✈	
Tm-cons-02	G-forces between 0.6 g and 1.4 g		✈	
Tm-cons-03	Minimum seat pitch of 90 cm and a seat width of 48 cm		✈	
Tm-cons-04	Minimum cabin height of 170 cm			✈
Tm-cons-05	Specific range of 1.25 km/kg		✈	
Tm-cons-06	Storage space for 12 times cabin luggage (60x45x25 cm)			✈
Tm-cons-07	Cabin temperature range of 20-24 °C		✈	
Tm-cons-08	Cabin altitude of at most 2000 m		✈	
Tm-cons-09	Operational temperature range from -50 to +90 °C		✈	
Tm-cons-10	Operating cost of less than 1800 EUR per flight hour [19]			✈
Tm-cons-11	Dispatch reliability of at least 98% [24]			✈
Tm-cons-12	Less than 5.75 days of maintenance downtime per 100 flight hours [25]			✈
Tm-tech-01	Easy to control by pilots and aerodynamically stable during operation		✈	
Tm-tech-02	Accommodate lavatory and partial galley			✈
Tm-tech-03	Include state-of-the-art fly-by-wire technology and glass cockpit avionics			✈
Tm-tech-04	Maximise business productivity by providing power sockets and internet connection			✈
Tm-tech-05	Comfortable and safe (de)boarding			✈

The first section will introduce the different operating phases. The next section will address the reserve fuel required to ensure loiter or redirection. Finally, the corresponding mission profile diagrams are presented in Figure 2.1.

2.2.1. OPERATIONAL PHASES

The mission consists of a number of different phases, namely: warm-up, take-off, transition, climb, cruise, descent, possibly loiter/redirection, transition and landing/shut-down, which can also be seen in Figure 2.1. For a detailed description of each of these phases the reader is referred to the Midterm report [29]. Some values, like the climb and descent rates and the times that certain phases take were changed since then. The new values are set and presented in Section 8.5.

2.2.2. RESERVE FUEL

FAR regulations [38, 39] state that helicopters are required to have a minimum fuel reserve when beginning a flight; it should be enough to be able to fly at normal cruising speed for 20 minutes in VFR conditions (§91.151) or 30 minutes in IFR conditions (§91.167).

Therefore, three mission profiles are possible, as shown in Figure 2.1:

The top figure shows a regular mission: No redirection or loiter is needed. This leaves enough reserves at all times during the flight.

The middle figure shows a mission where the reserves were used up on the first trip. In this case it is possible to refuel at the landing site to make sure there is enough fuel for the second trip and a reserve.

The bottom shows the situation where the reserve was used up on the first leg and there is no refuelling possible. In this case the flight plan has to be changed in order to refuel during the second trip to make sure that there are always enough reserves on board. It is safe to assume that there is always a refuelling opportunity available within a 500 km radius [29].

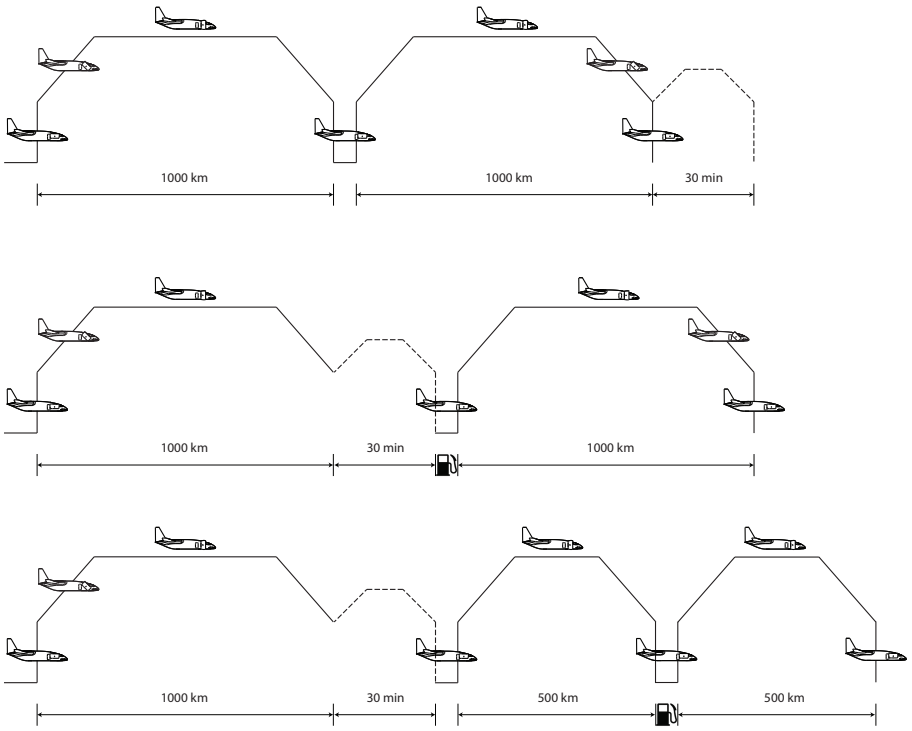

Figure 2.1: Mission profile diagram

2.3. MARKET ANALYSIS

The VTOL business aircraft is to be designed to seat 10 people, with a range and speed much higher than that of a helicopter and most likely lower than that of a business jet. It is clear that the market for a VTOL aircraft will grow out of the existing market for business jets and corporate helicopters of comparable sizes.

A VTOL aircraft matching the given requirements is ideal for those customers who wish to transport a small group of people from an office building, for example, to another location as fast as possible. It may be slower than a traditional business jet but its VTOL capabilities remove the need to travel to an airport, often through heavy city traffic or by helicopter transfer. It is faster, flies further and is most likely quieter and less expensive to operate than the existing corporate helicopters. Currently the midway between business jets and corporate helicopters is chosen as the only potential market. Other roles such as patrol, search and rescue (S&R), and emergency medical services (EMS) are neglected here. There is most likely a potential market for a successful civilian VTOL aircraft in these roles, but this is outside the scope of this Design Synthesis Exercise.

Extrapolation of expected helicopter and business jet values yields a potential market for some 26,500 VTOL business aircraft over the span of 20 years, worth more than $450 billion. Averaging the price in the potential market and adjusting roughly for inflation, a unit price of about $20 million can be used as an estimate. In that case, sales of 500 aircraft over 20 years would lead to a market share of only 1.9%, a rather realistic slice of the cake, yet still $10 billion in revenues. For a more elaborate market analysis the reader is referred to the Baseline Report [28]. A market outlook is also presented in Section 10.4.

2.4. CONCEPT SELECTION PROCESS

This section outlines a short recap on the procedures taken during the previous two phases of the project. Preliminary concepts for the design of the InVADe aircraft were investigated and traded off based on the set requirements. To get more insights into the preliminary concepts and the work performed in the Baseline and Mid-Term Report, the reader can refer to these two reports, [28], [29].

2.4.1. CONCEPT CREATION & FEASIBILITY CHECK

During the baseline reporting, the group started the concept formation of InVADe by a brainstorm session; this resulted in a list of 18 VTOL concepts. The brainstorm session was followed by further research on the plausibility of these technologies. Through a preliminary feasibility check, the non feasible ideas were excluded from the concepts. Hence, a list of 8 preliminary concepts was formed to be further developed as potential and practical concepts for the design of InVADe. These concepts are shortly described below:

1. *4 Ducted Fans*
   Based on the Bell X-22 aircraft; an aircraft with 4 tilting ducted fans.

2. *Deflected Slipstream*
   The idea is to deflect the slipstreams from the engines downwards to approximately 90 degrees with respect to the horizontal flow, to achieve upward thrust at take-off.

3. *Hexplane*
   A three-surface aircraft powered by six independent tilting propeller engines.

4. *Blended Wing Body (BWB)*
   Comparable to the tiltrotor, the BWB concept has two tilt rotors placed within the wing.

5. *Heliplane*
   A fixed wing aircraft with a helicopter rotor mounted on top of it

6. *Joint Strike Fighter BWB*
   Based on the propulsive system found in the F35B, a VTOL fighter jet developed in the Joint Strike Fighter program. This concept combines that engine with a blended wing body.

7. *Tiltrotor*
   Based on the V280 aircraft; using two powered rotors mounted on rotating engine pods at the tips of a fixed wing.

8. *Tiltrotor with retracting blades, TRAC*
   Based on the tiltrotor concept. However, unlike a conventional tiltrotor, it uses retracting blades which allow the rotor to optimise for hover and cruise by varying the blade size.

2.4.2. PRELIMINARY TRADE-OFF

Having introduced the 8 practical InVADe concepts, they were further examined to acquire more knowledge on the main characteristics of each concept. This was done in order to investigate the extent to which they could fulfil the requirements set by the clients and the airworthiness regulations. Once the concepts were further elaborated, a preliminary trade-off was performed, on the basis of the 10 criteria which emerged from the requirements. These criteria were as follows:

1. Noise
2. Speed
3. Weight
4. Readiness
5. Controllability & Stability
6. Cost
7. Transition
8. Propulsive Efficiency
9. Redundancy
10. Complexity

For the trade-off, all eight concepts were graded based on their compatibility with the criteria introduced above. The following three concepts with the highest overall scores in the trade-off were selected for further investigation for the final design of InVADe:

1. *4 Ducted Fans*

2. *Helipane*

3. *TRAC*

2.4.3. FINAL THREE CONCEPTS

The three final possible concepts for InVADe, mentioned above, entered the Mid-Term report. In the Mid-Term report the three concepts were investigated into more depth. Through initial Class I weight estimations and sizing, general sizing parameters of these concepts were determined. With deeper studies, estimations of key characteristics of each concept such as speed, weight and cost was determined. This was done such that it gave the group the proper concept-based knowledge required to compare all three concepts and select the most appropriate concept for the design of InVADe.

Below, a more detailed description of the final three concepts is shown, along with an illustrations of all concepts.

4 Ducted Fans

The 4 Ducted Fans concept, which was primarily based on the Bell X-22, has like the name suggests four ducted fans. These fans can be tilted to transform the aircraft from a vertical flying machine into a horizontally flying one.

The fans are powered using a series of drive shafts and gear boxes which transfer the power generated by the two turboshaft engines to the fans. An illustration of this concept is shown in Figure 2.2.

Figure 2.2: Illustration of the 4 Ducted Fans concept

Table 2.3: 4 Ducted Fans Preliminary Calculations

Parameter	Value	Unit
1. Noise	76	dB
2. Unit Cost	8.43 M	EUR
3. Weight	8,105	kg
4. Specific Range	1.12	km/kg
5. Operating Cost	2,216	EUR/h

Heliplane

The heliplane is simply a fixed wing aircraft with a helicopter rotor mounted on top of it. In this way, the vehicle can really perform a take off as a helicopter would and after that, fly as a normal aircraft. In the latter the rotor can be used as a stop rotor or as an autogyro. This layout is illustrated in Figure 2.3. Outcomes from preliminary calculations are presented in Table 2.4

Figure 2.3: Illustration of the Heliplane concept

Table 2.4: Heliplane Preliminary Calculations

Parameter	Value	Unit
1. Noise	86	dB
2. Unit Cost	7.62 M	EUR
3. Weight	7,761	kg
4. Specific Range	1.43	km/kg
5. Operating Cost	2,032	EUR/h

TRAC

The TRAC concept is based on the tiltrotor aircraft, which generates lift and propulsion by using turboshaft engines. The engines are mounted at the tip of a fixed wing. The most comparable aircraft for the TRAC concept are the AgustaWestland AW-609 and V-22 Osprey. The two turboshaft engines can be rotated upwards and downwards to perform take-off and cruise flight, respectively. An illustration of this concept is given in Figure 2.4.

Figure 2.4: Illustration of the TRAC concept

Table 2.5: TRAC Preliminary Calculations

Parameter	Value	Unit
1. Noise	92	dB
2. Unit Cost	7.28 M	EUR
3. Weight	7,029	kg
4. Specific Range	1.54	km/kg
5. Operating Cost	1,923	EUR/h

2.4.4. FINAL TRADE-OFF

The final trade-off consisted of the comparison of the final three InVADe concepts, based on the modified trade-off criteria, shown below:

1. Noise
2. Readiness Level
3. Control & Stability
4. Specific Range
5. Weight
6. Unit Cost
7. Safety
8. Operating Cost
9. Complexity
10. Sustainability

The result, after performing a sensitivity analysis to validate the trade-off methodology, presented the *4 Ducted Fans* concept as the winner and thus the appropriate concept for the InVADe aircraft; it was followed by the Heliplane in second place. This concept is further investigated and designed in this report to produce a preliminary design for InVADe.

2.4.5. FINAL DESIGN

Up until this moment, the design of the 4 Ducted Fans concept is based on the design of reference aircraft like the Bell X-22 and Curtiss-Wright X-19. Although these designs would be able to fulfil the mission requirements set by the client and the engineering team, the design would not employ new, innovative technologies. It was decided to innovate both internally and externally, not just for the sake of employing new technologies, but to improve existing weaknesses of the existing designs. Therefore, the shortcomings of the reference aircraft were examined. These reference aircraft include the Bell X-22, Curtiss-Wright X-19 and the Doak VZ-4. The result of this analysis yielded the following deficiencies:

- Small Range
- Low Payload-to-MTOW ratio
- Low Lift-to-Drag ratio

As it can be seen in Figure 2.5, comparing to the initial 4 Ducted Fans concept (Figure 2.2) , the two rear fans are no longer placed at the tip of a rectangular straight main wing; in the new design, the rear fans will be housed inside the main wing, which is now a tapered wing and of a trapezoidal shape. With this new design, the rear fans will no longer be tilting during transition, thus they will only be used during take-off and landing, and will not assist the two front fans during cruise flight.

Figure 2.5: Illustration of the final 4 Ducted Fans design during VTOL operations

3

INVADE DESIGN

The following chapter will present the final design of InVADe. The first section will present the weight estimation. The weight estimation can be subdivided in a Class I and Class II weight estimation. The subsequent sections elaborate on the exterior and interior design of InVADe. Finally, the last section discusses the lift division.

3.1. WEIGHT ESTIMATION

Throughout the course of the project all weight estimation methods in aircraft design are categorised in so-called classes. Four different classes can be distinguished in terms of aircraft design [73]. These classes are listed below.

- Class I: Early Conceptual Methods
- Class II: Conceptual Methods
- Class III: Preliminary Design Methods
- Class IV: Detailed Design Methods

The scope of this project limits itself to a Class I and Class II weight estimation, as any more refined estimations would require a detailed design of the subsystems, which is not done in this preliminary design. The Class I weight estimation was performed using the fuel fraction method outlined by Roskam [101]. Additionally, the statistical based set of empirical formulae developed by Torenbeek [113] will be used for the Class II weight estimation. The following section will outline the characteristics of the Class II weight estimation and aims at explaining the iterative process which resulted in the final weight estimates. Below a small recap on the Class I weight estimation is given. For a more detailed description, the reader is referred to the Mid-Term Report [29].

3.1.1. CLASS I WEIGHT ESTIMATION

The Class I weight estimation was performed using the fuel fraction method. A fuel fraction is the ratio between the weight at the end and the weight at the beginning of a particular flight phase. For example, the fuel fraction for cruise flight is defined by Equation 3.1.

$$FF_{cruise} = \left(\frac{W_{end}}{W_{begin}}\right)_{cruise} \tag{3.1}$$

The fuel fraction method revolves around one important equation, namely Equation 3.2. Using this equation one can make a first order estimate of the MTOW of the to be designed aircraft. From requirements the value for the payload weight can be derived. The fuel fraction method can be used to compute the mission fuel fraction ($FF_{mission}$) and the reserve fuel fraction $FF_{reserve}$. The mission fuel fraction indicates the ratio between MTOW and Maximum Zero Fuel Weight (MZFW). It is assumed that the MZFW is attained at the end of the mission profile, which is described in section 2.2. The reserve fuel fraction $FF_{reserve}$ is ratio of reserve fuel over total fuel. A regression analysis of the relation between MTOW and OEW of reference aircraft will yield the values for the coefficients C_1 and C_2. The remainder of this subsection will elaborate on the fuel fraction method. For more information on how the regression analysis was performed, the Mid Term Report can be consulted [29].

$$W_{MTOW} = \frac{C_2 + W_{Payload}}{1 - C_1 - (1 - FF_{mission}) \cdot (1 + FF_{reserve})} \tag{3.2}$$

The value of the mission fuel fraction is computed by product of all fuel fractions of the corresponding flight phases. The sequence of fuel fractions was determined in the section on the mission profile (2.2) and can be seen in Equation 3.3.

$$\begin{aligned} FF_{mission} = & FF_{start} \cdot FF_{take-off} \cdot FF_{transition} \cdot FF_{climb} \cdot FF_{cruise} \cdot FF_{descend} \cdot FF_{transition} \cdot FF_{landing} \cdot FF_{shutdown} \cdot \\ & FF_{start} \cdot FF_{take-off} \cdot FF_{transition} \cdot FF_{climb} \cdot FF_{cruise} \cdot FF_{descend} \cdot FF_{loiter} \cdot FF_{transition} \cdot FF_{landing} \cdot \\ & FF_{shutdown} \end{aligned} \tag{3.3}$$

First, the cruise fuel fraction (FF_{cruise}) is computed using the following parameters as input in Equation 3.4: range (Ra), lift-to-drag ratio (L/D), specific fuel consumption (SFC), propeller efficiency (η_p).

$$Ra = \left(\frac{\eta_p}{g \cdot SFC}\right)_{cruise} \cdot \left(\frac{L}{D}\right)_{cruise} \cdot \ln(FF_{cruise}) \tag{3.4}$$

Second, the loiter fuel fraction (FF_{loiter}) is computed using Endurance (En), lift-to-drag ratio (L/D), specific fuel consumption (SFC), propeller efficiency (η_p) and loiter speed (V_{loiter}) as input in Equation 3.5.

$$En = \left(\frac{\eta_p}{V \cdot g \cdot SFC}\right)_{loiter} \cdot \left(\frac{L}{D}\right)_{loiter} \cdot \ln(FF_{loiter}) \tag{3.5}$$

The values of the remaining fuel fractions are determined using Roskam [99]. The decision was made to use the fuel fractions which are derived for regional turboprop aircraft. The values that Roskam suggest for the fuel fractions of different mission phases are listed below. Unfortunately, literature did not provide a value of the transition fuel fraction ($FF_{transition}$). It was estimated that this parameter has a value of 0.995 for both types of transition, i.e. transition from hover to climbing flight and vice versa.

- FF_{start} = 0.990
- $FF_{take-off}$ = 0.995
- FF_{climb} = 0.985
- $FF_{descent}$ = 0.985
- $FF_{landing}$ = 0.9975
- $FF_{shutdown}$ = 0.9975
- $FF_{transition}$ = 0.995

Moreover, the mission reserve fuel fraction $FF_{reserve}$ has to be determined. FAA regulations ([38] and [37]) state that an aircraft should have a minimum of 40 min and a helicopter a minimum of 30 min of extra fuel aboard to facilitate loiter or redirection in IFR conditions. In order to calculate the mission reserve fuel fraction, the assumption is made that the amount of reserve fuel is proportional to the loiter time fraction. The loiter time fraction is defined as loiter time divided by the total mission time. Calculations have shown that the mission will last for a maximum of 3.3 hours. Therefore, the loiter time fraction was computed to be equal to 0.15. Because of the aforementioned assumption, $FF_{reservefuel}$ was estimated to have a value of 0.15.

Using data from the regression analysis in combination with the values for the mission fuel fraction ($FF_{mission}$ and the reserve fuel fraction $FF_{reserve}$ one can estimate the value for MTOW using Equation 3.2. Following that, the OEW can be estimated using Equation 3.6. Finally, the amount of fuel can be estimated by subtracting the OEW and payload mass from the MTOW, as is indicated in Equation 3.7.

$$W_{OEW} = C_1 \cdot W_{MTOW} + C_2 \tag{3.6}$$

$$W_{Fuel} = W_{MTOW} - W_{OEW} - W_{Payload} \tag{3.7}$$

3.1.2. CLASS II WEIGHT ESTIMATION

The Class II weight estimation is based on empirical formulae derived from statistical reference data. As was advised by Dr. ir. R. Vos the Torenbeek method was used. In contrast to the Class I weight estimation the Class II weight estimation uses a large number of design characteristics as input. The weights of the following component groups are estimated by the Torenbeek method for the category 'Transport Aircraft':

- Fuselage
- Furnishings
- Engines
- Main Wing
- Haudralics/Electrics
- Fuel Tanks
- Canard
- Flight Controls
- Main Landing Gear
- Avionics
- Pressurisation System
- Powerplant Controls
- Vertical Tail
- Noise Landing Gear
- Oil System
- Paint
- Oxygen Systems

The above mentioned component groups are typically all groups a conventional aircraft is comprised of. However, in case of InVADe extra component groups are added which are listed below. Based on reference data, the value of these components and system were estimated.

- Front Ducts
- Back Ducts
- Tilt Mechanism
- Electrical Drivesystem

Finally, by taking the sum of all component groups one can estimate the value of the OEW. By rearranging the formula given in Equation 3.6, one can derive Equation 3.8. Using this equation, the corresponding value of the MTOW can be estimated. Finally, the fuel weight can be estimated using Equation 3.7.

$$W_{MTOW} = \frac{W_{OEW} - C_2}{C_1} \tag{3.8}$$

3.1.3. CLASS I-II ITERATION

The Class II weight estimation uses the outputs of the Class I weight estimation. However, the loop can be completed by redirecting the output of the Class II weight estimation and using it as an input for the Class I weight estimation, as explained in the next paragraph. If the output of the Class II converges once a number of n cycles are performed, one can assume the system is stable.

Although the MTOW and OEW are not directly used as input in the Class I weight estimate, a method was devised that enabled the incorporation of new output data into the next cycle. Equation 3.2 is used to compute the MTOW in the Class I weight estimate. One can see the inputs include the coefficients a and b. The coefficients a and b are derived from the regression analysis of several data points illustrating the ratio of OEW and MTOW of reference aircraft. These reference aircraft include the Bell X-22, Doak VZ-4 and Curtiss-Wright X-19. In order to make an iterative calculation possible, a MATLAB script was written that performs a regression for each cycle. During each new cycle, the output of the previous Class II estimate was added as another reference aircraft to the regression analysis.

In total, a number of 100 cycles were performed. Already after the 20th cycle the output values of MTOW and OEW do not vary more than 0.1%. Hence, it can be concluded that the values converge and the system is stable. Figures 3.1a and 3.1b indicate the value of MTOW and OEW throughout the first 20 cycles of the iterations. The final values of MTOW and OEW were determined to be 8290 kg and 5510 kg respectively. Table 3.1 indicates the weights of the main component groups.

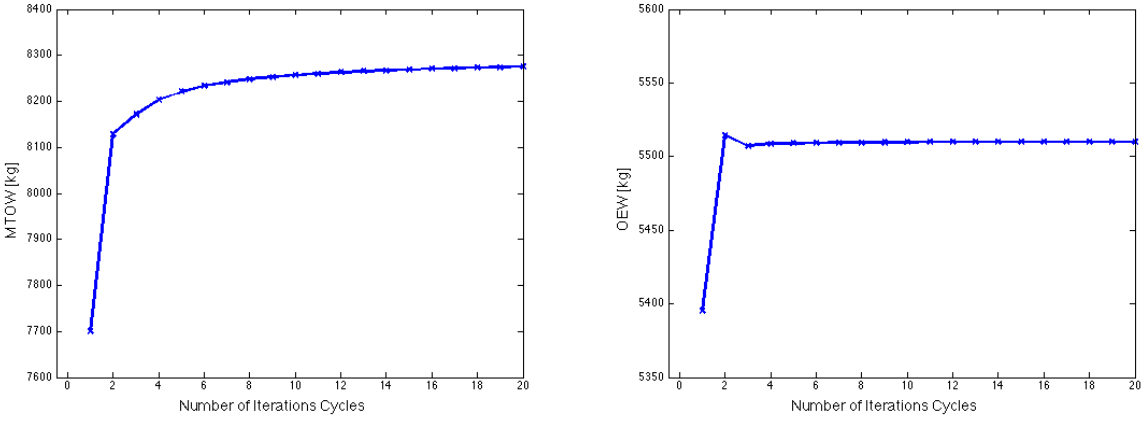

(a) MTOW per iteration

(b) OEW per iteration

Figure 3.1: Weight estimation iteration results

Table 3.1: Components weights and percentage of OEW of InVADe according to Class II weight estimate

Component Group	Weight [kg]	Percent [%]	Component Group	Weight [kg]	Percent [%]
Fuselage	732	13.3	Main Landing Gear	169	3.0
Front Ducts (inc. motors)	600	10.8	Avionics	120	2.1
Aft Ducts (inc. motors)	600	10.8	Pressurisation System	101	1.7
Furnishings	548	9.9	Tilt Mechanism	100	1.7
Electrical Drive System	500	9.1	Power Plant Controls	99	1.7
Engines	450	8.2	Vertical Tail	96	1.6
Main Wing	308	5.6	Equipment	38	1.6
Hydraulics/Electrics	257	4.7	Nose Landing Gear	38	0.6
Fuel Tanks	247	4.5	Oil System	32	0.5
Canard	245	4.4	Paint	23	0.4
Flight Controls	195	3.5	Oxygen Systems	11	0.2

3.2. EXTERIOR DIMENSIONS

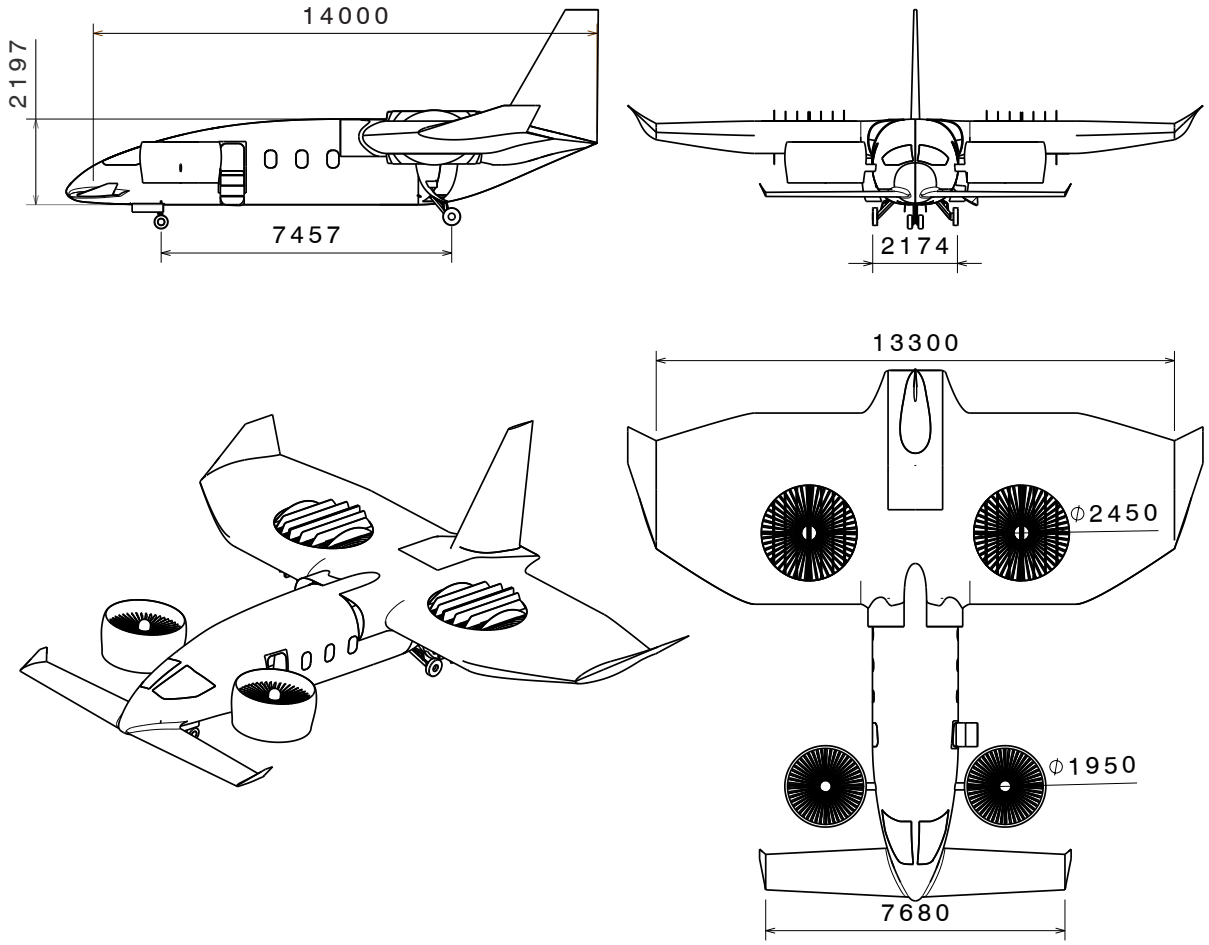

Figure 3.2: Technical drawings of InVADe

Figure 3.2 shows the exterior dimensions of an InVADe aircraft. Additional renders are presented in Appendix A.7.

3.3. INVADE INTERIOR DESIGN

The internal design of InVADe compromises several aspects. These are presented in the list below and will be elaborated upon in the next sections.

1. Cabin layout
2. Cockpit layout

3. Fuel system

4. Engines and electrical systems

3.3.1. CABIN LAYOUT

To size the inside of the fuselage the following parameters need to be set: flight deck length, door size, seat size, cabin size.

Table 3.2: Details of cabin components and the corresponding source

Component	Value	Unit	Source
Flightdeck length	2.5	m	La Rocca[71]
Door size	1.22x0.61	m	CS23 [35]
Aisle width	0.38	m	CS23 [35]
Emergency exit	0.48x0.66	m	CS23 [35]
Galley	0.76x0.92	m	Torenbeek [113]
Toilet	0.92x0.71	m	Torenbeek [113]
Seat pitch	0.90	m	Requirement Tm-cons-03
Seat width	0.48	m	Requirement Tm-cons-03
Baggage compartment	0.81	m^3	Requirement Tm-cons-06

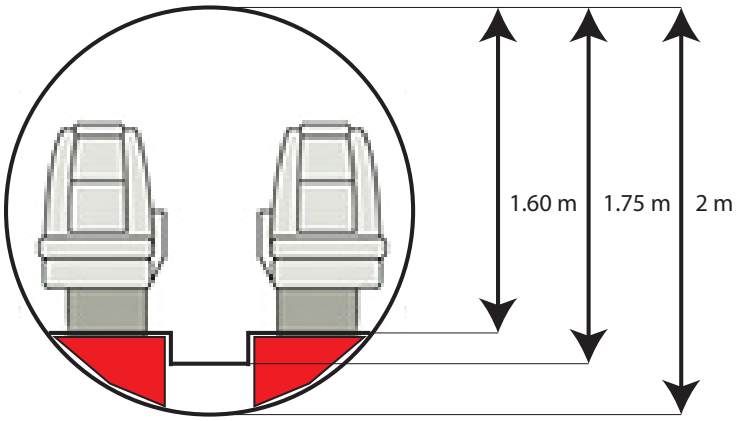

Figure 3.3: Cross-section of the cabin

In Figure 3.4 two cabin layouts are presented. Both layouts provide space for 10 passengers, a toilet, baggage compartment and small galley. The main difference between the two cabin configurations is the placement of the toilet, baggage compartment and galley. Configuration 1 (upper) locates the toilet and baggage in the back, while the galley is situated in the mid cabin. Configuration 2 (lower) is favourable since the passengers in this configuration are placed closer to the aircraft's center of gravity. Also more space is created for the wing structure with configuration 2.

Both configurations exhibit a main entrance and emergency exit as is obliged by the CS-23 regulations. Also the minimum aisle width of 0.38 m is taken into account. To ensure a comfortable head space the aisle floor is lowered, providing a cabin height of 1.75 m. The seat level is 0.15 m higher than the aisle floor creating room enough for the fuel tanks stored below (subsection 3.3.3). This is all illustrated in Figure 3.3. The seats are assigned such that the requirement on seat pitch is maintained. The cabin currently leaves room for wider seats than required, or other furniture such as small tables. The cabin also offers enough space to incorporate space for Wi-Fi equipment and power sockets. In terms of material use in the cabin design, degradable composites [20] are a good possibility to ensure sustainability of InVADe.

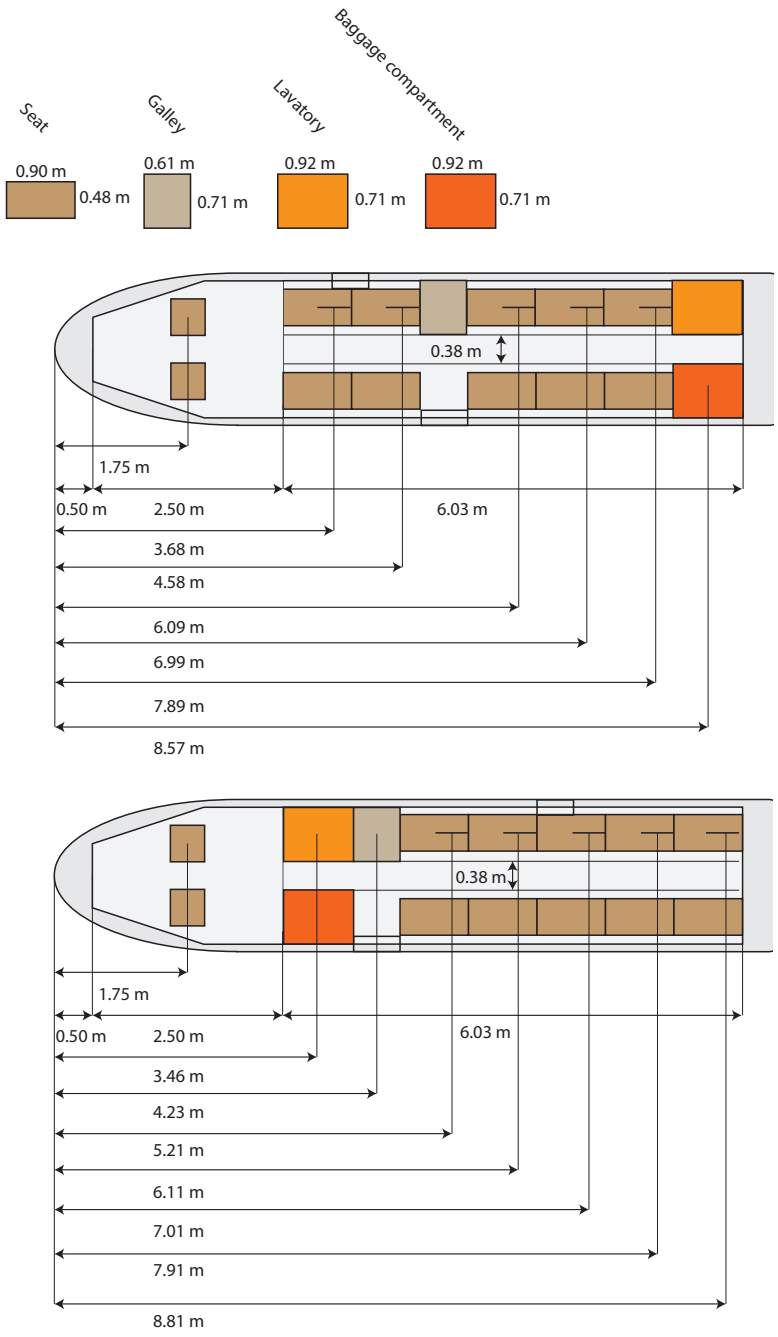

Figure 3.4: Two possible cabin layouts

3.3.2. COCKPIT LAYOUT

The cockpit design of the InVADe aircraft will incorporate a glass cockpit, in order to accommodate the digital instrument displays and gauges that will be installed. The flight deck has a length of 2.5 m, with room behind the pilots to store avionics systems and flight control computers.

As stated by CS-29 regulations, subpart CS 29.773(a)(1), " Each pilot compartment must be arranged to give the pilots a sufficiently extensive, clear, and undistorted view for safe operation " [34]. Since InVADe has a canard up front, the nose cone will be densely packed with structural elements and control lines. Also a weather radar is placed in the nose cone. This limits the space available for a window in the bottom of the cockpit. To ensure the pilots have sufficient sight during vertical landing and take-off, a camera will be installed, enabling a clear view on the ground. With the glass cockpit installed, this camera view can easily be projected on one of the center screens in the cockpit, while keeping important screens like the Primary Flight Display (PFD) active.

For control, the aircraft will be equipped with a Fly-by-Wire system. This means that no mechanical wires or rods are present and all control inputs will be send digitally to the corresponding control surfaces. The benefit

of this system is that every input of the pilot can be processed in a flight computer, checking if the input can be achieved and how the corresponding control surface should deflect. Especially with the configuration of InVADe such a system is very convenient to control the thrust generated by each engine and regulate the transition phase in terms of control. To provide input to the system the pilot has a joystick and a trust lever similar to the Airbus cockpit philosophy [4].

The cockpit will contain two Primary Flight Displays (PFD) which display the artificial horizon, speed and altitude. Two Multi Function Displays (MFD) can be used for navigation, engine gauges and the camera view upon landing and take-off. A Flight Computer Unit (FCU) will be used to program the autopilot. A general cockpit layout can be seen in Figure 3.5. A more detailed drawing of the sidestick is shown in Figure 3.6.

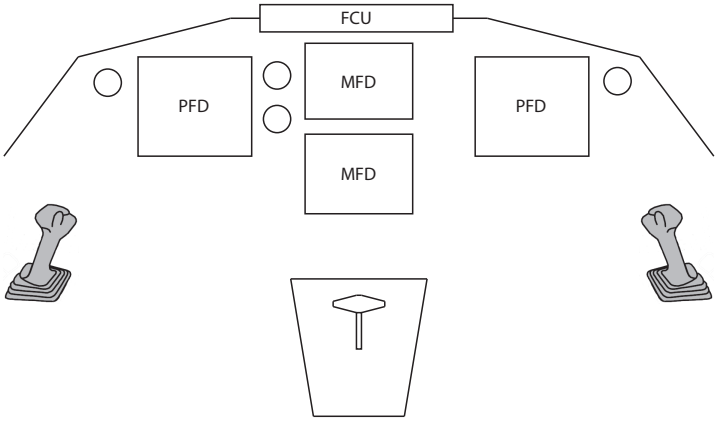

Figure 3.5: Basic cockpit layout

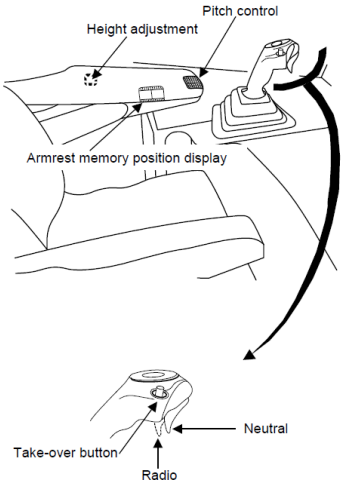

Figure 3.6: Joystick functions

3.3.3. FUEL SYSTEM

Fuel used by the aircraft is stored in four tanks. Two tanks are located underneath the cabin, and two more are present in the wings. As the aircraft center of gravity (c.g.) position is more or less in the fuselage center, the fuselage contains a large part of the fuel. It is favourable to have a large percentage of the fuel close to the aircraft c.g. position . This way the fuel burn will have only a minor influence on the aircraft c.g. location.

When fully loaded, the aircraft will contain 2,090 L of Jet A-1 fuel. To estimate the required space for fuel tanks, this number is slightly increased. From the AE2101 lecture slides [72] it was estimated that 4% of the fuel tank volume is taken up by systems. Also, a margin of 5% volume is required to account for fuel expansion during operations. The remaining 91% of tank volume is fuel. Taking this into account, the total volume required for fuel tanks is 2,297 L.

A total amount of 1,290 L of fuel will be stored under the cabin floor. The fuel tanks are indicated in Figure 3.3 as the shaded triangular areas below the cabin floor. The remaining 1,007 L is stored in two main wing tanks. These are located outboard of the ducts to relieve the bending loads of the wing during flight.
The fuel is fed to the engines powering the aircraft.

3.3.4. ENGINES AND ELECTRICAL SYSTEMS

The power plant is detailed in 5.5 and consists of two turboshaft engines, four generators, cables for distribution, a battery pack, and four electric motors.

The engines weigh 180 kg each and are roughly cylindrical with a diameter of 66 cm and a length of 124 cm. They are located in the top of the tail cone with air inlets located in the wing-fuselage intersection. The generators have the same diameter as the engines. Two generators are connected to the shaft of each engine and are located to the rear. The length of one generator is 21 cm and they weigh 95 kg each.

The main cables run from the generators to the electric motors. A large amount of secondary cabling will also be needed for all the small electric components in the aircraft. The weight is estimated to be 25 kg and it is distributed over the aircraft, thus has little effect on c.g. location.

The electric motors are each located in the hubs of the fans, where they are assumed to use the full diameter. The front motors weigh 103 kg each and are 61 cm long, the aft motors weigh 90 kg and are 34 cm long.

The battery pack is located in the tail cone of the aircraft and weighs 119 kg with a total volume needed of 0.25 m^3.

3.4. LIFT DIVISION

For the InVADe aircraft, five parts are selected to produce lift during flight. These parts, the main wing, canard, fuselage and the two ducted fans in the front, will produce the total lift needed during the flight phase. The process of dividing the lift to these specific parts is shown in Figure 3.7. From literature it can be stated that the fuselage of the Piaggio Avanti II generated 20 % of the total lift of the aircraft [45]. Therefore, the design of InVADe's fuselage will be an aerodynamic airfoil shape similar to the Avanti. As an assumption, 10 % of the lift is assumed to be obtained by this fuselage design. The remaining 90% is then divided over the other areas. According to the scissor plot obtained from the control & stability, the lift that shall be produced by the main wing is set to be 70%. The remaining 20% of the lift is then divided over the canard (15.1%) and the ducted fans in the front (4.9%), based on the amount of lift that can be generated by the ducted fans as will be explained below. A total overview of the lift division can be found in Figure 3.8.

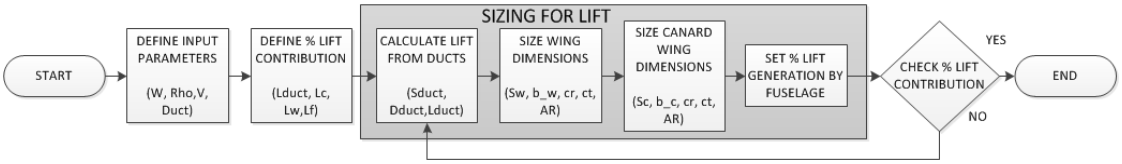

Figure 3.7: Lift division process

The total lift during cruise can be found by simplifying Equation 3.9 to Equation 3.10 using the following assumptions:

- Horizontal flight, $\gamma = 0$
- Horizontal flight, $\frac{d\gamma}{dt} = 0$
- Thrust points in direction of velocity, $\alpha_T = 0$

$$\frac{W}{g} V \frac{d\gamma}{dt} = L - W\cos\gamma + T\sin\alpha_T \tag{3.9}$$

$$L = W \tag{3.10}$$

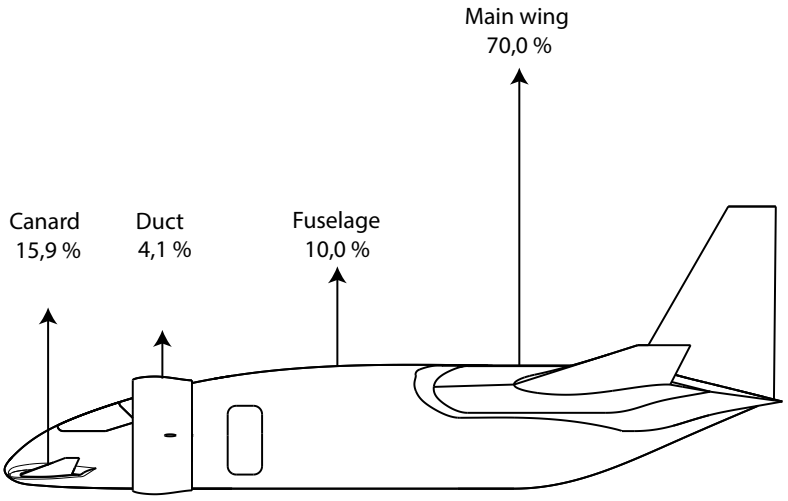

Figure 3.8: Division of lift between components

4

AERODYNAMICS

Looking at the mission profile, three different flight phases can be defined which are important for aerodynamic aspects. First, the transition phase, that is the phase after vertical take-off and in front of the conventional climb, as well as the phase after the conventional descend and in front of the vertical landing manouvre. Secondly, the climb/descend phase, which includes a conventional climb and descend profile. And last, the cruise flight phase, which is basically horizontal steady flight. For VTOL design, it is assumed that the transition phase is the critical flight phase. Therefore the wings are designed with respect to both cruise and transition characteristics. In order to distribute the lift components on the aircraft, a lift division has been set up, which can be found in Section 3.4. In the pages that follow, the aerodynamic design process will be described. Starting with some general aerodynamic relations, the aerodynamic characteristics for the main wing, canard, front ducted fans and vertical tail are computed. Then, a drag estimation is performed in order to find drag coefficients for each specific part of the aircraft. An analysis on the vortex generation of the main wing and canard is done, resulting in implementation of winglets to the design. At the end of this section a table with all the results is given. Finally, this chapter is closed with a verification and validation plan.

4.1. GENERAL EQUATIONS

In order to compute the general aerodynamic parameters for the aircraft, some basic equations are used. Each parameter will be discussed briefly below and results can be found in Section 4.9.

Aspect ratio

The aspect ratio (AR) is defined as a ratio of wing span (b) and wing area (S) and gives an indication of the slenderness of the wing. In general, the AR of the canard should be higher than that of the wing in order to stall first. A relation for aspect ratio (AR) can be found in Equation 4.1.

$$AR = \frac{b^2}{S} \tag{4.1}$$

Taper ratio

The taper ratio λ, being the ratio between the tip chord (c_t) and the root chord (c_r), is defined as in Equation 4.2. The main reason for adding taper to the wing is to affect the spanwise lift distribution of the wing. Increasing the taper ratio, that is increasing the tip chord length, results in more lift generated at the tip.

$$\lambda = \frac{c_t}{c_r} \tag{4.2}$$

Reynolds number

The non-dimensional velocity, the Reynolds Number (Re), is defined as a ratio of inertia force and viscous force (μ). A relation for this number can be found in Equation 4.3.

$$\mathrm{Re} = \frac{\rho \cdot V \cdot \frac{1}{2}(c_t + c_r)}{\mu} \tag{4.3}$$

Dynamic pressure

The kinetic energy per unit volume of a fluid particle is defined as the dynamic pressure ($\bar{q}$). A relation for this quantity can be found in Equation 4.4.

$$\bar{q} = \frac{1}{2} \cdot \rho \cdot V^2 \tag{4.4}$$

Mean aerodynamic chord

The mean aerodynamic chord (MAC) of a wing planform is an aerodynamic parameter which is used in aerodynamic and stability analysis for aircraft design. The MAC is defined as the chord of an imaginary airfoil which would have force vectors throughout the flight range identical with those of the actual wing. To calculate the length of the MAC ($\bar{c}$), Equation 4.5 is used. The spanwise position of the MAC ($\bar{Y}$) is then defined by Equation 4.6.

$$\bar{c} = \frac{2}{S} \int_0^{b/2} c^2 dy \tag{4.5}$$

$$\bar{Y} = \frac{b}{6} \cdot \left(\frac{1+2\lambda}{1+\lambda} \right) \tag{4.6}$$

4.2. MAIN WING

In this section the aerodynamic wing design will be discussed. First the methodology used is described and visualised. Then, a 2D analysis is done in order to select an appropriate airfoil for different parts of the main wing. From this 2D analysis, some 3D characteristics are translated. By having the wing lift coefficients defined, High Lift Devices can be selected as described in Section 4.2.5. Finally, the results of these analyses can be found in Section 4.9.

4.2.1. METHODOLOGY

To start designing a wing, the lift that the wing should generate must be defined. As a first estimate, the lift has been set equal to the weight during both transition and cruise phases, as shown in Equation 3.10. Having the weight defined, the design lift coefficient can be computed by the use of Equation 4.8, with factor k_c= 0.9 because of the canard configuration. Having the design lift coefficient, the maximum lift coefficient in both transition and cruise phase can be calculated using the general lift formula which can be found in Equation 4.7. By knowing the design ($C_{L_{des}}$) and maximum ($C_{L_{max}}$) lift coefficients, an appropriate airfoil can be selected as is done in Section 4.2.2. For the main wing, as well as the canard, it is assumed that the lift force acts at a quarter chord length of the wing. The wing area can be computed as a function of lift coefficient (C_L) and the lift. Finally, aspect ratio and wing span will follow from the wing area. This whole process is visualised in Figure 4.1.

Figure 4.1: Wing design process

$$C_L = \frac{2L}{\rho \cdot V^2 \cdot S} \tag{4.7}$$

$$C_{L_{des}} = \frac{k_c}{\bar{q}} \left\{ \frac{1}{2} \left[\left(\frac{W}{S} \right)_{start\,cruise} + \left(\frac{W}{S} \right)_{end\,cruise} \right] \right\} \tag{4.8}$$

4.2.2. AIRFOIL SELECTION (2D ANALYSIS)

In this section the airfoil selection process for the main wing will be discussed. The wing is designed to be a lifting surface. In order to understand how this lift force is generated, the wing cross section, that is the airfoil, must be studied. To determine the airfoil for InVADe an airfoil from a database by NACA & Eppler can be selected. Alternatively, a modified airfoil can be designed. Since the design of the airfoil is a complex and time-consuming process, the selection method is preferred.
To select an airfoil, the following aerodynamic parameters are needed:

- Airfoil design lift coefficient ($C_{l_{des}}$)
- Airfoil maximum lift coefficient ($C_{l_{max}}$)
- Reynolds number (Re)

To determine the lift coefficients (2D) of the airfoil ($C_{l_{des}}$), first the lift coefficients (3D) of the main wing ($C_{L_{des}}$) must be determined. This value can be obtained by the use of Equation 4.9. The maximum lift coefficient ($C_{l_{max}}$) of the airfoil is assumed to be equal to the maximum lift coefficient ($C_{L_{max}}$) of the wing (Equation 4.10) [103].

$$C_{l_{des}} \approx C_{L_{des}} \tag{4.9}$$

$$C_{l_{max}} \approx C_{L_{max}} \tag{4.10}$$

The main wing planform is divided in two sections, the outer and the inner. The inner section of the wing houses the ducted fans and the outer section consists of a conventional airfoil. Hence, two types of airfoils are selected for the main wing. This is done in order to design the main wing as much conventional as possible. Because of the ducts inside the inner section, the main wing would be of weird shape if a constant taper was introduced instead of two separate airfoils. To select a proper airfoil for the main wing, the following selection criteria are used [103]:

- The airfoil with proper design lift coefficient ($C_{l_{des}}$)
- The airfoil with highest maximum lift coefficient ($C_{l_{max}}$)
- The airfoil with lowest minimum drag coefficient ($C_{d_{min}}$)
- The airfoil with highest lift-to-drag ratio ($(C_l/C_d)_{max}$)

OUTER WING SECTION

For the outer section of the main wing, as defined in Figure 6.1, the following required aerodynamic design parameters are determined by the use of Equations 4.9 and 4.10 which are used for the airfoil selection process:

- $C_{l_{des}} = 0.2$
- $C_{l_{max}} = 1.6$

Thus for the airfoil selection one has to look for the NACA airfoil section that yields a design lift coefficient of 0.2 and a maximum lift coefficient of 1.6. To make selection process faster, a graph of maximum lift coefficient ($C_{l_{max}}$) versus design lift coefficient ($C_{l_{des}}$) for several NACA airfoil from Aircraft Design-A System Engineering Approach [103] is used. According to this graph, for a design lift coefficient of 0.2 and a maximum lift coefficient of 1.6 the following NACA profiles can be selected: 63(2)-215, 64(1)-212, 65(2)-215. These airfoils are evaluated at Reynolds number (Re) of 3 million. To evaluate the aerodynamic parameters of these airfoils at a Re of 17.2 million in cruise, XFLR5 is used. In Table 4.1 the results of evaluation of the aerodynamics design parameters for the three NACA profiles are compared against each other.

Table 4.1: Comparison of NACA profiles

No.	NACA	$C_{l_{max}}$	$C_{d_{min}}$	$C_{l_{des}}$	$(C_l/C_d)_{max}$	α_s (deg)	$(t/c)_{max}$(%)
1	63(2)-215	1.6339	0.00617	0.2	131	22.5	15
2	64(1)-212	1.6954	0.00656	0.2	130	19.5	12
3	65(2)-215	1.5855	0.00686	0.2	125	22.1	15

As mentioned before, the criteria as stated in Section 4.2.2 are used for the selection of the airfoil. Applying these selection criteria on these three evaluated airfoil will result in an airfoil to be used for the outer wing section. As can be seen form Table 4.1 the three airfoils have the same design lift coefficient. Comparing now the ($C_{l_{\max}}$) value, one can see that the NACA 63(2)-215 fulfils the required ($C_{l_{\max}}$) value of 1.6. This airfoil has the lowest ($C_{d_{\min}}$) value which yield highest maximum speed compared to other to airfoils. Also it has the highest $(C_l/C_d)_{\max}$ value which yields highest endurance and higher stall angle which yield lowest stall speed. Therefore the NACA 63(2)-215 is selected for the airfoil of the outer wing section of InVADe. Figure 4.2 shows the cross section of NACA 63(2)-215. In Figures 4.3a and 4.3b the graphs of the C_l-α and C_l-C_d are shown.

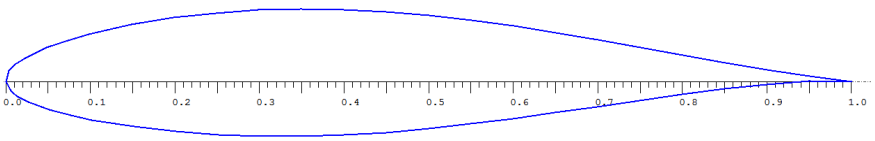

Figure 4.2: NACA 63(2)-215 airfoil for InVADe

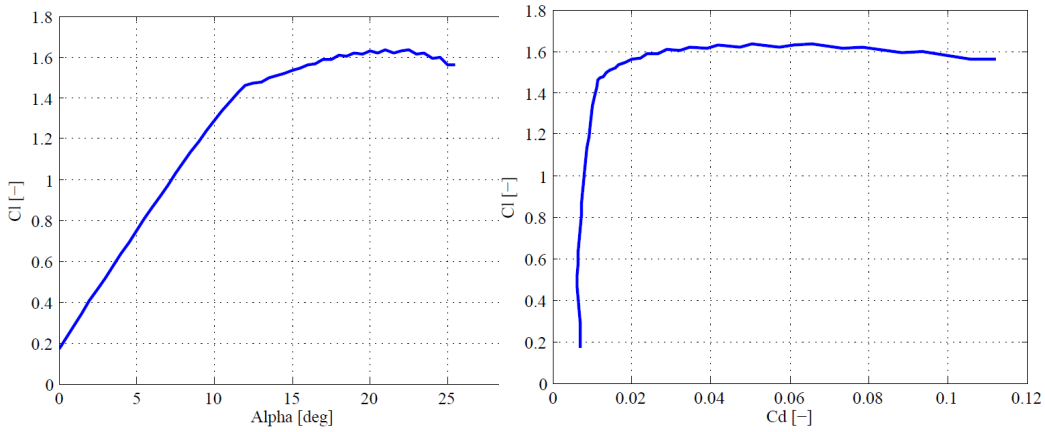

(a) C_l-α curve (b) C_l-C_d curve

Figure 4.3: Outer wing section characteristics

INNER WING SECTION

The inner section of the main wing is where ducted fans are placed. The ducts makes the selection of airfoils from existing NACA series very difficult. The ducts require a constant thickness over chord range. An airfoil with constant thickness over wide range of its chord length is difficult to find, therefore a new airfoil is designed. The design of the new airfoil is based on the NACA 12121 series which has a maximum thickness to chord ratio of 21 %. This airfoil is modified such that it has constant thickness for the chord length where the ducts are placed. For this modification XFLR5 is used to modify the shape of the airfoil such that the upper and lower part of the airfoil contains a flat part. The resultant shape of this airfoil is shown in Figure 4.4.

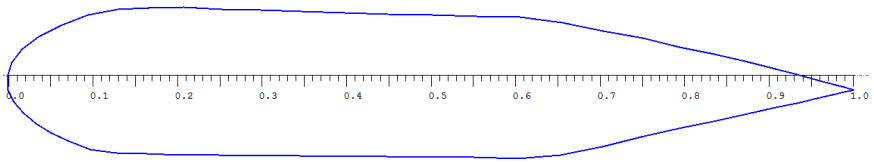

Figure 4.4: Inner wing section airfoil based on NACA 12121

Using XFLR5 the aerodynamic performance of this airfoil was investigated. The result are shown in Figure 4.5.

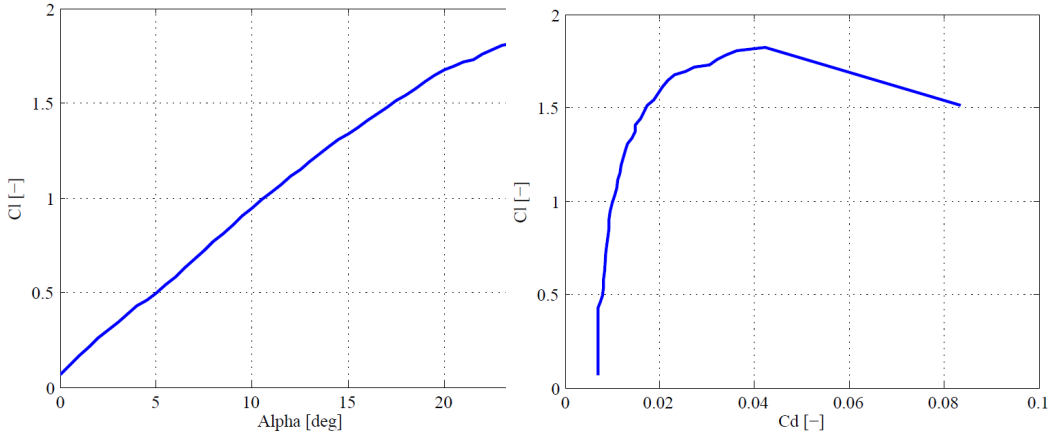

(a) C_l-α curve (b) C_l-C_d curve

Figure 4.5: Inner wing section characteristics

4.2.3. 3D LIFT CHARACTERISTICS

In order to get from the $C_l - \alpha$ to the $C_L - \alpha$ curve, Equation 4.11 is used from Raymer [96]. Analysing the outer section of the main wing, the lift curve slope and stall angle in 3D can be computed. From this formula a lift curve slope of 0.09 $\frac{1}{\text{deg}}$ is found. The stall angle is defined in Equation 4.12 and is computed to be 18.12 degrees, with $\Delta\alpha_{C_{L\text{max}}}$ equals to 1.5. Analysing the wing during transition phase, the inner section of the wing will be disturbed

in generating lift as the shutters of the main ducts will be opened. When the aircraft is approaching the transition point, the shutters will open in such a way that first half of the duct is opened, so that the other part still generates lift (see Figure 4.6). Because of the turbulent flow, it is assumed that that specific part of the wing, namely the half of the duct, is generating half of its actual lift. Although this is a rough estimate, it suffices for a first estimation of this lift component. Because this value is estimated, it is included in the risk assessment as can be found in Section 9.4.

$$C_{L_\alpha} = \frac{2\pi \cdot AR}{2 + \sqrt{4 + \left(\frac{AR \cdot \beta_M}{\eta}\right)^2 \left(1 + \frac{\tan^2 \Lambda_{0.5C}}{\beta_M{}^2}\right)}} \tag{4.11}$$

$$\alpha_s = \frac{C_{L_{\max}}}{C_{L_\alpha}} + \alpha_{0_L} + \Delta\alpha_{C_{L_{\max}}} \tag{4.12}$$

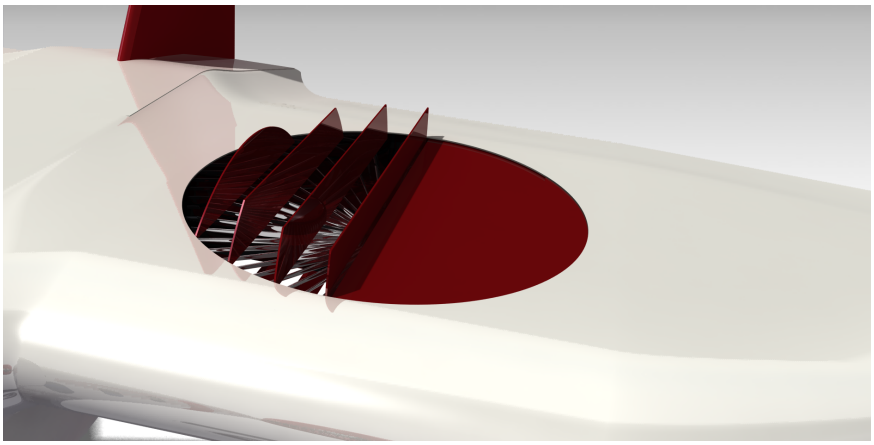

Figure 4.6: Duct half closed during transition phase

4.2.4. LIFT DISTRIBUTION

To determine the lift distribution of the main wing, lifting line theory is applied. This theory is applied to determine the lift generated along the span by the wing (lifting surface) without the use of Computational Fluid Dynamics (CFD). Using the lifting line theory method as explained in Aircraft Design [103], the lift distribution of the wing and canard is determined. For this method the geometry (chord and span) and the aerodynamic properties (α_0 and C_{l_α}) of the wing and canard must be known, which can be found in Section 4.9. In this method the one half of wing is divided into (N) segments and for each the corresponding angles χ which are a function of the lift distribution along one half of the wing. This angle varies between 0 for the last segment and 90 degrees for the first segment. The lift distribution is determined by using the lifting line relation as described in Equation 4.13.

$$\mu_L(\alpha_0 - \alpha) = \sum_{i=1}^{N} A_i \sin(i\chi) \left(1 + \frac{\mu_{L_i}}{\sin(\chi)}\right) \tag{4.13}$$

The parameter μ_L in Equation 4.13 can be determined as follows:

$$\mu_L = \frac{C_i \cdot C_{l_\alpha}}{4b} \tag{4.14}$$

In this equation C_i denotes the mean geometric chord of a segment, C_{l_α} the lift curve slope of segment(1/rad), and b the wing span. By using Equations 4.13 and 4.14, the coefficients A_i can be obtained. Afterwards Equation 4.15 used to determine the lift coefficient of each segment:

$$C_{L_i} = \frac{4b}{C_i} \sum A_i \sin(i\chi) \tag{4.15}$$

Using this equation the lift distribution of half span of the wing is plotted. In Figure 4.7 the lift distribution for the wing can be found. As the effect of the two different airfoils isn't analysed in detail yet, the lift distribution as in the figure is still preliminary. It is assumed that the influence of two different airfoils will affect the lift distribution, but this needs to be tested by wind tunnel tests or flow analysing programs.

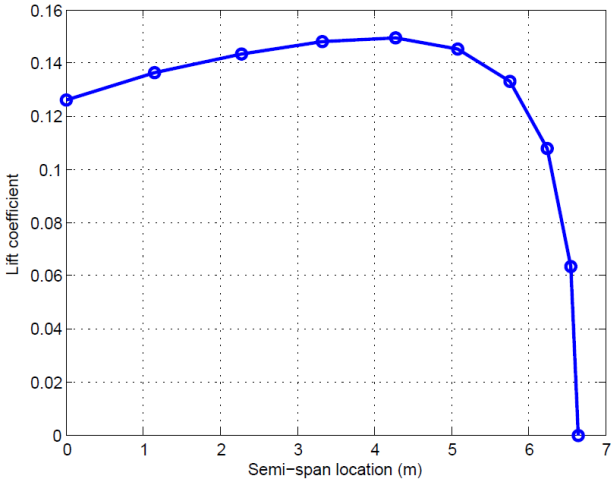

Figure 4.7: Lift distribution curve of the main wing

4.2.5. HIGH LIFT DEVICES

In this section, the methodology for selecting the high lift devices (HLDs) is explained. In order to size these HLDs, a step-by-step approach is used which will be explained by Figure 4.8. Having set the difference in $C_{L_{\max}}$, the suitable HLD device or combination of these devices can be selected. To do this, the chord fractions according to Raymer need to be set. This is done by Equation 4.16, being a function of the chord fractions. By knowing these values, Equation 4.17 can be used to find the so-called flapped area (S_{wf}). As a result, the use of fowler flaps is found to be the most optimal solution.

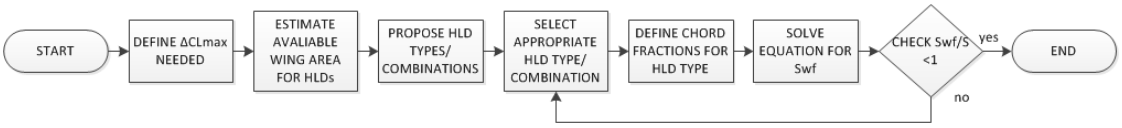

Figure 4.8: High lift devics selection process

$$\Delta C_{l_{\max}} = 1.3 \cdot \frac{c'}{c} = 1.3 \cdot \left(1 + \frac{\frac{\Delta c}{c_f} c_f}{c}\right) \tag{4.16}$$

$$\Delta C_{L_{\max}} = 0.9 \Delta C_{l_{\max}} \frac{S_{wf}}{S} \cos \Lambda_{hinge\_line} \tag{4.17}$$

4.3. CANARD

For designing the canard wing, the same procedure as in Section 4.2.1 is used. Figure 4.1 shows the procedure of the canard wing design. In the next section an appropriate airfoil will be selected and from that, 3D parameters will be computed.

4.3.1. AIRFOIL SELECTION (2D ANALYSIS)

The modified canard airfoil, as in Figure 4.9, has a camber value of 1.60 % chord at maximum position of 42 % chord and thickness of 10.75 % chord at maximum position of 39 % chord. In order to prevent wing stall, it is required for the canard to stall first. This will automatically result in pitch down of the aircraft. As mentioned in 4.2 the outer wing section stall at an angle of attack of 22.5 degrees. This means that the canard will stall first since the angle of attack of 21.1 degrees at the maximum lift coefficient is lower than that of the outer section of the main wing. In Figures 4.10a and 4.10b the 2D characteristics of this canard airfoil are shown.

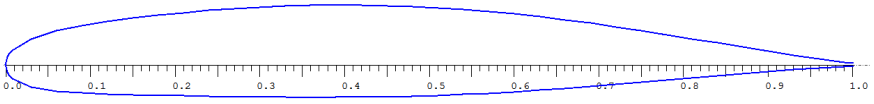

Figure 4.9: Selected airfoil for canard

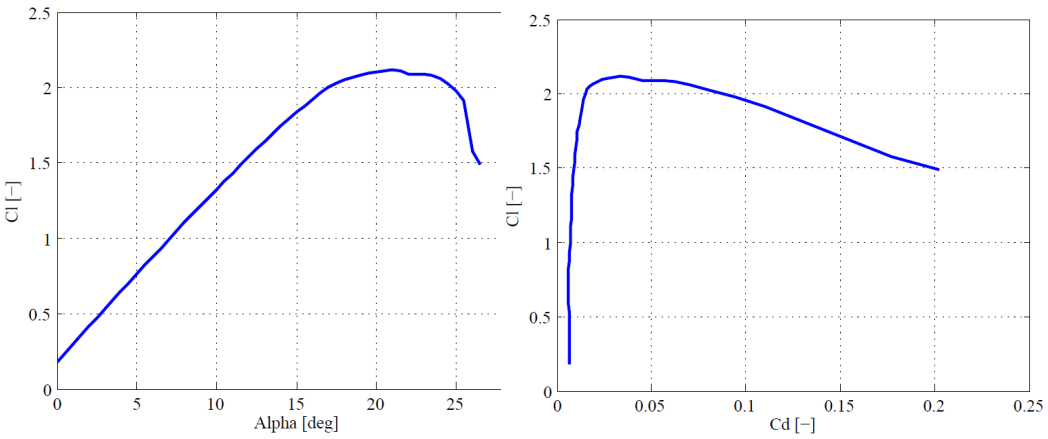

(a) C_l-α curve (b) C_l-C_d curve

Figure 4.10: Canard airfoil characteristics

4.3.2. 3D LIFT CHARACTERISTICS

To get the slope of the 3D $C_L - \alpha$ curve, Equation 4.11 is used. The slope of this curve is computed to be $C_{L_\alpha} = 0.089 \frac{1}{\text{deg}}$. The corresponding stall angle is computed to be $\alpha_s = 17.4\,\text{deg}$.

4.3.3. LIFT DISTRIBUTION

Using the same method as in Section 4.2.4, a lift distribution diagram for the canard has been generated as can be found in Figure 4.11.

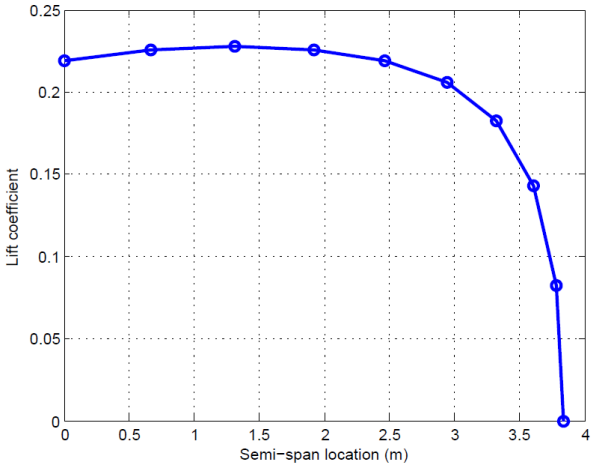

Figure 4.11: Lift distribution curve of the canard

4.4. FUSELAGE DESIGN

With respect to the sizing of the wings, the fuselage is designed in such a way that it produces 10% of the total lift of the aircraft. This value is based on a reference fuselage profile of the Piaggio Avanti. Although, Piaggio claims that their fuselage is able to generate 20% of the lift [45]. As a first estimate, half of this percentage is used to design the fuselage. The four lifting surface design balances lift over a larger surface arrea, which contributes to both the aerodynamics as well as stability & control. All wing surfaces produce postive lift and will therefore contribute to the design. The unique fuselage design of the Piaggio Avanti contains a single continuous aerodynamic curve, which reduces the drag dramatically. A detailed visualisation of the fuselage can be found in Section 3.2.

4.5. FRONT DUCTED FANS

In this section the aerodynamic analysis on the front ducted fans is described. First, the methodology to define the lift generation by the ducts is elaborated on. Then, the lift generating area is defined, followed by the airfoil selection of the front ducted fans. Results relating to these calculation can be found in Section 4.9.

4.5.1. METHODOLOGY

As the front ducts are providing the thrust during cruise and transition flight phases, the profile of the ducts is designed in such a way that it will produce lift. The top part of the duct, that is the upper part during cruise flight, contains an airfoil. In the following section the lift generating area of the front ducts is defined. Secondly, a brief explanation can be found on the lift generated by the ducted fans in front. In the last part, a summary of all the important parameters with respect to the lift contribution of the ducts can be found.

4.5.2. LIFT GENERATING AREA

The distance covered by the airfoil is shown in Figure 4.12 as a function of θ_{duct}. By knowing this angle θ_{duct}, the surface area of the lift generating part of the ducted fan can be defined as can be found in Equation 4.18.

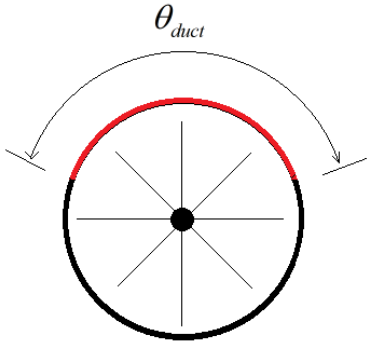

Figure 4.12: Definition lift generating area of duct

$$S_{duct} = \left(\frac{\pi \cdot \frac{d_{duct}}{2} \cdot \theta_{duct}}{180} \right) \cdot l_{duct} \tag{4.18}$$

4.5.3. 2D AIRFOIL ANALYSIS

To select an airfoil for the front ducted fans it is assumed that the airfoil must have a design lift coefficient of approximately 0.1 which is lower than that of the main wing and the canard. Furthermore at zero angle of attack it is not providing any lift. Therefore a symmetrical airfoil has been chosen for the front ducts which starts generating lift at an angle of attack of 1 degree. The shape of this airfoil is shown in Figure 4.13. The characteristic curves of this airfoil can be found in Figures 4.14a and 4.14b.

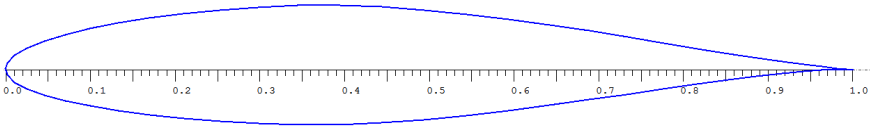

Figure 4.13: Front ducts airfoil

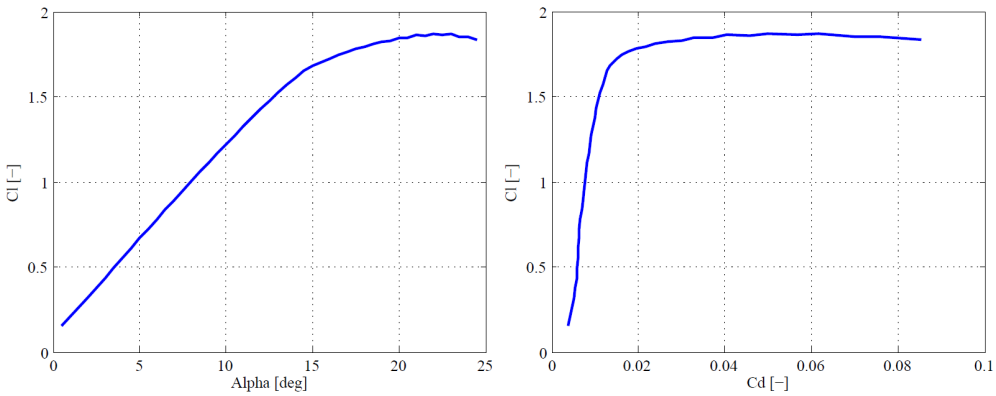

(a) C_l-$alpha$ curve (b) C_l-C_d curve

Figure 4.14: NACA 64-114 airfoil characteristics

4.6. VERTICAL TAIL

In this section the aerodynamic analysis of the vertical tail is described. First, a brief methodology description is given, followed by an elaboration of the airfoil selection process.

4.6.1. METHODOLOGY

Having obtained the geometric parameters from the control & stability calculations, in Section 7.2.2, the tail profile can be selected. This selection is done based on the surface area and length of the vertical tail.

4.6.2. 2D AIRFOIL SELECTION

To select an airfoil for the vertical tail, it should be noted that it also has vertical tail lift coefficient. One of the basic aircraft design requirements is the symmetry about xz plane of the aircraft. To ensure this symmetry, the airfoil of the vertical tail plane should be symmetric. Also since the vertical tail plane must be clean of compressibility effect, the Mach number there must be lower than the Mach number at the wing. To achieve this, the airfoil of the vertical tail must be thinner than the wing airfoil. When the outer part of the main wing has maximum thickness-to-chord ratio $(t/c)_{\max}$ of 0.15 (15 %), a symmetrical airfoil with maximum thickness-to-chord ratio $(t/c)_{\max}$ of 0.09 (9 %)can be selected for vertical tail [103] . The selected airfoil will be NACA 0009 airfoil, as shown in Figure 4.15 .

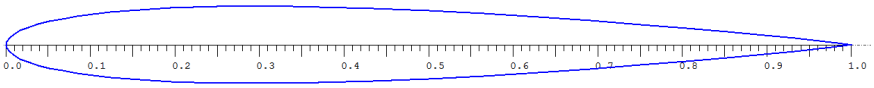

Figure 4.15: Selected NACA 0009 airfoil for vertical tail

4.7. DRAG ESTIMATION

In this section the drag force of the whole aircraft is estimated. First, the methodology is provided, including the division of the aircraft in parts. Then, for each part the relating drag coefficients are computed. Results relating to the calculations performed in this section can be found in Section 4.9.

4.7.1. METHODOLOGY

In order to determine the drag, the drag coefficient of the whole aircraft should be obtained. To do so, the aircraft is sub-divided in specific parts:

- Fuselage
- Main Wing
- Canard
- Vertical Tail
- Nacelles, that is the fairing around the front ducts
- High Lift Devices

For these parts, the relating zero-lift drag coefficient is computed in the sections below [102]. From this zero-lift drag coefficient, together with the lift coefficient of that specific part, the drag coefficient can be computed. Then, from these values the total aircraft drag can be calculated.

4.7.2. FUSELAGE

Similar to the design of the Piaggio P.180 Avanti fuselage design, the fuselage of InVADe will be designed in such a way that it is optimised for aerodynamic efficiency. The fuselage will be shaped in such a way that it promotes laminar flow. Using Equation 4.19, the drag of the fuselage is computed to be 0.00013.

$$C_{D_{o,fuselage}} = C_f \cdot f_{LD} \cdot f_M \cdot \frac{S_{wet,f}}{S} \tag{4.19}$$

Where C_f is the non-dimensional skin friction coefficient, determined by the use of the Prandtl relationship for laminar flow in the following equation:

$$C_f = \frac{0.455}{(\log \mathrm{Re})^{2.58}} \tag{4.20}$$

f_{LD}, the fuselage length-to-diameter ratio is defined as in Equation 4.21, with l_f and d_f being the fuselage length and diameter respectively.

$$f_{LD} = 1 + \frac{60}{\left(\frac{l_f}{d_f}\right)^3} + 0.0025\frac{l_f}{d_f} \tag{4.21}$$

Then, parameter f_M is used to correct for the Mach number the aircraft is flying at. This value is a function of the Mach number only as can be found in Equation 4.22.

$$f_M = 1 - 0.08MN^{1.45} \tag{4.22}$$

The wetted area of the fuselage is computed by the use of the CATIA model.

4.7.3. MAIN WING, CANARD AND VERTICAL TAIL

As the main wing is a lifting surface, having a Reynolds number relative to the chord length of the wing, the zero -lift drag coefficient can be computed by the use of Equation 4.23, where f_{tc} being a function of the maximum thickness ratio as defined in Equation 4.24. Regarding the zero-lift drag of the canard wing profile, the same method as for the main wing is used, with respect to the canard. As the vertical tail is, just like the canard and the main wing, a lifting surface, the same method can be used to estimate the zero-lift drag. Therefore the zero-lift drag of the vertical tail profile is calculated to be 0.0020, the same method as for the main wing.

$$C_{D_{0,wing}} = C_{f_w} f_{tc_w} f_M \left(\frac{S_{wet_w}}{S}\right)\left(\frac{C_{d_{\min_w}}}{0.004}\right)^{0.4} \tag{4.23}$$

$$f_{tc} = 1 + 2.7\left(\frac{t}{c}\right)_{\max} + 100\left(\frac{t}{c}\right)^4_{\max} \tag{4.24}$$

4.7.4. NACELLES

As the air flow is in direct contact with the engines, a method needs to be found to reduce the engine drag. The front ducts will be covered by nacelles, which function as an aerodynamic cover of the fans. Therefore, the zero-lift drag estimation, consists of the same equations used for the fuselage. As the nacelle length-to-diameter ratio is lower than two, it is assumed to be two for the calculations.

4.7.5. HIGH LIFT DEVICES

HLDs are used to enable the aircraft to generate more lift at low airspeeds. These devices will produces a lot of drag as well. To estimate the zero-lift drag created by the HLDs, Equation 4.25 is used, with $\frac{c_f}{c}$ being the fraction between the average flap chord and the average wing chord. δ_f is defined as the deflection angle of the flaps in degrees. The zero-lift drag generated by the HLDs is calculated to be 0.0174.

$$C_{D_{0,flap}} = \left(\frac{c_f}{c}\right) 0.00018\left(\delta_f\right)^2 \tag{4.25}$$

4.8. VORTEX ANALYSIS

The vortices that are active when the aircraft is flying will be analysed in this section. This section is split up into two paragraphs discussing the wake vortices generated by the ducted fans as well as the vortices due to the lift that is generated by the wings. From literature some assumptions on wake vortices are made in order to select the most optimal wing planform. Then, a simple model is used to visualise the tip vortices on both the canard and the main wing.

4.8.1. WAKE VORTEX

One of the most important steps in establishing the aircraft's planform is the effect of the propulsion system on the wing. As the outlet air stream of a propulsion system is disturbed with respect to the inlet stream it has a negative contribution to the aerodynamics of the aircraft. From literature, the downstream of a ducted fan contains wake vortices [127] [6]. These vortices contain so-called fan swirls, which reduce the propulsive as well as the aerodynamic efficiency [126] [111]. The contribution of these swirls can be complied with by adding an extra factor to Bernoulli's equation. Another option is to use a flow straightener after the fan in order to minimise the wake vortex.

Although the analysis above is based on a small amount of literature, the findings suggest that the airflow downstream of a ducted fan will affect the laminar flow over a wing, which is placed after the propulsion system. Therefore it can be said that the most efficient configuration of wings and propulsion system is as follows:

- A low-wing canard in front of the aircraft
- Two mid-wing placed ducted fans, one on both sides of the aircraft
- A high-wing placed main wing

Now, the number of limitations is reduced to a minimum by using this configuration. As the canard produces a downwash, the inflow of the ducted fans will not be influenced to a large extent. Since the ducts are positioned at mid-wing level and the main wing at high-wing level, the effect of the outlet stream of the ducts is minimised. This wing planform is visualised in Section 3.4.

4.8.2. WING TIP VORTEX

The effect of wing tip vortices can be modelled using the simple model represented in Figure 4.16a. This model is based on the lifting-line theory, where each component is modelled as a separate horseshoe vortex [70]. Trailing vorticity will be generated by the change in bound circulation on the wing. This vorticity then rolls up from the tip. Vorticity can be defined as a function of the angular velocity of a small volume in space. In a velocity field, the curl of the velocity is equal to the vorticity as defined in Equation 4.26. The vorticity is related to the circulation of the flow along a closed path by the Stokes equation.

$$\xi = 2\omega = \left(\frac{\delta \bar{w}}{\delta y} - \frac{\delta \bar{v}}{\delta z}\right) i + \left(\frac{\delta \bar{u}}{\delta z} - \frac{\delta \bar{w}}{\delta x}\right) j + \left(\frac{\delta \bar{v}}{\delta x} - \frac{\delta \bar{u}}{\delta y}\right) k = \nabla \times V \tag{4.26}$$

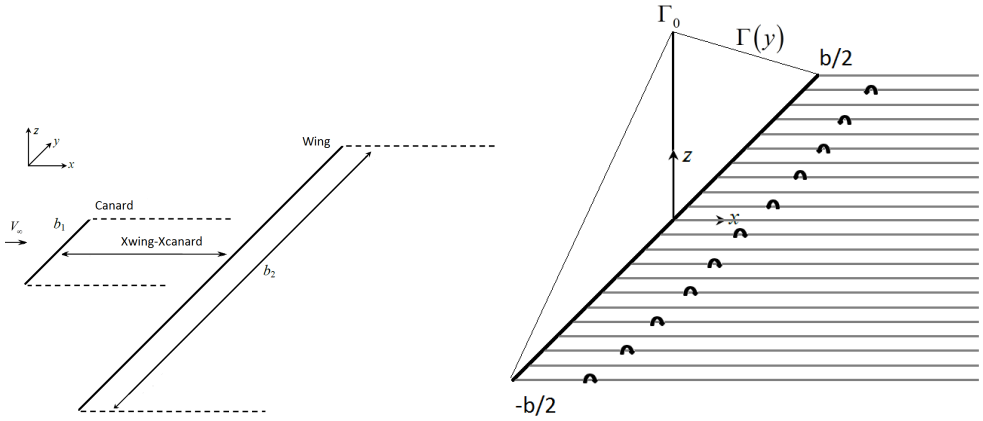

(a) Lifting-line vortex model (b) Vortex model main wing

Figure 4.16: Lifting-line and main wing vortex models

According to the model shown in Figure 4.16a, Equations 4.27, 4.28, 4.29, 4.30, 4.31 and 4.32 can be defined. As the main wing consists of two different airfoils, two different functions for the circulation have been set up.

$$\Gamma_{inner} = \Gamma_{0,inner}\left(\frac{b}{2} + \frac{y}{0.35b}\right), \; for \; -0.35b < y < 0 \tag{4.27}$$

$$\Gamma_{inner} = \Gamma_{0,inner}\left(\frac{b}{2} - \frac{y}{0.35b}\right), \; for \; 0 < y < 0.35b \tag{4.28}$$

$$\Gamma_{outer} = \Gamma_{0,outer}\left(0.15b + \frac{y}{0.15b}\right), \; for \; -0.15b < y < 0 \tag{4.29}$$

$$\Gamma_{outer} = \Gamma_{0,outer}\left(0.15b - \frac{y}{0.15b}\right), \; for \; 0 < y < 0.15b \tag{4.30}$$

$$\Gamma_{canard} = \Gamma_{0,canard}\left(\frac{b_{canard}}{2} + \frac{y}{0.5b_{canard}}\right), \; for \; -0.5b_{canard} < y < 0 \tag{4.31}$$

$$\Gamma_{canard} = \Gamma_{0,canard}\left(\frac{b_{canard}}{2} - \frac{y}{0.5b_{canard}}\right), \; for \; 0 < y < 0.5b_{canard} \tag{4.32}$$

From this vortex model, the induced velocity of the canard at the main wing can be determined by the use of the Biot-Savart equation, defined in Equation 4.34. With χ_A and χ_B calculated from Equation 4.33,

$$\chi_A = \chi_B = \tan^{-1} \cdot \left(\frac{x_{wing} - x_{canard}}{b_{canard}/2}\right) \tag{4.33}$$

the induced velocity of the canard, V_{canard} becomes:

$$\Delta V_{canard} = \frac{\Gamma}{4\pi b}\left(\cos\varphi_A + \cos\varphi_B\right) \tag{4.34}$$

Next, the strength of the vortex wake at spanwise position y, corresponds to the local change in bound circulation $\frac{d\Gamma}{dy}$.
As it is difficult to predict the exact vortices created in this stage of the project, this section can be elaborated on in future detailed design phases. Therefore, as a recommendation, this model can be visualised using CFD programs.

4.8.3. WING TIP DEVICES

As a result of generating lift, wings produce air motion. This air motion causes circulation in the downward direction below the wing and upward outboard of the wing tips. Because of this, the lift vector of the wing will be directed slightly backward, resulting in an increase of induced drag. In order to reduce the drop in the aircraft's performance due to wing tip vortices, the aircraft's flow field needs to be changed. Wing tip devices can be used for that purpose. These devices help reduce the effective angle of attack of the wing through the induction of downwash. As a result, the fuel burn will decrease as well, resulting in a payload and/or range increment.

In recent years, there has been an increasing amount of literature on wing tip design. Several studies from Boeing and Airbus claim that their own type of blended winglet designs, winglets and sharklets respectively, result in a drop of induced drag, emissions as well as community noise [46]. Although, the winglets will only influence the noise during horizontal flight, that is the time between transition after departure and transition after cruise, it is still a useful feature to have in an aircraft. Summarising, winglets will add a positive contribution on the sustainability of this aircraft design. As there are lots of wing tip devices, the most suitable solutions for InVADe will be discussed below.

BLENDED WINGLETS

To reduce the total kinetic energy of the flow field of the wing, upward-swept extensions can be mounted on the wing tips. This is the blended winglet principle. A large ratio, together with a smooth chord variation in the transition section, increase the geometric wingspan of the aircraft [95].

RAKED WING TIP

Raked tips are beneficial for unloading tips without reducing the tip chords that much. Because raked wing tips are commonly used on long haul high speed aircraft only, this may not be the ideal option for InVADe.

ACTIVE WINGLETS

Recently Tamarack Aerospace [112] came up with a new type of winglet design. This winglet, the active winglet, is supposed to offer weight-saving aerodynamic improvements to the aircraft design. As this solution is still new, a lot of research can be done in the coming years. Therefore, as a recommendation, research can enable the use of this type of winglets for InVADe.

INVADE WING TIP DESIGN

For now, based on devices that have been researched, the blended winglets are used for InVADe. Although, as mentioned above, new types of winglets that will improve the design can be studied.

4.9. RESULTS

All calculated aerodynamic parameters can be found in Table 4.2.

4.10. VERIFICATION

XFLR5 was used for airfoil selection. This program computes the aerodynamic parameters including lift coefficient (C_l), drag coefficient (C_d) and moment coefficient (C_m) of the airfoil. To verify the results of XFLR5, JavaFoil is used. When comparing the result of JavaFoil with XFLR5, a difference of approximately 25 % was found for maximum lift coefficient for a Reynolds number of 17.2 million. This difference can be explained by the fact that JavaFoil gives quite inaccurate results when the airfoil is analysed beyond stall. Moreover, JavaFoil does not model the laminar separation bubble phenomenon and flow separation. The results are incorrect if either of those errors occur. Therefore XFLR5 is preferred over JavaFoil, and is used primarily.

The aerodynamic parameters are calculated using Raymer's [96] and La Rocca's [103] methods. The results of these methods can be verified with Roskam [99]. However, Raymer and La Rocca are reliable sources, these results should be checked in the next phase.

4.11. VALIDATION PLAN

In this validation plan several methods to validate the results obtained from the aerodynamics chapter are described. First the computational fluid dynamics (CFD) principle is described, together with the specific topics that can be validated using this principle. Next, wind tunnel testing is discussed. Finally, value checking, based on reference aircraft data is performed.

Table 4.2: Results Aerodynamics

Parameter	Symbol	Value	Unit
Aircraft			
Lift over Drag Ratio	L/D	9.17	-
Lift Coefficient Aircraft	$C_{L_{aircraft}}$	0.22	-
Drag Coefficient Aircraft Cruise	$C_{D_{aircraft}}$	0.0244	-
Drag Coefficient Aircraft Transition	$C_{D_{aircraft}}$	0.0418	-
Zero-Lift Drag Coefficient Fuselage	$C_{D_{0,fuselage}}$	$1.2983 \cdot 10^{-4}$	-
Zero-Lift Drag Coefficient Wing	$C_{D_{0,wing}}$	0.0020	-
Zero-Lift Drag Coefficient Canard	$C_{D_{0,canard}}$	0.0035	-
Zero-Lift Drag Coefficient Tail	$C_{D_{0,tail}}$	0.0057	-
Zero-Lift Drag Coefficient Nacelles	$C_{D_{0,tail}}$	0.0078	-
Zero-Lift Drag Coefficient HLDs	$C_{D_{0,tail}}$	0.0174	-
Drag Force Cruise	D_{cruise}	8,344	N
Main Wing			
Aspect Ratio	AR	6.19	-
Wing Span	b	13.3	m
Wing Area	S	28.64	m^2
Wing Loading	W/S	223.3	kg/m^2
Taper Ratio	λ	0.41	-
Root Chord	c_r	4.9	m
Tip Chord	c_t	2.0	m
Oswald Factor	e	0.846	m
Mean Aerodynamic Chord length	$\bar{c}$	3.66	m
Maximum Lift Coefficient Outer Part	$C_{L_{\max}}$	1.63	-
Maximum Lift Coefficient Inner Part	$C_{L_{\max}}$	1.86	-
3D Lift Curve Slope	C_{L_α}	0.09	$\frac{1}{\text{deg}}$
3D Stall Angle	α_{stall}	18.12	deg
HLDs			
Flapped Surface	Swf	5.2	m^2
HLD Lift Coefficient	$\Delta C_{L_{\max}}$	0.3	-
Maximum Deflection Angle	δ_f	25	deg
Canard Wing			
Aspect Ratio	AR	6.95	-
Wing Span	b	7.68	m
Wing Area	S	8.49	m^2
Wing Loading	W/S	146.6	kg/m^2
Taper Ratio	λ	0.41	-
Root Chord	c_r	1.3	m
Tip Chord	c_t	0.91	m
Oswald Factor	e	0.831	m
Maximum Lift Coefficient	$C_{L_{\max}}$	1.55	-
3D Lift Curve Slope	C_{L_α}	0.089	$\frac{1}{\circ}$
3D Stall Angle	α_{stall}	17.4	deg
Front Ducted Fans			
Angle Lift Generating Area	θ_{duct}	120	deg

4.11.1. COMPUTATIONAL FLUID DYNAMICS

By the use of the verified MATLAB code and a verified conceptual model, CFD simulation can be performed in order to validate the values computed in the mathematical analysis. As CFD uses mathematical equations in the code, it is possible to contain errors, this should not be the only way to validate. The vortex model, as described in Section 4.8, can be analysed by the use of CFD in order to get a good visualisation of the flow behaviour at the wing tips.

4.11.2. WIND TUNNEL TESTING

Validation of several parts of the aircraft can be done by wind tunnel testing. To do so, accurate wind tunnel models shall be designed. To minimise the uncertainty of the simulation outcomes, the models must be to scale with respect to the actual design, so that the the performance of the actual design can be translated from the test

results. The Reynolds number of the scale model should be the same as for the large object when working under its design conditions (principle of dynamic similarity). The lift curves generated with XFLR5 and JavaFoil can be validated using wind tunnel test data. This can be done by analysing the points on the airfoil where turbulent flow occurs.

4.11.3. VALUE CHECKING

The drag parameters obtained from the calculations in Section 4.7, can be validated through the use of reference aircraft data [49]. The drag coefficient of InVADe is within a range between the Learjet 24 and Cessna 182 as can be found in Table 4.3.

Table 4.3: Drag coefficient checking

Parameter	**InVADe**	**Learjet 24**	**Boeing 787**	**Cessna 182**
C_D	0.0244	0.022	0.024	0.027

4.11.4. EFFECT OF ASSUMPTIONS ON RESULTS

As, for this preliminary design process, some simplifying assumptions were made, the effect of this assumptions should be analysed. For transition, it is assumed that the aircraft's lift equals its weight. Although, during transition, the aircraft does not fly horizontally, but climbs or descends. Therefore there won't be a 100% force equilibrium between lift and weight. As a result, the values obtained are not 100% accurate. To start the detailed design, a more accurate estimation should be done in order to get more precise values.

5

PROPULSION

InVADe's propulsion systems are discussed in this chapter. First, the design of the fans and the ducts will be discussed in Section 5.1, which is followed by the analysis on the required engine powers in various phases of the flight, presented in 5.2. Next, Section 5.3 includes an analysis on the noise emissions of InVADe, followed by a discussion of possible mitigation methods in Section 5.4. Last, in Section 5.5 the power plant design is considered. This includes a trade-off between options, sizing of all relevant components and finally engine selection.

5.1. DUCTED FAN DESIGN

Being the key components of the InVADe aircraft, the design of the ducted fans is considerably important. During the Midterm report [29], as it was briefly mentioned in Section 2.4.3, the design of the InVADe aircraft was mainly based on the Bell X-22 design, shown in Figure 5.1. The final design of the ducted fans in the Mid-term indicated a fan size of 2.95m.

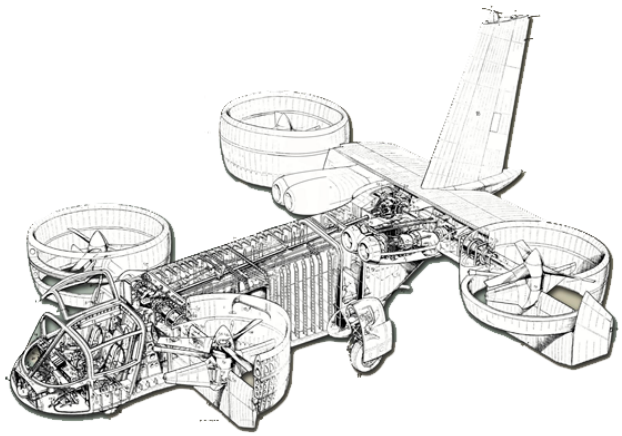

Figure 5.1: Bell X-22 cut-out drawing [42]

However, as elaborated in Section 2.4.5, this design was changed and as a final design, the rear fans were housed within the main wing and will not be tilting during transition. Thus they are only used for vertical take-off and landing. Also the front and rear fan diameters are not identical anymore. The rear fans are now larger in diameter, thus producing a larger portion of the thrust at take-off, and only the front fans will be used during the cruise. An illustration of the final design is shown in Figure 2.5.

The division of thrust produced by the front and the rear fans, as explained in more details in Section 7.3.2, indicated after several iterations that 65 % of the thrust at take-off is produced by the rear fans and the other 35 % by the front fans; whereas the front fans are purely responsible for the propulsion during the cruise flight.

Following the new InVADe design and the division of take-off thrust, new fan diameters were selected for the front and the rear fans. As elaborated in Section 5.4, a smaller fan diameter will result in a higher noise level; thus the attempt was to have the largest fan which could fit into the design, however, the size of the fan is limited due to aerodynamic issues and available space. This is mainly true for the rear fans in the main wing. In order to select the proper fan sizes, several iterations were performed; these included iterations regarding the division of thrust at take-off and the location of the center of mass, elaborated further in Section 7.3.2, and also various iterations

using the BEM approximation for ideal twist from Prouty [[94], p. 15], in which the fan diameter, the required thrust and the propeller rpm were tested. Following these iterations, a front fan diameter of 1.95 m and a rear fan diameter of 2.45 m were selected for the final design.

For the BEM approximation, Equation 5.1 is used; it relates several parameters such as fan diameter, pitch angle, number of blades and the propeller rotational speed, rpm to the total propeller thrust:

$$T = \frac{\rho}{2}(\Omega \cdot R_b)^2 \cdot N_b \cdot c_b \cdot R_b \cdot C_{L_\alpha}\left(\frac{\theta_t - \phi_t}{2}\right) \tag{5.1}$$

where T is the total propeller thrust, ρ is the air density, N_b is the number of blades, Ω is the rotational speed, R_b is the radius of the blade, c is the blade chord, C_{L_α} is the slope of the airfoil curve, θ_t is the pitch angle at the blade tip, and ϕ_t is the inflow angle at the tip. For this purpose, 50 was selected as the number of propeller blades in each fan, and the blade pitch angle was selected at 23 degrees, based on the Bell X-22 design [10]; through iteration of parameters such as fan diameter, rpm and blade chord, the BEM theory resulted in the best compromise between noise emissions, complexity and structural size. The corresponding fan rpm's were 1,440 and 1,575 rev/min for the rear and front fans, respectively. It also resulted in a blade chord of 0.05 m for all fans. The corresponding noise level will be outlined in Section 5.3.

5.1.1. CONTRA-ROTATING FANS

The possibility of using contra-rotating fans was investigated. The concept consists of two fans mounted axially, one behind the other, which rotate in opposite directions and are driven by a single engine.

This set-up takes advantage of the fact that the front fan, produces a tangential flow that can, in this case, be used by the second fan to produce extra thrust. Furthermore, it can eliminate asymmetrical torque caused by a single fan or propeller. Contra-rotating propellers have shown to be between 6% and 16% more efficient when compared to simple propellers [117].

The main issue with this concept is the increased noise emission it causes. It has been found that a contra-rotating propeller set-up will be at least 10 dB louder than a similar simple propeller [117]; even more in the higher frequencies, which cause the most nuisance. For that reason, contra-rotating fans have been deemed not appropriate for the current design, which has a very strict noise requirement.

5.2. POWER REQUIREMENTS

With the size of the fans selected in Section 5.1, the next step is to determine the required power during different phases of the flight, namely take-off/landing, transition and cruise. This is done using aerodynamic relations that relate the characteristics of the fan and the aircraft to the performance parameters throughout each flight phase. These influencing parameters include duct size, number of ducts, aircraft weight, drag and velocity.

5.2.1. TAKE-OFF

The analysis of performance and the required power during the take-off phase of the flight is done by examining the characteristics of this phase and relating the produced thrust to the required power. For this purpose, the momentum theory is applied [22]. Based on this theory,

$$\frac{T_i}{P_i} = \frac{2}{V_e} = \frac{2\sqrt{\varsigma_A \cdot \rho \cdot A_R}}{\sqrt{T_i}} \tag{5.2}$$

in which T_i is the static thrust in N, P_i is the ideal induced power in W, V_e is the duct exit velocity, ς_A is the ratio of the exit area of the duct to the area of the fan, shown in Figure 5.2, ρ is the air density, and A_R is the area of the fan.

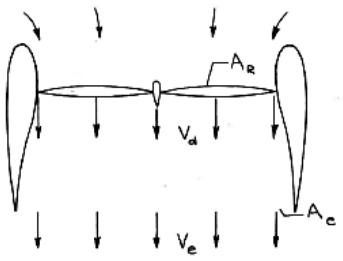

Figure 5.2: Flow through a ducted propeller [22]

From Equation 5.2, one can write P_i as a function of T_i, as follows:

$$P_i = \frac{T_i^{3/2}}{2 \cdot \sqrt{\varsigma_A \cdot \rho \cdot A_R}} \tag{5.3}$$

For a free propeller, ς_A from Equation 5.3 equals 1/2, whereas for a ducted propeller ς_A starts from a minimum of 1 for a straight duct; implementing the ς_A ratios of free and ducted propellers indicates that the lift efficiency, T_i/P_i increases by 41.4 % in a ducted propeller [22]. This beneficial effect of the duct around the fan is already implemented in Equation 5.3.

To calculate ς_A for the front and the rear fans, Equation 5.4 is used:

$$\varsigma_A = \frac{A_e}{A_R} = \left(\frac{D_s}{D_f}\right)^2 \tag{5.4}$$

with A_e is the duct exit area, D_s is the diamter of the duct, which is 3 cm larger than D_f, the diameter of the fan, for structural clearance purposes. This leads to values of 1.05 and 1.06 for $\varsigma_{A,rear}$ and $\varsigma_{A,front}$ respectively.

As P_i refers to the power required by a an idealised actuator disc regardless of the drag of the actual blades, the actual power required, P_R is thus higher than P_i. The ratio of P_i to P_R is known as the figure of merit (FM) given in Equation 5.5; this ratio is affected by the number of blades per propeller and whether the propeller is dual or single rotation [82].

$$FM = \frac{P_i}{P_R} \tag{5.5}$$

As explained in Section 5.1, the number of blades for the current design is 50. Comparing this value to the test results on FM ratios [82], a FM value of 0.85 is used throughout this chapter.

Substituting Equation 5.3 into Equation 5.5 will result in P_R rewritten as a function of T_i :

$$P_R = \frac{T_i^{3/2}}{2 \cdot FM \cdot \sqrt{\varsigma_A \cdot \rho \cdot A_R}} \tag{5.6}$$

where:

$$A_R = \frac{\pi \cdot D_f^2}{4} \tag{5.7}$$

Implementing Equation 5.7 into Equation 5.6 leads to a final expression for P_R:

$$P_R = \frac{T_i^{3/2}}{FM \cdot \sqrt{\varsigma_A \cdot \rho \cdot \pi \cdot D_f^2}} \tag{5.8}$$

Having obtained the equation for P_R, one will only have to determine T_i which is the only unknown variable in Equation 5.8. To estimate the amount of vertical thrust required for vertical flight, the ratio of thrust available at take-off, T, to the maximum take-off weight, W, is required to exceed 1.0; for an acceptable response, a T/W ratio of 1.1 is used [96]. With the W_{MTOW} in kg, this gives a total required thrust at take-off of:

$$T_{shr} = \frac{T}{W} \cdot W_{MTOW} \cdot g \tag{5.9}$$

T_{shr} is the total thrust which is obtained by the ducted fans onboard, W_{MTOW} is the maximum take-off weight, and g is the gravitational acceleration of 9.81 m/s^2 at sea level. The subscipt 'shr' for the thrust refers to the fact that this thrust is produced by 'shrouded' fans. Using a modified version of the momentum theory [82], T_{shr} can be related to the thrust of an unshrouded fan via:

$$\frac{T_{shr}}{T_i} = 1.26 \cdot \left(\frac{D_s}{D_f}\right)^{2/3} \tag{5.10}$$

Thus, T_i can be calculated using Equations 5.9 and 5.10, and then substituted in Equation 5.8 to yield P_R in terms of T_{shr}:

$$P_R = \frac{T_{shr}^{3/2}}{\sqrt{2} \cdot FM \cdot D_s \cdot \sqrt{\varsigma_A \cdot \rho \cdot \pi}} \tag{5.11}$$

Thrust & Power Division Per Rear & Front Fans

Due to the division of the thrust at take-off, T_{shr} will not be identical for the front and the rear fans. Taking the thrust portion of each fan into account, T_{shr} and the resulting P_R per fan at take-off can be calculated using Equations 5.12 and 5.13:

$$T_{shr_{fan}} = T_{por} \cdot \frac{T}{W} \cdot W_{MTOW} \cdot g \tag{5.12}$$

where T_{por} is the portion of the take-off thrust produced by each fan. Hence, the power required by the engine per fan is given by:

$$P_{R_{fan}} = \frac{{T_{shr_{fan}}}^{3/2}}{\sqrt{2} \cdot FM \cdot D_{s_{fan}} \cdot \sqrt{\varsigma_{A,fan} \cdot \rho \cdot \pi}} \tag{5.13}$$

Results

Applying Equations 5.10, and 5.12 to 5.13, T_i, T_{shr} and P_R for the rear and the front engines can be computed. Tables 5.1 and 5.2 represent the input and the output parameters emerging from these equations, respectively:

Table 5.1: Momentum theory inputs

Input Parameter	**Symbol**	**Value**	**Unit**
Rear Fan Area Ratio	$\varsigma_{A,rear}$	1.05	-
Front Fan Area Ratio	$\varsigma_{A,front}$	1.06	-
Air Density	ρ	1.225	kg/m^3
Front Fan Diameter	$D_{f_{front}}$	1.95	m
Rear Fan Diameter	$D_{f_{rear}}$	2.45	m
Figure of Merit	FM	0.85	-
Front Duct Diameter	$D_{s_{front}}$	2.01	m
Rear Duct Diameter	$D_{s_{rear}}$	2.51	m
Maximum Take-Off Weight	W_{MTOW}	8290	kg
Portion of $T_{shr_{tot}}$ produced by rear fan	$T_{por_{rear}}$	32.5	%
Portion of $T_{shr_{tot}}$ produced by front fan	$T_{por_{front}}$	17.5	%

Table 5.2: Momentum theory outputs

Output Parameter	**Symbol**	**Value**	**Unit**
Front Shrouded Thrust	$T_{shr_{front}}$	15.7	kN
Rear Shrouded Thrust	$T_{shr_{rear}}$	29.1	kN
Front Static Thrust	$T_{i_{front}}$	12.2	kN
Rear Static Thrust	$T_{i_{rear}}$	22.7	kN
Front Required Power	$P_{R_{front}}$	403.3	kW
Rear Required Power	$P_{R_{rear}}$	813.4	kW

In summary, the total T_{shr} and P_R at take-off are given below:

$$T_{shr_{tot}} = 2 \cdot T_{shr_{front}} + 2 \cdot T_{shr_{rear}} = 89,457[N] \tag{5.14}$$

$$P_{R_{tot}} = 2 \cdot P_{R_{front}} + 2 \cdot P_{R_{rear}} = 2,433.3[kW] \tag{5.15}$$

Power check at take-Off

So far, the total required power from the engines and the produced shrouded thrust at take-off have been calculated. Next, the estimation of the required power for vertical climb is found using Equation 5.16 [77]:

$$\left(\frac{P}{P_h}\right)_{req} = \frac{V_c}{2 \cdot V_i} + \sqrt{1 - (\frac{V_c}{2 \cdot V_i})^2} \tag{5.16}$$

where P is the available power, P_h is the necessary power during hover, $(\frac{P}{P_h})_{req}$ the required power ratio at take-off, V_c is the climb velocity which is given in the project requirements as 9 m/s, and V_i is the induced velocity at hover, given by Equation 5.17.

$$V_i = \sqrt{\frac{2 \cdot T_{shr_{fan}}}{\rho \cdot \pi \cdot D_f^2}} \tag{5.17}$$

where $T_{shr_{fan}}$ is the shrouded thrust per fan. From Equation 5.16, only the induced velocity is yet unknown. Using the $T_{shr_{fan}}$ shown in Table 5.2, V_i is calculated per front and rear fans and the P/P_h is calculated to be 1.09 and 1.08 for the front and rear fans respectively, which gives an overall required P/P_h value of 1.085 for the aircraft.

In order to examine the excess power available onboard at take-off, the ratio of proportionality of the thrust produced by a ducted fan to the power required [82] can be used, Equation 5.18:

$$\left(\frac{P}{P_h}\right)_{avail} = (\frac{T_{av}}{W_{MTOW}})^{\frac{3}{2}} \tag{5.18}$$

With $\left(\frac{P}{P_h}\right)_{avail}$ the available power ratio at take-off, and T_{av} the available thrust onboard at take-off. Using $T_{shr_{tot}}$ from Equation 5.14, $\left(\frac{P}{P_h}\right)_{avail}$ equals 1.15. Comparing the required power ratio and the available excess power ratio during take-off, one can conclude that the power available meets the requirements during the take-off maneuvres.

5.2.2. CRUISE

To determine the required power during cruise flight, one will need to make use of the total drag of the aircraft, as the required power is given by:

$$P_{R_{cruise}} = D \cdot V_{cruise} \tag{5.19}$$

where $P_{R_{cruise}}$ is the power required during cruise flight, D is the total drag of the aircraft and V_{cruise} is the cruise velocity of the aircraft.

Next, to consider the efficienty of the engines onboard, the propulsive efficiency of the engines must be accounted for. For this purpose, a propulsive efficiency of 0.9 is used [108]. Using this efficiency, the required available power is calculated using Equation 5.20:

$$P_{A_{cruise}} = \frac{P_{R_{cruise}}}{\eta_{prop}} \tag{5.20}$$

with η_{prop} the propulsive efficiency, set at 90 %, to account for future propulsion improvements of propellers [108].

The project requirements state that the aircraft should be flying at a cruise speed of 600 m/s while using 75 % of its maximum cruise rating; hence, the maximum rated power for cruise, $P_{max_{rated}}$ can be computed as:

$$P_{max_{rated}} = \frac{P_{A_{cruise}}}{0.75} \tag{5.21}$$

In order to use the above equations, the only unknown variable being D needs to be computed first; from Section 4.9, D equals 8,344 N.

Next, substituting the values of D andV_{cruise} into Equation 5.19 and subsequent solving of Equations 5.20 and 5.21 leads to the following:

$$P_{R_{cruise}} = 1{,}390.7 \text{ kW}$$

$$P_{A_{cruise}} = 1{,}545.2 \text{ kW}$$

This gives a maximum rated power of 2,060.3 kW required for cruise flight.

5.2.3. TRANSITION

In order to reduce the complexity of the calculations regarding this phase of the flight, the methodology is simplified such that the the method in Section 5.2.2 can be applied to determine the required power during the transition. For this purpose, Equations 5.19 & 5.20 are used once again, with D in Equation 5.19 now referring to the total drag during the transition; this is calculated using the following:

$$D = D_{par} + D_{ind} \tag{5.22}$$

where D_{par} is the parasite drag and D_{ind} is the induced drag, calculated using Equations 5.23 and 5.25 respectively:

$$D_{par} = C_{D_0} \cdot S \cdot \bar{q} \tag{5.23}$$

where C_{D_0} is the zero lift drag of the aircraft, S is the wing area, and $\bar{q}$ is the dynamic pressure, calculated using Equation 5.24:

$$\bar{q} = \frac{1}{2} \cdot \rho \cdot V_{tr} \tag{5.24}$$

with V_{tr} the velocity during transition in m/s.

Next, the induced drag is given by:

$$D_{ind} = \frac{{C_{L_{max}}}^2}{\pi \cdot AR \cdot e} \cdot \bar{q} \cdot S \tag{5.25}$$

where $C_{L_{max}}$ is the maximum lift coefficient, AR is the Aspect Ratio, and e is Oswald factor.

Equations 5.23 to 5.25 are derived from the aerodynamic analysis presented in Section 4.9. The values used are summarised in Table 5.3.

Table 5.3: Input Parameters for Drag Calculations

Input Parameter	Symbol	Value	Unit
Zero Lift Drag	C_{D_0}	0.0321	-
Wing Area	S	37.13	m^2
Air Density at 100 m	ρ_{100}	1.213	kg/m^3
Transition Velocity	V_{tr}	60	m/s
Max Lift Coefficient	$C_{L_{max}}$	1.9	-
Aspect Ratio	AR	6.19	-
Oswald Factor	e	0.846	-

Among the parameters in Table 5.3, some are dedicated to the transition phase; C_{D_0} is higher with respect to the C_{D_0} of cruise, since it also includes the effect of the high lift devices which will be active during transition. Also, $C_{L_{max}}$ is used in the calculations, since the maximum C_L will be used to perform the transition at the low speed. These values are derived and elaborated in Chapter 4.

Using these input parameters in Equations 5.22 to 5.25 and substituting V_{tr} and the resulting D into Equations 5.19 and 5.20 leads to the required power during transition by an engine:

$$P_{R_{tr}} = 1,223.8[kW] \tag{5.26}$$

Considering the propulsive efficiency of the engines, the total required power to be available on-board is thus equal to:

$$P_{A_{tr}} = 1,359.8[kW] \tag{5.27}$$

5.2.4. VERIFICATION

Throughout Sections 5.2.1 through 5.2.3, calculations were initially performed via an analytical approach, in which the results were obtained by analytically evaluating the results from the formulas described in these sections. Next, to verify the results, a Matlab script was written to numerically obtain the results and verify if they matched those obtained from the analytical analysis.

The analytical results differed from the numerical by only about 3%. Hence, the results from the analysis can be considered reliable.

5.2.5. VALIDATION

In order to validate the numerical results for the power requirements, the design parameters of a reference aircraft can be used and substituted into the numerical analysis used in this section; obtaining the practical values of the reference aircraft would validate the numerical approach used. For this purpose, the Bell X-22 aircraft is used as the reference aircraft.

To perform the validation, several X-22 related parameters [10] were used; these are shown in Table 5.4:

Table 5.4: Input Parameters for the X-22 Power Calculations

Input Parameter	**Symbol**	**Value**	**Unit**
Wing Area	S	39.56	m^2
Air Density at 7500 m	ρ_{7500}	0.5566	kg/m^3
Cruise Velocity	V_{cruise}	111.11	m/s
Aspect Ratio	AR	3.86	-
Fan Diameter	D_f	2.13	m
Fan Rotational Speed	Ω	2650	rev/min
Duct Diameter	D_s	2.19	m
Maximum Take-Off Weight	W_{MTOW}	8170	kg
Blade chord	b_c	25	cm
Thrust to Weight Ratio	T/W	1.35	-

The X-22 aircraft had a W_{MTOW} of 8170 kg, which is only 120 kg lighter than InVADe. This aircraft had fan diameters of 2.13 m, and a rotational speed of 2650 rpm. The next step in the validation procedure was to insert these values into the Matlab code used for the numerical analysis and compare the results. The outcomes from this analysis are summarised in Table 5.5:

Table 5.5: Outcomes of the X-22 numerical analysis

Input Parameter	**Symbol**	**Value**	**Unit**
Total Shrouded Thrust	$T_{shr_{tot}}$	108.2	kN
Shrouded Thrust Per Fan	$T_{shr_{fan}}$	27.05	kN
Total Power Required at Take-Off	$P_{R_{tot}}$	3.35	MW
Required 'Power to Hover Power' ratio	$\left(\frac{P}{P_h}\right)_{req}$	1.19	-
Available 'Power to Hover Power' ratio	$\left(\frac{P}{P_h}\right)_{avail}$	1.56	-
Required Power at Cruise	$P_{R_{cruise}}$	0.36	MW

The outcomes shown above can now be compared. The X-22 had four turboshaft engines, each delivering 945 kW of power [10], resulting in a total power of 3.78 MW. Comparing this with the $P_{R_{tot}}$ of 3.35 MW from the numerical analysis, it can be seen that the results are in fact in accordance with the actual maximum power on board at take-off, and the real design covers the required take-off power.

The values for $\left(\frac{P}{P_h}\right)_{req}$ and $\left(\frac{P}{P_h}\right)_{avail}$ were also examined. To be able to take-off, the aircraft had to be able to cover its requirement for $\left(\frac{P}{P_h}\right)_{req}$. From the analysis, the values for $\left(\frac{P}{P_h}\right)_{req}$ and $\left(\frac{P}{P_h}\right)_{avail}$ came out to be 1.19 and 1.56 respectively, proving that the aircraft has the ability to take-off vertically, and thus validating the method used for power check at take-off.

Lastly, in order to validate the BEM theory used, X-22 parameters such as D_f, W_{MTOW}, T/W, and b_c were substituted into the BEM theory. Using 3 as the number of blades and an rpm of 2650, the $T_{shr_{fan}}$ was calculated to be 27.7 kN, which is 1.02 times the value of $T_{shr_{fan}}$ (27.7 kN); with such a small divergence from the $T_{shr_{fan}}$, the validation of the numerical analysis and the results in this section can be validated.

5.3. NOISE CALCULATION

The noise produced by a ducted fan VTOL aircraft comes from a few different sources, such as engine, fan, airframe, and gear boxes. Of particular importance to the calculations are the engine noise and fan noise.

ENGINE NOISE

Statistics about engine noise are difficult to find. For a turboshaft engine, a useful empirical approximation is given in Mantle [82]:

$$SPL_{30} = 72 + 8.2\log(P) \tag{5.28}$$

where SPL_{30} is the 'Sound Pressure Level' as measured from a distance of 30 meters from the source, and P stands for the shaft power $[hp]$ delivered by the engine. A prediction for SPL at 100 meters follows from the conversion

$$SPL_{100} = SPL_{30} - 20\log\left(\frac{100}{30}\right) \tag{5.29}$$

It must be noted that the estimate is based on engines built in 1980. Hence, it is necessary to account for the trend of decrease in noise emissions of aero engines from 1980 to 2030, when Invade is expected to fly. As can be seen in Figure 5.3, ACARE predicts a 10 dB decrease in noise levels of turbofan engines from 1995 to 2020 [44]. Extrapolating that graph to include the decrease from 1980 to 1995 and from 2020 to 2030, by applying the same trend, a 20 dB drop can be expected from the 1980 level to the 2030 level.

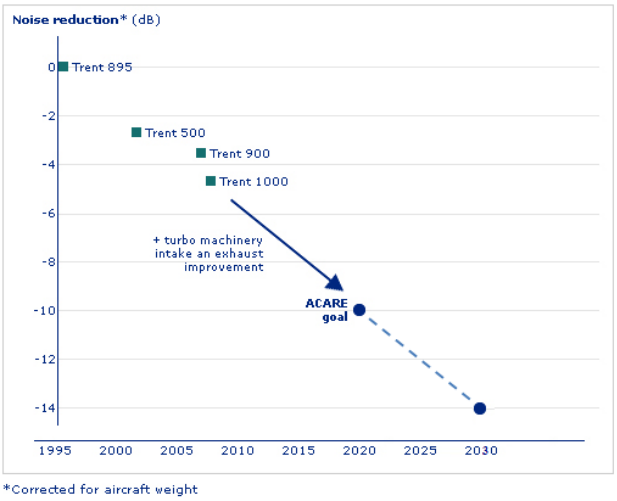

Figure 5.3: ACARE engine noise level prediction

A further attenuation of 3 dB is applied to account for the fact that the engines will be housed inside the fuselage, where acoustic treatment can be applied to reduce noise.
Then, adding together all noise from both engines, a final engine noise is determined.

FAN NOISE

Fan noise can be estimated using the principles of a turbofan engine [83], where in this case, only the fan stage part is taken into account.
The energy flux per unit area (Φ_E) can then be calculated using:

$$\Phi_E = \frac{H_T \dot{m}}{A_a} \tag{5.30}$$

where the annulus rotor area A_a is derived from the fan and hub diameters. The total enthalpy H_T can be read from an ideal gas chart, corresponding to a discharge total temperature, which in turn is calculated through the use of the pressure ratio and isentropic relations. Finally, $\dot{m}$ represents the mass flow through the fan.

Next, Figure 5.4 is used to find the overall power level (OPL), using the energy flux per unit area, calculated in Equation 5.30.

Once the value of OPL is determined from Figure 5.4, Equation 5.31 can be used to calculate the Sound Power Level, PWL, corresponding to the value of OPL:

$$OPL = PWL - 10\log\frac{A_a\omega}{N_B}\left(\frac{D_H}{D_F}\right)^2 \tag{5.31}$$

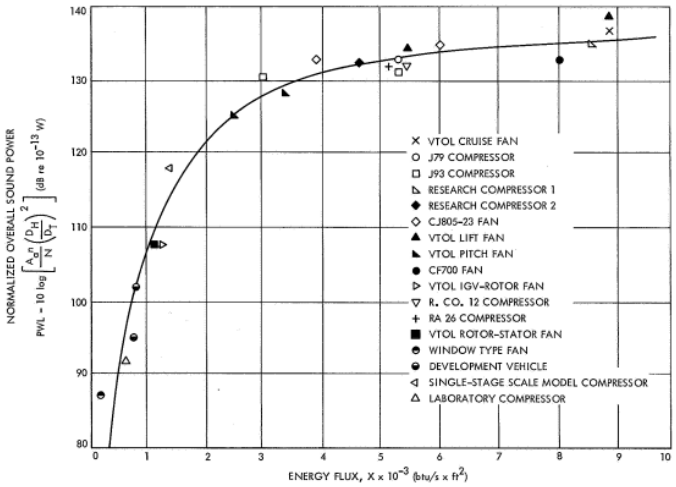

Figure 5.4: OPL vs energy flux

where ω represents the fan rotational speed in rad/s, N_B is the number of blades, and D_H and D_F are the diameters of the fan hub and fan outer diameter, respectively.
The SPL level at 30 m from the source is then given by:

$$SPL_{30} = PWL + DI - 20\log(R) - 10.5 \tag{5.32}$$

Where DI stands for the directivity at the angle of maximum noise. From experimental data, a value of $DI = 5$ is used [83]. Furthermore, R refers to the distance from the source, measured in feet.

Finally, as was done for engine noise, Equation 5.29 can be used to convert SPL_{30} to SPL_{100}.

The result is the SPL for each fan. It must be pointed out that the final design uses different fan diameters and rpm for the front and aft fans, which will lead to different noise emissions for front and aft. For the combination of four fans, the levels can be added together in the logarithmic scale, yielding to the total SPL for all fans.

TOTAL NOISE

The last step before arriving at the Total noise would be to add the noise caused by the engines to the fan noise. However, if indeed, as was done in the calculations, the attenuation due to the housing of the engines in the fuselage, as well as the expected improvement of noise emissions of future engines are taken into account, then the resulting engine noise of 69 dB is 20 dB (or a factor of 100) lower than the fan noise. For that reason, engine noise is neglected in the noise calculations from this point on.

Even though the extrapolation of Figure 5.3 to include the decrease from 2020 to 2030 may seem too optimistic, it should be realised that the extrapolation to this period results in only 4 dB further reduction in engine noise, which when compared to the overal fan noise of 88.7 dB, will have no significant effect (only 0.1 dB) and can thus be neglected. Finally, the total noise emission of the aircraft, considering only the open fan noise, and without accounting for duct shielding attenuation, is estimated at 88.7 dB.

5.3.1. VERIFICATION AND VALIDATION

To verify the results, the noise was calculated again using an alternate method. This script, written by Pinker [93] outputs decibel levels for observers at varying angles from the source. Figure 5.5 shows the results of the alternate method, where the maximum noise, at the 130 degrees direction reads 89.7 dB. The results obtained using this method agree well with the ones obtained using the original method, with only about 1 dB discrepancy. This lends credit to the results of the original method.

For a validation plan, it would be relevant to use data from InVADe's closest existing match, the Bell X-22, and check that the results for noise level at 100 meters obtained using the empirical method match the actual values measured from the aircraft. However, partly due to its military application, data and parameters for the X-22 are not readily available. Neither is there enough reliable data on other ducted fan prototypes. If, during further development of InVADe, relevant data from the above mentioned aircraft becomes available, such validation would be valuable in confirming the noise estimation.

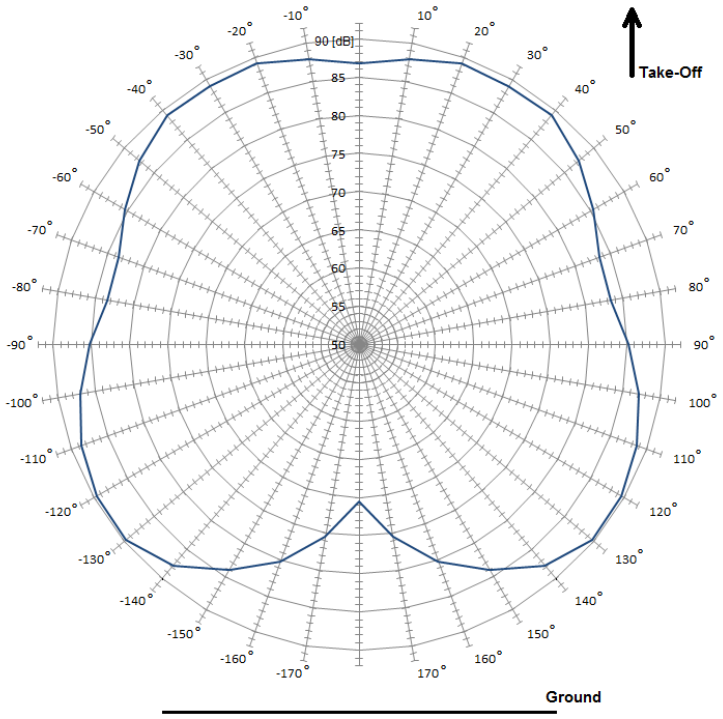

Figure 5.5: Noise in SPL around the fan (alternate method)

5.4. NOISE ABATEMENT

On the previous section, the noise emission of the aircraft was estimated using empirical approaches, based on a basic fan configuration and without any shielding effects of the duct on the noise produced by the fan. In the previous section, the result, 88.7 dB, substantially exceeds the initial requirement of 70 dB. Although the requirement is virtually impossible to reach for such a large aircraft using current or near-future technology, there are some abatement measures that can be taken that will bring the final noise level to a more tolerable level. These are presented in the following sections.

5.4.1. DUCT SHIELDING

An immediate advantage of using ducted fans is the noise shielding or damping effect provided by the ducts themselves. This effect can provide a substantial attenuation, and should not be ignored. However, attenuating effect of shielding on the noise level is notably difficult to predict. Although it is the subject of ongoing research, there is currently no empirical method that can be applied to estimate the amount of shielding attenuation delivered by a certain duct configuration. Since no reliable source could be obtained for this value, it was only estimated that the shielding can provide a 2 dB attenuation to the fan source noise. This value is conservative, and it is taken into account that shielding limited to where the duct is present around the fan. For the aft ducts, although the duct can partially shield the directions of maximum noise, not all angles of propagation can be properly shielded. As for the narrower, longer front ducts, the shielding effect is more thorough.

5.4.2. DUCT INTERIOR LINING

In order to further improve the noise attenuation of the duct, a special lining can be applied to the inside of the duct that will absorb certain frequencies of the sound emitted by the fan, and thus contribute to reduction of the overall noise emission. Experiments conducted with efficient noise treatment liners in the exhaust duct showed a further reduction in the overall noise level of 3-4 dB [51]. The liner is especially effective for high tip speed fans, and the specific acoustic liner material and configuration should be selected according to the frequency range of the emitted noise [84]. Therefore, if the proper acoustic liner material is selected, it is estimated that this technique can provide a 3 dB attenuation of the noise of all four ducts. Figure 5.6 shows some examples of acoustic lining, as applied to a turbofan engine. Again, it is taken into account that the rear ducts do not provide thorough damping for all directions.

5.4.3. FORWARD SWEPT/INCLINED BLADES

Research has been done on the benefits of applying forward swept blades for noise reduction of a ducted fan. One effective noise source is the interaction of the rotating blades with the incoming small-scale which results in unsteady blade forces. This mechanism of noise generation is concentrated at the front part of the profile and

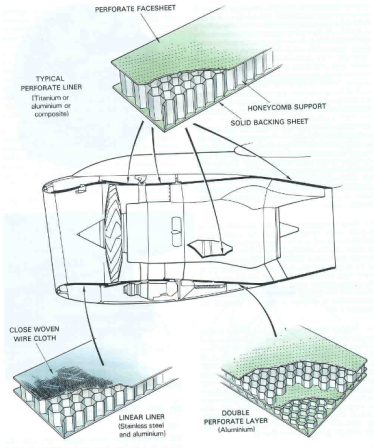

Figure 5.6: Examples of acoustic lining configurations taken from a turbofan engine

can thus be alleviated by sweeping the leading edge [9]. Other noise sources are the turbulent boundary layer and its interaction with the blade's trailing edge. Ffowcs Williams and Hall [64] discovered that the presence of a scattering half plane in a turbulent fluid largely increases the noise generated and that the intensity is dependent on the angle between the flow and the plane (the blade's trailing edge sweep angle) [9]. According to experimental data, applying forward sweep to the blades can reduce the overall noise level of the fan by 3 to 4 dB. For the current design, this technique is considered a viable and effective way of further reducing the noise emissions. Therefore, a high forward sweep of 50 degrees [89] is applied to the rotor blades, providing an estimated reduction of 3 dB to the overall noise emission of the aircraft, when compared to a baseline blade design with no sweep. Figure 5.7 shows a schematic of the swept blades.

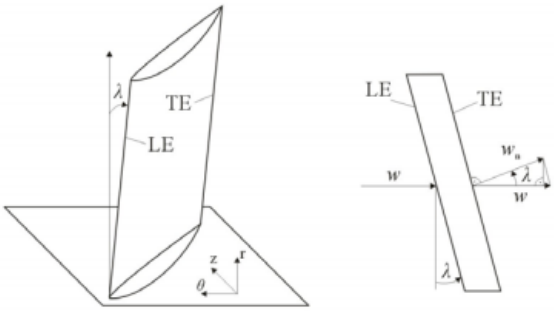

Figure 5.7: Schematic of proposed swept fan blades [9]

5.4.4. FINAL NOISE RESULTS & ANALYSIS

By applying all three techniques to the design, it is estimated that a combined reduction of 8 dB, with respect to the open fan noise level, can be achieved. This brings the overall noise level for the aircraft down to 80.7 dB at 100 m distance. Noise results are displayed on 5.6.

Table 5.6: Final Noise results for InVADe

Parameter	**Unit**	**Result**
Passengers	[-]	10
MTOW	[kg]	8,290
RPM front ducts	[rev/m]	1,575
RPM aft ducts	[rev/m]	1,440
Number of blades per fan	[-]	50
SPL front ducts	[dB]	80.8
SPL aft ducts	[dB]	84.0
Total abatement	[dB]	8
Final Overall SPL_{100}	[dB]	**80.7**

While final overall SPL is still very much above the initial requirement set by the client, it can be considered quite an achievement for an aircraft of this size. A similar payload helicopter, the Eurocopter EC155 [58], for example,

produces 90.2 dB at 100 m. The Bell X-22, a concept aircraft with a similar duct configuration and MTOW, exhibits a SPL of 105.8 dB at 100 meters [10]. Moreover, studies suggest that SPL values around 80 dB are safe for humans, and will not cause any permanent damage if exposure does not exceed 16 hours per day [47], which is far beyond the expected duration of the take-off and landing phase, estimated at no more than three minutes.

If one wishes to produce an aircraft with noise levels below 70 dB, the aircraft needs to be designed with a lower payload. Preliminary estimates using the current methods suggest that if the aircraft were designed to carry only four passengers, it could be scaled down to a point where the noise emissions would be very close to meeting the 70 dB requirement. Table 5.7 summarises the noise results for a hypothetical, scaled down version of InVADe for four passengers, including the same noise abatement values as the original version.

Table 5.7: Noise results for a hypothetical, scaled down 4 passenger version of InVADe

Parameter	**Unit**	**Result**
Passengers	[-]	4
MTOW	[kg]	3,000
RPM front ducts	[rev/m]	910
RPM aft ducts	[rev/m]	1,240
Number of blades per fan	[-]	50
SPL front ducts	[dB]	67.3
SPL aft ducts	[dB]	75.4
Total abatement	[dB]	8
Final Overall SPL_{100}	[dB]	**71.0**

5.5. POWER PLANT

Unlike more conventional aircraft engines such as turbofans and turboprops, ducted fans do not incorporate a turbine as a power plant. Also, due to the location and shape of the ducts in the aircraft, there is no room to put a turbine or piston engine close-by. Due to the power and weight involved the choice of turbine engines is obvious due to their high power-to-weight ratio.

This section details the selection and design of the power plant system and its components. First a trade-off between power plant options is done, followed by detailed design of components in Section 5.5.2 and engine selection in Section 5.5.3.

5.5.1. POWER PLANT TRADE-OFF

There are three foreseeable methods to drive the fans: mechanically through a shaft, electrically by a motor, and electromagnetically via the duct. This last method was not examined in detail due to a lack of information and readiness of the technology, though it would save weight from motors or shafts and would allow a more efficient duct design.

The mechanical system needs engines that efficiently drive a set of shafts and gearboxes. For that reason dual turboshaft engines were envisioned, a type of turbine that mainly produce shaft power. Two engines are preferable for redundancy, common practice for helicopters of comparable size to the InVADe aircraft. This system of turboshafts, drive shafts and gearboxes is reasonably similar to the CH-47 Chinook with its tandem rotors, shown in Figure 5.8.

The electric system needs electrical energy to either be stored in some form of fuel cell or battery, or a turboshaft-generator combination. Basic calculations with an expected 2030 battery capacity of 400 Wh/kg [87] show total battery mass in the area of 14,000 kg. As Jet A-1 kerosene has a much higher energy density of at least 42.8 MJ/kg (11,888 Wh/kg) [12] the turboshaft-generator combination is clearly more effective even with the efficiency losses involved in converting mechanical energy to electrical and back again.

The electric and mechanical options for transmitting power were traded off according to their estimated total weight. Other issues were identified but neglected, as in the end of this section. An electric power plant of this scale hasn't been applied before and lightweight electrical components needed for such a large amount of power aren't yet designed. The Boeing 787's 1 MW of electrical power [1] comes close enough to expect the technology to be mature by 2030, however. Efficiently transferring the electrical currents involved and shielding sensitive components from the electromagnetic interference created will be a challenge. The mechanical option has not been applied to this degree since the Bell X-22 and will involve a large number of sensitive drive shafts and gearboxes. The layout out of the aircraft does not facilitate efficiently placing the engines to minimise the amount of gearboxes necessary.

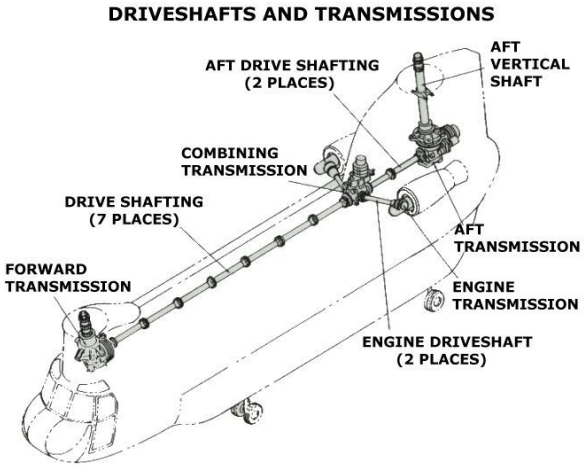

Figure 5.8: CH-47 Chinook drive train schematic [50]

MECHANICAL SYSTEM

Figure 5.9 shows helicopter drive train weights related to their input power, from Weden and Coy [123]. Linear extrapolation gives the relation shown in Equation 5.33. Here P is the power in kW and W the weight in kg.

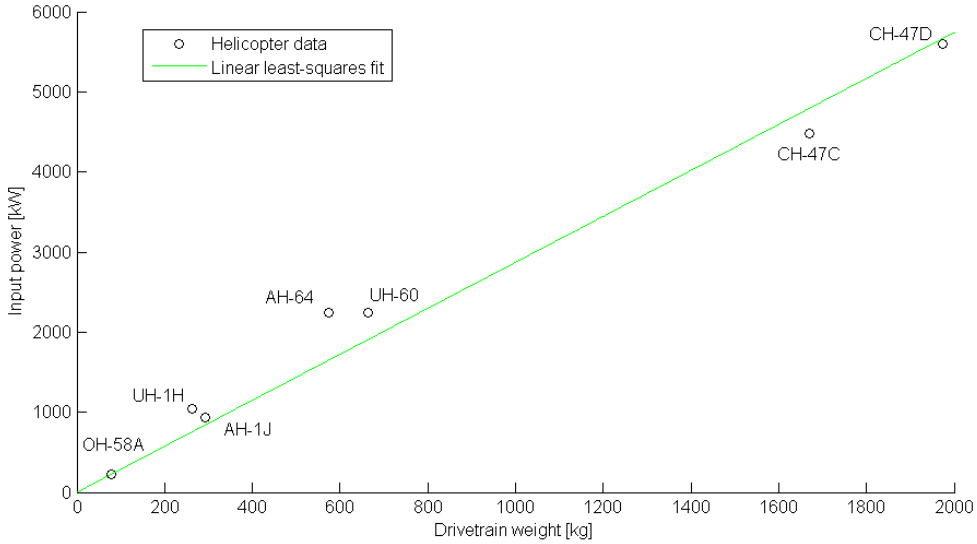

Figure 5.9: Linear regression of helicopter drivetrain weight (R^2=0.97)

$$P_{drivetrain} = 2.87 \cdot W_{drivetrain} \tag{5.33}$$

The data used for Equation 5.33 is from the 1980's but has a high correlation (R^2=0.97) and includes two versions of the CH-47 Chinook. Helicopters generally have a shorter distance between their engines and rotors and they have fewer rotors/fans to drive. This effect is assumed to cancel out any weight decrease since the 1980's. The total loss in the mechanical system was estimated in the order of 5%.

The weight of an auxiliary power unit (APU) large enough to power aircraft systems during engine failure is estimated from the Hamilton Sundstrand T-62T-46-2 [52] APU which powers the V-22 Osprey. This is multiplied by a factor 2 for installed versus dry weight from Torenbeek [113]. The breakdown is shown in Table 5.8.

ELECTRICAL SYSTEM

For the electric option another method had to be used. As motors and generators are technically very similar components both were estimated using an expected power-to-weight ratio. For electric generators and motors an estimated 2030 value of 10 kW/kg is used, explained further in section 5.5.2. Losses of 15% are assumed, corresponding to 90% efficiency on the generators and 95% on the motors. Weight of cabling was estimated at 25 kg from the density of high power copper cabling.

The mass of the generators is determined by the maximum total power in the system, whereas the motors are determined by the maximum power for each duct. For the front ducts this is the cruise power, for the aft ducts it is the power needed to provide 65% of the necessary take-off thrust. This value was determined for stability reasons in section 7.

Instead of an APU a back-up electrical system is envisioned for this option. The batteries are designed to provide 50% of the highest power requirement for 2 minutes, and the energy density is again expected to reach 400 Wh/kg. The breakdown is shown in Table 5.8.

Table 5.8: Comparison of Electrical and Mechanical power plant schemes in kg

Component	Weight
Generator	300
Front motors	228
Aft motors	200
Cabling	25
Batteries	190
Turbines	492
Total	**1435**

Component	Weight
Drivetrain	981
APU	150
Turbines	492
Total	**1623**

TRADE-OFF

As shown in Table 5.8, the power plant options were purely selected based on the weight involved. Other trade-off criteria could include cost and sustainability but were neglected due to a lack of available data. For both systems the engine weight was assumed equal to that of two GE CT7-8A5s [36]. Due to the weight benefit the electric option was selected, which will be developed in more detail in the next section.

Other benefits of electric propulsion include the innovation demonstrated by implementing such a new system and the perceived sustainability associated with electrical power. Business aviation is the primary niche for the aircraft and such indirect benefits can make a difference in sales.

5.5.2. ELECTRONICS

To get the power produced by the turboshaft engines to the ducts a number of components are needed, as was hinted at in the power plant trade-off. Mechanical energy is converted to electricity by a set of generators. It is then transferred to all the ducts at a relatively high voltage to reduce losses, and converted back to mechanical energy by a set of electric motors. This covers propulsion, but a number of other components are needed to power flight systems and connect the back-up batteries, among others. Selection of all these components will be done in this section.

ELECTRIC MOTORS

Each fan contains one electric motor in its rotor hub. Fan thrust is varied by changing rotor rpm. Thus direct drive induction motors are most suitable. These are assumed to be tailor-made for InVADe during sizing. These motors have no need for a gearbox and rpm output varies with input electrical frequency according to Equation 5.34 [30].

$$n_{motor} = \frac{120 \cdot \bar{f}}{N_p} \tag{5.34}$$

Here n_{motor} is the rotational speed in rpm, $\bar{f}$ is the supplied frequency in Hz and N_p is the number of magnetic poles in the motor. Motor efficiency is assumed to be 95%, based on expert advice [3]. The motors will run on three-phase AC power. Using an estimated average of 1500 rpm for the fan (see Section 5.1), conventional 400 Hz aircraft power [1] gives 32 poles needed per motor. This is not an unconventional value for motors [21] and no further analysis was done into precise electrical specifications.

The power-to-weight ratio was estimated based on the fact that induction motors and generators are physically almost identical. With the method applied in the next section, 10 kW/kg was assumed. This value is uncertain for large scale application according to an expert [3]. However, alternative developments such as High-Temperature Superconductor (HTS) motors for aircraft applications have been predicted to reach as high as 25 kW/kg. These HTS motors also offer efficiencies up to 99.9%, though requiring significant cooling [114]. Clearly some improvement over modern values may be anticipated and 10 kW/kg is used for sizing. For sizing the Enstroj EMRAX 228 [33], shown in Figure 5.10 is used and upscaled, that has a peak power-to-weight of 8.2 kW/kg nowadays. Its dimensions of 0.228 m diameter and 0.086 m length lead to a volume power density of 28.5 MW/m^3. The motors are assumed to be roughly cylindrical to fit in the fan hubs.

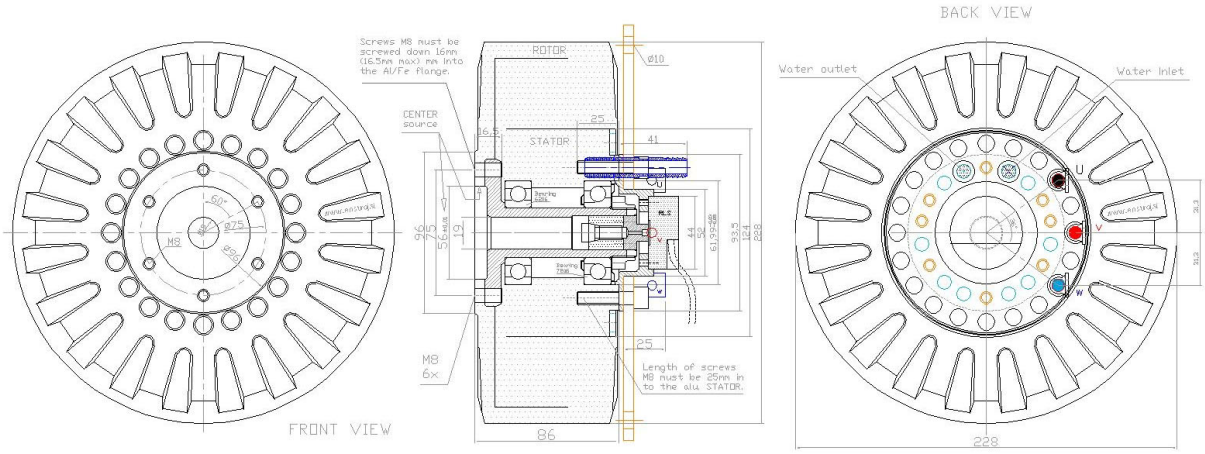

Figure 5.10: Enstroj EMRAX 228 dimensions [32]

For the front motors the power available at cruise is leading, 1030 kW per motor. The hub diameter of 0.40 m leads to a motor length of 0.61 m. As the front duct length is 1.07, this motor length is reasonable. The weight is estimated to be 103 kg per motor. The take-off power available of 904 kW drives the aft motor design. The hub diameter of 0.50 m leads to a estimated aft motor length of 0.34 m. The wing thickness is 1.03 m at the rear fans, so this motor length is somewhat short. 10 kW/kg gives a weight of 90 kg per motor.

Whether electric motors can be upscaled this simply is unknown. Thus calculations were also performed with exisiting EMRAX 228 motors applied in parallel to provide enough power. Its maximum rpm rating of 4000 and efficiency of 93-96% [33] match system requirements. The resulting length is 0.89 m for the front ducts and 0.78 m for the aft ducts. The power-to-weight ratio is still assumed to improve before 2030 and thus does not significantly affect the weight.

GENERATORS

For redundancy 4 generators are chosen, 2 per turboshaft engine. These will be cross-linked so that 3 generators can still power the whole aircraft. This is kept in mind during final sizing, so the generators must be able to handle 4/3 times their normal maximum load. Hawsey et al [53] researched generators for electrical aircraft in 1989, the most promising of which reached 11.7 kVA/kg. Assuming a power factor of 0.8 this leads to a power-to-weight ratio of 9.36 kW/kg. This technology has not progressed rapidly since 1989 so a value of 10 kW/kg is assumed for 2030. Based on the same data from Hawsey et al [53] a volume power density of 13.5 MW/m^3 is estimated. Generator efficiency was estimated at 0.95 using expert advice [3].

The total power output needed from the generators equals the maximum power output of the motors divided by the motor efficiency: 2,846 kW. To make sure 3 generators can power the entire aircraft, 3794 kW total power is needed or 949 kW per generator. The power-to-weight ratio gives 95 kg weight per generator. A cylindrical shape is again assumed, and the diameter is matched to the final engine selected in Section 5.5.3. With this diameter of around 0.66 m, the length needed for a cylindrical shape is 0.21 m per generator. Using the GE CT7-8A5 [36] turboshaft as an example, rpm's in the range of 19855-24350 can be expected. This varying rpm makes an induction generator the best choice. Induction generators can also be used as motors [115], therefore the turboshaft engines will be started by providing battery (or external) power to the generators.

BATTERIES

During initial design the possibility of battery-assisted take-off was explored. Though current power requirements make this ability redundant, battery power can still be used as a back-up in the case that one turboshaft engine fails. As InVADe is already an All-Electric Aircraft [18], using battery power as a back-up for the turboshaft engines is more efficient than separately installing a conventional auxiliary power unit (APU) with a turbine and generator included.

The batteries are estimated to have to replace the maximum power of one turboshaft for a period of two minutes. This requirement mainly ensures safe landing if failure occurs in VTOL flight. Turboshaft engines also have a two minute one engine inoperative (OEI) rating, as will be discussed in Section 5.5.3, that is significantly higher than their continuous rating. Thus 50% of the total maximum power includes a comfortable safety margin. For OEI conditions in cruise flight calculations are performed in Chapter 8.

Battery specific energy is estimated to be 400 Wh/kg, based on current state-of-the-art cell technology from Envia Systems [87]. This same cell has an energy density of approximately 190 kWh/m^3. 50% of the take-off (generator) power is 1423 kW, which gives a total energy draw of 47.4 kWh. The total mass of the batteries is 119 kg, and the total volume is 0.25 m^3. Batteries generally work at around 3 VDC. Though the system voltage is not yet determined, the batteries will have to be combined in multiple parallel sets to reach the needed voltage. An inverter is needed to convert DC to AC and a rectifier is needed to recharge the batteries with AC power, these will be examined in more detail in section further on.

Further analysis into energy storage must be done in detailed design. Hydrogen fuel cell technology is promising for All-Electric-Aircraft [18] and is perceived as more sustainable than battery technology.

POWER DISTRIBUTION

Though not a part in the strictest sense, the power distribution network is a critical subsystem for electrical propulsion. The maximum generated power is 2,846 kW, and even if the power factor is assumed to be 1, this still means 2,846 kVA. Conventional aircraft power systems use 115 VAC power, and the Boeing 787 with its 1 MW of electrical power uses 230 VAC [1]. With 230 V and the power factor and losses ignored, this gives a current of 12.4 kA. Equation 5.35 relates heat power to current and resistance of wiring via a mechanism known as Joule heating.

$$P_{heat} = I_{wire}^2 \cdot R_{wire} \tag{5.35}$$

Here P is power, I is current and R is resistance. The largest type of copper wiring in the American Wire Gauge (AWG) system, 0000 gauge, has a resistance of 0.161 Ω/km [41]. Estimating 8 m distance for wiring to the front ducts (this wiring has the highest power over the longest distance during cruise flight), the heat power is 198 kW. With an estimated 25 m^3 of cabin air, and a volumetric heat capacity of 0.001297 J/cm^{3}K yields an estimated temperature increase of 6.1 K/s. This is far beyond the amount of heating an air-conditioning unit can work with and more elaborate power distribution is needed.

The Boeing 787 [1] would have a heat power of 24.3 kW in the same model, though this is assuming the same total resistance in the system. Clearly the power distribution on board is more complicated than one thick cable as 24.3 kW is still unacceptable and the related 4.35 kA of current creates a strong magnetic field. Electromagnetic interference (EMI) is a major problem in modern aircraft [74] [26] though much research exists into EMI filtering [78] and shielding [80]. Filtering is done by including purpose-made electronics in the power circuit, while shielding is done both around the cabling and generators that cause EMI and the sensitive electronics that are affected by it. For further calculations 460 VAC power is assumed. This is a multiple of common aircraft voltage 115 and 230 [1], facilitating component design in a later stage yet also decreasing current needed for the same power.

No further analysis was done into the power distribution on InVADe. The issues that must be handled are clear, and the 787 has solved comparable issues. It is assumed that by 2030 the technology needed will be commonplace. Spreading the power across multiple cables and routing them to avoid interfering with sensitive electronics will both decrease heat loss and EMI effects.

OTHER COMPONENTS

Components for InVADe that are common to other aircraft include the environmental control system (ECS), avionics, anti-icing, in-flight entertainment systems, motors for landing gear and control surfaces etc. Practically all modern aircraft use a combination of 28 VDC, 270 VDC, 115 VAC and 230 VAC for various systems [1]. A bus bar is generally used for the main voltages, to which the various components are then connected.

Motors for control surfaces, landing gear, and fuel pumps use 270 VDC [1] power. This requires use of a transformer and a regulator (a so called transformer regulator unit (TRU) from the 460 VAC the power system uses. As the environmental control system is expected to be relatively powerful, this will also use 270 VDC. Conventional aircraft batteries charge on 28 VDC, but for the high power expected in InVADe 270 VDC is expected. Future, more powerful, avionics are expected to run at 270 VDC instead of 115 VAC. Legacy components such as anti-icing, fuel management systems, lighting and smaller neglected systems use 28 VDC.
The total power draw of all these components is estimated to be in the order of 100 kW and at this stage is not taken into account in the design. All the components discussed in the previous sections are assembled into an Electric Block Diagram in Appendix A.4.

5.5.3. ENGINES

Engine sizing and selection depends largely on the maximum power needed during the mission. During early design this was assumed to be the take-off phase, however with a more sophisticated approximation of the thrust from the ducted fans and iterated values for drag during cruise the balance shifted. Also, in practice turboshaft engines have multiple ratings (for sea level). The lowest rating is the continuous rating, used for cruise calculations. The take-off (TO) rating is often significantly higher. For the CT7-8A5 used in the trade-off in section 5.5.1

the continuous rating is 1608 kW and the TO rating is 1964 kW [36].

POWER RATING FOR SELECTION

From section 5.2 the power required during cruise is 1391 kW. This gives 1545 kW power available (needed) with a propulsive efficiency η_{prop} of 0.90 . The 75% rating in requirement Ct-cons-04 means that the system must be able to deliver 2060 kW to the front fans. The power only has to pass through the generators and motors, all of which have an efficiency of 0.95. The total efficiency is 0.90, thus the engine must produce 2283 kW. This is also shown in Table 5.9. The efficiency of turboprop and turboshaft engines decreases with air density, as given by Soban [108] in Equation 5.36.

$$\frac{P_{alt}}{P_{SL}} = \left(\frac{\rho_{alt}}{\rho}\right)^{0.7} \tag{5.36}$$

Table 5.9: Power outputs and efficiencies of electrical system from fan to engine

Step	Efficiency	Power [kW]
Electric motors	0.95	2060
Distribution	1	2168
Generators	0.95	2168
Engines	-	2283

Here P_{alt} is the engine power at cruise altitude, P_{SL} is the engine's sea level rating and ρ_{alt} the air density at the cruise altitude. With a ρ_{alt} of 0.6582 kg/m^3 and ρ of 1.225 kg/m^3 [63], P_{SL} is determined: 3,526 kW.

ENGINE SELECTION

The 3,526 kW given in the previous section means 1,763 kW cruise rating for the turboshaft engine to be selected. This rating is some 150 kW above the range of ratings offered by major western manufacturers, including Pratt & Whitney, GE Aviation, Rolls-Royce plc, and Turbomeca. This range of engines is intended for medium-sized helicopters which cuts off slightly below the InVADe MTOW. Larger engines exist for heavy helicopters, but are 2-3 times more powerful than needed. CS-23 limits single-engined aircraft to 5,670 kg MTOW [35], thus a single powerful turboshaft is not an option.

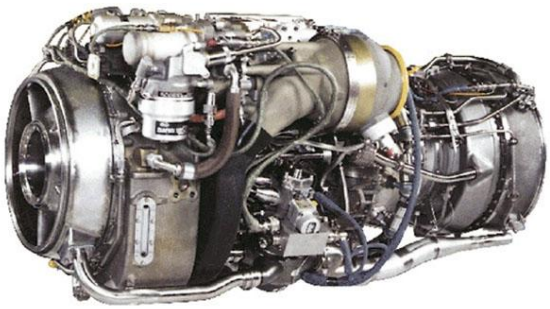

Figure 5.11: Photo of GE CT7-8 [60]

The GE CT7-8A5 engine (see Figure 5.11) used in the power plant trade-off (Section 5.5.1) is rated at 1,608 kW continuous power, too low for application on InVADe. It was certified in November 2004 [36] and has a specific fuel consumption (SFC) of 0.274 kg/kWh [65]. It is quite common for engine manufacturers to design a new variant within existing engine series for a new aircraft design. It is thus likely that by 2030 a new variant of the CT7 turboshaft engine will be able to produce enough power for the same installed weight. For reference, an overview of CT7-8A5 performance data is given in Table 5.10.

A promising development is the ATEC HPW3000, a new military turboshaft being developed for the U.S. Army's Improved Turbine Engine Program (ITEP). The target power is 3,000 shp (2,237 kW) and ATEC claim 25% more fuel efficiency and 50% more power than the current engine (GE T700, military version of the CT7 series) for the same weight [8]. Initial production is scheduled for 2022-2023 [122]. Applying this technology to replace the commercial CT7 engine would result in a rated power of 2,412 kW and a SFC of 0.206 kg/kWh for the same weight of 249.5 kg. The development timeline of the AgustaWestland AW609 and its Pratt & Whitney PT6C-67A turboshaft

Table 5.10: CT7-8A5 engine data [36]

Length	Width	Height	Dry weight	Max. cont. power	5 Min. TO power	Cont. OEI power	2-Min. OEI power	SFC
123.9 cm	66.0 cm	63.5 cm	245.9 kg	1608 kW	1964 kW	1897 kW	2043 kW	0.274 kg/kWh

engines [66] demonstrates that it is feasible to apply this future engine in the InVADe design by 2030. InVADe has no use for a total 4,824 kW of power and a scaled down engine option will most likely be available. Scaling down from 2,412 kW to the 1,763 kW needed linearly results in the weight decreasing from 245.9 kg to 180 kg.

If the HPW3000 technology is not ready for 2030 and an improved version of the CT7-8A5 (or alternative engine) is not certified either, the client will have to accept a compromise. Overpowered engines may be fitted into the design, negatively affecting weight and all parameters related to it via the snowball effect. If the CT7-8A5 is installed in its current state, cruise speed must be decreased to 582 km/h for 75% rating or the rating must be increased to 82% at a cruise speed of 600 km/h.

5.5.4. SUMMARY

Table 5.11 contains all relevant parameters discussed in this section.

Table 5.11: Summary of power plant parameters

Component	Number	Power needed [kW]	Weight [kg]	Efficiency	Dimensions (LxWxH) [m]
Front motors	2	1030	103	95%	0.61x0.40x0.40
Aft motors	2	904	90	95%	0.34x0.50x0.50
Generators	4	949	95	95%	0.21x0.66x0.66
Batteries	-	1423	119	-	0.25 m^3
Cabling	-	-	25	-	-
Engines	2	1763	180	(Equation 5.36)	0.124x0.66x0.635

6

STRUCTURES & MATERIALS

One of the main challenges in the design of InVADe was to ensure its structural integrity. In this chapter the work which was done on the structural design will be presented. The scarce resources were used to preliminary design those parts that are critical and must be developed in non-conventional ways due to the design of InVADe. These parts include the main wing structure, the canard structure, supporting structure for the ducted fans and the duct-fuselage connection. In addition, design proposals for two other critical systems are given. These critical systems comprehend the landing gear, fuselage-wing connection and the shutter system for the rear ducts.

Wherever possible, conventional designs were chosen for the load bearing structure. Therefore, the canard is outfitted with a thin wing box. The supporting structure for fans will be comprised of I-beams. However, due to the large cut-out for the back ducts, special measures had to be taken. In order to effectively transfer loads between the wing and the fuselage it was decided to place a wing box in the outer wing section. The load carrying structure in the inner wing section is composed of two spars that transfer the loads between the outer wing section and the fuselage. A preliminary sketch of the load bearing structure in the main wing can be seen in Figure 6.1. The cut-out in the wing box is only there to illustrate the presence of the stringers. As will be explained throughout the chapter, a total mass of structural elements per wing was estimated to be 191.1 kg.

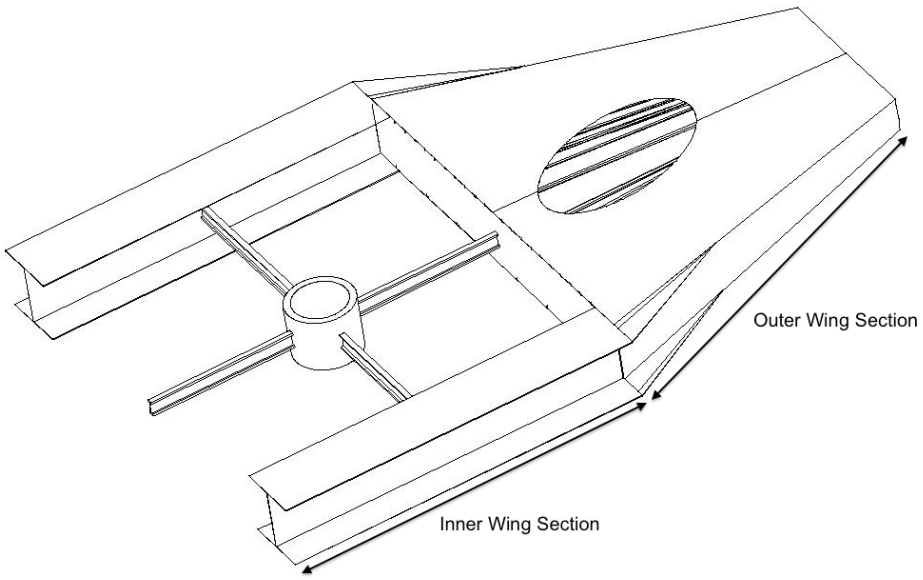

Figure 6.1: Preliminary sketch of the load bearing wing structure

This chapter will outline the design principles, designs and design proposals for the above mentioned parts. The first section will present the structural design framework. This framework will elaborate on the load analysis, in which the load factors for the different phases are determined. A distinction is made between gust load factors and load factors described by CS-23. The framework will also describe the material choice for structural elements. Finally, the section will discuss the general assumptions and equations. Section 6.3.3 until 6.5 describes the preliminary designs of the main wing structure, canard, fan supports and the duct-fuselage connection. In

each section, the methodology, reference frame, results and verification is discussed. Section 6.7 outlines design proposals for critical parts including the fuselage-wing connection and the shutter system for the rear ducts. The proposed validation procedure is described in section 6.6. The recommendations for the structural design of InVADe can be found in section 14.3.

6.1. STRUCTURAL DESIGN FRAMEWORK

Throughout the design of structural components one must incorporate a number of factors and constraints. These are explained in the following section and can be subdivided in the following subsections: load factors, material selection, general assumptions and general equations.

6.1.1. CRITICAL LOADS AND LOAD FACTORS

While in operation the structural components of InVADe will be exposed to different load factors. This subsection aims at identifying the maximum range of load factors that will occur. In order to determine the maximum range, one must calculate the critical load factors. These are typically either the manoeuvre load, the gust load or the crash loads. Crash load requirements do not apply to the parts that are designed in the following sections. The reason for this is that only parts that could injure, or need to protect the passengers in case of a crash landing should be able to remain intact after a crash. Examples of these vital structures include the cabin interior and fuselage structure. This leaves the manoeuvre and gust loads to be computed. The computation of the load factors is performed using methods described by the CS 23 regulations [35].

MANOEUVRING LOAD FACTOR

According to CS 23.337 [35] the positive limit manoeuvring load factor is described by Equation 6.1. The symbol W signifies the maximum take-off weight in pounds. With a maximum take-off weight of 8,290 kg this results in a manoeuvring load factor of +2.95. The negative load factor may not be less then -0.4 times the positive load factor, resulting in -1.18. In order to find the ultimate manoeuvring load factor the load factors have to be multiplied with the safety factor of 1.5 [35]. The ultimate manoeuvring load factors are therefore +4.42 and -1.77.

$$n_L = 2.1 + \frac{24,000}{W + 10,000} \tag{6.1}$$

GUST LOAD FACTOR

Bad weather conditions and turbulence are able to impose greater load factors on the aircraft than the load factors computed in the previous section. Gusts can suddenly increase the angle of attack and airspeed experienced by the lift-generating surfaces and therefore cause high loads. The gust load factors can be computed using Equation 6.2, 6.3 and 6.4 which are given in CS 23.341.

The gust load factor was computed for different speeds (V), using different gust velocities (U_{de}) between 25 and 66 feet per second at the cruising altitude of 6,000 m. The value of C_{L_α} can be computed for different Mach numbers using the DATCOM method [69]. All other parameters of the aircraft are known: air density at sea level $\rho_0 = 1.225$ kg/m^3, gust velocity $U_{de} = 25/50/66$ ft/s, weight at the end of the cruise segment $W = 74,752$ N, total wing surface (main wing and canard) $S = 37.13$ m^2, air density at cruise altitude $\rho = 0.6582$ kg/m^3, mean aerodynamic root chord $c = 3.66m$ and $g = 9.81$ m/s^2. It can be seen that the resulting gust loads depend strongly on the wing loading W/S, altitude and velocity of the aircraft. Additionally the maximum possible accelerations that the wing can produce are calculated for every velocity.

$$n_L = 1 \pm \frac{k_g \cdot \rho_0 \cdot U_{de} \cdot V \cdot C_{L_\alpha}}{2 \cdot \frac{W}{S}} \tag{6.2}$$

$$k_g = \frac{0.88 \cdot \mu_g}{5.3 + \mu_g} \tag{6.3}$$

$$\mu_g = \frac{2 \cdot \frac{W}{S}}{\rho \cdot c \cdot C_{L_\alpha} \cdot g} \tag{6.4}$$

Combining the possible accelerations (the solid curves), the limit and ultimate manoeuvre loads (dotted horizontal lines), the gust loads for different speeds (dashed or dotted curves) and the stall, cruise and dive speed (dashed vertical lines) in a graph for the whole speed range gives the graph shown in Figure 6.2. From this graph the maximum design loads as well as the flight envelope are derived.

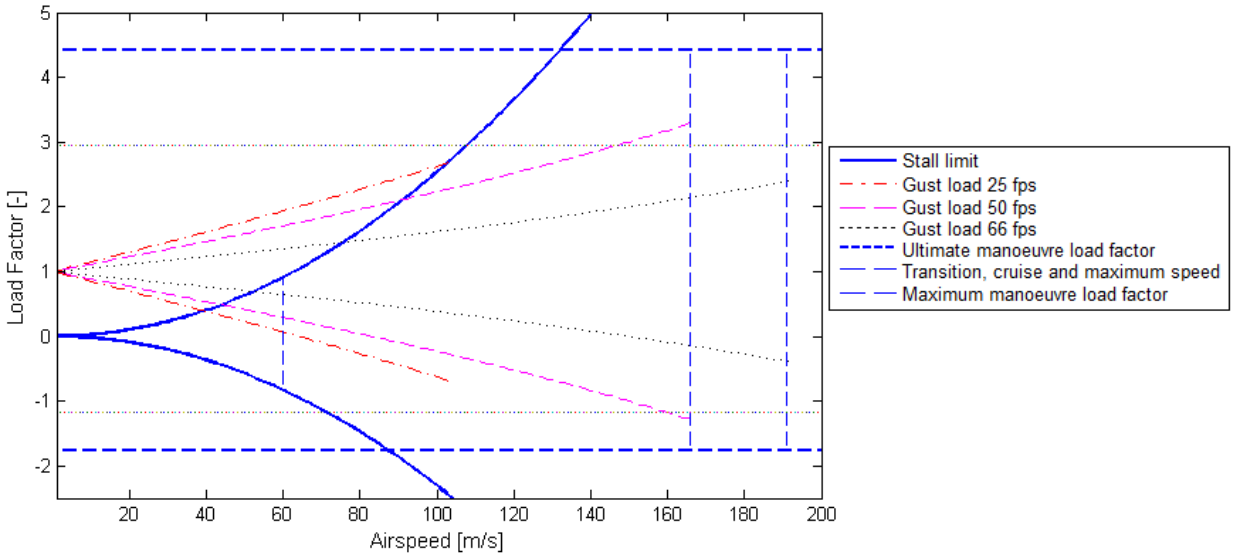

Figure 6.2: Gust and manoeuvre load factor versus velocity

Figure 6.2 indicates that after applying a safety factor of 1.5 the highest load factor to be expected are the gust loads at cruise speed with a load factor of +4.93 and -1.93. The structure therefore needs to be able to handle these load factors in order to ensure safe operations in the whole flight envelope (subsection 8.3).

6.1.2. MATERIAL SELECTION

The choice of material for the structural elements that will be used throughout the report is based on five key criteria. These criteria, listed below, were used as guidance during the selection of material used in the structural elements of InVADe.

- Strength-to-weight ratio
- Endurance limit
- Material and production costs
- Manufacturability
- Sustainability

The first decision entailed the choice between two materials often used in the aerospace industry, namely composites and metal alloys. Composites are usually glass fibre or carbon fibre reinforced polymers. Occasionally, aramid fibers are used. Metals used in the aerospace industry are mostly aluminium alloys. However, titanium, steel or magnesium alloys are used when the qualities of composites or aluminum do not suffice.

Due to their high material cost aramid fibers and titanium were discarded. Steel was rejected due to the low strength-to-weight ratio. Finally, magnesium alloys were dropped because of its low strength-to-weight ratio and poor fatigue resistance. At this point, aluminium alloys and glass/carbon fibre composites are the two materials which are not discarded. To decide between these materials their strengths and weaknesses were examined. The results of this analysis can be seen in Table 6.1. Using engineering judgement aluminium alloys were chosen due to its low costs, easy manufacturing, sustainability and sufficient mechanical properties.

Table 6.1: Strengths and weaknesses of composite of aluminium alloys

	Composites	**Aluminium Alloys**
Strengths	High ultimate strength Low weight Few geometrical constraints	Relatively low costs Well known fatigue characteristics Good manufacturability Recyclable
Weaknesses	High material cost Expensive and complicated manufacturing Fatigue is hard to predict Not recyclable	Lower ultimate strength More geometrical constraints

Based on the fact good fatigue characteristics are essential to the structural design of the load bearing components, the choice was made to use aluminium alloys. Since the four fans and two gas turbines will create high-frequency vibrations, a large amount of loading cycles will occur. Hence, a high fatigue resistance of the the material is important. Therefore, Aluminium 2024-T4 was the most suitable aluminium alloy. Although Aluminium 2024-T4 has a lower strength-to-weight ratio than many other aluminium alloy, the resistance to fatigue qualities are excellent. The endurance limit of 2024-T4 is given as 138 [MPa] [67]. Therefore, the material won't fail for as a long the stresses are below this level. In other words, fatigue is brought back to an absolute minimum. All parts will be designed such that their maximum Von Mises Stress is below that 138 [MPa], resulting in a safe-life design of the main structural elements.

Additionally, the usage of the same alloy for all structural elements facilitates the end-of-life disposal requirements. The manufacturability of Aluminium 2024-T4 is good and in comparsion to composites Aluminium 2024-T4 has a low production cost.

6.1.3. GENERAL ASSUMPTIONS

A total of eight general assumptions (GAs) are made to facilitate the stress and buckling analysis of the load-carrying structures in the wing, canard and ducted fans. These assumptions are valid for any method used throughout this chapter. Assumptions which apply to only a certain component are listed in their respective section.

GA1: Weightless wing The wing structure, including all subsystems and fuel, are assumed to be weightless. This will increase bending moments, shear forces and torsional forces as weight serves as a load relief. Nonetheless, the weight of the wing is low compared to the amount of lift generated. Preliminary calculations based on the results of the Class II weight estimation show this ratio is equal to 9%.

GA2: Absence of drag force The total drag force on one wing equals approximately 700 N. During cruise the wings generate a total lift of 48.8 kN, or 24.4 kN per wing. Since the drag force equals 3% of the lift per wing, the stresses generated by the drag are negligible.

GA3: Load carrying structure does not warp If the wing structure were to exhibit a change in geometry due to the stresses, the stress distribution will change. To facilitate the preliminary analysis of the load bearing structures, warping is neglected.

GA4: Material is isotropic The material is assumed to have the constant properties. These properties include Young's Modulus, yield stresses and density. In reality, these properties are not constant and deviations exist due to material imperfections, manufacturing and processing.

GA5: Resultant lift force acts on the quarter chord line Indepedent of local properties of the wing, the lift force is assumed to act on the quarter chord line.

GA6: Resultant lift force is proportional to the local chord length The local force is calculated using the ratio between the local chord and the lift force. This ratio is set equal to the wing loading. Hence, formula 6.5 can be applied. In this equation W/S is equal to the wing loading, $c(i)$ to the chord length at section i and $z(i)$ to the width of section i.

$$L(i) = W/S \cdot c(i) \cdot z(i) \tag{6.5}$$

GA7: Direct stresses The direct stresses in the load carrying structures is comprised of bending stresses only. No normal stresses are present.

GA8: Skin does not carry loads All loads are carried by the load-bearing structure. The skin of the wing does not carry any loads.

6.1.4. GENERAL EQUATIONS

This subsection will elaborate on the general equations (GEs) that are used throughout the design of the structural elements. All formulae are derived from Megson [86].

GE1: Centroid The centroid of a cross-section with respect to a given axis can be determined using Equation 6.6. For example, if one were to calculate the centroid with respect to the y-axis, the total area is defined as A_t, a number of N separate areas as A and the y-coordinate as y.

$$\bar{y} = \frac{\sum_{i=1}^{N} A_i y_i}{A_t} \tag{6.6}$$

GE2: Moment of inertia The second moment of inertia around the x-axis I_{xx} can be calculated using Equation 6.7. The height of a part (y-direction) of a cross-section is defined as h and the width (x-direction) as w. The symbol A stands for the area of the respective part and y_c is the distance in y-direction between a part of a cross-section and the centroid. If the parameters are changed accordingly, Equation 6.7 can be used to compute the values of I_{yy} and I_{zz}. If the structure does not have an axis of symmetry, the product second moment of inertia I_{xy} is non-zero. Using Equation 6.8 one can compute this value.

$$I_{xx} = \sum_{i=1}^{n} \frac{1}{12} w_i h_i^3 + A_i y_{ci}^2 \tag{6.7}$$

$$I_{xy} = \sum_{i=1}^{n} y_{ci} x_{ci} B_i \tag{6.8}$$

GE3: Bending stress The bending stresses can be computed using Equation 6.9. The moment around the x-axis and y-axis are define as M_x and M_y respectively. Sinc the drag force is assumed to be zero, M_x will be zero. If the structure is symmetric around atleast one axis, the product second moment of inertia is zero. If one of the latter statements occurs, Equation 6.9 will be greatly simplified.

$$\sigma_z = \frac{M_y I_{xx} - M_x I_{xy}}{I_{xx} I_{yy} - I_{xy}^2} x + \frac{M_x I_{xx} - M_y I_{xy}}{I_{xx} I_{yy} - I_{xy}^2} y \tag{6.9}$$

GE4: Shear flow One can calculate the shear stress for an idealised boom structure using Equation 6.10. Is has been assumed that the skin carries shear stress only. Therefore the direct stress carrying skin t_D is equal to zero. Since only a lift load is present S_x can be neglected. Thus the shear stress is only dependent of the shear force in y-direction S_y, the boom area, the second moments of inertia, the distance to the neutral axis in y-direction y_r and if the section is asymmetrical also the product second moment of inertia and the distance to the neutral axis in x-direction x_r.

$$q_s = -\frac{F_{S_x} I_{xx} - F_{S_y} I_{xy}}{I_{xx} I_{yy} - I_{xy}^2} \left[\int_0^s t_D x ds + \sum_{r=1}^{n} B_r x_r \right] - \frac{F_{S_y} I_{yy} - F_{S_x} I_{xy}}{I_{xx} I_{yy} - I_{xy}^2} \left[\int_0^s t_D y ds + \sum_{r=1}^{n} B_r y_r \right] + q_{s,0} \tag{6.10}$$

GE5: Shear stress Shear stress can be computed by dividing the local shear flow q_s by the local thickness t, as is depicted in 6.11.

$$\tau = \frac{q_s}{t} \tag{6.11}$$

GE6: Von Mises stress The Von Mises stress is often used to indicate if the yielding of the structure wil occur. The wing structure will yield when the Von Mises yield stress is greater than the material yield stress. However, because all forces other than the lift force are neglected, only the terms σ_{11} and τ_{12} will be nonzero.

$$\sigma_v = \sqrt{0.5((\sigma_{11} - \sigma_{22})^2 + (\sigma_{22} - \sigma_{33})^2 + (\sigma_{11} - \sigma_{33})^2) + 3(\tau_{12}^2 + \tau_{21}^2 + \tau_{31}^2)} \tag{6.12}$$

GE7: Buckling Although a web or flange might have sufficient strength to withstand certain shear and bending stress levels, buckling might still occur. Therefore, Equation 6.13 and 6.14 must be used to verify if the stress values do not exceed the critical stress levels for buckling in the web. Likewise, 6.15 can be used to check the stress levels in the flange. In these equations, E, ν_e represent the Young's Modulus and Poisson's ratio respectively. The local thickness and width are signified by t and w respectively. The symbol k_s denotes the shear buckling stress coefficient and is dependent on the aspect ratio of the plate and boundary conditions. Similarly, k_b and k_c designate the bending-buckling coefficient and compressive-buckling coefficient.

$$\tau_{cr} = \frac{\pi^2 k_s E}{12(1 - {\nu_e}^2)} \left(\frac{t}{w} \right)^2 \tag{6.13}$$

$$\sigma_{cr} = \frac{\pi^2 k_b E}{12(1-{\nu_e}^2)} \left(\frac{t}{w}\right)^2 \tag{6.14}$$

$$\sigma_{cr} = \frac{\pi^2 k_c E}{12(1-{\nu_e}^2)} \left(\frac{t}{w}\right)^2 \tag{6.15}$$

When a section has to cope with potential critical bending and shear stresses, it is important to look at the combined loading. This can be done by calculating the margin of safety (MoS), which can be done by using Equation 6.16 in which τ and σ are the actual shear and bending stress respectively. The value should be preferable be zero, because then the plate is not over designed. However, the value should not be below zero, otherwise the plate will buckle earlier than predicted.

$$MoS = \frac{1}{\sqrt{\left(\frac{\tau}{\tau_{cr}}\right)^2 + \left(\frac{\sigma}{\sigma_{cr}}\right)^2}} - 1 \tag{6.16}$$

6.2. WING BOX

The following section will elaborate on the design of the wing box found in the outer section of the main wing. First, an explanation of the calculation method is presented, followed by the reference system definition. Subsequently, the results of the stress and buckling analysis are elaborated. Finally, the reader is presented with the verification of the calculation method.

6.2.1. METHODOLOGY

The first step is to divide the wing box in sections with respect to the z-axis. Bending and shear stresses will be determined in each section. The stress calculation method is based on idealising the complex structural cross-section of a wing box into a specific amount of booms, which are concentrations of area. The direct stress in each boom is assumed to be constant and they are are located at the mid-line of the skin. Figure 6.3 gives a visualisation of a cross-section idealised by booms. Note that the areas of the booms and the skin thickness of all parts are not yet defined at this stage.

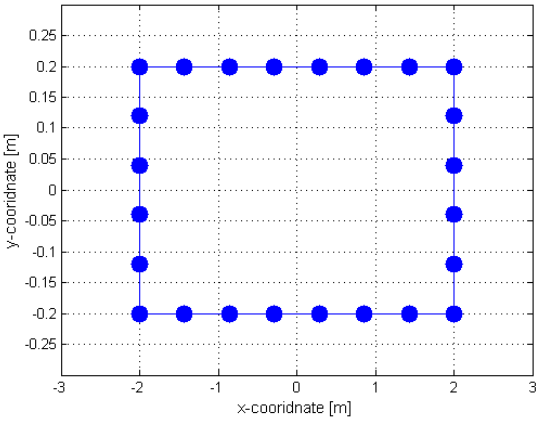

Figure 6.3: Visualisation of a wing box cross-section idealised by booms

The skin of the wing box is mainly effective in resisting shear, but carries some direct stresses as well. However, applying idealised structure methods it is assumed that the booms carry all the direct stresses and the skin all shear stresses. Summarising, the following assumptions are applied:

- The booms carry direct stresses only
- The skin carries shear stresses only

BOOM SIZING AND SECTION PROPERTIES

The sizing of the booms, thus calculating the area of the booms, can be done using Equations 6.17 and 6.18. In a non-idealised structure the thickness of the skin adjacent to the boom is defined as $\bar{t}_D$, which is the direct stress carrying skin. The parameter $\bar{b}$ is the perpendicular distance between the boom i and boom $i+1$. The ratio $\frac{\sigma_2}{\sigma_1}$ can be determined by dividing the y-coordinate of the second boom by the y-coordinate of the first one. The second equation is used for calculating the boom area of the second boom. Note that to determine the boom area, one

should take all the booms into account, which are directly connected to the boom for which the area is to be determined. Thus in the case of a rectangular wing box, shown in Figure 6.3, the number of equations needed is two. The resultant value from the two equations can be superposed to get the right boom area. The centroid of an idealised cross-section can be calculated by using Equation 6.6. For an idealised structure, only the area and location of the booms should be taken into account.

$$B_1 = \frac{t_d \bar{b}}{6}\left(2 + \frac{\sigma_2}{\sigma_1}\right) \tag{6.17}$$

$$B_2 = \frac{t_d \bar{b}}{6}\left(2 + \frac{\sigma_1}{\sigma_2}\right) \tag{6.18}$$

SHEAR STRESS EQUATIONS

One starts with calculating the shear stress by cutting a wall between two booms. A wall adjacent to the cut section will be the first wall for which the basic shear stress will be calculated. This is composed of all the terms in Equation 6.10 except for the $q_{s,0}$, which is the shear flow due to torsion. The basic shear stress in the next wall is equal to the separate calculated basic shear stress plus the basic shear of the previous and so on.

The total shear flow can be obtained by adding the torsional shear flow to the basic one. The torsional shear flow can be computed by taking the moments around the point where the line of action of the local shear force crosses the neutral axis. The moment caused by a certain wall is equal to the basic shear flow of the wall times its length and the perpendicular distance to the point crossing. The torque created by $q_{s,0}$ by Equation 6.19. In this equation A is the enclosed area. When setting the moment to zero one can determine the only unknown, namely $q_{s,0}$. When the direct stresses and the shear stresses are known, the Von Mises yield stress can be calculated using Equation 6.12.

$$M_T = 2A_{encl} \cdot q_{s,0} \tag{6.19}$$

BUCKLING OF WING BOX COMPONENTS

As was explained in paragraph 6.1.4 on buckling, one should not only look at the Von Mises stress to determine the critical thicknesses and geometry of a structural element. Buckling must also be accounted for. The critical compression buckling stress, for the lower and upper plate, can be determined using Equation 6.15. Similarly, the critical bending buckling stress and shear buckling stress in the right and left side can be determined using Equations 6.14 and 6.13 respectively.

During flight the upper panel of a wing box is in compression. To improve the properties regarding the buckling of the upper plate of a wing box, one can place stiffeners along the z-axis of the wing. This increases the t/w value in Equation 6.15 since the value of w is decreased. It was assumed that the stringers divide the upper and lower skin in sections which are simply supported at the edges. The edges of the right and left side of the wing box were assumed to be clamped. The resulting K_c, K_b and K_s are given in Table 6.2.3 [16].

6.2.2. REFERENCE SYSTEM

The reference system used for the stress calculation is shown in Figure 6.4a. The origin is located in the centre of gravity of the root section, which is assumed to be symmetrical about the x- and y-axis. The origin of the axis system does not change if the section should be made asymmetrical about the two axis, which would result in a different centre of gravity location. The z-axis is directed outward of the paper. Further, the variables of each section are shown in the figure, namely the thickness t and the width and the height of a certain section. The reference system, looking down at the wing planform, can be seen in Figure 6.4b. One could introduce a taper, a sweep angle or a combination of them both.

6.2.3. RESULTS STRESS AND BUCKLING ANALYSIS

The parameters used for the stress calculation for the outer wing box of the main wing and the canard are shown in Table 6.2.3.

The thicknesses are proportional to the width or the height of the box. The factors in the skin thickness definitions were determined by performing a first weight optimisation in which the factors were varied together with the size of the stiffeners and the amount of stiffeners. The lightest combination, that still met the Von Mises yield stress and the buckling criteria, was chosen.

The iteration started of with an initial guess followed by 2500 iterations. Every time an iteration fulfilled the requirements, it was compared to the weight of a configuration that also fulfilled them in front of it. This gave 6 different configurations, which are shown in Figure 6.5. The weight is on the right y-axis. On the left axis is the

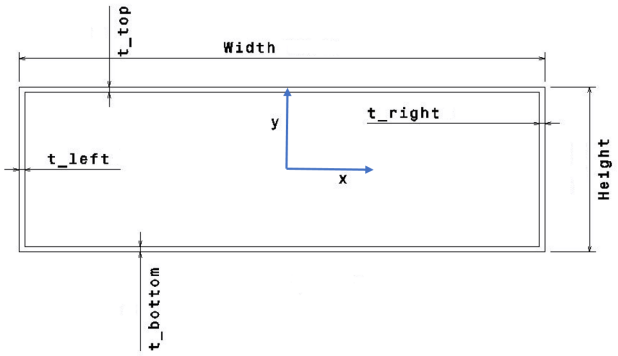

(a) The axis system on the root section. The positive z-axis is pointing out of the paper. This is the reference system used during this whole section. The right side of the box is the leading edge and the left side the trailing edge.

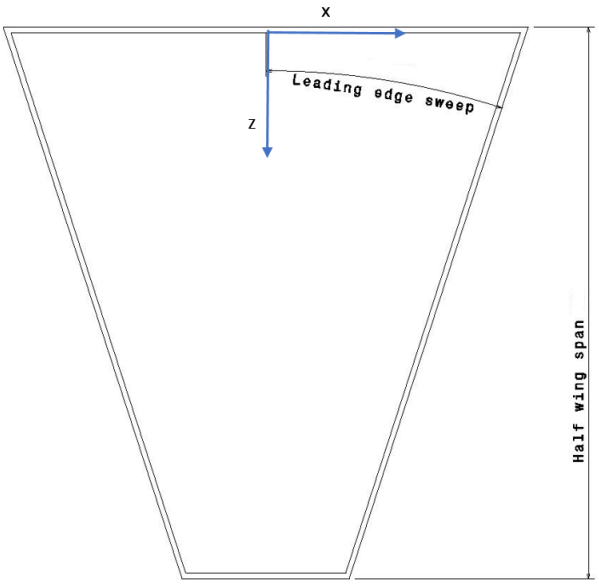

(b) The axis system looking down at the planform of the wing. The positive y-axis is pointing out of the paper.

Figure 6.4: Reference systems

margin of safety (MoS) regarding the critical bending and shear stress for the right side of the wing box. By pushing the limit for a minimum amount of weight, the MoS decreases as well. Optimally this margin is zero, because then the maximum limit has been reached (Note that the safety factors are already included). The optimisation gave a final MoS of 0.0058, which was calculated using Equation 6.16.

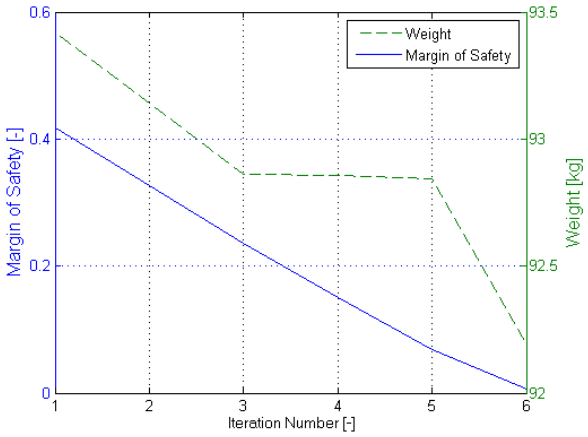

Figure 6.5: Weight optimisation Wing Box and resulted Margin of safety for the right skin

The resulted stresses of the final configuration are shown in Figure 6.6a. The highest direct and shear stresses occur near the root. Figure 6.6b shows the Von Mises stress at every location on the wing box. The highest stresses are located at the leading edge near the root.

In the stress calculations the maximum gust load was taken into account, see section 6.1.1. However, one should also keep the negative gust load in mind. The stress calculations for the latter case have been performed as well. The result was that extra stringers needed to be placed on the bottom skin to withstand buckling during negative gust loading.

Figures 6.6c and 6.6d show the critical buckling stresses for the right side, which is about the same as for the left side, and the top side of the box, respectively. The critical bending stress in the right skin is very large comparable to the critical shear stress. It therefore can be concluded that the thickness determination of the right skin, which is true for the left skin as well, is not effected by the bending stress at all. Further, the Von Mises Yield stress is definitely not reached in the right and left side. Thus the thicknesses of the left and right side are driven by having

Parameter	Symbol	Main wing	Canard	Unit
Wing Loading	W/S	223.3	146.6	$[kg/m^3]$
Half the span	$b_{\frac{1}{2}}$	2.77	3.84	[m]
Leading edge sweep	Λ	19	1.28	[°]
Width root	w_{root}	3.18	0.6	[m]
Height root	h_{root}	0.47	0.12	[m]
Width tip	w_{tip}	1.28	0.42	[m]
Height tip	h_{tip}	0.26	0.086	[m]
Thickness top skin	t_{top}	$0.0004 \cdot w_i$	$0.0021 \cdot w_i$	[m]
Thickness bottom skin	t_{bottom}	$0.00063 \cdot w_i$	$0.0018 \cdot w_i$	[m]
Thickness right skin	t_{right}	$0.0095 \cdot h_i$	$0.0123 \cdot h_i$	[m]
Thickness left skin	t_{left}	$0.0067 \cdot h_i$	$0.0094 \cdot h_i$	m]
Shear bucklling coefficient	K_s	8	8	[-]
Buckling coefficient	K_b	24	24	[-]
Compression buckling coefficient	K_c	4	4	[-]
Corner stiffener area	A_{cs}	$400e^{-6}$	$400e^{-6}$	$[m^2]$
Stringer area on top and bottom skin	A_{ms}	$100e^{-6}$	$100e^{-6}$	$[m^2]$
Number of stringers on the top skin	N_{st}	24	8	[-]
Number of stringers on the bottom skin	N_{st}	8	6	[-]
Weight	W	91.8	42.1	[kg]

Table 6.2: Input parameters to compute the stress distribution in the wing box

Parameter	Symbol	Value	Unit
Wing Loading	W/S	250	$[kg/m^3]$
Half the span	$b_{\frac{1}{2}}$	3	[m]
Leading edge sweep	Λ	19	[°]
Width root	w_{root}	0.6	[m]
Height root	h_{root}	0.12	[m]
Width tip	w_{tip}	0.3	[m]
Height tip	h_{tip}	0.06	[m]
Thickness top skin	t_{top}	$0.001 \cdot w_i$	[m]
Thickness bottom skin	t_{bottom}	$0.001 \cdot w_i$	[m]
Thickness right skin	t_{right}	$0.02 \cdot h_i$	[m]
Thickness left skin	t_{left}	$0.02 \cdot h_i$	[m]

Table 6.3: Comparison cross-section

no shear buckling.

The thickness of the top skin and the amount and size of the stringers are driven by the the critical bending stress and the Von Mises yield stress. The fatigue stress to have a safe life (Section 6.1.2), should never be reach with this configuration, because the maximum Von Mises stress is 129 MPa. One can come closer to the 138 MPa stated in section 6.1.1, by decreasing the step size of the variables in the optimisation process.

The same optimisation has been done for the canard. The results are shown in Figures 6.7a, 6.7b, 6.7c and 6.7d. The maximum Von Mises stress is 137.5 MPa and is therefore still under the fatigue stress given in section 6.1.2. This time the thickness of the left and right skin is mainly driven by the Von Mises yield stress. The margin of safety of the right skin is 0.15. The compressive buckling stress drives, together with the Von Mises yield stress, the thickness of the upper skin and the amount of stringers and the cross-sectional area of those. The weights of the wing box of the wing and the canard are presented in Table 6.2.3.

6.2.4. VERIFICATION

To determine the validity of the method, a simple rectangular cross-section, of which the geometry is given in Table 6.2.4, has been investigated. The input input wing loading is given as well. So-called unit tests were performed, which is checking step by step instead of comparing the final results. The difference between the numerical solution and the analytical one (formulas presented in Megson [86]) was determined for the moments of inertia, the bending moment and shear force and the shear stress and direct stress.

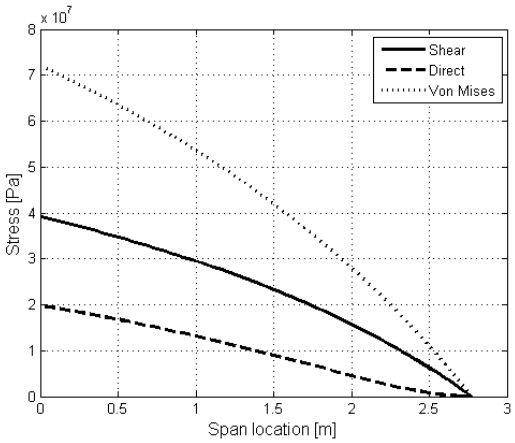

(a) The maximum shear, bending and Von Mises stress along the span of the wing box.

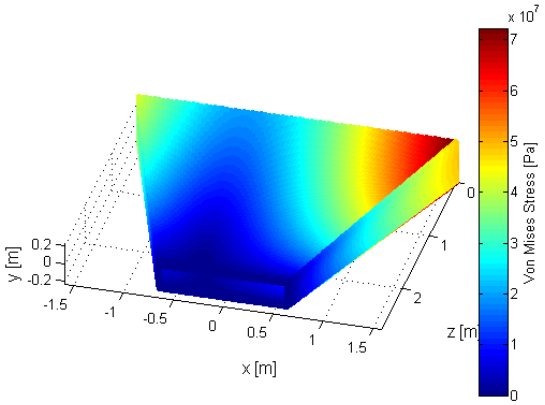

(b) The Von Mises yield stress distribution in the wing box of the wing.

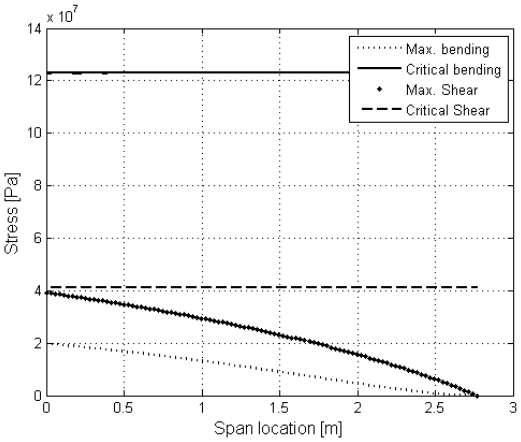

(c) The critical stresses compared to the maximal stress per section in the right skin.

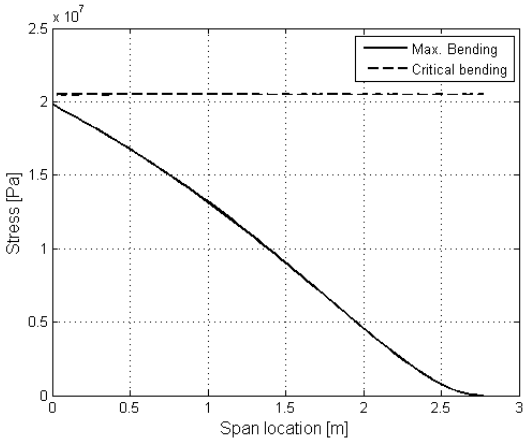

(d) The critical bending stress compared to the maximal bending stress per section in the top skin.

Figure 6.6: Stresses in the wing box of the wing

During the analytical solution, the structure was assumed to be thin-walled, which is safe to make if the ratio of half the height over the thickness of the bottom or top of the box is bigger than 10. According to Megson [86] the error will only be 6% to a maximum. Further, the direct stresses will could be higher, because when using thin-walled the moment of inertia will be smaller.

The results are shown in Table 6.2.4. As can be seen the difference is minimal and thus the numerical solution can be used to determine the stresses. The given shear flow max is the shear flow created by the local shear force, which is for the root 11.5 N (When dividing the wing in 300 sections). To check whether or not this calculation of local shear force is correct, one can simply sum up all the local shear forces and compare them to the wing loading time the total area. This is shown in the table as well. The difference is again minimal.

6.3. MAIN SPARS

The following section will elaborate on the design of the main spars found in the inner section of the main wing. The spars are shaped as I-beams and are only connected to each other by the fan hub supports. However, during the following analysis the assumption is made this support does not carry anu loads. This section will describe the reference system first, followed by the methodology. Subsequently, the results of the stress and buckling analyses are presented. Finally, the verification results are presented.

The spars must be designed for the most critical load case. The two load cases which are considered are cruise flight and VTOL manoeuvres. For cruise flight a maximum load factor of 5.1 is calculated, whereas this factor is only 1.1 for VTOL manoeuvres. The total bending moment in cruise conditions has a peak value of 380 kNm. During VTOL manoeuvres a maximum bending moment of 40 kNm is encountered. Two reasons can be identified to explain the large difference between these values. First and foremost, the ultimate load factor is 78% greater during cruise. The second reason involves the moment arm. During cruise this moment arm can be as large as 6

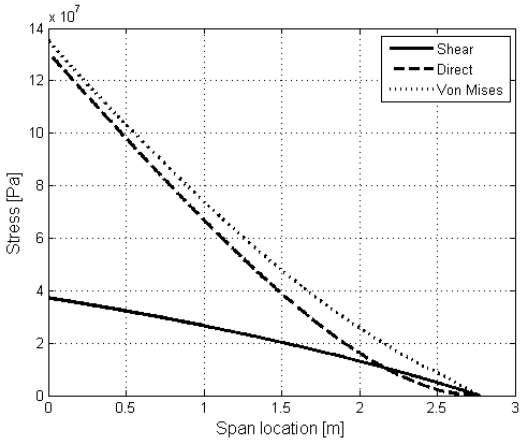

(a) The maximum shear, bending and Von Mises stress along the span of the canard.

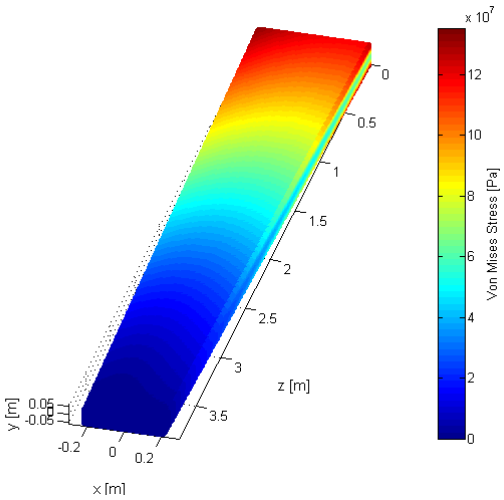

(b) The Von Mises yield stress distribution in the wing box of the canard.

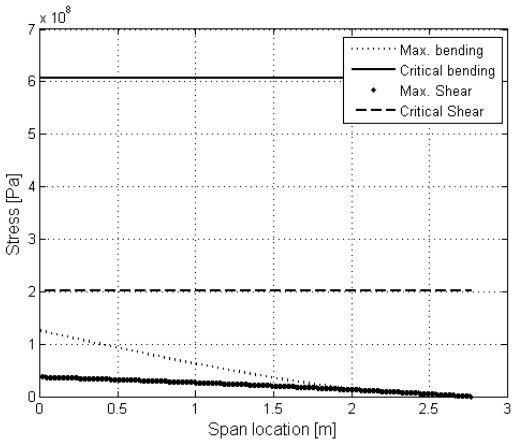

(c) The critical stresses compared to the maximal stress per section in the right skin.

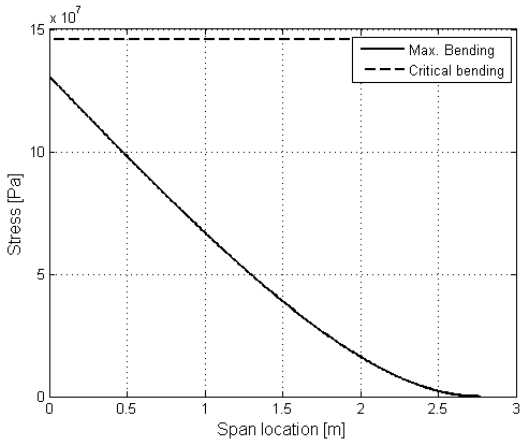

(d) The critical bending stress compared to the maximal bending stress per section in the top skin.

Figure 6.7: Stresses in the wing box of the canard

m, whereas the moment arm of the duct has a maximum of 2.735 m. In conclusion, the critical load case is cruise with the maximum gust load factor. Therefore the spars will be sized based on cruise flight loads.

6.3.1. METHODOLOGY

A substantial part of the methodology used in the design of the main spars is identical to the methods used in the design of the wing box. Therefore, the reader is referred to subsection 6.2.1 on the idealisation principles, boom sizing and buckling respectively. Since the airfoil dimensions remain constant throughout the length of the section, the height and width of the spars remain constant. This will enable the transition of the loads from the outer wing skin to the spars as the spars are always in contact with the skin. In order to keep weight to a minimum the skin thickness of flanges and web decrease linearly along the length of the section and its proportional to the z-coordinate of the section.

The factors in the skin thickness definitions were determined by performing a first-order weight optimisation in which the factors were varied over a certain range. The lightest combination with the lowest margin of safety for the web that still met the Von Mises yield stress and the buckling criteria was chosen.

In the stress calculations the maximum gust load was taken into account, see Section 6.1.1. However, one should also keep the negative gust load in mind. The stress calculations for the latter case have been performed as well.

6.3.2. REFERENCE SYSTEM

To calculate the stresses in a load bearing structure, one must define a reference system. The reference system used in the calculation of the stresses in the main spars can be seen in Figure 6.8a. Using a top-view perspective,

Parameter	Numerical (Idealized structure)	Analytical (Thin- walled)	Unit
I_{xx}	3.281e-6	3.283e-6	$[m^4]$
I_{yy}	7.337e-6	7.344e-6	$[m^4]$
I_{xy}	0	0	$[m^4]$
$Shear force$	3.3146e3	3.3109e3	$[N]$
$BendingMoment$	4.4035e3	4.4145e3	$[Nm]$
σ_{max}	8.0573e7	8.0679e7	[Pa]
q_{max}	62.3170	62.3707	[N/m]
$TotalLift$	3.3136e3	3.3109e3	[N]

Table 6.4: Numerical and analytical solution comparison for the root of the verification wing box

the reference system can be seen in Figure 6.8b. The origin of the system is located at half the chord length at the root at a height of a tenth chord as measured from the bottom skin.

Figure 6.8a and 6.8b also indicate the main dimensions of the spars, whose height and width were sized using constraints of the airfoil shape and duct geometry.The height and width were sized such that the spars connect to the upper and lower skin at all times, in order to facilitate the transfer of pressure loads on the skin.

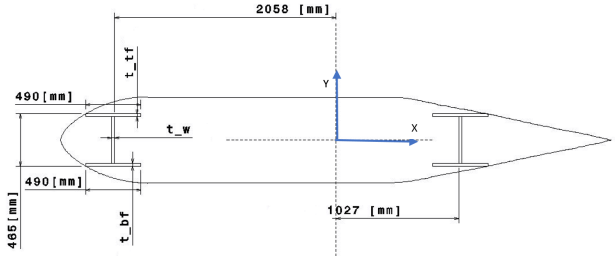

(a) The reference system relative to the root section. The positive z-axis is pointing out of the paper.

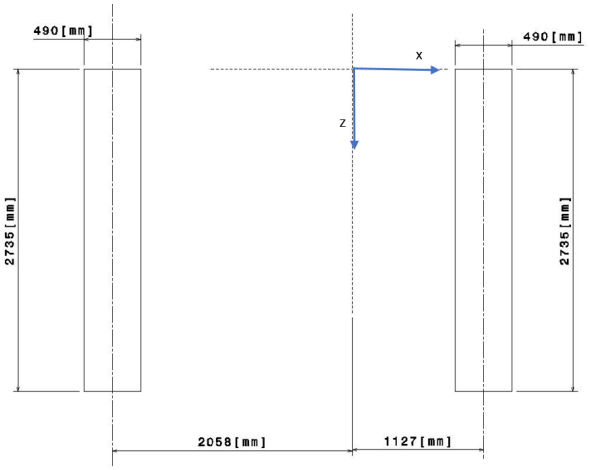

(b) The reference system looking down at the planform of the inner section of the wing. The positive y-axis is pointing out of the paper.

Figure 6.8: Reference systems

6.3.3. RESULTS STRESS AND BUCKLING ANALYSIS

Because of the location of the spars, 74% of the lift generated by the inner section of the wing is carried by the leading edge spar. Hence, the remaining 26% of the lift generated is carried by the trailing edge. In order to complete the systems, the boundary conditions at the tip of the spars were calculated using data from the wing box calculations in section .

Figure 6.10a indicates the margin of safety of the web in the leading edge spar and trailing edge spar. Both spars were subjected to 4096 different combinations of thicknesses for the upper flange, web and lower flange. Since the imposed stresses are greater in the leading edge spar, less combinations sufficed all conditions and hence only 989 iterations are plotted. Since the stresses in the trailing edge spar are smaller, more combinations of thicknesses sufficed all conditions. In the end, the thickness distribution with the smallest positive margin of safety was chosen for each spar. The webs have a margin of safety of 0.04 and 0.06 for the leading edge and trailing edge respectively. A margin of safety of close to 0.0 might seem unsafe. However, one must remember this margin of safety was computed for the absolute maximum load case with a safety factor of 1.5.

The following results were obtained using a total of 200 sections with 707 booms each. Using the material properties described in subsection 6.1.2 on material selection, the maximum Von Mises stress must be limited to 138 MPa. The shear, bending and Von Mises stress for the leading edge spar and trailing edge spar are plotted in Figure 6.10b and 6.10c respectively. A graphical representation of the Von Mises stress in both spars is given in Figure 6.9. The maximum Von Mises stress equals 101 Mpa in the leading edge spar, and 71 MPa in the trailing edge. The main parameters of the spars are summarised in Table 6.5.

Parameter	Symbol	Leading Edge Spar	Trailing Edge Spar	Unit
Wing Loading	W/S	223.3	223.3	$[kg/m^3]$
Half the span	$b_{\frac{1}{2}}$	2.375	2.375	[m]
Leading edge sweep	Λ	0	0	[°]
Width root	w_{root}	0.49	0.49	[m]
Height root	h_{root}	0.465	0.465	[m]
Width tip	w_{tip}	0.49	0.49	[m]
Height tip	h_{tip}	0.465	0.465	[m]
Thickness top flange skin	t_{tf}	$0.0014 \cdot w_i$	$0.0009 \cdot w_i$	[m]
Thickness web skin	t_w	$0.00092 \cdot w_i$	$0.00088 \cdot w_i$	[m]
Thickness bottom flange skin	t_{bf}	$0.0014 \cdot w_i$	$0.0004 \cdot w_i$	[m]
Shear bucklling coefficient	K_s	8	8	[-]
Buckling coefficient	K_b	24	24	[-]
Compression buckling coefficient	K_c	5.5	5.5	[-]
Weight	W	50.4	29.3	[kg]

Table 6.5: Input parameters to compute the stress distribution in the main spars

The reason why the maximum Von Mises stresses do not approximate 138 MPa closely is because other constraints is in place. These constraints are the buckling criteria. Using Equation 6.13 and 6.14 the shear buckling stress and bending buckling stress were computed for the web. In order to be conservative the web was assumed not to be clamped, yet simply supported would be too conservative. The shear buckling stress proved to be critical for for the decision of the thickness distribution in the web.

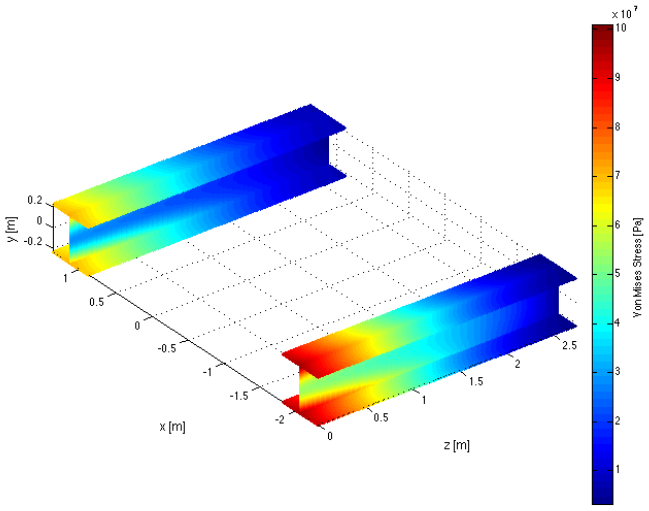

Figure 6.9: A graphical representation of the Von Mises stress in both spars

In addition to buckling of web, buckling of the upper flanges due to compressive stresses was also examined. Equation 6.15 was used to compute the compression buckling stress for the flange. The assumption was made that the flange is divided in two separate plates, with the division made at the location where the web intersects with the flange. This results in two plates, clamped at the connection with the web and simply supported at the free end. Using those assumptions, a value of k_c was chosen. Buckling due to compression stresses turned out to be critical and was therefore driving for the thickness distribution of the trailing edge spar. This resulted in a lower local Von Mises stress of maximum 71 Mpa.

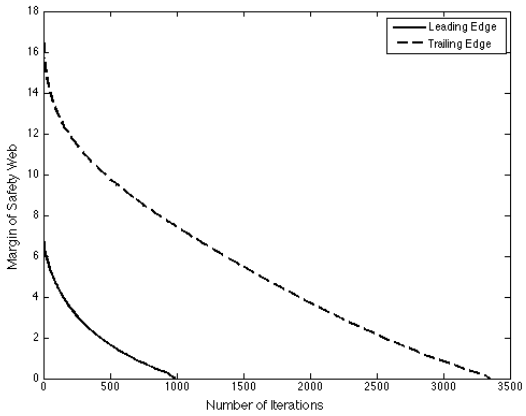

(a) Margin of safety of the web versus the number of iterations

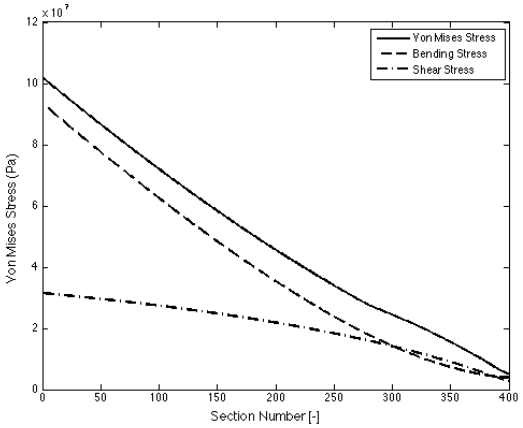

(b) Maximum shear, bending and Von Mises stress along the span of the leading edge spar

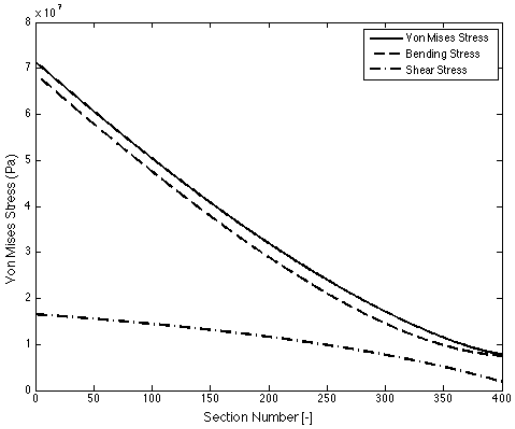

(c) Maximum shear, bending and Von Mises stress along the span of the leading edge spar

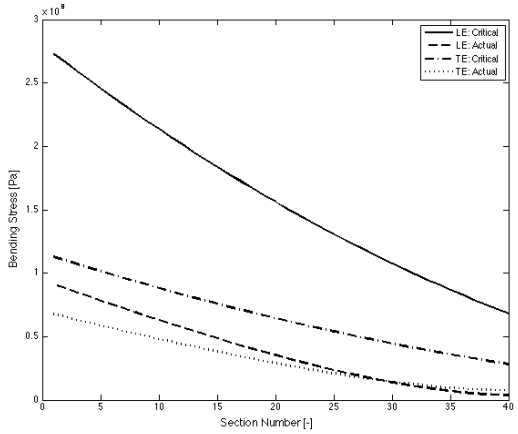

(d) Critical buckling bending stress compared to the maximal bending stress per section of the top flange

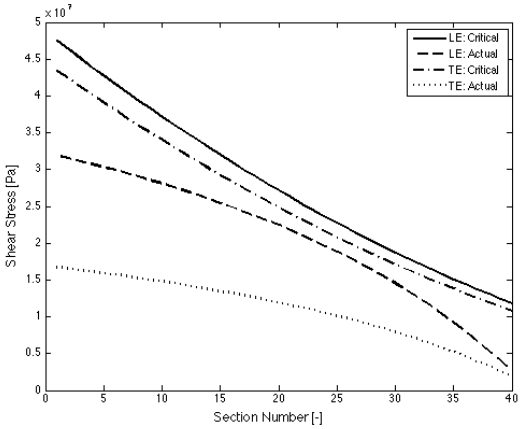

(e) Critical buckling shear stress compared to the maximal shear stress per section of the web

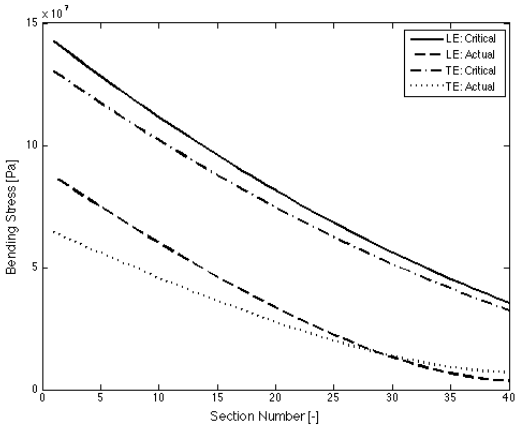

(f) Critical buckling bending stress compared to the maximal bending stress per section of the web

Figure 6.10: Stresses in the main spars

6.3.4. VERIFICATION

To ensure the numerical model accurately represents the analytical equations, a total of seven unit tests are performed. Dependent on the parameter, these unit tests compute the values at predetermined locations along the length of both spars or cross-section. Cross-sectional properties that are calculated for six different sections include cross-sectional area, moment of inertia, shear force and bending moment. Properties that vary within each cross-section are shear flow, shear stress and bending stress and are calculated for predetermined locations on the cross-section at two different locations along the wing. The author must note the parameter inputs, including thicknesses, are not those of the final spars.

The verification was performed using a total of 1,000 cross-sections with 3,007 booms each using preliminary thickness distributions. The results can be seen in Table 6.6. In reality, each unit test was conducted for atleast 6 different sections. In order to keep the table concise, not all results are depicted in this report. The numerical solution approximates the analytical solution to a deviation of 0.2%, excluding the bending moment and bending stress. However, due to significance these deviations can be neglected. For the bending moment and bending stress the deviation equals 4.15 ± 0.05%. Since the value of the bending stress is linearly dependent on the bending moment, it can be concluded the error is related to the bending moment calculation.

Table 6.6: Verification data main spars

	Cross-Sectional Area [m^2]					
	Leading Edge			**Trailing Edge**		
	Analytical	Numerical	% Δ	Analytical	Numerical	% Δ
0·N	$1.11\ 10^{-2}$	$1.11\ 10^{-2}$	0.0	$0.66\ 10^{-2}$	$0.66\ 10^{-2}$	0.0
1·N	$0.70\ 10^{-2}$	$0.70\ 10^{-2}$	0.0	$0.32\ 10^{-2}$	$0.32\ 10^{-2}$	0.0
	Moment of Inertia [m^4]					
	Leading Edge			**Trailing Edge**		
	Analytical	Numerical	% Δ	Analytical	Numerical	% Δ
0·N	$4.78\ 10^{-4}$	$4.76\ 10^{-4}$	0.1	$2.41\ 10^{-4}$	$2.39\ 10^{-4}$	0.2
1·N	$3.17\ 10^{-4}$	$3.14\ 10^{-4}$	0.1	$1.18\ 10^{-4}$	$1.16\ 10^{-4}$	0.2
	Shear Force [N]					
	Leading Edge			**Trailing Edge**		
	Analytical	Numerical	% Δ	Analytical	Numerical	% Δ
0·N	$1.50\ 10^5$	$1.50\ 10^5$	0.0	$0.59\ 10^5$	$0.59\ 10^5$	0.0
1·N	$0.43\ 10^5$	$0.43\ 10^5$	0.0	$0.22\ 10^5$	$0.22\ 10^5$	0.0
	Shear Flow [N/m]					
	Leading Edge			**Trailing Edge**		
	Analytical	Numerical	% Δ	Analytical	Numerical	% Δ
0.25·N	$1.65\ 10^5$	$1.65\ 10^5$	0.0	$0.79\ 10^5$	$0.79\ 10^5$	0.0
0.5·N	$1.28\ 10^5$	$1.28\ 10^5$	0.0	$0.64\ 10^5$	$0.64\ 10^5$	0.0
	Shear Stress [N/m^2]					
	Leading Edge			**Trailing Edge**		
	Analytical	Numerical	% Δ	Analytical	Numerical	% Δ
0.25·N	$2.57\ 10^7$	$2.57\ 10^7$	0.0	$1.31\ 10^7$	$1.31\ 10^7$	0.0
0.5·N	$2.32\ 10^7$	$2.32\ 10^7$	0.0	$1.25\ 10^7$	$1.25\ 10^7$	0.0
	Bending Moment [Nm]					
	Leading Edge			**Trailing Edge**		
	Analytical	Numerical	% Δ	Analytical	Numerical	% Δ
0·N	$2.67\ 10^5$	$2.56\ 10^5$	4.1	$1.14\ 10^5$	$1.09\ 10^5$	4.1
1·N	$0.033\ 10^5$	$0.032\ 10^5$	4.1	$0.033\ 10^5$	$0.032\ 10^5$	4.1
	Bending Stress [N/m^2]					
	Leading Edge			**Trailing Edge**		
	Analytical	Numerical	% Δ	Analytical	Numerical	% Δ
0.25·N	$-9.26\ 10^7$	$-8.87\ 10^7$	4.2	$-8.48\ 10^7$	$-8.13\ 10^7$	4.1
0.5·N	$-5.80\ 10^7$	$-5.56\ 10^7$	4.2	$-5.93\ 10^7$	$-5.67\ 10^7$	4.1

6.4. FAN HUB SUPPORT

This section deals with the supports that hold the fans and electric motors in place and connect the hub to the ducts surrounding the fan. The cross section of the beams is chosen to be an I-beam, since this is a very efficient cross section when bending is the dominant load. The hub is held by four beams which are assumed to be clamped on the hub and have a pin connection at the duct or wing spars. This has the advantage that the whole propulsion unit can be easily taken off for maintenance and it also avoids that bending moments are introduced into the spars or ducts around the fan. Additionally these connectors can be designed in such a way that they dampen the vibrations of the fan. As an example, lugs with damping mechanisms can be found on certain aircraft and rocket launchers and reduce the propagation of vibrations significantly.

6.4.1. METHODOLOGY

The first step in the sizing of the fan hub supports is the computation of the shear forces and bending moments. For the rear ducts these are the thrust load and bending moment during vertical take-off and landing. Furthermore, during flight gust load factors must be applied. For the front ducts the thrust forces and moments during take-off are calculated as well as the loads during cruise combined with the extreme values of the gust load.

An optimisation algorithm is used to find the lightest cross section that fulfils the requirements and constraints. The calculation starts by determining the forces and moments. Next the area moment of inertia of the cross section is calculated using Equation 6.7. Subsequently, the shear stresses and bending stresses are calculated using Equations 6.11 and 6.9 respectively. In order to check to check if the maximum predetermined stress level of 138 MPa is not exceeded, the Von Mises stress is calculated and multiplied with the safety factor.The two most critical points on the cross section, the center of the flange and the center of the web, are subjected to this calculation. After the optimisation algorithm finds the smallest cross sectional area that fulfils the requirements the weight is calculated.

INPUTS FRONT DUCTS

With a thrust to weight ratio of 1.1, a MTOW of 8,290 kg and assuming 15% of the total thrust per front fan the thrust force in take-off is up to $T_{TO} = 21,130N$.In cruise each fan produces $T_{cr} = 4,172N$ of horizontal thrust. Additionally the maximum vertical gust load causes a vertical force of $F_{gu}9037N$ (assuming a weight of 280 kg for the hub, fan and electric motor and a gust load factor of 3.29). Since the gust loads can be handled in tension/compression by the vertical supports these loads only cause very low stresses of about 6 MPa, making the take-off the driving load case.The length of the struts from the hub to the duct is 0.77 m.

Restrictions for the cross section are a maximum height of 100 mm due to the limited space, a minimum thickness of 3 mm (to resist high velocity impacts of objects and buckling) and a maximum width of 50 mm (to make sure that the airflow is not disturbed more than necessary).The maximum stress is set as 138 MPa in order to avoid fatigue problems. Lastly the web of the beam is checked for the limit buckling load.

INPUTS MAIN WING DUCTS

Using a thrust to weight ratio of 1.1, a MTOW of 8,290 kg and assuming 35% of the total thrust per rear fan the thrust force in take-off is $T_{TO} = 31,310N$.During cruise the fan does not produce any thrust, therefore the maximum force acting on the structure is the weight of the fan and electric motor assembly, which is assumed to have a weight of 2943 N, multiplied by the maximum guest load factor in cruise of 3.29: $F_{cr} = 9,682N$. It is clear that the structure needs to be sized for take-off loads.The distance from hub to the connection point at the spars is 1.08 m.

Restrictions for the cross section are a maximum height of 150 mm, a minimum thickness of 3 mm and a maximum width of 50 mm, for the same reasons as mentioned before.The maximum stress is again set as 138 MPa in order to avoid fatigue problems. Lastly the web of the beam is checked for the limit buckling load using Equations 6.13 and 6.14.

6.4.2. REFERENCE FRAME

The reference frame is a 2D x-y Cartesian coordinate system. The x-axis runs horizontally through the center of the cross section and the y-axis runs vertically through the center of the cross section. The cross section can be mirrored about both axis.

6.4.3. RESULTS STRESS AND BUCKLING ANALYSIS

These inputs and restrictions result in I-beams with the following characteristics:

Table 6.7: Characteristics of the fan support struts

	Front Ducts	**Rear Ducts**
Flange size	37 mm wide / 13 mm thick	40 mm wide / 16 mm thick
Web size	74 mm high / 3 mm thick	118 mm high / 3 mm thick
Maximum stress (incl. safety factor)	137.2 MPa	137.5 MPa
Mass (per duct)	10.1 kg	19.6 kg
Critical shear/bending buckling stress	677 MPa / 2032 MPa	327 MPa / 981 MPa

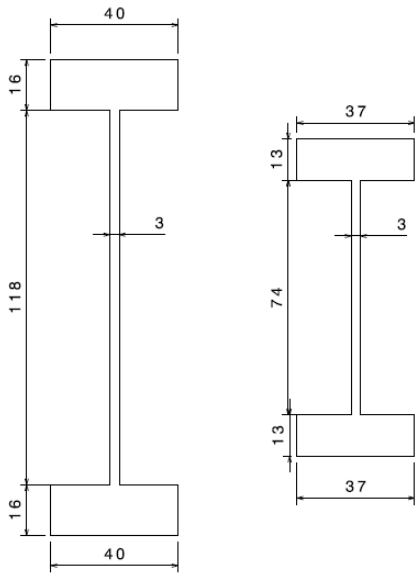

Figure 6.11: Cross section of the struts in the rear and front duct respectively, in millimeters respectively

A plot of the margin of safety versus the number of iterations for the struts in the front duct can be seen in Figure 6.12. The plot for the rear ducts is not shown here since it uses the same method and optimization with different inputs which results in a nearly identical plot.

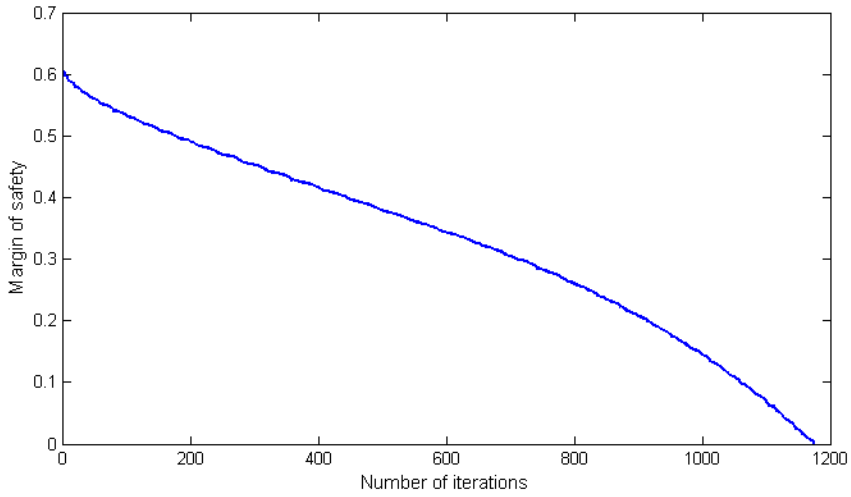

Figure 6.12: Margin of safety versus number of iterations for the struts in the front duct

The weight could be reduced further by tapering the structure towards the outside of the duct where the bending moment decreases. This is not done because these are very essential parts that should also be able to withstand high speed collisions with debris of unknown impact force.The limit buckling load for both cross sections are way higher than the design stress and therefore no issue.

6.4.4. VERIFICATION

In this method no discretisation or simplification methods is used, when compared to an analytical calculation by hand. Hand calculations were done to verify the code and produced the same results.

6.5. DUCT-FUSELAGE CONNECTOR

Another important structural element is the connection between the fuselage and the front ducts. Since the front ducts are tiltable and used in VTOL and cruise the connection between the duct and the fuselage need to be designed for a number of different load cases, just like the fan hub support.

The connector is a 0.3 m long tube that is fixed to the fuselage on the one end and with a big bearing on the other end where the duct is connected. A shaft runs through the inside of the tube that is connected to the duct and

transfers the torque for the tilting of the duct while the outer tube transfers all the loads from the duct to the rest of the aircraft. An aerodynamic fairing is added to the back of the tube to house cables and decrease drag.

6.5.1. METHODOLOGY

The design starts by analysing the forces and moments that have to be considered for the different situations, which are similar to those for the fan hub support analysis. During take-off the connector needs to handle the force and moment created by the vertical thrust. During cruise it needs to handle the forward thrust, the gust loads but also the lift created by the ducts.

The area moment of inertia I is calculated based on the outer (D_o) and inner (D_i) diameter with:

$$I = \pi \cdot \frac{D_o^4 - D_i^4}{64} \tag{6.20}$$

The bending stress is calculated using Equation 6.9. Since it is a round cross section the shear flow Equation 6.10 was adapted for polar coordinates by using $y = r \cdot \sin\theta$ and $da = r \cdot d\theta$ (θ being the angle between the radius vector and the horizontal) resulting in this equation for the shear flow:

$$q_s = \frac{S}{I} \cdot R_o^2 \cdot t \cdot \cos\theta \tag{6.21}$$

After the bending and shear stresses are calculated they are added using the von Mises yield criterion. For the cruise case two different shear forces and bending moments in different directions need to be added.Lastly the point with the highest stress is determined and this stress is multiplied with the safety factor.

INPUTS

The vertical thrust force during take-off can be computed to be $T_{TO} = 21,130N$ (each front duct produces up to 24% of the total thrust, depending on the c.g.).During cruise each fan produces $T_{cr} = 4,172N$ of horizontal thrust. The force due to a gust load is $F_{gu} = 9,682N$ (assuming a duct mass of 300 kg and a gust load factor of 3.29) and the lift of the duct is $F_{ld} = 1,568N$.The moment arm of the force is 1.275 m.

To limit the aerodynamic drag the outer diameter of the tube is set at 200 mm. The maximum stress to ensure no fatigue damage is 138 MPa.

6.5.2. REFERENCE FRAME

The reference frame is a 2D x-y Cartesian coordinate system. The x-axis runs horizontally through the center of the cross section and the y-axis runs vertically through the center of the cross section. The cross section can be mirrored about both axis.

6.5.3. RESULTS STRESS AND BUCKLING ANALYSIS

The only variable which is left and which is also the result of this calculation is the thickness of the tube. During the analysis it turned out that again the take-off condition was critical, even though during cruise flight three forces act on the structure at the same time. The reason for this is that the gust load and lift always act in opposite directions and thereby reduce each other.

The optimal tube thickness is chosen as 9.3 mm which results in a maximum von Mises stress (including safety factor) of 137 MPa and a mass of 2.38 kg per connector. Since there is only one variable there is no need for a computerized optimization process.

6.5.4. VERIFICATION

Just like the fan hub support no simplifications or discretisations were used. Hand calculations during the verification therefore resulted in the same results.

6.6. VALIDATION WING STRUCTURE

This section discusses a proposal on how the validation of the wing box could be performed. First, it is advised to do different unit tests, in which the properties of parts of the wing box will be determined separately. Finally, the complete wing box should be tested. After that, some suggestions of other tests, which are not directly connected to the numerical calculations are given.

6.6.1. STATIC COMPRESSION AND TENSION TESTING UPPER AND LOWER PLATE

The upper plate of the wing box has to deal mainly with compression loads. Thus the upper plate should be tested separately in a compression bench from which the critical compression stress and ultimate stress can be determined. Tension testing is not needed, because the maximum tension stresses during negative gust are lower in

the upper plate than the maximum compression forces during maximum gust load.

A mismatch in the resulted buckling stress and the calculated one could have a couple of reasons. First, the chosen compression coefficient was not correct. Second, there has been no real lower limit for the cross-sectional area of the stringers, so that they still divide the plate in different sections. This can be investigated doing the compression test. However, no real research has been done in this subject yet. It is recommended to investigated this fist rather then start testing it immediately 14.3.

The lower plate will mainly be under tension, thus it should be tested performing a tension test. However, the lower plate needs to have a certain resistance against buckling as well, because of the negative gust loading 6.1.1. Thus the lower plate has to be tested for compression as well.

Another aspect that can be tested during the compression tests is the rivet spacing. Up to now the rivet spacing has not been mentioned. It is therefore recommended to do more research regarding the rivets 14.3.

6.6.2. STATIC BENDING TESTING MAIN SPARS

A single spar can be exposed to a static bending load. The bending moment on a spar is known and therefore one can validate the critical bending, shear and compression stresses. Again, differences could occur because of wrongly selected coefficients. However, the coefficients were chose in a very conservative, or pessimistic way. Therefore the critical bending stresses are probably higher.

A difference in ultimate stress could possibly be caused by a manufacturing fault. For example if the I beams are welded, a weld imperfection could cause the spars to fail earlier than predicted. (Note that research still needs to be done on the manufactering process of the different parts 14.3.

6.6.3. STATIC BENDING TESTING COMPLETE WING STRUCTURE

After the units tests are performed, the complete wing structure should be tested to investigate how all the different parts work together as a whole. Differences in calculated stresses and measured stressed could be again because of manufacturing faults.

6.6.4. STATIC LOAD AND FATIGUE TESTING JOINT

One of the extra tests that need to be performed is the fatigue test for the joint between the main spars and the wing box. The wing will be vibrating a lot, especially during the transition phase. The wing fans are causing vibrations and the wing is vibrating because of aerodynamic forces. The joint is thus very fatigue sensitive and should be tested by putting it under cyclic loads. Possible solutions for the joint are given in section 14.3.

6.6.5. CRACK TESTING

Finally, the strength of the structure should be investigated once there is crack initiation. The different parts first need to be tested in unit tests, only this time create a small crack in critical spot of that part.

6.7. DESIGN PROPOSALS

The following section will present the design proposals for the three critical systems that due the limited resources could not be designed in the same detail as the components described earlier in the chapter. In this section, the landing gear, fuselage-wing connection and shutter system are elaborated on. Each subsection will present the reader with a brief description of the functionalities of each component. In addition, a design strategy is given.

6.7.1. LANDING GEAR

This subsection aims at explaining the functionality, loads and preliminary sizing in relation to the landing gear. The decision was made to size the landing for a conventional landing. This way, if the transition were to fail or power were to be lost, a conventional landing could be performed without landing gear failure. Five different functions for the landing gear can be identified [119].

- Absorb landing shocks and taxiing shocks
- Provide ability for ground manoeuvring
- Provide braking capability
- Allow for aircraft towing
- Protect ground surface

The landing gear must be sized to handle different loads, which include vertical loads due to the touchdown rate and rough surface taxiing. Additionally, the landing gear must be able to handle longitudinal loads due to spin

up, braking and rolling friction. Finally, lateral loads can occur due to crabbed landing, cross-wind taxiing and ground turning.

The first step in the preliminary sizing of the landing gear is the definition of the type of landing gear. Since the cruise speed of the aircraft exceeds 150 Kts, the landing gear will be retractable. Although this will add to the complexity of the mechanism and will induce a weight penalty, the increase in aerodynamic efficiency is likely to outweigh these disadvantages. Nonetheless, drag estimates must be performed to check if this statement is valid. InVADe will feature a landing gear design that is similar in concept to the landing gear of AgustaWestland's AW609 for the reason that wheel track must be large as possible to improve roll stability. An indication of the landing gear is depicted in Figure 6.13.

Figure 6.13: Landing gear configuration of InVADe, based AgustaWestland's AW609 landing gear

A rough weight and balance statement resulted in a noise landing gear that is positioned at 2.5 m from the nose and rotates clockwise as seen from the door side of the aircraft. The main landing gear is positioned at a distance of 9.5 m from the root and pivots outwards of the fuselage. Additionally, the maximum static load on the main landing gear and nose landing gear is 88.6 kN and 43.9 kN respectively. These numbers were calculated using a safety factor of 1.5. Multiple load cases were analysed to find the highest static load per landing gear unit.

Using the static load distribution, one can start designing the main landing gear and nose landing gear. The list below describes the remaining steps in the Class I method for landing gear sizing. Once these steps are completed, a preliminary design of the landing gear is the output and one can consult Class II sizing methods to refine the design.

- Decide on strut disposition
- Calculate the maximum static load per strut
- Decide on the number of wheels used
- Select tire size based on statistical values
- Position the tires in the general arrangement of the aircraft
- Check if gear can be retracted into designated volumes

6.7.2. FUSELAGE-WING CONNECTION

As was explained in section 4.8 on vortex analysis, a high wing configuration is preferable in terms aerodynamic efficiency. Structurally, a low wing cuts through areas highly loaded in compression and, therefore, imposes a greater penalty to skin panels in the case of a high wing. On the other hand, a high wing produces greater penalties to the frames than a low wing. Nonetheless, the decision was made to implement a high wing in the design of InVADe.

Figure 6.14a shows a conventional carry-through structure of a high wing structure. Due to the fact that the fuselage of InVADe has a cross-section of 2 m and the spars have a height of 0.465 m, a carry-through construction would impose considerable limitations on the inside cabin volume. In order to solve the problem, the wings could be lifted by atleast 0.4 m to enable a carry-through section without compromising the space in the passenger cabin. In return, this solution would decrease the aerodynamic efficiency of the aircraft.

Another option features a forging bulkhead forging displayed in 6.14b. Using a large forging will eliminate the off set needed to house the structure and offers a strong structure on which other structural elements can be attached. For example, one could think of a stiffening structure between the front ducts and the forging bulkhead.

Additionally, the trailing spar can be connected using a conventional carry-through structure as this spar is positioned far enough backwards to not perturb the passenger cabin.

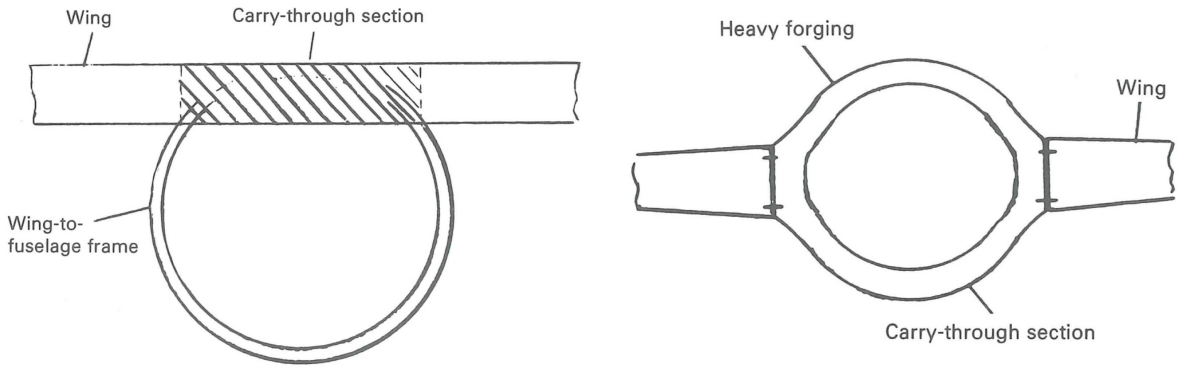

(a) Conventional carry-through structure

(b) Circular bulkhead structure

Figure 6.14: Fuselage-wing connection in a high wing configuration

No quantitative studies have been done for the implementation of a bulkhead forging in commercial business jets. Although successful applied in military aircraft such as the F-16 and F-35, further research must point if the advantages of a bulkhead forging outweigh the disadvantages in case of a VTOL business jet.

6.7.3. SHUTTER MECHANISM

The ducts in the main wing need to be open during take-off and landing and closed during cruise flight. To achieve this a number of different options were investigated. The requirements for the shutter mechanism are:

- Needs to handle the aerodynamic loads
- Should be as compact and light as possible
- Should enable partial opening/closing
- Should create a smooth surface in flight and not obstruct airflow too much when opened

It was decided to use a system of eight flaps on the upper and lower side that either cover the duct, or when they are turned 90° make it possible for the airflow to pass through the duct. In order to provide a smooth transition, as many flaps as possible are ideal. However, a large number of flaps increases the complexity of the system. Therefore, a midway value of eight flaps was chosen. Further research should point out the most efficient number of flaps. Each flap consists of a skin panel attached to a rod. This rod will take most of the loads and also act as an axle when the flaps are opened or closed.

The flaps are directed in flight direction. This has the advantage that they obstruct the airflow less and it also makes it possible to only open the duct partially during transition to avoid loosing too much lift immediately. Moreover this system is relatively easy to implement, does not take up much space and is proven by Ryan XV5a concept.

Connecting these rods to the main spars also improves the stiffness and strength of the wing structure at this point and could result in lower stresses and a lighter design of the two main spars.

7

STABILITY & CONTROL

In this chapter InVADe's stability and controllability will be assessed. To start the analysis, first an understanding of the center of gravity (c.g.) of the aircraft is needed. This will be covered in 7.1 explaining the determination of the empty aircraft c.g and various loading diagrams. Next, the cruise phase will be discussed in Section 7.2. The canard and wing will be sized and positioned for stability and controllability. A final revision of the center of gravity is done based on the new input from the canard size and wing position. Then, the vertical tail is sized and dynamic stability is discussed. A subsection on control during cruise closes this section. Section 7.3 discusses the stability and control during hover as Section 7.4 does for transition.

7.1. CENTER OF GRAVITY

The location of the c.g. of the aircraft has a big effect on its stability and control aspects. It is primarily composed of the c.g. positions of all parts of the aircraft and their individual weights. These parts contribute to the aircraft empty weight. Their weights and positions are fixed; therefore they sum up to a fixed c.g. position for the empty aircraft.

In addition, the c.g. position is influenced by the payload and fuel on board the aircraft. These contributions however, are variable during operation, so the c.g. position varies as well. Payload, i.e. the amount of passengers and their baggage, is different for each individual mission. Also, passengers may want to move around the aircraft during flight. Fuel is burned throughout the mission, which means that its weight varies over each mission. This has another significant contribution to the variation of the c.g. position. These contributions lead to a c.g. range over which the aircraft should be both stable and controllable in all flight modes.

Both contributions are examined in the following subsections.

7.1.1. CENTER OF GRAVITY OF THE EMPTY AIRCRAFT

As mentioned above, the c.g. of the empty aircraft will be derived from the individual weights and locations of components. The weights of the main components were calculated with the Class II method in section 3.1 of the structures chapter. Locations of the components were then estimated to establish a first estimate for the aircraft c.g. Where most components have a fixed position, independent of the position of the main wing, some components are positioned dependent on the wing. These systems are the wing structure, the fuel tanks in the wing, and the fans in the wing. As a first estimate the main wing is placed at the very rear of the aircraft and the canard completely in the front. In Section 7.2.1 an optimum canard surface area and wing position are found to account for the c.g. shift.

The c.g. of the whole aircraft should be positioned such that there is equilibrium between the thrust of the front fans and the thrust of the back fans. Originally a division of 30% - 70 % (front - rear) was set; resulting in a c.g. position relatively far to the rear of the aircraft. During the placements of the subsystems like engines and electronics this was considered as much as possible. However, at a certain point the subsystems could not be moved backwards. A division of 35% - 65% (front - rear) was set, which is what the propulsion units are sized for in Section 5.1. This will be an important figure during the hover phase which influences the thrust division needed. In the end Figure 7.1 and Table 7.1 summarise the final weights and locations of the various components.
The next step is to find out how the center of gravity moves during operations.

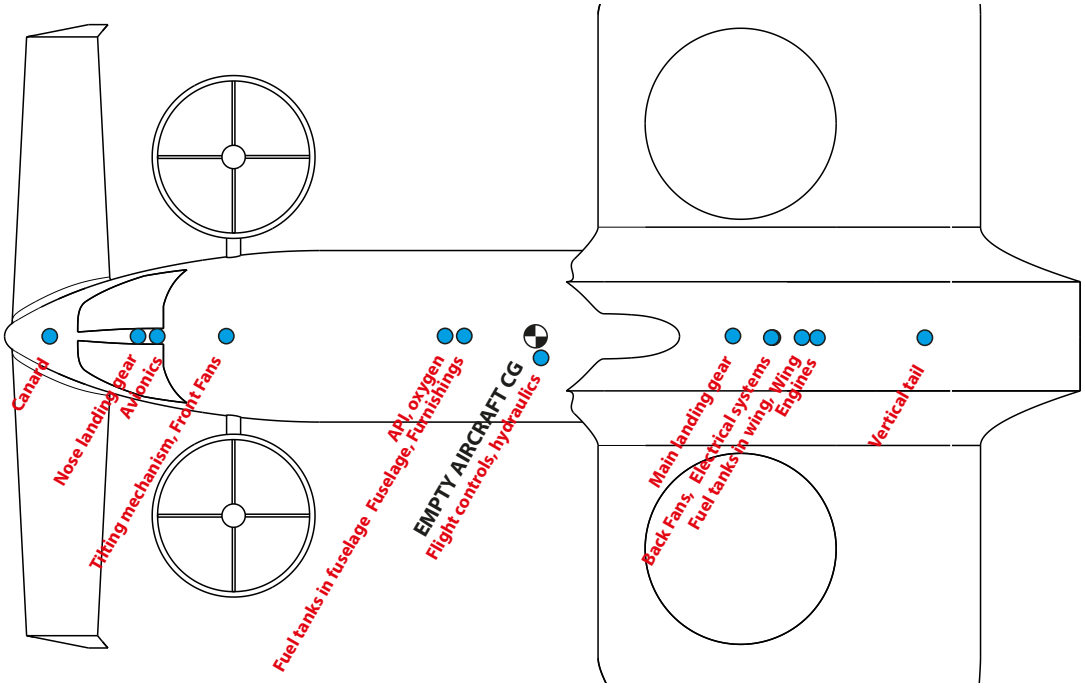

Figure 7.1: Top view of InVADe with the final c.g. positions of the various weight components

Table 7.1: Final weight components and corresponding locations, relative to the aircraft nose

Component	Weight	Location
Canard	245 kg	0.6 m
Nose Landing Gear	38 kg	1.75 m
Avionics	120 kg	2 m
Tilting Mechanism	100 kg	2.9 m
Front Fans	600 kg	2.9 m
API	140 kg	4.75 m
Oxygen	11 kg	4.75 m
Fuel tanks fuselage	132 kg	6 m
Fuselage	732 kg	6 m
Furnishing	548 kg	6 m
Flight Controls	195 kg	7 m
Hydraulics/Electrics	257 kg	7 m
Main Landing Gear	169 kg	9.5 m
Electrical Systems	500 kg	10 m
Back Fans	600 kg	10 m
Fuel tanks wing	116 kg	10.4 m
Wing	308 kg	10.4 m
Engines	450 kg	10.6 m
Vertical Tail	96 kg	12 m

7.1.2. CENTER OF GRAVITY SHIFT DURING OPERATIONS

This section outlines how the variations of payload and fuel distribution over the aircraft affect the c.g. position. To evaluate these variations, a loading diagram is constructed as discussed by La Rocca [73]. This diagram is constructed from all possible c.g. positions under different loading cases.
A loading diagram consists of three main contributions:

1. **Baggage/Cargo**. The baggage compartment provides storage space for 12 pieces of luggage of 60x45x25 cm. This is a fixed weight which does not change during flight. In terms of loading it would be preferable if the baggage compartment is located in the front of the aircraft. This way the passengers loading will be better situated around the c.g.

2. **Passengers**. The cabin provides seating space for 10 passengers, excluding the pilots. Since the number of passengers is relatively small, the pilots will also be taken into account for the loading of the aircraft.

In terms of passenger loading, passengers can either take their places from front to back, or back to front. Both cases are investigated. Seat and cabin baggage compartment positions follow from the aircraft internal layout in section 3.3.1.

3. **Fuel**. Fuel is stored in the various fuel tanks in the aircraft. Similar to passenger loading, the influence on the c.g. position is different when the front fuel tanks are filled or emptied first, or the aft tanks. Fuel tanks located in the wing change in position as soon as the wing is relocated.

To account for passenger movements, landing gear extensions, previous assumptions and other influences, a suitable loading margin is selected. This margin extends the c.g. range both forward and rearward. According to La Rocca [73], a margin of 2% is common for passenger aircraft.

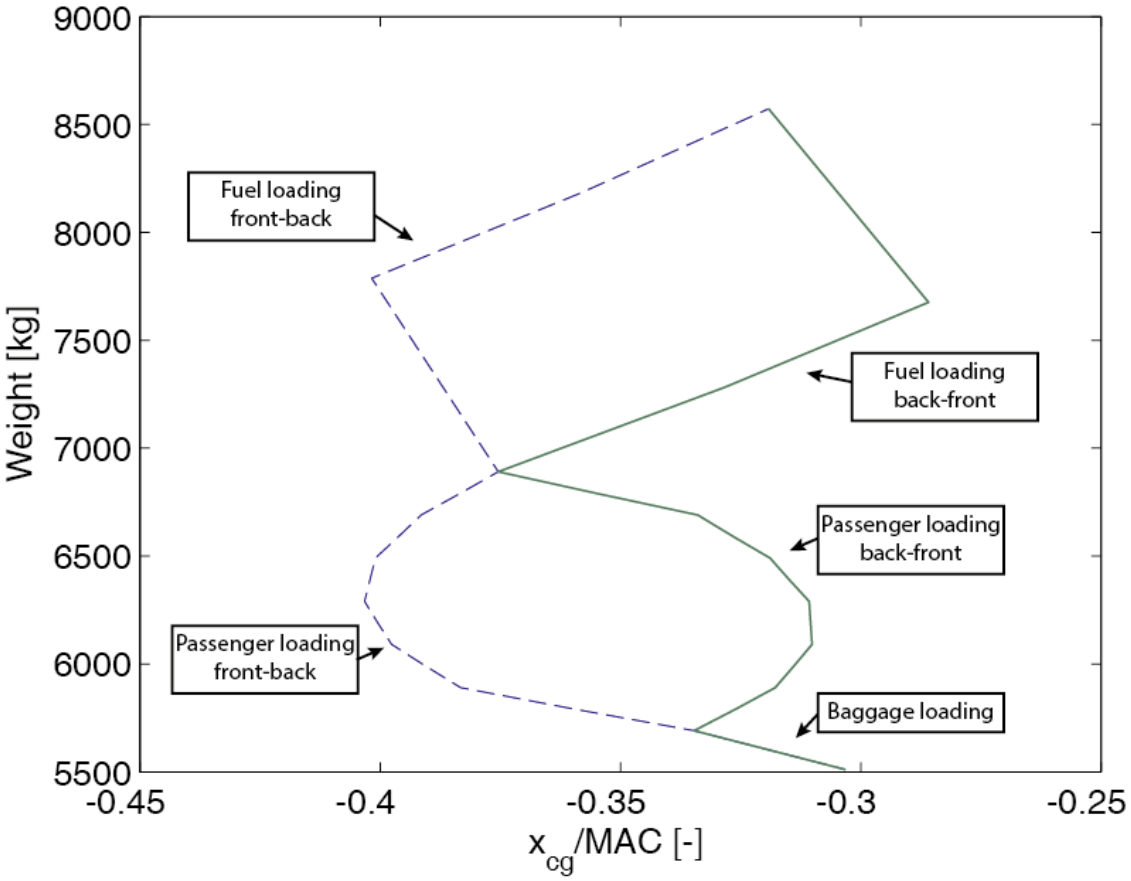

Figure 7.2: Loading diagram with the wing positioned such that the LEMAC position is 8.20 m

Figure 7.2 illustrates the loading diagrams as discussed above. To keep the loading as close to the empty aircraft c.g. as possible, it was decided to store the fuel partially in the fuselage. This results in smaller c.g. range which has a positive effect on the canard sizing.
Using three different loading diagrams for different wing locations, a c.g. range for the various wing positions can be established. Each loading diagram has a minimum and maximum c.g. location represented as the x location over the mean aerodynamic chord (MAC). The positions are defined relative to the Leading Edge of the Mean Aerodynamic Chord (LEMAC) of the wing. Combining these minimum and maximum c.g. locations for various wing locations generates a c.g. range plot (Figure 7.3). This plot will be used in the canard sizing and final wing positioning.

7.2. CRUISE

In this section the stability and control in cruise will be analysed. First the canard and wing are sized and positioned respectively to ensure stability during cruise. With this new data a revision of the c.g. is made and the locations for the weight components are fixed. Next, the vertical tail is sized for one engine inoperative and a preliminary dynamic stability analysis is carried out. The section concludes with a brief discussion on how to control the aircraft in cruise.

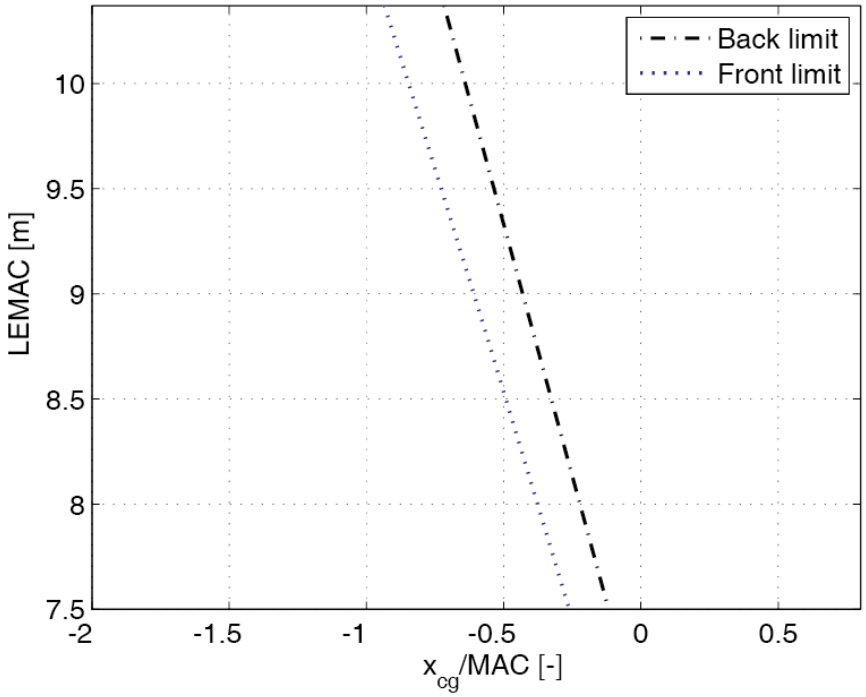

Figure 7.3: C.G. range based on the loading diagrams for various wing positions

7.2.1. CANARD SIZING AND WING POSITION

This section elaborates on the process of wing positioning and canard sizing. To determine these parameters, the loading diagram and scissor plot will be used as tools. First step is to create loading diagrams for different positions of the wing. By shifting the wing forward or backward the loading diagrams will change. For each of the loading diagrams a minimum and maximum location of the c.g. is determined, creating a range of minimum and maximum c.g. locations for different wing positions. One example loading diagrams was presented in Figure 7.2.

With the c.g. range calculated, a scissor plot is needed to determine the final wing position and canard size. A scissor plot consists of two lines, one representing the controllability limit and the other the stability limit. The convenience of a scissor plot is that it allows the designer to select an optimal canard size and wing position for both stability and controllability. It is important to note that the stability curve is generated for cruise speed, whereas the controllability curve is generated for transition speed. For a complete understanding of all the equations involved with a scissor plot, it is highly recommended to read the corresponding lecture slides [73]. These provide methods to derive most of the quantities in these equations.
The two main equations involved with a scissor plot are shown in Equations 7.1 and 7.2. These equations form c.g. limits that need to be satisfied to be both stable and controllable.

$$\bar{x}_{cg} = \bar{x}_{ac} - \frac{C_{m_{ac}}}{C_{L_{A-h}}} + \frac{C_{L_h}}{C_{L_{A-h}}} \frac{S_h l_h}{S\bar{c}} \left(\frac{V_h}{V}\right)^2 \tag{7.1}$$

$$\bar{x}_{cg} = \bar{x}_{ac} + \frac{C_{L\alpha_h}}{C_{L\alpha}} \left(1 - \frac{d\varepsilon}{d\alpha}\right) \frac{S_h l_h}{S\bar{c}} \left(\frac{V_h}{V}\right)^2 - S.M. \tag{7.2}$$

Here, $\bar{x}_{cg}$ is center of gravity divided by the Mean Aerodynamic Chord (MAC). The location of the aerodynamic center $\bar{x}_{ac}$ is also divided by the MAC. In addition, all positions are relative to LEMAC. $C_{L\alpha}$ is the lift gradient of the complete aircraft, which is determined using Equation 7.3.

$$C_{L_\alpha} = C_{L_{\alpha_{A-h}}} + C_{L_{\alpha_h}} \frac{S_h}{S} \left(1 - \frac{d\varepsilon}{d\alpha}\right) \left(\frac{V_h}{V}\right)^2 \tag{7.3}$$

Using estimation methods described by La Rocca [73], input values for the c.g. limits are obtained. These are shown in Table 7.2. The resulting scissor plot can be seen in Figure 7.4. The parameters involved with the scissor plot are explained and shown in Table 7.2.

To derive an optimal canard area and wing location from the scissor plot, the shift in c.g. should be taken into account. By taken the c.g. range into account stability and controllability can still be ensured during shifts in

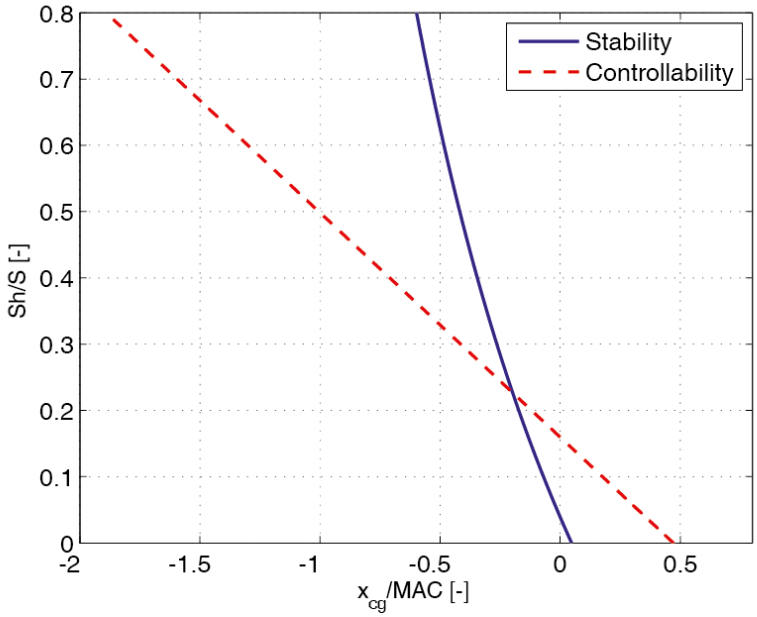

Figure 7.4: Scissor plot of InVADe, showing the controllability and stability c.g. limits

the aircraft c.g.. The c.g. range graph from Figure 7.3 is used to achieve this. By overlaying the c.g. range with the scissor plot a canard size and wing position can be determined. In Figure 7.5 the result of the overlay can be seen. Both graphs are shifted such that both lines of c.g. range graph intersect the curves of the scissor plot horizontally. This intersection then fixes the location of the LEMAC and canard area over wing area S_h/S which can be read from the y-axis. The S_h/S position is indicated on the left axis, the LEMAC position on the right axis.

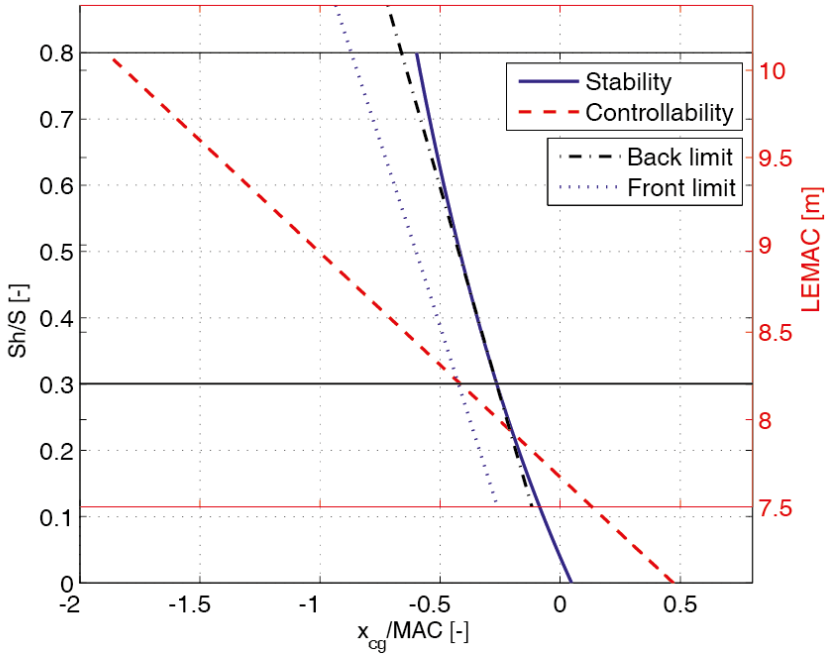

Figure 7.5: Overlay of the scissor plot with the c.g. range plot.The black line shows the intersection of the front c.g. limit with the controllability curve, at the same S_h/S and LEMAC where the back c.g. limit and stability curves intersect.

The final values of the sizing are presented in Table 7.2. Also, the final c.g. limits corresponding to the LEMAC position are given.

7.2.2. VERTICAL TAIL SIZING

The vertical tail is sized using a one engine inoperative (OEI) scenario. To check if this method provides a realistic value for the vertical tail area, tail areas of reference aircraft are compared.

Table 7.2: Results of the wing positioning and canard sizing

Input parameters for scissor plot	**Symbol**	**Value**	**Unit**
Location of aerodynamic center (a.c.) of aircraft without canard	$\bar{x}_{ac}$	0.0685	-
Pitching moment coefficient at aerodynamic center	$C_{m_{ac}}$	-0.384	-
Lift coefficient of aircraft without canard, at transition speed	$C_{L_{A-h}}$	0.953	-
Lift coefficient of canard, at transition speed	C_{L_h}	1.55	-
Distance between canard a.c. and aircraft without canard a.c.	l_h	-8.89	-
Ratio between airspeeds at canard and main wing	$\frac{V_h}{V}$	1	-
Lift gradient of the canard	$C_{L\alpha_h}$	5.25	1/rad
Lift gradient of the wing minus canard	$C_{L\alpha_{A-h}}$	7.65	1/rad
Downwash effect of wing on canard	$\frac{d\varepsilon}{d\alpha}$	0	-
Stability Margin	$S.M.$	0.02	-
Mean Aerodynamic Chord	$\bar{c}$	3.66	
Output parameter	**Symbol**	**Value**	**Unit**
Location of LEMAC (LEMAC)	x_{LEMAC}	8.20	m
Ratio between canard and wing areas	$\frac{S_h}{S}$	0.30	-
Canard surface area	S_h	8.49	m^2
Front c.g. limit	$x_{cg,f}$	6.66	m
Back c.g. limit	$x_{cg,b}$	7.23	m

ONE ENGINE INOPERATIVE

Usually, a OEI scenario means that one of the engines of the aircraft fails. For this aircraft this means that one of the fans fails to provide thrust. To maintain control, the other fan provides maximum thrust to keep the airspeed such that the aircraft can still fly. However, this induces a yawing moment, which is to be countered by the vertical tail. The vertical tail needs to be sufficiently large to achieve this. The method is given by La Rocca [73] and uses several parameters such as, P_{eq}, S_r, S, W_{TO} to size the tail. Figure 7.6 shows the graph used to size the vertical tail. Once the parameter on the x-axis is determined, the y-axis value is read from the graph using the curve for 2 engine aircraft. The x-axis value is determined using Equation 7.4

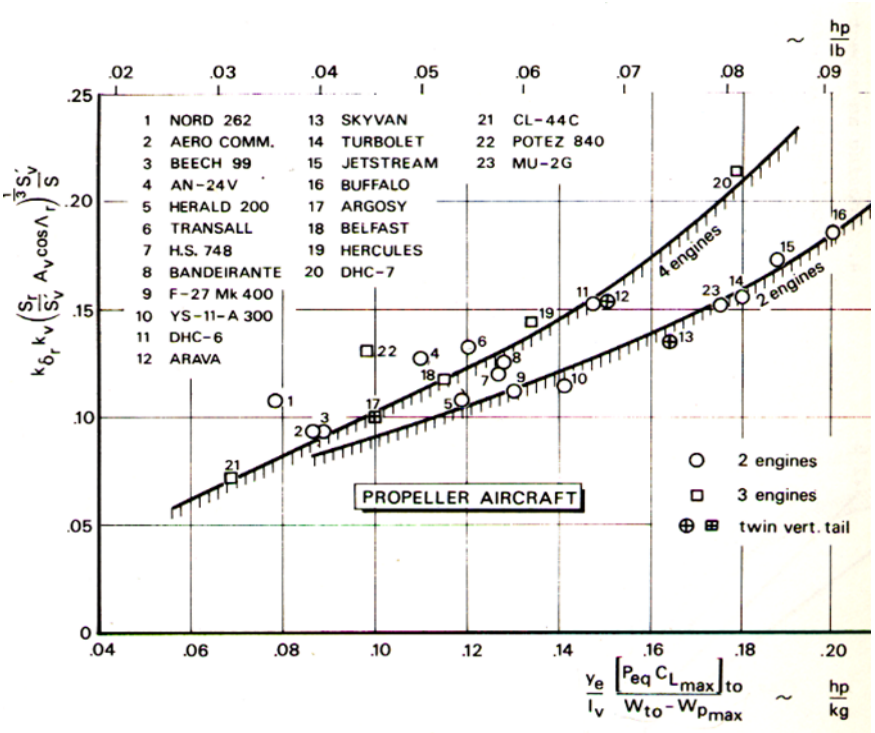

Figure 7.6: Reference data curve for the sizing of the vertical tail for OEI condition [73]

$$x_{axis}\ value = \frac{y_e}{l_v}\frac{[P_{eq}C_{L_{max}}]}{W_{MTOW} - W_{p_{max}}} \tag{7.4}$$

Here, y_e is the lateral distance of the engine from the center line [m], l_v is the distance between the c.g. and the

vertical tail aerodynamic center [m], P_{eq} is the maximum power that can be produced by one front duct, in horsepower [hp] as used in the graph, W_{TO} is the Maximum Take-Off Weight [kg], $W_{p_{max}}$ is the maximum payload [kg].

With this value for the x-axis, the graph in Figure 7.6 provides the value for the y-axis. Equation 7.5 is then used to relate this value to design parameters of the vertical tail:

$$y_{axis}\ value = k_{\delta_r} k_v \left(\frac{S_r}{S_v'} AR_v \cos\Lambda_r \right)^{\frac{1}{3}} \frac{S_v'}{S} \tag{7.5}$$

Here, k_{δ_r} and k_v are obtained from Figure 7.7, S_r is the rudder area [m^2], S_v' is the area of the tail not covered by the rudder [m^2], AR_v is the aspect ratio of the vertical tail [-], Λ_r is the rudder hinge line sweep [°], S is the wing area [m^2].

The value for k_{δ_r} is selected for a rudder deflection $\delta_{r_{max}} = 30°$ which is not to be exceeded [73]. S_r and S_v' depend on the amount of tail chord that is taken up by the rudder, c_{rudder}. They are linked to each other, and the total tail area S_v, by Equations 7.6:

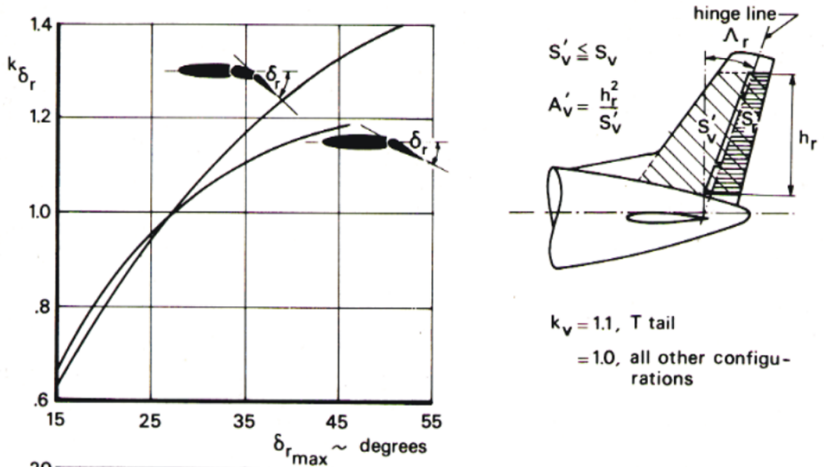

Figure 7.7: Sizing of the rudder surface area [73]

$$\begin{aligned} S_r &= S_v c_{rudder} \\ S_v{}' &= S_v(1 - c_{rudder}) \end{aligned} \tag{7.6}$$

According to La Rocca [73], c_{rudder} is approximately 0.30 to 0.35 of the tail chord. An optimum value for this was found to be 0.31 for the given configuration. The hinge line sweep is estimated by using Equations 7.7 given by La Rocca [72]:

$$\begin{aligned} \tan\Lambda_r &= \tan\Lambda_v - (1 - c_{rudder}) \frac{2C_{r_v}}{b_v} (1 - \lambda_v) \\ AR_v &= \frac{2b_v}{c_{r_v}(1+\lambda_v)} \end{aligned} \tag{7.7}$$

which combine into Equation 7.8

$$\tan\Lambda_r = \tan\Lambda_v - (1 - c_{rudder}) \frac{4(1 - \lambda_v)}{AR_v(1 + \lambda_v)} \tag{7.8}$$

Combining Equations 7.6 with Equation 7.5, the y-axis value from Figure 7.6 is used to determine the final vertical tail area S_v. An aspect ratio AR_v of 1.9, a taper ratio λ_v of 0.3 and a leading edge sweep Λ_v of 35° are common initial sizing values for vertical tails [73]. Table 7.3 shows the input values applied, and the resulting vertical tail area.

REFERENCE AIRCRAFT

To verify the 6.77 m^2 obtained using the one engine inoperative sizing method, the tail volume coefficient sizing method is used. This method is presented in the AE3201 System Engineering & Aerospace Design course [73]. A tail volume coefficient $\bar{V}_v$ is a non-dimensional indication of tail size of an aircraft. An average value for this is determined from values of reference aircraft. Reference tail volume coefficients are obtained from Roskam [100] and are classified either within the 'Twin Engine Propeller' or 'Regional Turboprop' class. The reference aircraft and their corresponding tail volume coefficients are listed in Table 7.4. In addition to the reference aircraft values, a typical value for two engine turboprop aircraft estimated by Raymer [96] is included in the list.

Table 7.3: Results of the vertical tail sizing using the OEI scenario

Input parameter	**Symbol**	**Value**	**Unit**
Engine spanwise position	y_e	1.98	m
Vertical tail arm	l_v	4.5	m
Maximum power produced by one duct	P_{eq}	$1.56 \cdot 10^3$	hp
Vertical tail type parameter	k_v	1.0	-
Rudder deflection constant	k_{δ_r}	1.05	-
Rudder chord partition	c_{rudder}	0.31	-
Aspect ratio	AR_v	1.9	-
Leading edge sweep	Λ_v	35	°
Taper ratio	λ_v	1.9	-
Output parameter	**Symbol**	**Value**	**Unit**
Resulting vertical tail area	S_v	6.77	m^2

Table 7.4: Final weight components and corresponding locations

Aircraft	**Tail Volume Coefficient**
Beech 1900D	0.076
Conquest I	0.071
Shorts 360	0.091
CASA C-212	0.072
Fokker F27-200	0.077
Cessna 402	0.080
DHC-6	0.077
Raymer 2 engine turboprop aircraft [96]	0.080
Average coefficient	0.078

This resulting tail volume coefficient is used to calculate the vertical tail area. This is done using Equation 7.9.

$$S_v = \frac{\bar{V}_v S b}{l_v} \tag{7.9}$$

Here, l_v is the length between the c.g. position and the aerodynamic center (a.c.) of the vertical tail [m]. The result of this method is presented in Table 7.5. The resulting value is somewhat smaller than the OEI method, yet the value is comparable. The result of the OEI method is therefore concluded to be realistic.

Table 7.5: Results of the vertical tail sizing using reference aircraft

Input parameter	**Symbol**	**Value**	**Unit**
Vertical tail volume coefficient	$\bar{V}_v$	0.078	m
Wing area	S	28.64	m^2
Wing span	b	13.3	m
Length between c.g. and a.c. vertical tail	l_v	4.5	m
Output parameter	**Symbol**	**Value**	**Unit**
Vertical tail area	S_v	6.35	m^2

7.2.3. DYNAMIC STABILITY

Once the static stability is analysed, the oscillatory responses of the aircraft to disturbances is investigated. The analysis of dynamic stability is useful because the dynamic response of the aircraft can be simulated for various eigenmodes. Eigenmodes are particular movements the aircraft can experience after a disturbance which need investigation to see if the motions are stable. This means that disturbance induced motions disappear without pilot interference. A division can be made between symmetrical and asymmetrical motions. A list of the five eigenmodes and a short explanation is presented below. Short period and phugoid both are symmetrical. The Dutch roll, aperiodic roll and spiral are asymmetric motions. CS23.181 [35] states requirements for some of these motions in stick fixed position. Stick free is beyond the scope of this report.

Short period The short period is a quick oscillatory mode, which tends to damp out in a number of seconds. In this mode, the aircraft pitches up and down rapidly in response to a disturbance, such as a short elevator

deflection. CS23.181(a) states that these motions should be heavily damped.

Phugoid The phugoid is a slow exchange of kinetic and potential energy. The aircraft is given a pitch angle, resulting in a higher altitude but smaller airspeed. Due to the smaller airspeed the aircraft will pitch down, descent again, gain airspeed, and the process starts over. This motion is generally a very slow motion with low damping. This motion should, according to CS23.181(c) "not be so unstable as to cause an unacceptable increase in pilot workload or otherwise endanger the aeroplane."

Dutch roll The dutch roll is a motion where yaw and roll are combined. The motion is started with a yaw and roll to the left/right which the aircraft will try to recover. Doing so, the aircraft overshoots the equilibrium position and the process continues until it is damped out. A quantitative requirement is given by CS23.181(b): the oscillations must be damped to 1/10 amplitude in 7 cycles.

Aperiodic roll Aperiodic roll is simply a roll motion. Of interest is the settling time of the roll rate. It can be investigated how quick the aircraft damps out the rolling motion.

Spiral A spiral can be started by a small disturbance bringing the aircraft in a rolling position. It the aircraft is unstable in spiral mode, the roll motion and airspeed continue increasing.

To analyse the motions described above, the equations of motion for an aircraft are used. For a derivation of these equations of motion refer to the Flight Dynamics Lecture Notes [88]. A thorough understanding of this reference is recommended to be able to fully understand the following content. The equations of motion are linearised and decoupled into symmetric equations of motion, and asymmetric equations. In addition, the results are written in non-dimensional form, as explained by Mulder et al [88]. The resulting symmetric equations of motion are given in matrix format in Equation 7.10:

$$\begin{bmatrix} C_{X_u}-2\mu_c D_c & C_{X_\alpha} & C_{Z_0} & 0 \\ C_{Z_u} & C_{Z_\alpha}+\left(C_{Z_{\dot\alpha}}-2\mu_c\right)D_c & -C_{X_0} & C_{Z_q}+2\mu_c \\ 0 & 0 & -D_c & 1 \\ C_{m_u} & C_{m_\alpha}+C_{m_{\dot\alpha}}D_c & 0 & C_{m_q}-2\mu_c K_Y^2 D_c \end{bmatrix} \begin{bmatrix} \hat{u} \\ \alpha \\ \theta \\ \frac{q\bar{c}}{V} \end{bmatrix} = \begin{bmatrix} -C_{X_{\delta_e}} \\ -C_{Z_{\delta_e}} \\ 0 \\ -C_{m_{\delta_e}} \end{bmatrix} \delta_e \tag{7.10}$$

and the asymmetric equations of motion are given in Equation 7.11:

$$\begin{bmatrix} C_{Y_\beta}+(C_{Y_{\dot\beta}}-2\mu_b)D_b & C_L & C_{Y_p} & C_{Y_r}-4\mu_b \\ 0 & -\frac{1}{2}D_b & 1 & 0 \\ C_{l_\beta} & 0 & C_{l_p}-4\mu_b K_X^2 D_b & C_{l_r}+4\mu_b K_{XZ} D_b \\ C_{n_\beta}+C_{n_{\dot\beta}}D_b & 0 & C_{n_p}+4\mu_b K_{XZ} D_b & C_{n_r}-4\mu_b K_Z^2 D_b \end{bmatrix} \begin{bmatrix} \beta \\ \varphi \\ \frac{pb}{2V} \\ \frac{rb}{2V} \end{bmatrix} = \begin{bmatrix} -C_{Y_{\delta_a}} \\ 0 \\ -C_{l_{\delta_a}} \\ -C_{n_{\delta_a}} \end{bmatrix} \delta_a + \begin{bmatrix} -C_{Y_{\delta_r}} \\ 0 \\ -C_{l_{\delta_r}} \\ -C_{n_{\delta_r}} \end{bmatrix} \delta_r \tag{7.11}$$

Equations 7.10 and 7.11 contain a vast variety of coefficients all describing the aircraft's response around a certain axis, for a certain input. These coefficients are also known as stability derivatives. To derive these coefficients one needs to know the geometry and weight of the aircraft as well as the flight conditions. A number of stability derivatives can be determined using the DATCOM program, as discussed in the next section. For the remaining derivatives, analytical methods are used.

DATCOM METHOD

Because the aircraft has a non-standard configuration, stability derivatives from conventional aircraft can not be used as a reference. The stability derivatives will have to be derived from scratch. To calculate stability characteristics of a certain configuration the DATCOM program can be used. This program was developed by the US Air Force in the 70's but is still a powerful tool to do these sort of calculations.

DATCOM enables the user to program a desired geometry into the program. This way main characteristics as the fuselage, wing, horizontal tail (canard), vertical tail and engines can be entered as input. Although the programming itself is a difficult task, eventually an entire aircraft can be programmed. Ailerons, elevators and flaps can also be added if this is required for the design. A picture of the DATCOM model of InVADe can be seen in Figure 7.8.

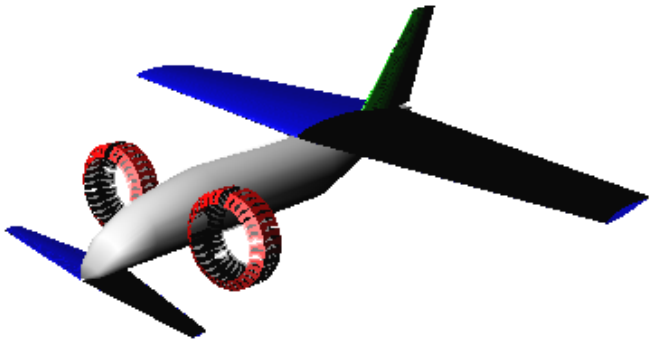

Figure 7.8: DATCOM model of InVADe

Once the aircraft is programmed, one can choose the flight condition for which the calculations need to be performed. A Mach number, altitude, speed and angle of attack range can be entered resulting in output for C_L, C_D, C_m and the stability derivatives. A complete list of outputs and inputs for the DATCOM program can be found in the DATCOM handbook, Volume I[85]. Examining the outputs DATCOM gives for InVADe, the values for C_L,C_D and C_m seemed unrealistic. As can be seen in Table 7.6 the values show a strange rise from 4.0 to 6.0 degrees. The results were compared to results from proven DATCOM models of Cessna Citation II and Boeing 737. These models did not show the jumps. A possible reason for this is the unconventional configuration of the aircraft. DATCOM is built to analyse conventional aircraft, and originally did not allow the use of canard configurations. Also, the large front ducts may have a considerable influence.

Table 7.6: DATCOM results for C_L, C_D and C_m with InVADe model

α	C_D	C_L	C_m
-2.0	.013	-.330	-1.1752
.0	.014	.479	1.1886
1.0	.015	.583	.8942
2.0	.018	.431	-.6612
3.0	.022	.352	-1.8818
4.0	.029	.600	-1.5521
6.0	.050	1.401	.5312
8.0	.079	1.246	-2.0389
10.0	.118	1.610	-1.9689
12.0	.161	2.207	-.4033
14.0	.202	1.842	-1.2071
15.0	.220	1.895	-1.2334

Although the data for C_L, C_D and C_m cannot be trusted in this stage, the stability derivatives do show more logical values. In Table 7.7 the derivatives generated by DATCOM are shown. For an understanding of what the derivatives mean physically it is advised to read the AE3202 Aerospace Flight Dynamics & Simulation reader [88]. Figure 7.9 provides a first insight in the meaning of the lateral stability derivatives.

Table 7.7: DATCOM results for the stability derivatives at $\alpha = 0$, compared to established values for the Cessna Ce500 Citation

Coefficient	**Value InVADe**	**Value Citation**
C_{Y_β}	-7.672E-01	-9.896E-01
C_{l_β}	-1.795E-01	-7.720E-02
C_{n_β}	1.878E-01	1.638E-01
C_{Y_p}	-9.601E-04	-8.700E-02
C_{l_p}	-3.008E+00	-3.444E-01
C_{n_p}	-2.752E-04	-1.080E-02
C_{l_r}	2.526E-01	2.800E-01
C_{n_r}	-5.284E-01	-1.930E-01

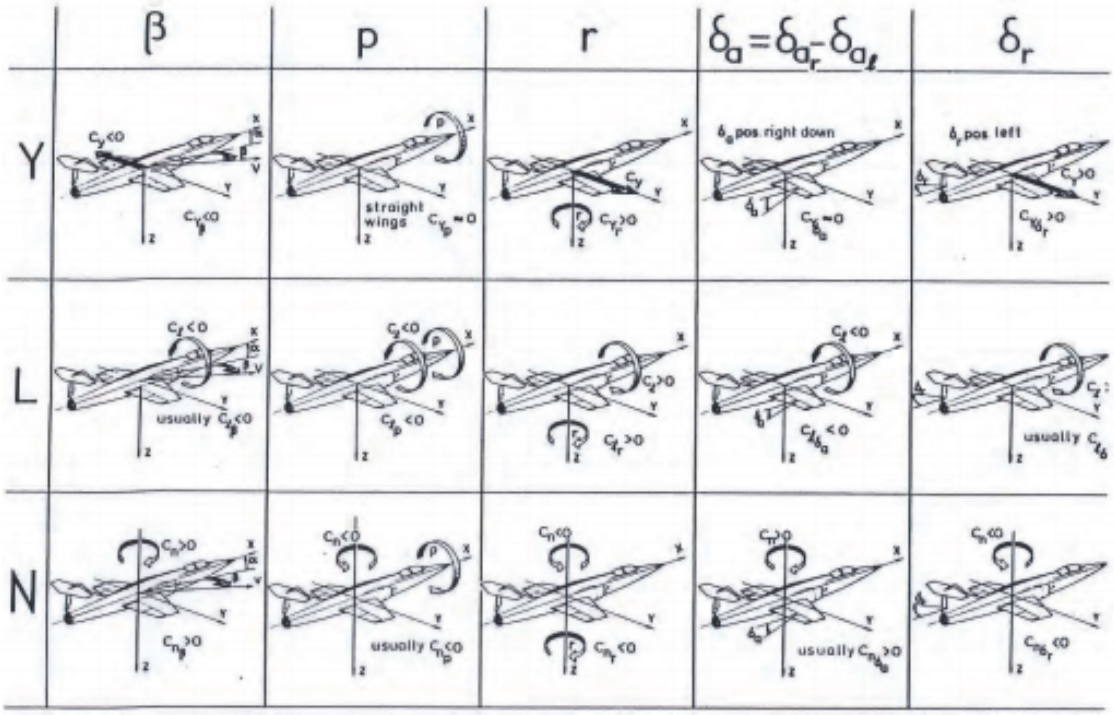

Figure 7.9: Explanation of asymmetric stability derivatives and their physical meaning [88]

A verification of the stability derivatives was done by comparing the values to those of a Cessna Ce500 Citation [88]. On the right side of Table 7.7 it can be seen that most coefficients are in the order of magnitude of that of the InVADE model. However, coefficients associated with roll (p) differ significantly from that of the Citation. This could be a direct result of the large wing planform of InVADe. Another reason could be a bug in DATCOM itself due to the unusual design. It is recommended that this difference is investigated in future work on the InVADe project to make sure these coefficients are correct.
An alternative program that may be used for the calculations is AVL [27], a freeware program from the Massachusetts Institute of Technology (MIT). The program uses an extended vortex-lattice model to determine aerodynamic properties of lifting surfaces and slender bodies, including stability derivatives. Howeverm due to time constraints, no full use of this program was made to provide adequate results.

METHODS TO DETERMINE REMAINING STABILITY DERIVATIVES

The AE3202 Aerospace Flight Dynamics & Simulation reader [88] provides analytic methods to estimate the values of several remaining stability derivatives. Some can be assumed 0; others are estimated using basic relations. Table 7.8 shows the methods used to determine the remaining values for stability derivatives. Also, mass and inertia parameters are determined. A Class I method from Roskam [101] is used to estimate the aircraft mass moments moments of inertia J_{xx}, J_{yy} and J_{zz}. Equations 7.12 are used, where radii of gyration $\overline{R_x}$, $\overline{R_y}$ and $\overline{R_z}$ are used for twin engine propeller aircraft as given by Roskam [101]. These values are: $\overline{R_x} = 0.34$, $\overline{R_y} = 0.29$ and $\overline{R_z} = 0.44$.

$$
\begin{aligned}
J_{xx} &= b^2 W \frac{\overline{R_x}^2}{4g} \\
J_{yy} &= l^2 W \frac{\overline{R_y}^2}{4g} \\
J_{zz} &= \left(\frac{b+l}{2}\right)^2 W \frac{\overline{R_z}^2}{4g}
\end{aligned}
\tag{7.12}
$$

RESULTING RESPONSES

With all the coefficients known, an analysis is done of the 5 different eigenmodes. Using methods described by Mulder et al [88], Equations 7.10 and 7.11 are converted into a so-called 'state-space system'. Once in this format, the equations are programmed into a MATLAB script used to simulate the response of the state-space system, using elevator, aileron and rudder deflections. Once again, the reponses are verified against the response of a Cessna Ce500 Citation, using the previously stated stability derivatives.

Table 7.8: Longitudinal and some lateral stability derivatives and remaining parameters. The resulting values are compared to established values for the Cessna Ce500 Citation [88]

Longitudinal stability derivatives	**InVADe value**	**Citation value**	**Remaining lateral stability derivatives**	**InVADe value**	**Citation value**
$C_{X_0} = \frac{W \sin\gamma_0}{\frac{1}{2}\rho V_0^2 S}$	0 ($\gamma_0 = 0$)	0	$C_{Y_{\dot\beta}} \approx 0$	0	0
$C_{X_\alpha} = C_L\left(1 - \frac{2C_{L_\alpha}}{\pi A e}\right)$	0.13	0.4653	$C_{Y_r} = C_{Y_{v_\alpha}}\left(\frac{V_v}{V}\right)^2 \frac{S_v l_v}{Sb}$	0.345	0.4300
$C_{X_{\dot\alpha}} \approx 0$	0	0	$C_{n_{\dot\beta}} \approx 0$	0	0
$C_{X_q} \approx 0$	0	0			
$C_{Z_0} = -\frac{W \cos\theta_0}{\frac{1}{2}\rho V_0^2 S}$	-0.31	-1.1360	**Other values**		
$C_{Z_u} = -2C_L$	-0.63	-2.2720	$\mu_c = \frac{m}{\rho S \bar c}$	122	102.7
$C_{Z_\alpha} = -C_{L_\alpha} - C_D$	-5.0	-5.16	$\mu_b = \frac{m}{\rho S b}$	34.3	15.5
$C_{Z_{\dot\alpha}} = -C_{N_{h_\alpha}}\left(\frac{V_h}{V}\right)^2 \frac{d\epsilon}{d\alpha}\frac{S_h l_h}{S\bar c}$	0.21	-1.43	$K_X{}^2 = \frac{J_{xx}}{mb^2}$	0.0289	0.012
$C_{Z_q} = -2C_{N_{h_\alpha}}\left(\frac{V_h}{V}\right)^2 \frac{S_h l_h}{S\bar c}$	7.3	-3.8600	$K_Y{}^2 = \frac{J_{yy}}{m\bar c^2}$;	0.300	0.980
$C_{m_u} \approx 0$	0	0	$K_Z{}^2 = \frac{J_{zz}}{mb^2}$;	0.0509	0.037
$C_{m_\alpha} = C_{N_{w_\alpha}}\frac{x_{cg}-x_{ac}}{\bar c} - C_{N_{h_\alpha}}\left(1 - \frac{d\epsilon}{d\alpha}\right)\left(\frac{V_h}{V}\right)^2 \frac{S_h l_h}{S\bar c}$	-1.82	-0.4300	$K_{XZ} = \frac{J_{xz}}{mb^2}$;	0	0.002
$C_{m_{\dot\alpha}} = -C_{N_{h_\alpha}}\left(\frac{V_h}{V}\right)^2 \frac{d\epsilon}{d\alpha}\frac{S_h {l_h}^2}{S\bar c^2}$	0.51	-3.7000			
$C_{m_q} = -1.1 \cdot C_{N_{h_\alpha}}\left(\frac{V_h}{V}\right)^2 \frac{S_h {l_h}^2}{S\bar c^2}$	-9.8	-7.0400			

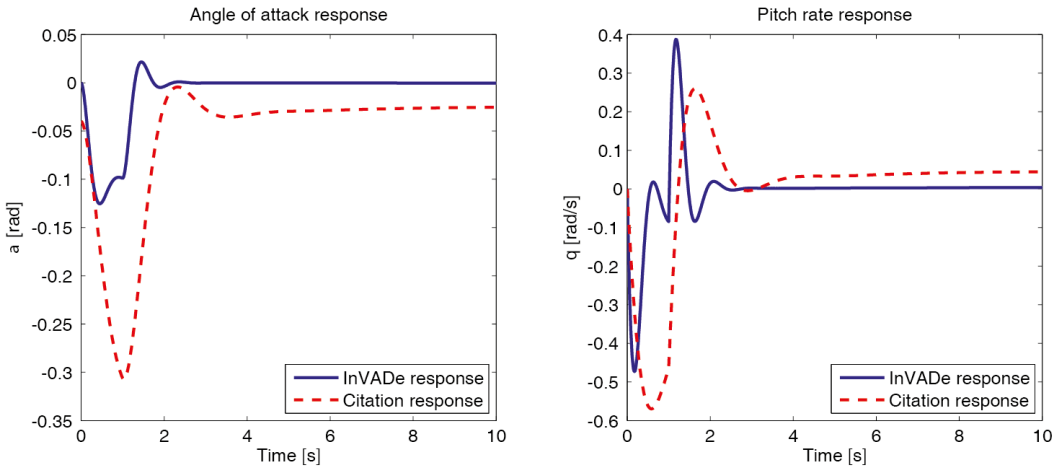

Figure 7.10: Short period response to a 10° pulse elevator deflection of 1 second.

First, a 10° pulse elevator deflection is used to start the short-period mode. In Figure 7.10 the angle of attack and pitch rate responses are shown. In comparison to the Citation, InVADe's oscillations are rapid and highly damped. Nevertheless, both motions show a similar path. When analysing the inputs, it was found that the inertia parameter ${K_Y}^2$ differs significantly from the value of the Citation. Also, other aircraft stated in the Flight Dynamics reader [88] have values of this parameter above 1. It is therefore likely that the estimate is not valid. However, during detailed design, more accurate estimates of the aircraft inertia may be made.

Next, a small step elevator input is provided to both aircraft to analyse the phugoid. The response in Figure 7.11 shows the airspeed increase and the pitch attitude of both aircraft. As expected, a slow oscillation is present, where velocity increases as the pitch angle decreases. In comparison, InVADe's motion has almost double the period of the Citation, and half the amplitude. This is no problem though, as the pilot now has plenty of time to react to the motion, and it is stable.

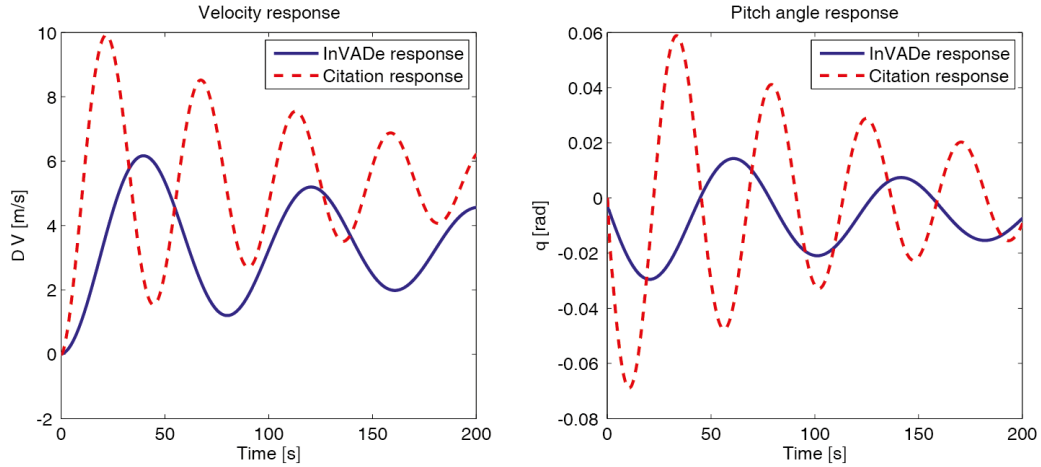

Figure 7.11: Phugoid response to a 0.3° step elevator deflection

Dutch roll is initiated by a very short pulse rudder deflection of 10°. Figure 7.12 shows the resulting roll and yaw rates of the aircraft, showing the typical behaviour of a Dutch roll. As the aircraft roll at their maximum speed, their yaw rate is at the equilibrium position, and vice versa. Both aircraft show a decent result, where the roll and pitch rates damp out swiftly. By analysing the peaks of the yaw rate, it was found that, while the motion starts with a roll rate of 0.0297, at the fourth peak the roll rate reaches a maximum value of 0.00085. This is 2.9% of the initial value, achieved within 3 periods. In comparison: within 3 periods the amplitude for the Citation drops from 0.0343 to 0.0022. The corresponding percentage is 6.4%. Using this estimate, the CS23 requirement concerning Dutch roll is satisfied for InVADe.

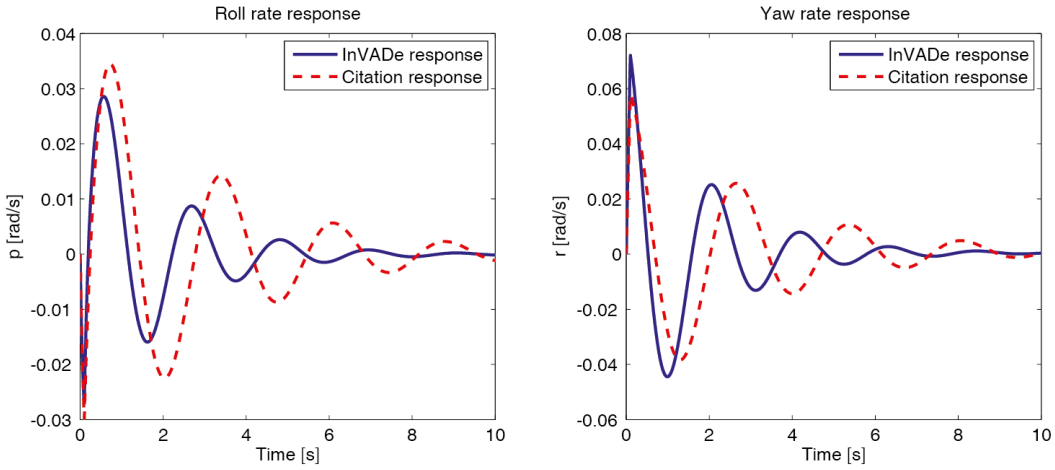

Figure 7.12: Dutch roll response to a 10° pulse rudder deflection of 0.1 s

Finally the spiral and aperiodic roll eigenmodes are examined. These motions are examined by initiating a roll by a 10° aileron deflection. At $t = 2$ s, the aileron is put back at 0°. The resulting roll angle and roll rate are examined in Figure 7.13. A clear difference between the aircraft is the difference in roll rate. This can be explained by the fact that InVADe has relatively large wings during cruise. Thus a high C_{l_p} value was estimated by DATCOM. Another difference is the stability of the spiral motion, visible in the roll angle plot. It has an extended time period, which shows that for the Citation, the roll angle keeps increasing. This means that, following an initial roll angle, it is tumbling into an unstable spiral. This is correct: the aircraft is designed unstable in spiral. Yet this is acceptable as long as the pilot has sufficient time to react. In comparison, InVADe rolls back to its initial state and is thus spirally stable.
The aperiodic roll of both aircraft takes place as expected. The roll rate damps out immediately, even faster for InVADE than for the Citation, which shows a small oscillation in the roll rate.

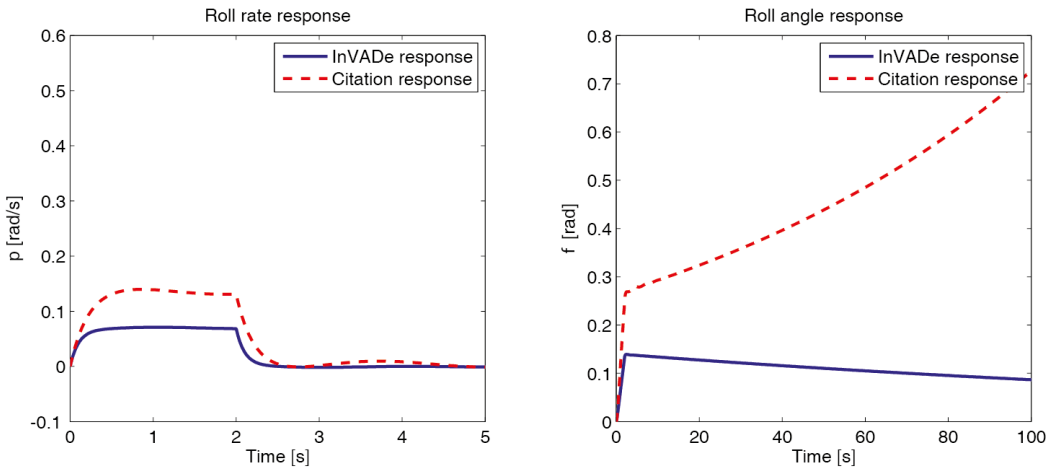

Figure 7.13: Spiral/aperiodic roll responses to a 2° pulse aileron deflection of 2 s

In conclusion, the dynamic stability analysis shows positive results for the current InVADe design. All eigenmodes are damped out swiftly and they are stable. The CS23 specifications for the eigenmodes are therefore satisfied. Further refinement is necessary, in order to establish more accurate stability derivatives. Also, more reliable mass moment of inertia estimates are required.

7.2.4. CONTROL

Flight control relies on different techniques throughout a mission. In cruise flight, control surfaces are used, while during hovering flight, differential thrust is employed. During transition, a mix of these mechanisms is used depending on the airspeed. It is, however, desirable to have a single control system for the pilot such that, independent of the flight mode, pilot input results into the same manoeuvre. To this end, a Fly-By-Wire control system is employed in the aircraft, which regulates the mix of deflections of the control surfaces, and thrust differentials. At cruise speed, aircraft control is provided by control surfaces. These are parts of the wing, canard and vertical tail that are deflected, such that the flight direction of the aircraft is controllable. Three types of control surfaces are used for the aircraft: elevators, flaperons and a rudder.

Elevators Elevators are used for pitch control. These control surfaces are located on the rear end of the canard. When deflected downwards, they increase the effective camber of the canard. This increases the lift generated by the canard, causing a pitch-up moment. Upwards deflection decreases the canard lift and generates a pitch-down moment.

Flaperons The ailerons are combined with the flaps in order to save space in the outboard wing. This is done so that full use of the outboard section is made for high lift devices usable for transition. By asymmetric deflection of these flaperons, a lift difference is generated between the left and right wings, causing the aircraft to roll.

Rudder The rudder is situated on the vertical tail. It provides directional control, enabling the aircraft to fly straight during crosswinds, and to overcome the OEI discussion in section 7.2.2. The size of the rudder has been determined for this condition.

7.3. HOVER

During hovering flight the aircraft is lifted into the air solely by thrust provided by the engines. This section discusses stability and control aspects of this flight mode. Starting from a free-body diagram, the aircraft is analysed in static equilibrium. Next, hover controlstatic stability is analysed qualitatively. Stability is discussed last.

7.3.1. FREE-BODY DIAGRAM

Figure 7.14 shows a Free-Body Diagram (FBD) of the aircraft in hovering flight, viewed from the side. Only two types of forces are acting on the aircraft: thrust forces and weight. Aerodynamic loads are negligible for this state, as the airspeed is very low during hovering flight. Four thrust forces act on the aircraft; two from the front ducts and two from the back ducts. This FBD shows the longitudinal balance of the InVADe aircraft. T_{ff} and T_{bf} are the thrust produced by the sums of both front and back fans respectively.

From this equilibrium state, Equations 7.13 are derived. This is done by summing up forces in vertical direction and moments around the center of gravity.

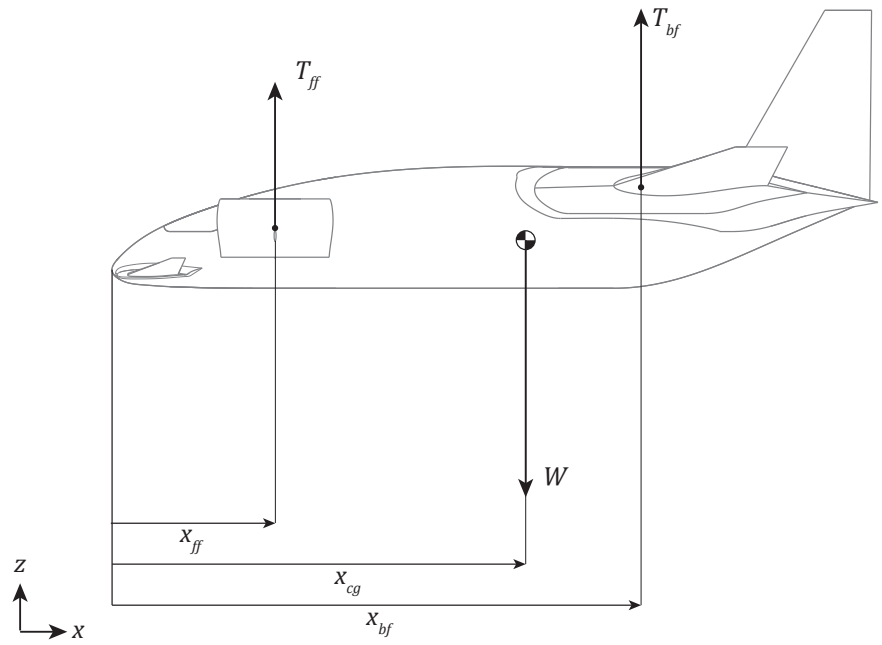

Figure 7.14: FBD of the aircraft in hover, in longitudinal equilibrium

$$\begin{aligned} \sum F_z: &\qquad T_{ff} + T_{bf} - W = 0 \\ \sum M_{cg}: &\quad T_{ff}(x_{ff} - x_{cg}) + T_{bf}(x_{bf} - x_{cg}) = 0 \end{aligned} \tag{7.13}$$

These equations show a relation between the duct positions relative to the center of gravity, and the different thrust values produced. Now the produced thrust can be divided over the front and the back engines. This is done such that the moment equation in Equation 7.13 is satisfied. To this end it is useful to define a total thrust T_{total} as the sum of $\cdot T_{ff}$ and $\cdot T_{bf}$ (in this case equal to W). By combining this with the moment equation, Equations 7.14 are obtained.

$$\begin{aligned} \frac{T_{ff}}{T_{total}} &= \frac{x_{bf} - x_{cg}}{x_{bf} - x_{ff}} \\ \frac{T_{bf}}{T_{total}} &= \frac{x_{cg} - x_{ff}}{x_{bf} - x_{ff}} \end{aligned} \tag{7.14}$$

These equations express the division of thrust over the front and back fans as a function of the center of gravity position. As the center of gravity position changes during operation, the thrust ratios change accordingly. It is therefore necessary to identify the thrust ratios for the center of gravity limits determined in Section 7.2.1. If the accompanying thrust values cannot be achieved by either the front or the back ducts, either the center of gravity range or the propulsion layout needs to be revised.

Table 7.9 shows the resulting forces required to balance the aircraft. The last determined c.g. positions were used as input values. However, these values differ from the distribution taken as a starting point as described in Section 7.2.1. The front fans take up more power than determined in Section 5.2.1; the back fans, on the contrary, require less power. This should not be an issue in further design as this would just require a new design iteration. In addition, the front fans are currently sized to provide sufficient thrust during cruise flight. The main result would be that the back fan is over-designed.

Table 7.9: Thrust ratios and forces required to balance the aircraft in hover

	$\frac{T_{ff}}{T_{total}}$	$\frac{T_{bf}}{T_{total}}$	T_{ff} at MTOW [kN]	T_{bf} at MTOW [kN]
Front c.g. limit (x_{cg} = 6.66)	0.47	0.39	38.4	42.9
Back c.g. limit (x_{cg} = 7.23)	0.53	0.61	31.9	49.5

7.3.2. CONTROL

Control during hover is provided by the fans. Control methods used on quadrotors are applied to the aircraft. The power supplied by the turboshaft engines is divided over the ducts. By altering the power distribution, differential

thrust is generated. Thus, the aircraft can be rolled and pitched. Yaw control is possible by altering the torques produced by the electric motors powering the fans. A qualitative assessment of these control methods by means of Free-Body Diagrams is provided in this section.

When powering the fan, a torque is exerted on the fan shaft to keep it spinning. Therefore, a reaction torque is also acting on the aircraft for each fan. Increasing the fan thrust requires a higher torque. The reaction torque exerted on the aircraft increases as well. This phenomenon can be used to yaw the aircraft, as is commonly done in quadrotor aircraft.

This method requires that the fans spin in certain directions. The two front fans should be counter-rotating, as well as the two back fans. However, a front fan and a back fan on one side of the aircraft should spin in opposite directions. This will be demonstrated when discussing yaw control. Figure 7.15 shows three FBDs that describe the motion. To maintain vertical equilibrium, the aircraft base thrust values T_{ff} and T_{bf} counter the weight W of the aircraft. But in addition, the thrust differentials should also add up to an equilibrium. Equation 7.15 describes this condition:

$$\sum F_z : \Delta T_{ff,1} + \Delta T_{ff,2} + \Delta T_{bf,1} + \Delta T_{bf,2} = 0 \tag{7.15}$$

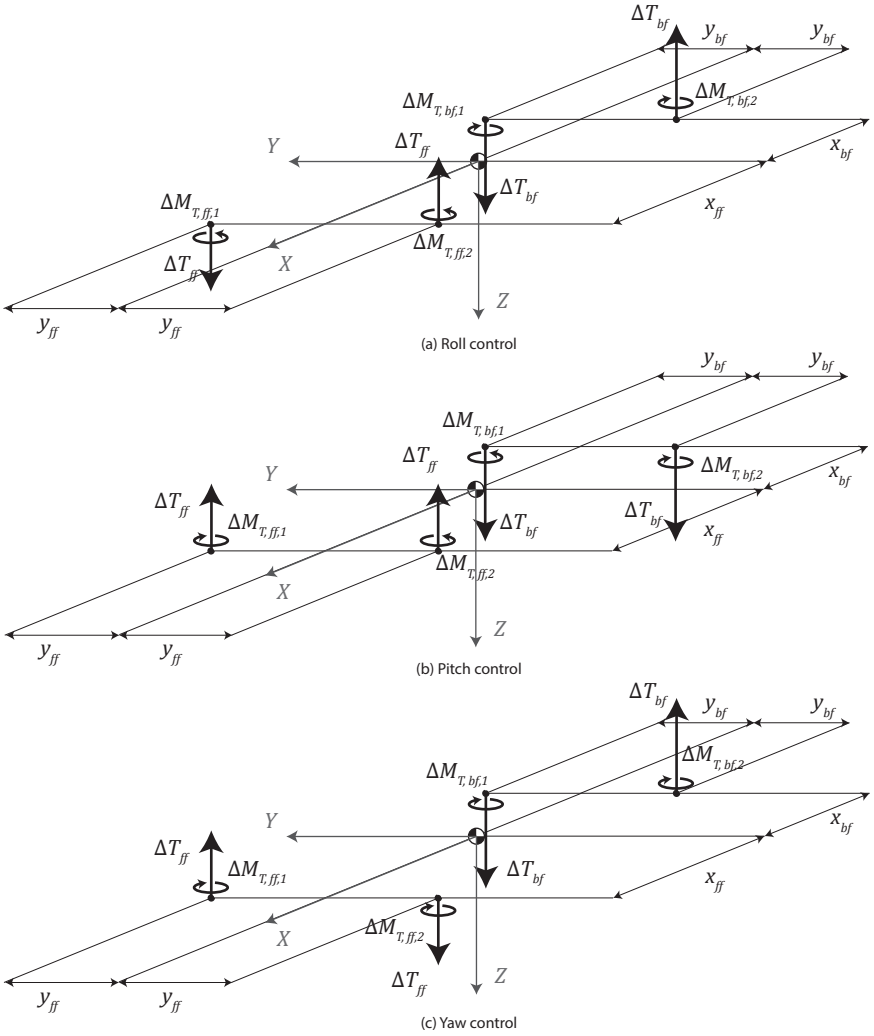

Figure 7.15: Free-body diagrams used to analyse control methods

ROLL CONTROL

A rolling moment is provided by providing differential thrust. To roll to the aircraft to the right, thrust is decreased at the right side fans, and increased by the same amount on the left side engines. Figure 7.15(a) shows the corresponding FBD. Here, ΔT_{ff} and ΔT_{bf} are thrust differentials generated by the front and back front ducts respectively. The applied rolling moment around the x-axis is composed in Equation 7.16:

$$M_{rolling} = 2\Delta T_{ff}(y_{cg} - y_{ff}) + 2\Delta T_{bf}(y_{cg} - y_{bf}) \tag{7.16}$$

PITCH CONTROL
By increasing the thrust provided by the front ducts, and decreasing the thrust from the back ducts, the aircraft is pitched up. From Figure 7.15(b) the corresponding pitching moment is derived, resulting in Equation 7.17:

$$M_{pitching} = 2\Delta T_{ff}(x_{cg} - x_{ff}) + 2\Delta T_{bf}(x_{cg} - x_{bf}) \tag{7.17}$$

YAW CONTROL
As opposed to the other two maneuvers, yaw control comes from the reaction torques exerted by the fans on the aircraft. Figure 7.15(c) shows how these torques add up. By applying a more powerful torque on the left front fan by increasing it's thrust by ΔT_{ff}, a yawing moment $\Delta M_{T_{ff,1}}$ is generated. To prevent vertical acceleration, the right front fan needs to reduce it's thrust by ΔT_{ff}. This reduces the exerted torque by the right front fan. If the fans are counter-rotating, the reduction of this torque generates an additional yawing moment $\Delta M_{T_{ff,2}}$.

Now, however, a rolling moment is also generated around the x-axis. To prevent this from occurring, the right back fan increases its thrust by ΔT_{bf}. Therefore, it's reaction torque increases by $\Delta M_{T_{bf,2}}$. The left back fan decreases its thrust by the same amount, and it's torque by $\Delta M_{T_{bf,1}}$.

If the fans are spinning as illustrated in 7.15(c), all reaction torques add up to a resulting yawing moment. This results in Equation 7.18:

$$M_{yawing} = \Delta M_{T_{ff,1}} + \Delta M_{T_{ff,2}} + \Delta M_{T_{bf,1}} + \Delta M_{T_{bf,2}} \tag{7.18}$$

To prevent rolling moments from occurring, Equation 7.19 must hold:

$$\sum M_x : 2\Delta T_{ff}(y_{cg} - y_{ff}) - 2\Delta T_{bf}(y_{cg} - y_{bf}) = 0; \tag{7.19}$$

MOVING THE AIRCRAFT
Vertical motion is attained by increasing or decreasing the total thrust. This must be done such that the balance discussed in section 7.3.1 is maintained. Horizontal motion follows from a combination of manoeuvres.

Forward velocity is achieved by pitching the aircraft nose-down. Once the aircraft is slightly pitched, the aircraft is no longer in static equilibrium. Figure 7.16 shows this state. A net horizontal force exists, accelerating the aircraft in longitudinal direction. By increasing the thrust force, the weight force is countered. Altitude is maintained, while the aircraft accelerates forward. Then, by pitching the aircraft back, the balanced state returns, while the aircraft maintains its forward velocity and drifts forward. The motion is terminated by pitching the aircraft nose-up (and increasing total thrust), slowing the aircraft down again.
In a similar manner, lateral motion is attained by rolling the aircraft.

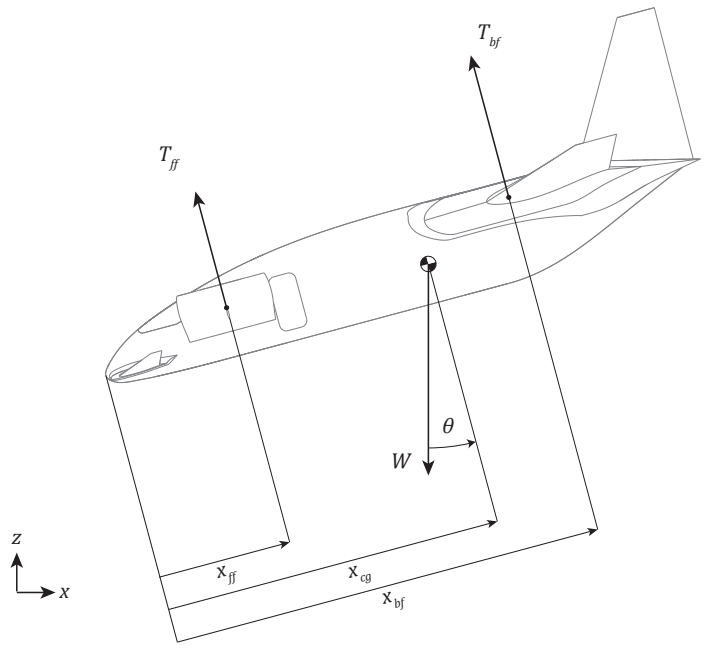

Figure 7.16: FBD of the aircraft in hover, pitched nose-down

7.3.3. STABILITY

Next, the effect of a disturbance on the equilibrium state is discussed. To investigate this, the aircraft is analysed at a general pitch angle θ (the disturbed state) rather than in equilibrium. This state is shown back in Figure 7.16. The forces provided by the ducts are independent of θ. The moment equilibrium does not change then. This means that the disturbance is not counteracted, but also not intensified. Hence, the aircraft is neutrally stable in an idealised case.

However, an exact estimate of the center of gravity is very hard to obtain. In addition, as shown in section 7.1, the center of gravity shifts. The slightest disturbance (e.g. passenger/pilot movement, movement of flaps or the landing gear) may influence this. In this case, the aircraft balance is disturbed and it tips over. The aircraft has therefore an unstable response to a center of gravity shift. This requires either a very good pilot or a stability augmentation system guiding the pilot.

Dynamic stability is another important issue in hovering flight. Two main differences are present in comparison to cruise flight. First, the aerodynamic forces and moments acting on the aircraft are very small. Second, gyroscopic influences of the propulsion system have a significant influence.They also couple longitudinal and lateral/directional motion.
Kohlman [22] provides a discussion of dynamic stability of V/STOL aircraft during hover. A short summary is presented here. Three relevant cases were analysed:

1. **Case 1**: Negligible gyroscopic and aerodynamic effects, no initial rotation

2. **Case 2**: Non-negligible gyroscopic angular momentum about the X-axis and Z-axis, no aerodynamic effects or initial rotation

3. **Case 3**: Initial rotation rate about the Z-axis (yaw), no gyroscopic or aerodynamic effects

Case 1 results in uncoupled longitudinal and lateral/directional motions that are neutrally stable. When investigating case 2, it is found that gyroscopic influences lead to another neutrally stable response. However, this response is oscillatory. The associated frequency $\bar{f}$ with this response is given by Equation 7.20:

$$\bar{f} = \sqrt{\frac{J_{xx}\bar{h}_x^2 - 2 \cdot J_{xz}\bar{h}_x\bar{h}_z + J_{zz}\bar{h}_z^2}{J_{yy}(J_{xx}J_{zz} - {J_{xx}}^2)}} \tag{7.20}$$

A problem with this mode is that unstable Pilot-Induced Oscillation (PIO) has a high probability of occurrence. Since the aircraft fans are counter-rotating, the angular momentum terms $\bar{h}_x$ and $\bar{h}_z$ are negligible during stable hover (hence, no oscillations are present). Then the result is the same as in case 1. But when the aircraft yaws, the reaction torques from the engines differ. This means that the fans spin at different angular rates and that a non-negligible angular momentum term exists. Then this oscillation becomes an issue again.
At an initial yaw rate, stability depends on the mass moments of inertia of the aircraft. For yaw, if $J_{xx} < J_{zz} < J_{yy}$, or if J_{yy} is the 'middle' moment of inertia, then the motion is dynamically unstable. Otherwise, the response is a neutrally stable oscillation. This result can be extended to initial roll and pitch rates. If for roll, J_{xx} is the middle moment of inertia, rolling is dynamically unstable. For pitching this holds if J_{yy} is the middle moment of inertia.

To summarise, most responses are neutrally stable, sometimes in an oscillating mode. An initial rotation may even produce an unstable response. This means that inherent dynamic stability will not be achieved by this aircraft, even when aerodynamic influences are neglected. These may seem unimportant, but according to Kohlman [22], aerodynamic forces and moments caused by gusts and inlet induced flow are small, but have a considerable effect on stability. It is recommended that for dynamic stability, additional augmentation systems are investigated.

7.4. TRANSITION

A critical part of the flight is the transition phase. It is the phase that connects hovering flight and conventional flight, in which the aircraft switches from powered lift to wing lift, or vice versa. When the aircraft is hovering, transition is initiated by slowly rotating the front ducts forward. Hence, a horizontal thrust component is generated, accelerating the aircraft. As the airspeed increases, the lifting surfaces of the aircraft take over the lifting capability from the fans,

7.4.1. FREE BODY DIAGRAM

Analysis on the transition phase is performed by setting up a FBD. This FBD is shown in Figure 7.17. It shows the thrust forces and aerodynamic forces and moments acting on the aircraft. The shown aerodynamic center is of the complete aircraft. The aircraft is flying at an angle of attack α. The front duct is tilted at an angle of attack α_T.

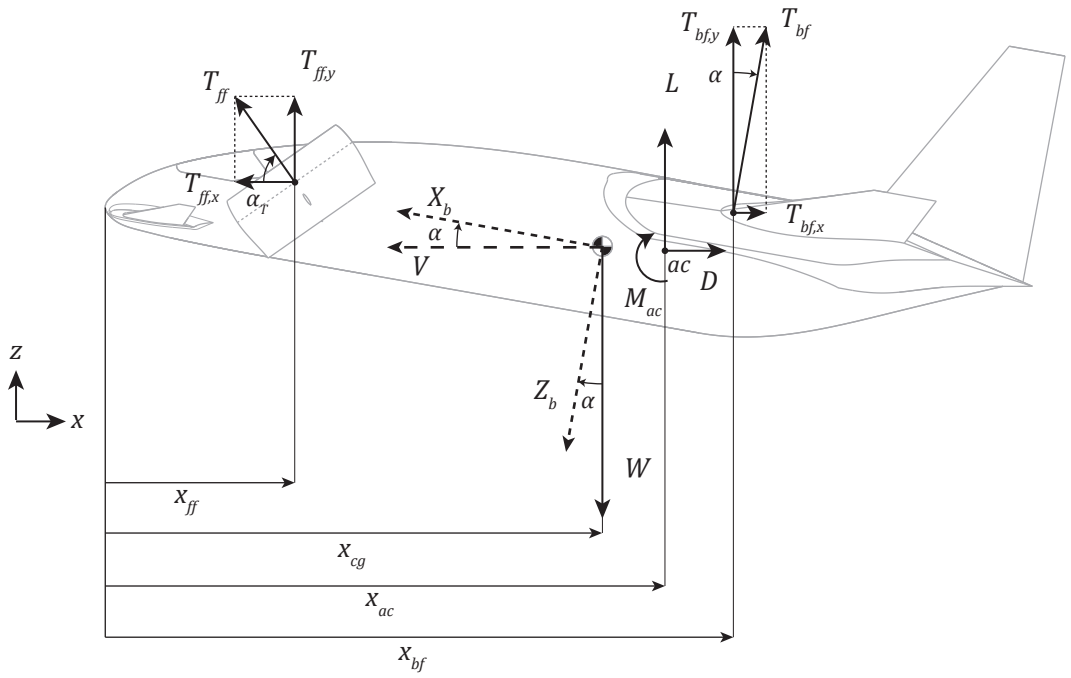

Figure 7.17: Free body diagram during the transition phase

In static equilibrium (i.e. no accelerations present), Equations 7.21 are derived from the free body diagram.

$$\begin{aligned} \textstyle\sum F_x: &\quad T_{ff}\cos\alpha_T = D \\ \textstyle\sum F_y: &\quad T_{ff}\sin\alpha_T + L + T_{bf} = W \\ \textstyle\sum M_{ac}: &\quad M_{ac} = T_{ff}\sin\alpha_T(x_{ff} - xac) - W(x_{cg} - x_{ac}) + T_{bf}(x_{bf} - xac) \end{aligned} \tag{7.21}$$

If aerodynamic forces and moments are given for a certain airspeed and angle of attack, these equations are used to determine the thrust forces from the engines to keep the aircraft balanced. Also, the required front duct angle is determined. After combining the equations and some rearranging, Equations 7.22 are obtained. These relations are used to analyse the equilibrium state of the aircraft at different velocities.

$$\begin{aligned} T_{bf} &= \frac{M_{ac}+L(x_{ff}-x_{ac})+W(x_{cg}-x_{ff})}{\cos\alpha(x_{bf}-x_{ff})} \\ \tan\alpha_T &= \frac{W-L-T_{bf}\cos\alpha}{D+T_{bf}\sin\alpha} \\ T_{ff} &= \frac{1}{\sin\alpha_T}(W-L-T_{bf}\cos\alpha) \end{aligned} \tag{7.22}$$

7.4.2. EQUILIBRIUM ANALYSIS

If equilibrium can be achieved at all aircraft velocities, a controlled transition is possible. Although estimated values of C_L are available, realistic drag and moment coefficients are difficult to estimate. The presence of an opened fan-in-wing requires a thorough analysis using a CFD model or a wind tunnel test. This means that a decent equilibrium analysis is not possible at this design stage.

7.5. VERIFICATION AND VALIDATION

In the Stability & Control analysis there is a thin line between verification and validation. Especially regarding the stability derivatives not a lot of values are presented and the model has to be verified and validated using the same coefficient values.

7.5.1. VERIFICATION

Up to this point in the design process, verification has mainly revolved around performing unit tests and system checking. For the scissor plot, the outcome was cross checked against example results from the AE3201 System Engineering and Aerospace Design [73] and found reasonable. Concerning stability derivatives, the AE3202 Flight Dynamics - Lecture Notes [88] was consulted and coefficient values were compared to that of several reference aircraft. Although some differences were presented, the coefficients were found to be in the same order of magnitude as that of reference aircraft. As an additional verification the AVL program [27] of MIT can be used.

7.5.2. VALIDATION

Throughout the calculation progress, results have been extensively compared to reference aircraft. The vertical tail sizing method has been checked with values of that of the Aerospatiale N 262. In terms of stability derivatives validation, the Cessna Ce-500 Citation has been the main comparison aircraft as was shown in Subsection . Although significant differences show up in the stability derivatives, the resulting eigenmode responses showed promising results. Also one should remember that InVADe has a canard configuration. This results in positive coefficients for $C_{Z_{\dot{\alpha}}}$, C_{Z_q} and $C_{m_{\dot{\alpha}}}$, compared to negative coefficients for a normal aircraft configuration.

8

PERFORMANCE

This chapter presents the relevant performance characteristics for an aircraft of this class. The characteristics are described in order of flight phases. Section 8.1 assesses InVADe climb performance and resulting service ceiling. Speed ranges are discussed in Section 8.2 and 8.3 presents the flight envelope. Fuel and emissions are calculated in Section 8.5 and finally an overview is shown in Section 8.8.

8.1. CLIMB PERFORMANCE

Climbing flight begins immediately after the transition. The unsteady rate of climb (ROC) when climbing to cruise altitude while accelerating can be calculated with the formula for unsteady climb [120]:

$$ROC = \frac{P_A - P_R}{W_{cl}} \cdot \frac{1}{1 + \frac{V}{g} \cdot \frac{dV}{dH}} \tag{8.1}$$

Doing this calculation for the whole speed range and different altitudes results in Figure 8.1. The highest line is the ROC at sea level, the other lines are the ROC in steps of 1,000 m up to the service ceiling of 7,000 m. The climb rate requirement of a maximum climb rate of 9 m/s at sea level is shown as a dotted line. According to CS 23.65 the climb speed should be at least 1.2 times the stall speed. The stall speed for every altitude was computed and using the factor the minimum climb speed was set and indicated by a dot on the line in the graph.

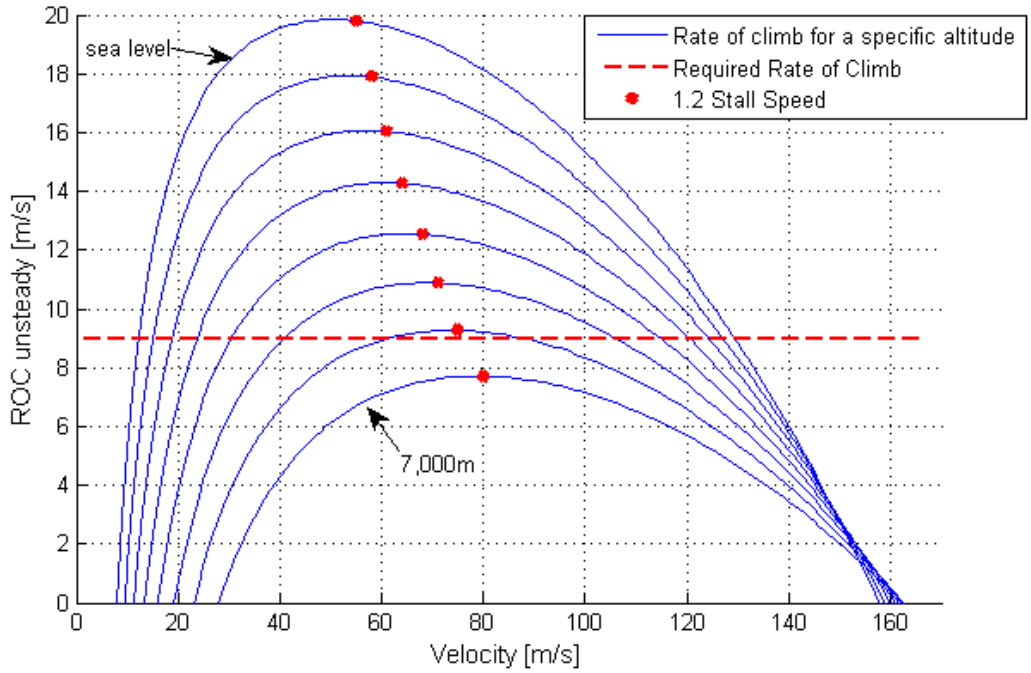

Figure 8.1: Rate of climb at cruise power

As can be seen in the graph the maximum rate of climb at sea level is 19.8 m/s, therefore the climb rate requirement is reached successfully. The maximum rate of climb that can be reached at cruise altitude is 9.2 m/s, this is

at speeds much lower than the cruise speed though.

With these climb speeds a climb from sea level to cruise altitude takes about 7.3 minutes when flying at the optimal rate of climb, which lies between 54 and 76 m/s. During a normal mission the aircraft will fly at higher speeds though, which will decrease the rate of climb.

8.1.1. SERVICE CEILING

The service ceiling is the maximum altitude at which a climb rate of 0.5 m/s can be reached.
For InVADe this criteria results in a service ceiling of 12,050 m at cruise power. Operating at this altitude however introduces more challenges: a stronger pressurised fuselage is needed and fatigue loads of the fuselage would also increase. Additionally a high service ceiling is only of limited use for short range business aircraft, since on short trips it is not worth it to climb to high cruise altitudes. Therefore, in the scope of this preliminary design, the service ceiling, set by the requirement, is limited to 7,000 m.

8.2. CRUISE AND MAXIMUM SPEED

Requirement Ct-cons-04 states a cruise speed of 600 km/h at 75% engine power. The power plant was sized (in Section 5.5.3) in order to meet this requirement and therefore the cruise speed that can be reached at cruise altitude is 600 km/h.

At 100 % engine power the maximum speed that can be achieved at cruise altitude can be calculated with the same method to be 661 km/h. The engines were sized to reach this power at cruise altitude, and hence can produce even more power with denser air, following Equation 5.36. The electronics however were sized for 100% engine power at cruise altitude and cannot handle more, therefore 100% engine power can only be used at cruise altitude or higher.

8.3. FLIGHT ENVELOPE

From Figure 6.2 the flight envelope can be derived. The flight envelope is important information for the design team as well as for the pilot later during operation. It shows the possible accelerations at every airspeed (which is useful to analyse climbing and manoeuvring abilities) and also the limits which have to be respected during operation.
The Flight envelope showing the limit manoeuvre and gust loads of InVADe is displayed in Figure 8.2.

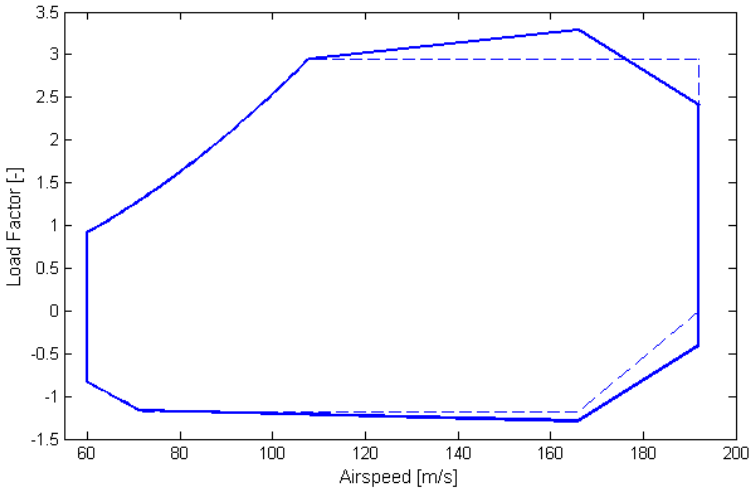

Figure 8.2: Flight envelope of InVADe

The gust loads depend, amongst others, on the density, which in turn is a function of the altitude. This means that the gust loads increase at lower altitudes. Therefore the pilot cannot be allowed to fly at the full cruise speed before the aircraft has reached it's cruising altitude of 6,000 m. This however is no big issue since the speed during the climb to cruising altitude is lower for better climb performance than the cruising speed at which the highest loads occur.

8.4. PAYLOAD-RANGE DIAGRAM

The requirements demand a maximum payload of 1,300 kg and also a range of 2,000 km (including a landing in between) with a payload of 1,000 kg. Therefore the maximum payload of 1,300 kg and the point of 2,000 km range

and 1,000 kg payload are fixed on the graph. The points of maximum range with 1,300 kg payload and without any payload (the ferry range) need to be determined.

To find these two points the Breguet range equation and fuel fractions from the Class I weight estimate were used to find a range value that corresponds to the decreased fuel weight (in case of 1,300 kg payload) and the decreased MTOW (in case of 0 kg payload). The outcome is 1,082 km range with full payload and 2,986 km range with zero payload and is presented in Figure 8.3. All the ranges include a landing and take-off in between. If there was no stop in between the total range of the mission can be increased.

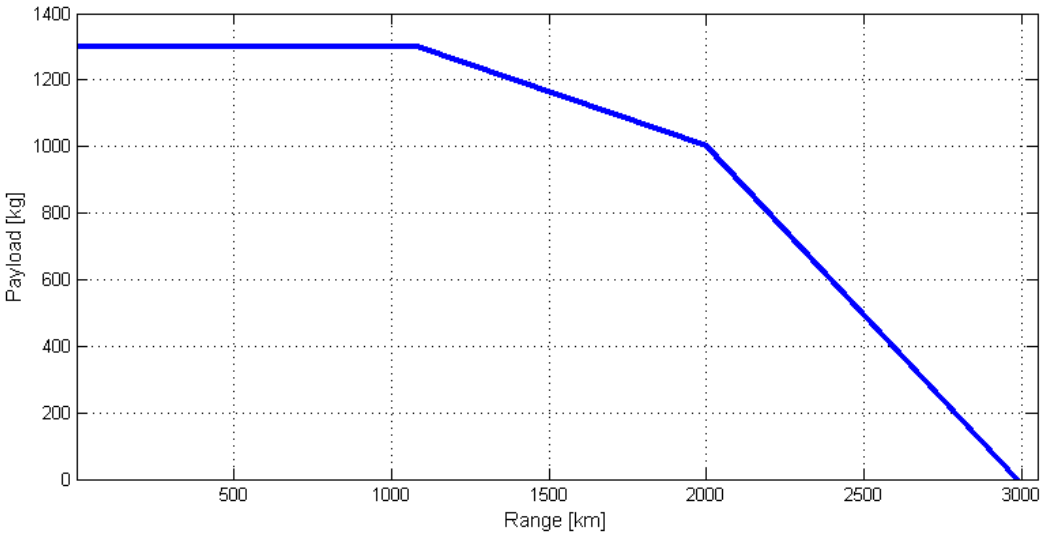

Figure 8.3: Payload-range diagram of InVADe

8.5. FUEL AND EMISSIONS

With the engine selected in Section 5.5.3 a more detailed fuel calculation can be done and particulate emissions can be estimated. First the mission must be worked out in more detail from the calculations in this chapter.

Both take-offs and landings are assumed to last for three minutes, including transition. This takes into account a small provision for engine start-up and taxiing at the three separate locations. The hover power setting of 2,995 kW is used here.

The mission's unsteady climb rate is assumed as 1,000 ft/min (5 m/s) to provide the passengers with a comfortable flight experienced without too quick changes in cabin air pressure. At the same rated power as cruise (75% maximum power) this allows for a forward speed of 130 m/s. Climbing to 6,000 m takes 20 minutes, and the aircraft travels 156 km.

The aircraft's cruise speed is 167 m/s, using 1,712 kW power available (75% of the power corrected for altitude). Excluding climb and descent, 766 km must still be travelled which takes 76.6 minutes.

The expected rate of descent is assumed as 2,000 ft/min (10 m/s), again due to passenger comfort. Around 530 kW of engine power is needed to maintain an average forward speed of 130 m/s again. Descent takes 10 minutes and the aircraft travels 84 km. Figure 8.4 gives an overview of the mission profile used for calculation.

The predicted specific fuel consumption (SFC) in 2030 is 0.206 kg/kWh. As a back-up, calculations were also performed with the current-day value of 0.274 kg/kWh. The future value yields fuel and CO2 masses of 1,295 kg and 4,080 kg respectively, meaning 1.54 km/kg fuel and 2.04 kg/km CO2. Both are well under the requirements set in Section 2.1. The fuel mass is also somewhat lower than the value used for the weight estimation after accounting for reserve fuel. Current-day values are 1,723 kg of fuel and 5,427 kg of CO2, thus 1.16 km/kg fuel and 2.71 kg/km CO2. These results fail to meet the requirements. Clearly stagnation in terms of engine technology would have a negative impact on the performance of InVADe.

CO2 emissions were calculated as 3.15 times the fuel burn, assuming complete combustion of kerosene [91]. Nitrous oxide (NOX), unburned hydrocarbons (HC), carbon monoxide (CO) and non-volatile particles/soot (PM) emissions were calculated with a method developed by Rindlisbacher [97]. This method determines emissions indicators (EI) in g/kg from the power available in shaft horsepower, derived from large amounts of data and split up into categories for single or dual engine helicopters. The results per single phase and for an entire mission are shown in Table 8.1.

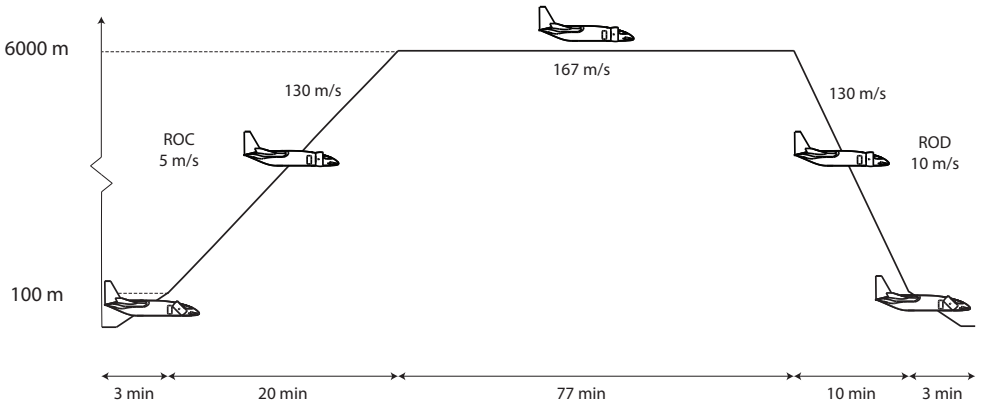

Figure 8.4: Mission profile of InVADe

Table 8.1: Overview of fuel burn and particulate emissions per singular phase and total for entire mission

Parameter	Unit	Take-off	Climb	Cruise	Descent	Landing	**Total**
Power	kW	2,995	1,712	1,712	530	2,995	-
Duration	minutes	3	20	76.6	10	3	**225**
Fuel	kg	30.9	117.6	450.2	18.2	30.9	**1295**
CO2	kg	97.2	370.3	1418.3	57.3	97.2	**4080**
NOX	kg	0.72	2.01	7.69	0.16	0.72	**22.6**
HC	kg	0.015	0.105	0.403	0.058	0.015	**1.19**
CO	kg	0.017	0.124	0.474	0.070	0.017	**1.41**
PM	kg	0.009	0.047	0.178	0.005	0.009	**0.49**

8.6. ONE ENGINE INOPERATIVE

The aircraft's performance must be assessed in the case that one of the turboshaft engines or electric motors fails during cruise. These calculations were done the same way as for normal operation, only the available power was assumed to be half of the cruise power normally available.

Rate of climb Since the rate of climb depends on the difference in power available (which is halved) and power required (which stays the same) it drops significantly. The results can be seen in Figure 8.5. The top line is again the rate of climb at sea level and the lines below show the performance for every additional 1000 m altitude. The dots indicate the minimum allowed rate of climb (1.2 times the stall speed).

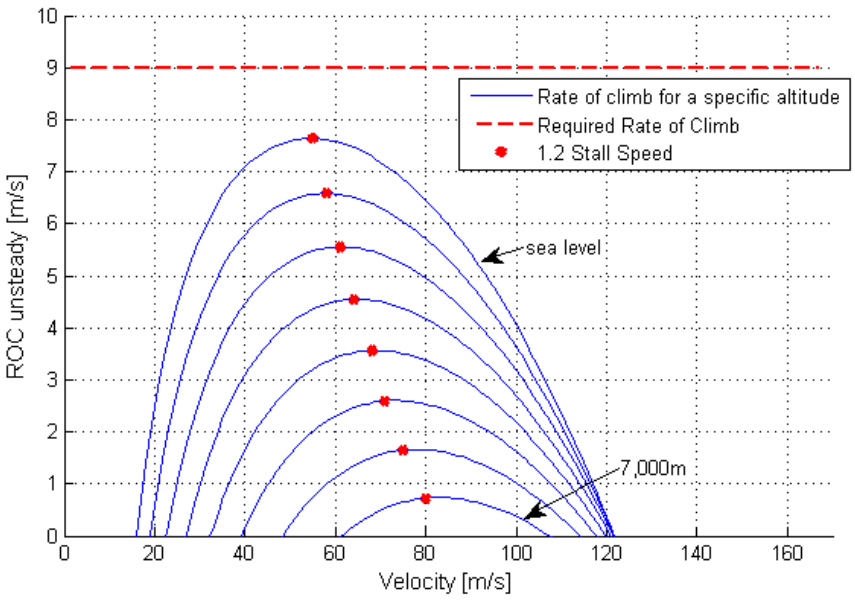

Figure 8.5: Rate of climb with one engine inoperative

The maximum rate of climb with only one engine is 7.6 m/s at sea level (compared to 19.8 with both engines) and climbing to 6,000 m would take a minimum of 25.8 minutes.

Service ceiling The altitude at which a rate of climb of 0.5 m/s can be reached with only one engine is 7,200 m. This means InVADe is still able to cruise at its design cruise altitude of 6,000 m which enables it to deviate efficiently to an alternative airport.

Cruise speed Using one engine at the normal cruise rating of 75% at the cruise altitude of 6,000 m results in a cruise speed of 476 km/h. When 100% engine power is used this can be increased to 524 km/h.

8.7. EMERGENCY LANDING

Accounting the unlikely event of malfunction of the tilting mechanism or failure of any other system which compromises the aircraft's ability to land vertically, InVADe is designed such that it is able to perform a conventional (emergency) landing on a runway or landing strip. In this section the runway length during conventional landing is analysed. To find the runway length, the approach and landing speeds need to be determined first. According to CS 23.73 the approach speed is 1.3 times the minimum speed in landing configuration and the touch-down speed is 1.2 times this speed. Using the minimum speed of 38.5 m/s in landing configuration this results in an approach speed V_A of 50.1 m/s and touch-down speed V_T of 46.2 m/s.
Having calculated these numbers and assuming the friction coefficient at maximum brake power (μ_{br}) equals to 0.4 [121], the landing runway length can be found by the use of Equation 8.2.

$$s = \frac{W}{2g} \cdot (-V_T)^2 \cdot \frac{1}{-\bar{D} - \mu_{br}\left(W - \bar{L}\right)} \tag{8.2}$$

The runway length needed (s), to land the aircraft with full payload after dumping fuel, equals to 301 m. This short distance can be explained by the low speed that is possible in landing configuration. According to regulations, the available runway length for landing should be 166.7 % of the runway length needed. The available runway length to perform a safe landing equals to 502 m. Then, for rainy conditions, another 15 % extra runway length is required. To be able to perform a safe landing with wet runway conditions, the runway length should be at least 577 m.
Checking these numbers with some relatively small airports in and around the Netherlands (Table 8.2), it can be concluded that even while having wet runway conditions, InVADe is able to land at all of these airports.

Table 8.2: Landing Distance Available (LDA) for small airfields within the Netherlands [61], Germany [5] and France [106]

	LDA (m)
Lelystad Airport	1,250
Den Helder	1,275
Seppe Airport	830
Hilversum	700 (grass)
Weeze	2,440
Mönchengladbach	1,200
Lille Lesquin	1,580
Reims Prunay	1,020

8.8. PERFORMANCE DATA OVERVIEW

Table 8.3 shows an overview of the most important performance figures during normal operation and also for the one engine inoperative condition.

Table 8.3: Performance data overview

	Normal Operation	**One Engine Inoperative**	**Unit**
Fan Power available	13,910	6,955	kW
Cruise Speed	600	476/524	km/h
Maximum Rate of Climb at Sea Level	19.8	7.6	m/s
Minium Time to Cruise Altitude	7.3	25.8	minutes
Service Ceiling	12,050 (limited to 7,000)	7,200 (limited to 7,000)	m
Range at 1,300 kg / 1,000 kg / 0 kg Payload	1,082 / 2,000 / 2,986	not applicable	km
Specific range	1.54	-	km/kg
CO2 production	2.04	-	kg/km

9

DEVELOPMENT ANALYSIS

This chapter begins with a description of the Operations and Logistics. Next, a plan for manufacturing is developed, followed by a plan for Assembly and Integration. After that, the risks are assessed, as well as the Reliability, Availability, Maintainability, and Safety (RAMS). Finally, in the last section, a Sensitivity Analysis is performed for the design.

9.1. OPERATIONS AND LOGISTICS

In this section, the operational and logistical aspects of the InVADe aircraft will be addressed for two phases of the aircraft operation. These two operation phases are the ground and the airborne operation. First the ground operation phase of InVADe is discussed in 9.1.1. After that the airborne operation phase is discussed in 9.1.2.

9.1.1. GROUND OPERATION PHASE

The ground operations of the InVADe aircraft include maintenance, cleaning, restocking, refuelling, pre-flight checks, etc. Appendix A.5 shows a detailed flow diagram for these operations. Ground operations are performed after landing the aircraft or after it has been taken out of the hangar for a new mission. These starting points are indicated as rectangular boxes with bold lines. They terminate when the aircraft is put in the hangar or takes off. Ground operations are led by the Operations Center (OC). This is an idealised body that leads all personnel in ground operations; in practice the structure will vary from client to client.

When the aircraft has landed and the passengers have deboarded, it is possible that another mission is to be performed immediately. Otherwise, a cleaning crew takes care of cleaning the cabin. Next, a check is done if any (mandatory) scheduled maintenance is needed. When necessary, it is performed as soon as possible to keep availability high. If a new flight is scheduled, cleaning will generally be skipped and the cycle for a new mission will be performed.

When a new mission is started, the first step is refuelling the aircraft.This is the responsibility of the refuelling personnel. If the aircraft was stored in a hangar, it is transported to the helipad and the pilot's work begins. The actions described here are generally performed by the copilot but - as requirement Ct-cons-03 dictates 1 or 2 crew members - the term 'pilot' is used here.

First, the pilot restocks the galley if needed. This is normal in business aviation, where the copilot is generally also the cabin attendant. Second, the pilot is responsible for checking the cockpit. This includes:

- Batteries, needed to power the aircraft's systems when grounded before the Auxiliary Power Unit (APU) is started.
- Multi-purpose Control Display Unit (MCDU), including the Flight Management Computer (FMC), which is needed for navigational purposes.
- Flight Controls, including the aircraft primary controls such as control yoke (roll and pitch), rudder pedals (yaw) and throttle (thrust).
- Avionics, including the communication equipment and navigation equipment (VOR, GPS, NDB).

If any issues are found within the cockpit, the defect is reported to the OC, which will dispatch a mechanic. Next, the pilot is responsible for checking the exterior of the aircraft. This entails the following steps:

- Checking for damages by performing a walk around. The pilot checks for large visible damages on the wings, engines, landing gear and the fuselage. If the case arises that the pilot finds a damaged part, he will inform the OC and a mechanic will be sent to inspect.

- After inspection by the mechanic, the pilot and maintenance crew decide together whether the specific part should be replaced or fixed or if it can be scheduled for later maintenance.

9.1.2. AIRBORNE OPERATION PHASE

Airborne operation phase involves airborne of the aircraft and their logistic support for execution of operational mission. The airborne operation is basically the mission profile of the InVADe aircraft as described in the Midterm report [29]. During each mission phase the pilot keeps contact with Air Traffic Control (ATC). ATC directs the aircraft through the airspace and warns the pilot of other aircraft in the vicinity. It also gives the pilot clearance to take-off or land the aircraft.

9.2. MANUFACTURING

A well-developed manufacturing structure is essential for aircraft production. The infrastructure should provide access to research and development facilities as well as equipment and advanced manufacturing facilities. The manufacturing location should have access to an adequate transportation infrastructure. Aircraft manufacturing is defined as the integration of materials, components and systems of other manufacturers with the subsystems within the aircraft itself. The mechanical structure, that is the total package of the system is developed by the manufacturer, contains the choices made with respect to the design, materials and production technologies [11]. In this section the main focus lies on the manufacturing process of the wing boxes of InVADe. The more general parts of InVADe are comparable with conventional aircraft and will therefore not be discussed in this report. Finally, the Lean Manufacturing process will be described.

9.2.1. WING BOXES

The manufacturing of the wing boxes is divided into two main topics, namely sheet forming and joining methods. To define a joining method that will be used for the wing boxes, some analysis is done on the effects of several methods on the aircraft weight, maintainability and sustainability as is elaborated in Chapter 11.

SHEET FORMING

Forming, a process that starts off with typical half-fabricates like sheet and plate metals, transforms the half-fabricate into a part that can be used for the product. The aluminium sheet, the half-fabricate, will have a small thickness in order to be formed into a stringer, spar or web. Single curved parts with a small bend radius, including stringers, are manufactured by the use of rubber forming. Rubber forming can be done with a moderate accuracy and keeps at least one side of the part without surface damage. Another advantage is the low cost operation, the rubber forming press is a universal tool which can be used for forming of several aircraft parts. Although, the cycle time is quite long and the press force needed is very high, this type of forming is preferred for manufacturing of stringers and spars of the wing box.

RIVETING

Riveting, a concept based on transferring loads through the use of loaded pins, is a common used joining method in aerospace industry. This concept is reliable due to the widespread use and extensive documentation. Next to that, these joints can be easily inspected and repaired. However, rivet joints are fatigue sensitive. Stress-concentrations can start fatigue cracks near the rives holes. Due to the fact that rivets cause small undulations of the surface, this riveted surface won't be totally smooth. Regarding sustainability, this method will be preferred over adhesive bonding, since a rivet can be recycled as a whole, where adhesive bonding cannot. To join the stringers to the webs of the wing box, solid rivets are used. The technique is based on plastic deformation of the rivet shaft. Having the holes drilled and aligned, the rivet is placed and the protruding tail end is deformed into manufactured rivet head. This deformation then results in the expansion of the shaft in the rivet hole.

BOLTING

Another principle which uses pin-loaded joints is known as bolting. This method will be used to join the web spars of the wing box with the vertical webs of the wing box. Reason for this choice is based on the fact that this region in the wing box, is set to be fatigue sensitive. Therefore this part should be easily accessible and replaced when needed. The use of bolts is more expensive than rivets, but they can be loaded in shear and tension.

9.2.2. LEAN MANUFACTURING

Lean Manufacturing, a way of thinking and acting, should focus on increasing the customer value all the time. The ultimate goal is to provide perfect value to the customer, having generated zero waste. But Lean Manufacturing is not only a manufacturing based philosophy, but a organisation based philosophy. Eliminating waste along entire value streams, results in less human effort, less space, less capital and less time to make products [76]. To be able to eliminate waste, the lean system needs to be knowledge-driven. Having good knowledge of the entire production process will result in recognition of waste. Waste is all that used resources, but does not contribute to the value of the product.

In a production process, different forms of waste can be identified. These forms are: overproduction, waiting time, work in progress (WIP), processing waste, transportation, movement, rework and underutilising people.

VALUE IDENTIFICATION
Value is defined as the way various stakeholders find worth, utility, benefit or reward in exchange for their respective contribution to the enterprise. The stakeholders, defined in this project as the buying customers and business partners, have set their requirements as described in Section 2.1.

VALUE PROPOSITION
Having defined the requirements, a plan for to create value according to these requirements can be developed. Based on these values, value streams can be generated. In this way people can contribute their resources to the value stream in order to create value. As part of the value proposition, a compliance matrix has been set up. This is done to show the the needs are met, in order to create confidence and commitment of the stakeholders. This compliance matrix can be found in Chapter 12.

VALUE DELIVERY
Value delivery is defined as adding value at every step of this value stream and delivering it to the stakeholders [11]. At this point, the value is delivered to both the stakeholders within the value stream and stakeholders that will use the product.

JUST-IN-TIME
Just-In-Time (JIT) is a system for producing and delivering the right items, at the right time and in the right amounts [11]. As InVADe is a design who's needs are analysed in the market analysis in Section 10.4 the production of this aircraft will be limited. Since this product is new in the business market, it is decided that the production of this aircraft connects best to the JIT principle. This means having no big stocks, but producing the parts that are needed just in time. This reduces cost and therefore waste. This decision is based on reference aircraft production lines such as Airbus [116] and Boeing [107].

9.3. ASSEMBLY AND INTEGRATION PLAN
In order to increase the production efficiency, line assembly of the aircraft is used. In the first stages of the assembly line, small subsystems are build. Then, outsourced parts like engines and avionics are ordered. By outsourcing parts of the process, the focus on core competencies increases. With this, a risk in controllability of the supply chain arises. Small assemblies are started to build the wings, tail, flight deck and interior cabin. Finally, the major components of the aircraft are assembled in the last stage of the assembly line.

9.3.1. PRODUCTION INTEGRATION PLAN
The InVADe production integration plan includes both the production and assembly processes. Parallel manufacturing will be performed in order to reduce the production time. Outsourced parts will be ordered from specific companies and will be added in the assembly at a later stage in order to minimise the risks of damaging such components. Generally, the production process takes place within the Netherlands in order to stimulate the Dutch economy. A flow diagram describing the assembly line can be found in Figure 9.1.

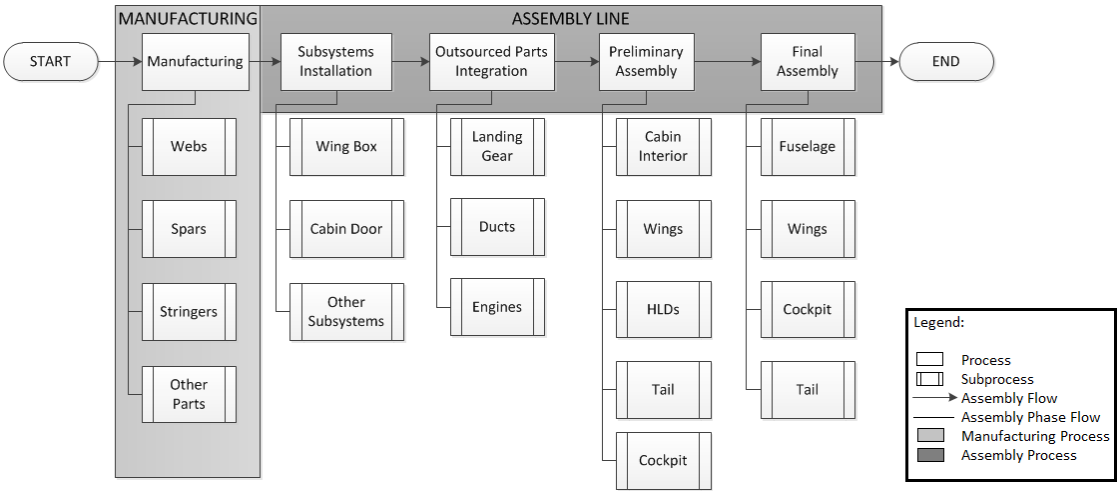

Figure 9.1: Assembly line InVADe

9.3.2. PRODUCTION FACILITY LOCATION
The location of the production facility has a large influence on direct labour and manufacturing overhead costs and therefore on the unit cost as well. A couple of reasons will be presented.

Transportation costs and available infrastructure Ideally the location of the facility would be in the centre of the market of the InVADe aircraft, which is primarily Europe and North America, as was concluded in the Market Analysis in Section 10.4. Minimising local motion is not only beneficial for the overhead costs, but for the environment as well. Of course the infrastructure around the facility should support the transportation of the necessary people, materials and products. Further, raw materials should be easily available.

Government regulations and labour skill The amount of rules that needs to be obeyed and the amount of taxes that needs to be paid influences again the manufacturing overhead costs. Therefore, placing the facility in a country with low taxes and a minimum amount of regulations is beneficial for the unit costs of the InVADe aircraft. Further, the direct labour costs is important. However, the employees should have enough skills to manufacture the aircraft.

The location of the production facility will be in Europe or in North America. Overall, these regions do not lack in infrastructure. When looking at the taxes, Turkey has the lowest [124]. But, according to Accenture [109], Turkey is lacking in skilled labour. However, Turkish companies are participating in the production of the F35 [79], thus they must be skilled. Switzerland, the US and Canada are other interesting locations, for their low corporate taxes as well. On the other hand the wages, especially in Switzerland are high comparable to the wages in Turkey [104]. The numbers are presented in Table 9.3.2. All mentioned countries are possible locations of the factory. Turkey has the lowest taxes and the wages, but more research is necessary regarding the labour skill. When the labour skill is at an acceptable level, Turkey seems the most promising location for the production facility.

Country	Corporate Taxes [%]	Wages [$]
Turkey	25	3,123
Switzerland	29	6,323
The United States	27	4,980
Canada	32	4,792

Table 9.1: Wages and Taxes of possible factory locations

9.4. RISK ASSESSMENT

Throughout the next phase of the development and also throughout its operational lifetime, InVADe will be exposed to a number of development risks and operational risks. These risks are described in this section and possible mitigation methods are introduced to decrease the effects and the severity of these risks.

9.4.1. DEVELOPMENT RISKS

During the further development several aspects need special attention. To discover which issues need more resources in the next phase of the design development, risks are identified and visualised in a risk matrix. Table 9.2 shows the identified development risks divided in 5 categories. First the general development risks are defined, and then an assessment of department specific development risks is made.
Having introduced the risks above, next they are placed in a development risk matrix. Figure 9.2 visualises the severity and probability of occurrence.

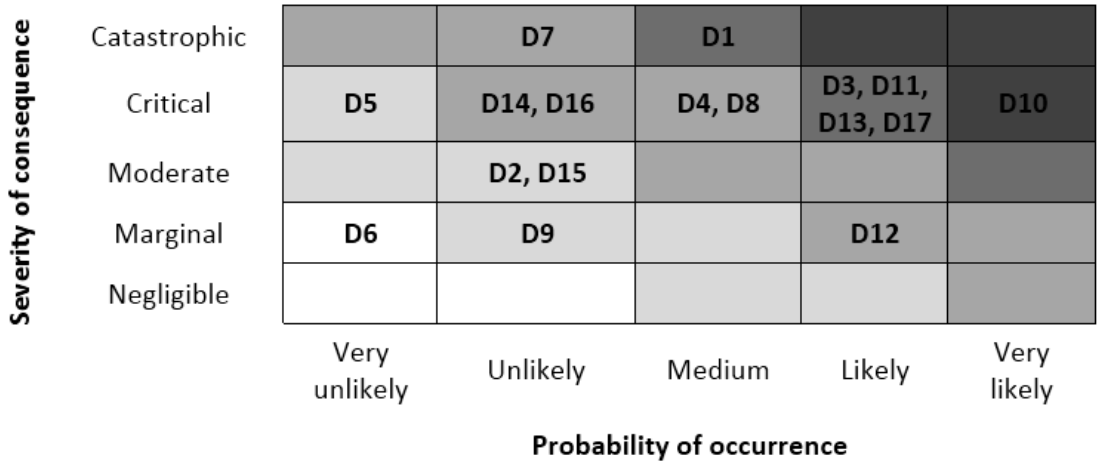

Figure 9.2: Development risks visualised in the risk matrix

Table 9.2: Further development risks

	Risk Number	Risk
General development risks	D1	Issues with CS-23 certification
	D2	Overrun of the unit cost
	D3	Overrun of the production schedule
	D4	Overrun of the development budget
	D5	New market insights
	D6	Range requirement failure
	D7	Safety issues
	D8	New insight into the characteristics & performance parameters
	D9	Geopolitical issues
Aerodynamics	D10	Lift loss due to opening of the shutter mechanism
	D11	Flow issues due to interaction of components
Structures	D12	Simplifications made are no longer applicable
	D13	New insight into the weight estimation
Propulsion	D14	Noise limits exceeded
	D15	Overrun on the emission requirements
	D16	Failure of the 155 kW power increase per engine by 2025
Stability & Control	D17	New insight into Stability & Control behaviour during hover/transition

As can be seen in the risk matrix in Figure 9.2, six of the identified development risks are in the high risk region. This means that during the further development of InVADe more resources will be required to deeper investigate and mitigate the possible consequences of these risks. For this reason, below a more detailed description of these risks is given, with an elaboration on their nature of occurrence and their consequences.

D1 - Issues with CS-23 certification
The InVADe design set out to be certified within the CS-23 regulations. If for some reason InVADe can not be certified the consequences will be catastrophic since it will not be allowed to fly. More resources will have to be applied to investigate the CS-23 regulations and make sure that the InVADe is designed in compliance with the CS-23 requirements.

D3 - Overrun of the production schedule
If at any point during the development of InVADe significant delays are introduced, it will be very difficult to reach the 2030 deadline with no extra countermeasures implemented. These delays can result in postponing the delivery of the aircraft. This way not only more costs are introduced into the production and possibly the final unit cost, but also resulting in unsatisfied customers and stakeholders. Due to the more complexity and novelty of the current design, the likelihood of this risk is set higher compared to other conventional commercial aircraft. The consequence is set as critical since various parties will influence negatively of a production delay.

D10 - Lift loss due to opening of the shutter mechanism
Up until now, the aerodynamics department has taken into account a factor for the loss of lift due to the shutter mechanism. As discussed in Section 4.2.3, this factor accounts for the disturbed airflow during the opening of the shutter mechanism. However, to make sure that this factor is correct and enough lift is generated during transition, more advanced computing techniques like Computational Fluid Dynamics (CFD) should be used. Also wind tunnel testing could help with a better understanding of the phenomenon around the main duct shutter mechanism during transition.

D11 - Flow issues due to interaction of components
From the layout of the current design, flow disturbance may take place due to the interaction of the canard, the front ducts and the main wing; to avoid the interaction of these surfaces, further research has to be done examining the direction of the flow. Wind-tunnel tests can help determine if the current design raises any concerns regarding the clean air flow. Due to the need for this further study, the likelihood is set at likely. Since the behaviour of the airflow is uncertain as this stage the consequence is set to critical.

D13 - New insight into the weight estimation
Advancing to more complex weight estimation techniques using Finite Element Methods (FEM), a more precise component weight can be determined. As a result, the Class II weight estimation needs to be updated which will affect all the other departments. Since this advanced weight estimation is likely to add weight to various components a probability of likely is assigned.The consequence is set as critical since especially Propulsion and Aerodynamics will have to revise all calculations and sizing.

D17 - New insight into Stability & Control behaviour during hover/transition
At this moment the canard is sized and the wing positioned to achieve adequate stability and control during flight. Transition and hover however are still complicated phases within the flight. First calculations show that stability and controllability can be guaranteed in this phases. With new insights into these phases it might be possible that extra controllers need to be added to make InVADe stable and controllable. Since hover and transition are complex dynamic phases it is likely that new insight will occur during further development. These new insights can be critical as new control computers need to be added to ensure the stability and controllability of InVADe.

9.4.2. OPERATIONAL RISKS

Having defined and ranked the risks in further development of the InVADe aircraft, in this section a number of operational risks which are specific to the current design will be discussed. This list is made specific only to this design and thus does not include common operational risks such as communication failure, fuselage decompression, fire and ground collision, which are considered of the same importance and consequence as commercial aircraft. The InVADe-related operational risks are shown in Table 9.3.

Table 9.3: Operational risks

Risk Number	Risk
O1	Lightning strike
O2	Fatigue
O3	Tilting mechanism failure
O4	Fan failure
O5	Electrical system failure
O6	Generator failure
O7	Control system failure

The operational risks O1 to O7 are mapped into the operational risk matrix, shown in Figure 9.3:

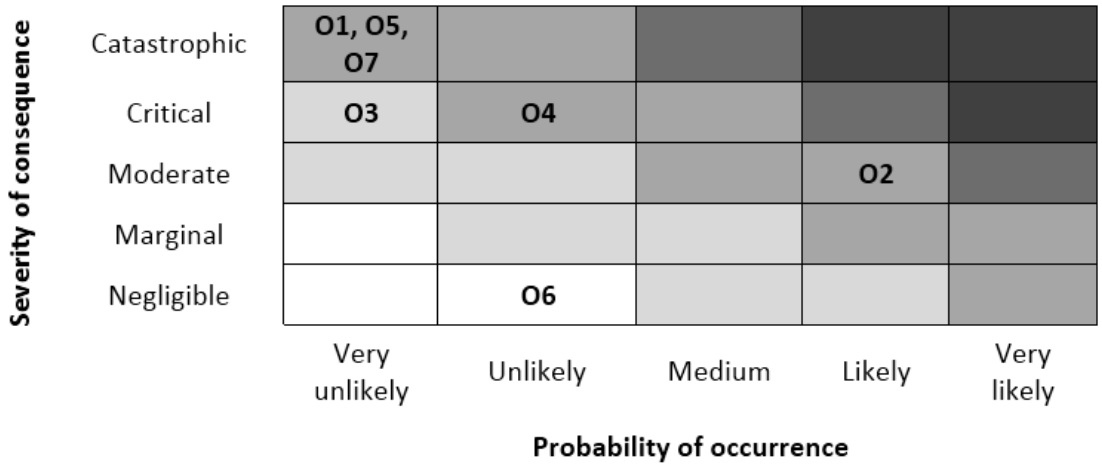

Figure 9.3: Operational risks visualised in the operational risk matrix

O1 - Lightning strike
What makes this design more vulnerable to lightning is the fact that during take-off, landing and transition the ducts will be facing upwards and the electrical motor at the duct will be vulnerable to direct hits by the lightning strike, thus showing a high risk of electrical failure within the aircraft. This results would be catastrophic for this risk. Methods to shield the ducts and the aircraft itself during flight will need further investigation to reduce the consequences of this risk.

O2 - Fatigue
Due to the nature of the InVADe design, fatigue should be considered as an important phenomena. To account for this, the structure department already implemented various measures to reduce the influence of fatigue. Vibrations however remain an issue which need further investigation to make sure the occurrence of this event is limited.

O3 - Tilting mechanism failure
The failure of the tilting mechanism can cause critical conditions for the aircraft during its flight. However, In-

VADe is designed to minimise the likelihood of occurrence of this malfunction. If failure occurs during cruise, InVADe can continue its flight and perform a conventional landing. If the failure occurs during transition, control of the aircraft will become harder and thus lead to a critical consequence for this failure risk.

O4 - Fan failure
Since in the design of the ducted fan, the fan blades are directly in contact with the open air, bird strike or lightning strike can directly hit the blades. Also mechanical failure could cause malfunctioning of the fan. InVADe is designed such that it can continue its flight with one inoperative engine, thus defined as a moderate risk on the risk matrix. The aircraft will have the chance to terminate its flight with 3 remaining engines, however continuation of the flight to the original destination should not be performed.

O5 - Electrical system failure
Even though InVADe will be designed such that the likelihood of failure in the electrical system should be very unlikely, the need for a redundant system is strongly felt. This is mainly because of the nature of this failure, which if occurred, would result in a catastrophic condition in which the aircraft components will not acquire the required electrical power to function properly.

O6 - Generator failure
Since four generators are present in InVADe the severity of one generator failure is negligible. The aircraft will still be able to continue its flight. Since four generators are present the probability of occurs is set to unlikely.

O7 - Control system failure
Although the probability of occurrence of a complete control system failure is very unlikely, the consequences can be catastrophic. Especially during hover and transition InVADe is more vulnerable because of the complex control system needed to make control and stability possible.

9.5. RELIABILITY, AVAILABILITY, MAINTAINABILITY AND SAFETY

In this section, the reliability, availability, maintainability, and safety (RAMS) characteristics of InVADe will be evaluated. First, a definition is given about each pillar of the RAMS method, followed by an analysis of the concept for each of these pillars.

9.5.1. RELIABILITY

Reliability is defined as the probability that a system will perform in a satisfactory manner for a given period of time when used under specific operating conditions. Since some of the concepts incorporated in InVADE are absolutely critical, reliability will be an important parameter to take into account. Especially if complex new technologies are introduced, the pre-set level of reliability will be more difficult to reach than with a conventional aircraft. In general, a design using complex new technologies will decrease the reliability level, whereas a design with proven technology will increase it.

The reliability is defined as a natural logarithmic function of the failure rate (λ) and time (t). This relation is defined in Equation 9.1. The failure rate differs for specific subsystems within the aircraft itself and is defined to be the inverse of the Mean Time Between Failure (MTBF) as in Equation 9.2.

$$Reliabilty = e^{-\lambda t} \tag{9.1}$$

$$\begin{aligned} \lambda &= \tfrac{1}{MTBF} \\ \lambda_t &= \lambda_1, \lambda_2, \lambda_3, ..., \lambda_n \end{aligned} \tag{9.2}$$

Structurally, the reliability of InVADe will be high in comparison to reference aircraft. The wing box, spars and other structural elements have been designed such that the endurance limit is not exceeded during even the most extreme flight conditions. These conditions contain the maximum gust load and a safety factor of 0.5. An issue of concern are the high frequency which originate in the fan-in-wings. Although joints between its structure and the main load bearing structure damping is present, fatigue might occur due to the high number of load cycles.
Although an electric drive system has not been incorporated in an commercially available VTOL business jet, it does offer advantages over a mechanical system. Fatigue and wear are decreased to a minimum by eliminating the need for driveshafts and gearboxes. Rosero [98] and Elhafez [31] indicate that electrical actuation can be considered reliable. Since AC electric engines are used, no moving parts other than the coil are present. The absence of other moving parts increased the reliability in comparison to DC electric engines.
The operational evaluation (OPEVAL) of the V-22 Osprey shows important design points, which are likely to faced during the development of InVADe:

1. Proprotor System

2. Flight Controls
3. Flight Control Computers
4. Drive System

9.5.2. AVAILABILITY

Availability is defined as the probability that a system will be ready or available when required for use. In order to quantify the availability, one must define which activities and phases cause the system to be unavailable. Following that, an assessment can be made on whether these activities cause the downtime to be in excess of the proposed limits.

The availability is described as a fraction of the MTBF and the Mean Time To Repair (MTTR). This relation is set in Equation 9.3.

$$Availability = \frac{MTBF}{MTBF + MTTR} \tag{9.3}$$

InVADe will be considered unavailable if the aircraft is not ready to perform a certain mission when it is required. Events and restrictions which can lead to the aircraft being unavailable include, for example, system failure, maintenance, unacceptable flight conditions, noise restrictions, and unavailability of crew.

System failure will inherently lead to unavailability of the aircraft. Depending on the severity of the failure and the level of maintainability, the aircraft can be repaired within an acceptable time frame.

Obviously, inadequate fuel facilities will ground the VTOL business jet, hence reducing the availability. During a typical mission InVADe will often serve to central business districts equipped with helipads, where competent fuelling facilities might not always be available.

Maintenance is essential to the safety and reliability of any given aircraft, or any system for that matter. Throughout the lifetime of the aircraft, maintenance will reduce the availability. Since the average customer is likely to use the business jet for short-range trips on a regular basis, longer periods of inactivity are not acceptable and hence the MTTR should be brought back to a minimum.

Unacceptable flight conditions are comprised of bad weather conditions, legal orders restricting flight, and other flight restrictions. Unavailability due to bad weather conditions can be avoided by making the flight envelope of the VTOL aircraft as large as possible. The flight envelope shown in Figure 8.2 indicates under which conditions the aircraft can be flown. Although not examined in this report, flight conditions during which hover can be performed are expected to be critical. More research on this matter is required to determine under which conditions InVADe can safely perform VTOL manoeuvres.

Special attention must be paid to the noise restrictions. A VTOL business jet is most likely to operate services in between central business districts, often areas where strict noise restrictions are in place. If noise restrictions of less than 80.7 dB at 100 m distance are in place, InVADe will not be able to operate.

Unless a crew is on constant standby, the aircraft might not always be able to perform any given mission. Nonetheless, this constraint is fully dedicated to the operation side of the aircraft, not to the engineering and design side of the project.

Active clients within the business jet market require a high availability of the products they buy. A typical customer will plan the usage of the jet on short notice and hence low availability will be unacceptable. Therefore, the system should have a high level of reliability. If these levels can not be reached, the product is unable to satisfy the customer's needs.

9.5.3. MAINTAINABILITY

Maintainability is a design parameter intended to reduce repair time, as opposed to maintenance, which is the act of repairing or servicing an item or equipment. Maintainability can be defined as the probability that a failed item or piece of equipment will be restored to an acceptable working condition within an acceptable period of time. In general, a more complex system will lower its maintainability. This section will outline possible hazards regarding the maintainability, which can be ran into whilst InVADe will be in operation.

The maintainability is defined as a natural logarithmic function of the repair rate (μ) and time (t). This relation is given in Equation 9.4 below. The repair rate itself, is defined as an inverse function of the mean time till repair (MTTR) as can be found in Equation 9.5.

$$Maintainability = 1 - e^{-\mu_t} \tag{9.4}$$

$$\mu_t = \frac{1}{MTTR} \tag{9.5}$$

The U.S. Department of Defense released a document [23] in 2001 describing the flaws and inaccuracies of the maintainability of the V22 Osprey. In this report, several recommendations are made within this domain. A critical part of any VTOL aircraft is the nacelles. The V22 is designed such that the two nacelles are positioned on the wing tip. The nacelles were made as compact as was technically possible, to ensure the drag component of the nacelles was kept to a minimum. This approach resulted in nacelles with a low maintainability.

During the development of InVADe a similar problem can be expected. Many components related to propulsive systems are purposely kept as compact as possible to reduce the overall drag coefficient of the aircraft. Examples of this include the tilt mechanism between the front duct and the implementation of the lift fans in the main wings. Due to the limited space available in the wing, systems such as the fuel tanks and HLD actuator devices are positioned such that the space within a wing is used optimally. For these reasons the maintainability of InVADe is expected to be low in comparison to conventional business aircraft.

The document by the U.S. Department of Defense [23] provides the reader with the following recommendations on the maintainability:

- *More quick-access panels*
- *High-reliability alternatives to the Mini Mark fastener*
- *User-friendly inspection access for critical parts and other exceptions to the flight control system redundancy design requirement*
- *Shortening of the hydraulic lines between switching valves and swash plate actuators*

As these recommendations point out, the nacelle of the V-22 was adequate while functioning, but did not have an acceptable level of maintainability. From the V-22 Osprey program it can be learnt that the engines compartments are going to be a critical issue within the domain of maintainability.

In addition to the fact that the compactness will be an issue, it is expected that the structural integrity of the main structure will be a point of concern with regards to the maintainability. There is a high probability that the design will be compact, resulting in a poor accessibility of major structural components. Examples of this include the bearings in the tilt mechanism. As the mechanism will be subjected to different loads throughout the entire flight cycle. Unless the entire mechanism is disassembled, the bearings can be accessed.

Poor maintainability might arise from the fact that InVADe will be on of the first commercially available VTOL business jets. Regular business jets have been around since the 1950's and have been trialled and tested. Furthermore, maintenance for these jets has evolved into a full-scale industry, with companies like Jet Aviation and TAG aviation offering specific maintenance services. Since the aircraft will most likely incorporate new technologies, maintenance providers will likely struggle to provide their services. Concluding, the maintainability of the VTOL business aircraft will be low.

9.5.4. SAFETY

Safety is the freedom from hazards to human and equipment. The VTOL capability of the aircraft introduces more risks since to achieve this capability, the system has become more complicated than a regular aeroplane.
Engine failure during take-off or landing in a tilt rotor configuration, a certain redundancy is needed such that both rotors remain powered. If an engine stops working, the aircraft can tip over as was the case during an accident with the Bell XV-15 in 1992. InVADe employs a set of batteries which have enough capacity to power the electric engines for two minutes during take-off or landing.
The report of the V-22 Osprey program [23] reflects on the safety of the V22 using accidents from the past. The most important safety risks are summarised in the list below:

1. Failure of automatic flight control system during transition could cause loss of control.
2. Loss of transition capability.
3. Bad signal to the flight control system could cause improper flight control response and loss of control.

4. Failure of the gearbox could lead to the loss of an engine resulting in loss of control.

One can see most safety risks are related to the transition phase. During the transition phase of InVADe is the shutter mechanism is critical system. If the mechanism were to fail during transition the balance of the aircraft will be disturbed, with catastrophic consequences. For a variety of reasons the shutter mechanism could jam after the cruise flight is completed. Although transition is impossible under those conditions, a conventional landing can still be performed.
Failure of the fans is another safety risk that must be examined in more detail. Due to the distribution of the loads and the location of the center of gravity, the aircraft will remain its stability in the case of a front duct failure. However, an unstable situation will occur if one of the back ducts fails. At this stage the exact geometry and actuators of the mechanism have not been defined yet. Therefore, no specific mitigation manners can be given at the time of writing.

Another risk which is not related to mechanical failure is electromagnetic interference. As the engines consume more power than any reference out there, electromagnetic interference might disturb the functionalities of the avionics equipment. In turn, this will negatively influence the flight characteristics of the aircraft. The severity of this issue is still unknown and more research should be conducted on the matter.
In summary, because the aircraft has VTOL capability, complex systems are added to the design which, if not engineered thoroughly, can cause additional safety issues. Regardless of which concept is chosen for the VTOL aircraft, the transition phase will safety-wise remain a difficult phase, if not the most difficult part.

9.6. SENSITIVITY ANALYSIS

This section will describe a general sensitivity analysis for InVADe. In the Mid-Term Report [29] a sensitivity analysis was performed for the trade-off results. This section will give a more general approach and discuss three points which had a major influence on InVADe. The three points were selected for their leading role in the design and their sensitivity within the design process.

9.6.1. WEIGHT

The MTOW of the aircraft is an input for every calculation performed within the departments. A small increase in the weight can lead to a chain of recalculations resulting the redesign of wing planform, canard size, engine power, and many other parts, which will, in turn, increase the weight of the aircraft once more, leading to another redesign and so on. Because of this instability, weight is selected as one of the main sensitivity pillars, meaning a change in this parameter will have substantial consequences for the entire design.

9.6.2. WING PLANFORM

Setting the wing area as a decision variable, the wing planform of the aircraft will be affected. As many aspects of aircraft design are subject to the snowball effect, the change of one parameter in the design phase will affect large parts of the design. Moreover, the optimal strategy should be to minimise the weight of InVADe without influencing the aircraft characteristics. Changing the wing area will affect the wing span and/or the wing's aspect ratio. Increasing the wing area slightly will increase the wingspan in order to keep the same slenderness ratio of the wing. Likewise, the control & stability of the aircraft will be affected. Increasing the wing area results in a larger moment contribution in the moment equation. With respect to the structures side of the design, a larger wing area will lead to a heavier structure, resulting in a larger aircraft weight. Because of this increase in weight, the aircraft will need more thrust to be able to generate enough lift during flight, which requires a more powerful engine.

9.6.3. MAIN DUCT DIAMETER

A fairly large diameter for the main duct was required in order to keep the noise levels as low as possible. A decrease in duct diameter will lead to a lighter and thinner wing and better aerodynamic characteristics. Then, a more conventional airfoil can be chosen. From that, a less disturbed airflow will occur near the wing and therefore the wing will generate more lift. Thus, the wing area of the main wing can be decreased, having a positive influence on the weight as well. If weight is decreased, the same process as in the section above will be started, affecting all other departments, like structures, control & stability, propulsion, and performance. However, a decrease in duct diameter would pay a huge toll in increasing noise emissions. On the other hand, if the ducts were increased, there would be a reduction in noise emissions, but would also cause major problems for the other departments, which would result in a much heavier design.

10

COST AND MARKET ANALYSIS

This chapter details the cost estimation and market outlook for InVADe. This was done after all design parameters were fixed and is thus the last major set of variables that were determined. First the unit cost estimation will be presented. The results from that are used to determine the sales price and calculate the return on investment. Next the operating costs are calculated. Finally a market outlook is presented in Section 10.4.

10.1. UNIT COST

The methods used in the mid-term report [29] to calculate unit and operating cost were mainly based on large passenger aircraft and thus gave a decent approximation, but a more accurate method was later needed. For the cost estimate of the more detailed, final design the Eastlake method was used. This method is presented by Gudmundsson [49] and is specifically developed for small business aircraft. Compared to the earlier used methods this method uses more inputs that are specific to the design which should increase the accuracy. Additionally the numbers are very recent (2012).

Gudmundsson's unit cost estimate method is based on the DAPCA IV methodology, just like the method from Raymer [96], however it is strongly modified and updated. A detailed breakdown of the different costs that make up the unit cost is shown in Appendix A.6. An useful feature of this method is that it takes into account the regulations under which the aircraft will be certified (part 23 or 25), especially since the InVADe design is close to the maximum take off weight for CS 23 (8,618 kg [35]) this is an interesting feature.

The most important inputs are the number of aircraft that are expected to be sold, maximum speed and the airframe weight of each aircraft. Additionally aircraft characteristics like tapered / untapered wing, pressurised / unpressurised fuselage, retractable / fixed landing gear, the percentage of composite parts, the type of flaps and engine horsepower are used as inputs. For parts that are bought in large amounts from suppliers, such as avionics, engines and in our case also electrical components, a quantity discount factor (QDF) is implemented which reduces the cost of these parts.

Based on a quoted price from Enstroj [33], the purchase price for the electric motors is estimated as 116,000 EUR per aircraft. Assuming the same price for the generators, 6,300 EUR for batteries [48] and 2,000 EUR for cabling the electric propulsion components add up to 240,300 EUR per aircraft without the QDF. Cost for designing, implementing and testing the electric system are already accounted for in the engineering cost.

The added complexity of the tilting and shutter mechanism and flight controls is accounted for by the higher airframe weight, nevertheless an extra 10% is added to the engineering hours. Flight testing costs are also increased by 20% and three flight test aircraft are assumed to account for extra VTOL and transition testing. A CPI inflation factor [17] of 1.01 is used to convert from 2012 to 2013 currency and a factor of 0.74 converts the price from USD to EUR.

The result is a unit cost of 6.55 million EUR. 1.813 million of that are sunk costs (such as research and development, tooling, testing and certification) and 4.736 million are marginal cost (manufacturing, materials, quality control, engines, electric propulsion system and avionics). The cost of the different elements of the cost breakdown structure and bought parts are presented in Table 10.1.

Table 10.1: Break-down of the unit cost per aircraft

Cost Element	Cost [EUR]
Engineering	1,165,994
Development Support	107,916
Tooling	494,117
Flight Testing	45,697
Manufacturing	2,354,204
Quality Control	313,109
Material	1,024,722
Avionics (incl. QDF)	42,048
Engines (incl. QDF)	844,482
Fans (incl. QDF)	5936
Electric Propulsion (incl. QDF)	151,714
Total	6,549,943

The certification basis (CS 23 or CS 25) makes a significant difference in the unit cost estimate. Using CS 25 instead of CS 23 increases the unit cost by 10.8% (7.256 million EUR). This shows that it is important to keep the MTOW below 8,618 kg during the design process, to confirm to CS 23 requirements [35] and avoid significant cost overrun.

The unit cost reduces further when the number of sold aircraft increases, but it also increases if the number of sold aircraft is lower than expected. If more aircraft are sold parts can be bought cheaper in bulk and the engineering, testing, tooling and certification costs can be spread over more aircraft. A graph showing the effect of this on the InVADe unit cost is shown in Figure 10.1.

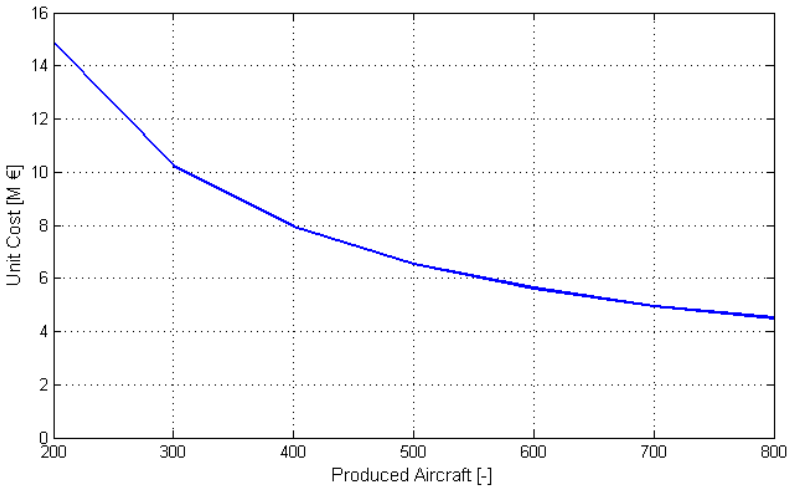

Figure 10.1: Unit cost depending on number of produced aircraft

10.2. SALES PRICE AND RETURN ON INVESTMENT

After considering the prices of business jets and helicopters and the unit cost the sales price is set at 10 million EUR, for more detail see the baseline report [28]. This corresponds to a 52% mark up of the unit cost price. This value is relatively high compared to conventional aircraft programs according to Irwin and Pavcnik [62] and Lanier Benkard [75]. However, for a complicated and innovative project like this the likelihood of an increase in development cost (and therefore an increase in unit cost) is significant. In case the unit cost increases too much the sales price will have to be adjusted accordingly.

With the variable and fixed unit cost and the sales price known the profit can be calculated. These numbers can be used to further calculate the profit margin, the multiple (the ratio of total profit over total investment), the break even point (Equation 10.1 [49]) and the yearly return on investment (RoI). The results are shown in Table 10.2.

$$N_{BE} = \frac{total\ fixed\ cost}{unit\ sales\ price - unit\ variable\ cost} \tag{10.1}$$

Table 10.2: Investment metrics for InVADe

Total development cost	906,863,000	EUR
Unit production cost	4,736,000	EUR
Unit cost	6,550,000	EUR
Unit price	10,000,000	EUR
Total profit	1,725,028,000	EUR
Mark-up	52.0	%
Profit margin	34.5	%
Multiple	1.90	-
Break even point	172	Aircraft
Yearly ROI	9.51	%

10.3. OPERATING COST

The Gudmundsson [49] operating cost method for business aircraft is different from the method for general aviation in that it accounts for better maintenance and professional crew cost.

The most important inputs are flight hours per year (assumed to be 750), the relation of maintenance to flight hours depending on the level of complexity of several subsystems), fuel flow, number of engines and crew and of course prices and salaries of fuel and personal. The method includes the cost for maintenance, storage, fuel, insurance, engine overhaul and crew. Additionally depreciation was added to these costs since this makes up a significant part of the total operating cost and makes it easier to compare the operating cost to civil flights. Another alteration that was made is a 30% increase in airframe maintenance cost due to the complexity of the VTOL specific subsystems such as the tilting and shutter mechanisms. At the end a CPI inflation factor [17] of 1.01 is used to convert from 2012 to 2013 currency and a factor of 0.74 converts the price from USD to EUR.

The result is a cost of 920 EUR per flight hour excluding depreciation and 1,374 EUR per hour including depreciation, which means that the operating cost requirement is met. A break down of the Operating cost can be found in Table 10.3.

Table 10.3: Operating cost contributions

Cost Element	**Cost [EUR/hr]**
Maintenance	216
Storage	12
Fuel	254
Insurance	203
Engine Overhaul	11
Crew	224
Depreciation	455
Total	1,374

Prices for short range business class tickets from Amsterdam with KLM to less popular destinations are estimated to be 389 EUR per flight hour per passenger per January 2014 (see Table 10.4). Based on this price the InVADe aircraft can be operated for a lower price per passenger than regular business class tickets as soon as it carries four passengers or more. Additionally since direct transport using InVADe saves time compared to public air traffic and $time = money$ [43] InVADe can save a company oodles of shillings.

Table 10.4: Destinations and price per passenger per flight hour

Destination	**Price [EUR/pax/hr]**
Bremen	389
Stavanger	370
Oslo	330
Hannover	433
Birmingham	395
Geneva	356
Leeds	456
Gothenburg	384
Average	389

10.4. MARKET OUTLOOK

This section elaborates on the market analysis of a VTOL business aircraft. Its main aim is to establish the competitive cost for the product and the volume for the market. In this analysis, two existing markets will be evaluated, namely the market for medium business jets and the market for corporate helicopters. This evaluation includes predictions for these markets, establishment of a new market for VTOL business aircraft, and, lastly, foreseen market share.

10.4.1. EXISTING MARKETS & FORECASTING

The VTOL business aircraft will be designed to seat 10 people, with a range and speed much higher than that of a helicopter and probably lower than that of a business jet. It is clear that the market for a VTOL aircraft will grow out of the existing market for business jets and corporate helicopters of comparable sizes. In terms of these requirements, business turboprops seem rather comparable. However, mode of usage is important, as are direct and indirect costs associated with the aircraft.

A VTOL aircraft matching the given requirements is ideal for those customers who wish to transport a small group of people from an office building, for example, to another location as fast as possible. It may be slower than a traditional business jet but its VTOL capabilities remove the need to travel to an airport, often through heavy city traffic or by helicopter transfer. It is faster, flies further and most likely is quieter and less expensive to operate than the existing corporate helicopters. In the analysis below, the midway between business jets and corporate helicopters is chosen as the only potential market.

BUSINESS JETS

Teal group's Richard Aboulafia [105] predicts 13,879 business aircraft (including turboprop) sales in 2013-2022 worth 310.3 billion USD. Of this amount, 10,249 are traditional business jets worth 249.5 billion. Bombardier's 2013 market forecast [15] predicts worldwide sales of 24,000 business jets in 2013-2032 worth 650 billion USD, of which 18,500 units are light to medium jets worth 357 billion. Figure 10.2 illustrates the market growth over this timespan. These jets range from the 7 passenger Learjet 40 to the 19 passenger Challenger 850, a range mostly equivalent to 'traditional jets' in Teal's forecast. According to FindTheBest [40] the Learjet costs around 8.1 million and the Challenger about 25.2 million. At both ends speed and range is considerably higher than for InVADe, though no VTOL capability is offered.

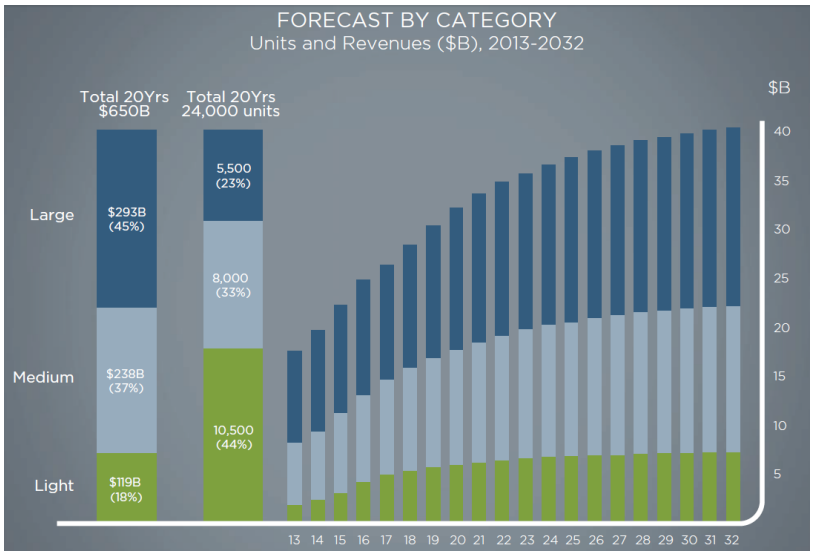

Figure 10.2: Bombardier's business jet market forecast for 2013-2032 [15]

CORPORATE HELICOPTERS

Honeywell states an expected market of 4900-5600 helicopters sales worldwide from 2013-2017, up from 4300 in the previous five-year-span [56]. 38% of these are corporate helicopters. No prediction in terms of market value is made. The Teal group [118] predicts 10,308 civil helicopter sales from 2013-2022. Assuming the division of corporate helicopters is the same, this number matches up well with Honeywell's estimate. The total value is estimated to be 60.3 billion USD, resulting in an average price of 5.85 million USD per helicopter. This is a relatively low price compared to business jets. A VTOL business aircraft would most likely be a bit more expensive; a reasonable trade-off for vastly improved speed and range, of course.

FORECAST RELIABILITY

Jets Bombardier's 2009 forecast [13] predicts 12,400 business jet sales from 2009-2028 or 620 average per year. Their 2013 forecast shows on average 550 sales per year from 2009-2012. Their forecasting is assumed to be accurate as constant sales per year is a gross simplification. The Teal group's 2009 outlook [2] states 9,300 business jet sales predicted from 2009-2018, which is comparatively high. For this reason Bombardier's estimate is leading in further analysis.

Helicopters Honeywell's 2008 outlook [55] predicted 4450 sales, fairly close to the 4300 realised. Their 2003 outlook [57] predicted 2600, where their 2008 outlook states 3000 sales realised. These numbers are close enough for predictions in this sector, especially when the 2008 economic crisis and its impact on sales is considered. No previous Teal group estimates were found for comparison, however the company is well-known for their aerospace analyses. The Honeywell estimate is leading in further analysis but the market value estimated by Teal is usable.

REGIONAL MARKETS

A division of Bombardier's expected deliveries over distinct regions is presented in Figure 10.3. This depicts the expected sales in the periods 2013-2022 and 2023-2032 for each region and for all sizes of business jets. The figures show that North America and Europe will still be the largest markets in 2032 and are also the largest in terms of absolute growth. For further design and marketing, the focus should still be on these markets. Fast growing markets such as India (153% over 20 years) will follow, and most likely no significant adaptation of the InVADe aircraft will be needed.

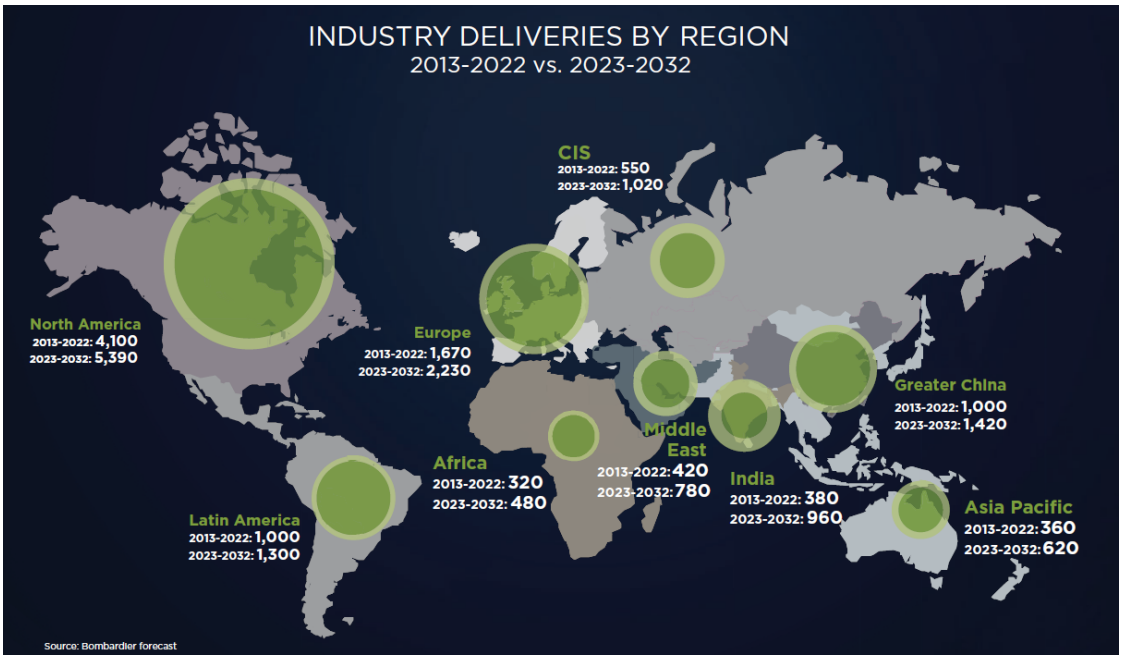

Figure 10.3: Bombardier's business jet market forecast for 2013-2032 [15]

10.4.2. BUSINESS VTOL MARKET

Bombardier's estimate of 18,500 aircraft worth 357 billion USD over 20 years is used for business jet prediction. Conservatively extrapolating Honeywell's forecast and Teal's value prediction, a helicopter market in the area of 8000 aircraft over 20 years is expected, with a total worth of some 47 billion USD.

Optimistically speaking, this means there is a potential market for some 26,500 VTOL business aircraft over the span of 20 years, worth more than 400 billion USD. The VTOL business aircraft is slated to be produced by 2030 - just before these estimates end. Thus, assuming that as always the market will keep growing, the actual potential market in the 2030-2049 period should be even larger. Averaging the price in the potential market and adjusting roughly for inflation, an average unit price of about 15 million USD follows. In that case, the sale of 500 aircraft over 20 years would lead to a market share of only 1.9%, a rather realistic slice of the cake.

At this moment no direct competition exists in the VTOL aircraft market itself. Existing VTOL aircraft are all built for military service, such as the Bell Boeing V-22 Osprey, the Harrier Jump Jet and the Lockheed Martin F35-B. The only comparable aircraft to nearly be on the market is AgustaWestland's AW609, of which they expect to sell 450 [60] for around 29 million USD. Expecting an expanding market, one might say that this shows 500 to be on the low end for the VTOL business aircraft. However, AgustaWestland had only 80 orders by 2010 [60] and they may

not reach 450 after all.

The sale price for an InVADe aircraft is 10 million USD, as explained in Section 10.2. This is somewhat higher than the average price of 5.85 million per helicopter, and low in the range of 8.1-25.2 million for jets in this outlook. The price chosen positions InVADe right in the middle, just as its performance does. The AW609's higher price may be explained by higher unit costs, but as the technology used in civilian VTOL applications will definitely mature by 2030, the cost for such aircraft is expected to decrease significantly. The client may consider aiming for a higher market share than 1.9%, in this case the unit price will also drop according to Figure 10.1.

10.4.3. ALTERNATIVE MARKETS

Other roles such as patrol aircraft, S&R and EMS were neglected for this market outlook. There is most likely a potential market for a successful civilian VTOL aircraft in these roles, but design for this is outside the scope of this DSE. The aircraft would need multiple design modifications to optimize it for each role. Several distinct possible markets are detailed below.

- **EMS**: Emergency Medical Services (EMS) roles are generally fulfilled by helicopters as they require VTOL capabilities. Possible missions include Search and Rescue (SAR) for coastguards and conventional EMS for hospitals. Honeywell [56] expects this usage to account for 19% of helicopter sales. EMS would require an extra door for stretcher access.
- **Oil&Gas**: The oil and gas sector makes extensive use of helicopters to transport personnel to and from oil rigs and ships. Honeywell expects this sector to account for 9% of civil helicopter sales. This is also the most profitable industry there is, and as $time = money$ (see Section 10.3), an industry that would gladly pay more for a faster VTOL aircraft. Practically no adaptation to the design should be needed for this sector.
- **VIP**: No figures are available as to the size of the VIP VTOL market, however this market overlaps largely with the corporate helicopter and business jet market and thus with the business VTOL market. The interior layout of the aircraft is usually adapted to the wishes of the owner in this sector.
- **Utility**: Possible utility role for law enforcement and military purposes. The AW-609 was also proposed for this role in its UV-609 variant [60]. Missions include border patrol, combat SAR, troop transport etc. Possible market size is unknown, however the military market is significantly larger than the civil market [118].
- **UAV ISR**: The Piaggio P.1HH Hammerhead [92] is a new Unmanned Aerial Vehicle (UAV) development for Intelligence, Surveillance and Reconnaissance (ISR) roles, developed from the P.180 Avanti. If this program succeeds, a UAV variant of InVADe may be considered. Its VTOL capabilities should provide a clear niche in the mid-size UAV market, though lower fuel efficiency than the P.180 may prove an issue.

11

SUSTAINABLE DEVELOPMENT STRATEGY

This chapter explains the principles behind Sustainable Development and how they were applied to the InVADe design. The World Commission on Environment and Development (WCED) defines Sustainable Development as development that meets the needs of the present without compromising the ability of future generations to meet their own needs [125].

The three main phases that can be identified in the design and production of a new aircraft are: production, operation, and end-of-life (EOL). Production as a phase is related to all possible environmental impacts that may occur during production of every single component of the aircraft and the assembly of these parts. Operation is the phase when the aircraft is in use and thus relates to every routine and non-routine operation performed on or by the aircraft during its life. EOL entails disposal and/or reuse of aircraft.

11.1. PRODUCTION

Production of any item may have strong environmental effects and a typical aircraft is no exception. Aircraft are generally made of large amounts of aluminium and/or reinforced fibres, contain lots of electronics, need a lot of chemical treatment, and require a lot of man hours to assemble. As such, their production has links to environmental, economic and social sustainability.

The main areas to focus on in terms of environmental sustainability are CO2 and particulate emissions during production. These are mostly caused during production of (metal) components, a very energy intensive process. This also ties in with embodied energy, another metric for environmental sustainability. In order to make the design more sustainable, embodied energy and CO2 production values have been considered when trading off materials for the final design.

The assembly process must, however, also be optimised to minimise environmental impact. Scrapping and production of waste, for example from packaging, must be reduced or re- cycled. Hazardous chemical substances must also be avoided in all phases of the production process. In order to account for these factors on InVADe, Lean Manufacturing is applied. Lean Manufacturing focusses on economy of resources and waste. For sustainability, that means minimising impact on the environment. A detailed explanation of Lean Manufacturing for the production process of InVADe can be found in Section 9.2.2.The location of the manufacturing facility should be strategically chosen in order to minimise the need for transportation of people and materials. Less locomotion means not only a decrease in cost, but also less emissions on the ground.

11.2. OPERATIONS

The most important sustainability parameters that can be measured pertaining to the operations of the aircraft are noise and particulate emissions. "The aviation industry has constantly strived to reduce emissions of CO2, NOx, and noise. Achievement of any one of these three parameters is challenging enough, but to achieve all three simultaneously requires considerable ingenuity, coupled with a clear understanding of the trade- offs that exist between them." [44] These are accounted for in the design in the form of strict requirements that were set early on; namely, noise and CO_2 emissions. These are explained in the following subsections.

11.2.1. NOISE

The impact of noise on the environment is not limited to a mere inconvenience for people living nearby. According to Passchier-Vermeer, exposure to noise constitutes a health risk. There is sufficient scientific evidence that noise exposure can induce hearing impairment, hypertension and ischemic heart disease, annoyance, sleep disturbance, and decreased school performance [90]. For that reason, and keeping in mind that InVADe is designed

to fly in densely populated areas, a strict noise requirement was set by the client, and a strive for minimising noise emission was a principal driving factor in the entire design. Reducing noise drove the design of the ducts and fans, for example. The duct diameter, operational rpm, pitch, chord, and number of blades were all optimised for noise reduction during Take-off and Landing. Moreover, noise mitigation measures were applied to further reduce noise. These are explained in Chapter 5.

11.2.2. CO2 EMISSIONS

A crucial aspect for sustainability of an aircraft is its particulate emissions. Client Requirements stipulate a limit for the CO_2 emissions at no more than 2.5 kg/km, thus the focus of this analysis.

It is important to note, however, that other particulate emissions, such as NO_x, SO_xO, soot, and even water vapour, also have an impact on the environment. Figure 11.1 exposes the composition of a kerosene fuelled jet exhaust. Assuming the current turboshaft engine, in order to minimise CO_2 emissions, the following should be addressed:

- Aircraft and Engine Technology - Intuitively, a more fuel efficient engine and aircraft will exhibit lower overall emissions. Fuel efficiency in aircraft is usually measured in specific range; a measure of how many kilometres the aircraft can fly on 1 kilogram of fuel. With sustainable design in mind, the team stipulated a minimum specific range at of 1.25 km/kg. The constraint reinforced a strive, throughout the design, for lower drag, lower weight, and higher engine efficiency.
- Fuel - For its high energy density and high flash point, Jet A is the fuel of choice for most current aircraft, although it is ultimately not a sustainable fuel. According to D. Lister [91], "There would not appear to be any practical alternatives to kerosene-based fuels for commercial jet aircraft for the next several decades. Reducing sulphur content of kerosene will reduce SO_xO emissions and sulphate particle formation."
- Operations - According to the Advisory Council for Aeronautics Research in Europe [44], improved operational practices and optimised aircraft deployment across a network may have the potential to reduce fuel-burn by about 5%, through measures such as better flight planning, speed management, selection of appropriate aircraft, equipment weight reduction and taxiing with one engine shut down after landing. Improved air traffic control resulting in more direct routes and reduced delays could reduce overall fuel burn by 6-12%.

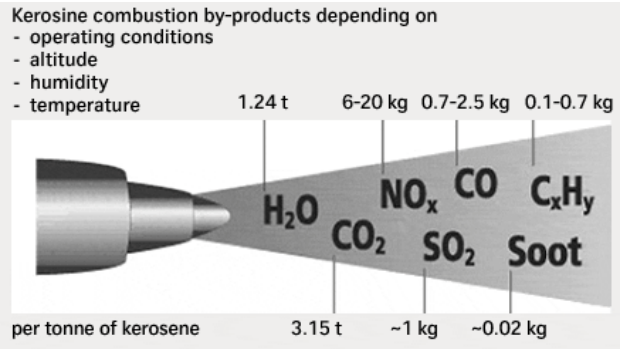

Figure 11.1: Composition of Jet Exhaust

11.3. EOL DISPOSAL PLAN

A plan for EOL (End of Life) Disposal is vital if one wishes to reduce the environmental footprint of an aircraft.

In general, the amount or weight of material that needs to be disposed of should be minimised. For that purpose, the use of materials with a higher specific strength, such as composites instead of aluminium, would be an obvious choice. However, according to C. Arnold and S. Alston [7], the production of composites has a factor of six more impact on the environment. Furthermore, composites cannot be recycled as easily as aluminium and, therefore, have a substantial impact on the EOL sustainability. The structural components of InVADe are made primarily of aluminium alloys. The material's durability and recyclability make it a smart choice when considering sustainability and a disposal plan for the aircraft. This was an important consideration when selecting the materials for structural components of the concept aircraft.

As for the non-structural parts, specifically in the aircraft's interior, there is more freedom to select sustainable materials. Natural fibres represent a traditional class of renewable materials which, nowadays, are experiencing a great revival, and the components obtained from these are mostly used to produce non-structural parts for the automotive industry such as covers, car doors panels and car roofs [81]. InVADe's interior features all possible

non-structural parts, such as seats, insulation, walls, linings, carpets, etc. made from natural fibre reinforced materials. Natural fibres such as flax, hemp, and corn fibres, are not only biodegradable, but also are light weight, inexpensive, and require significantly less energy in production, when compared with glass fibre, for example, as can be seen in Figure 11.2 [20]. As such, the impact on the environment upon disposal can me minimised, without compromising the interior design and comfort for the passengers.

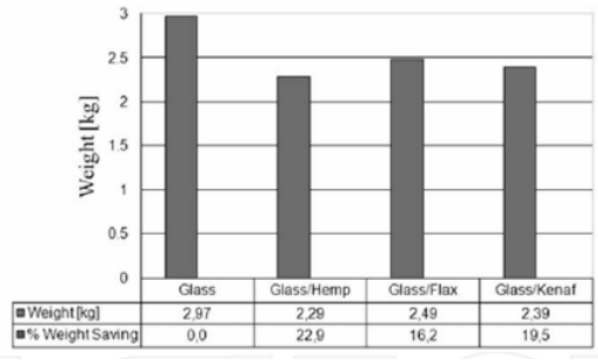

(a) Weight comparison

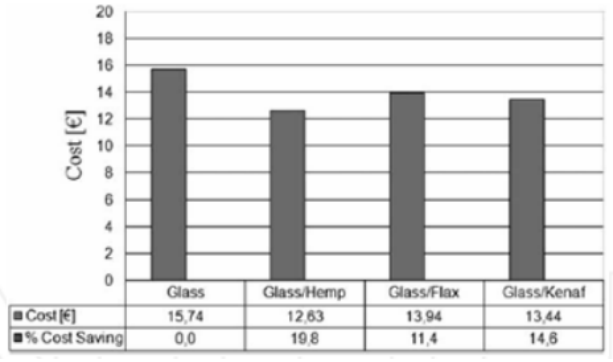

(b) Cost comparison

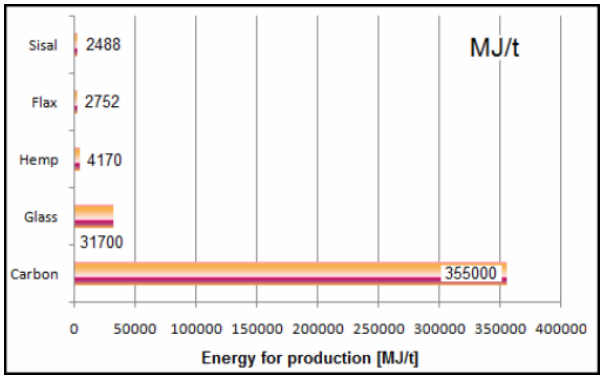

(c) Energy required for production

Figure 11.2: Comparison of different fibre characteristics [20]

Aircraft that exit operations often contain parts that are still usable on existing aircraft. Examples are flight instruments, electronic components, wiring, panels, etc. Some components may need to be repaired, and all should be recertified, yet many parts have the potential to be reused as spare parts for aircraft in service. Companies exist that can make revenues of disassembling aircraft and selling spare parts [59]. Keeping this in mind, wherever possible, components can be selected which can, at the end of the aircraft's lifetime, be re-installed in other aircraft.

In conclusion, EOL disposal is very important in the design of a vehicle. In the aircraft industry a demand for spare parts exists and companies exist that profit from dismantling and recycling aircraft. This is however simplified if generally used parts are selected for the design, which has been considered in the InVADe design. Most leftover material after the end of its operation can be either recycled, reused, or is biodegradable.

11.4. INVADE SUSTAINABILITY

The importance of sustainability in this design is evident in the requirements for the project. Limits on noise and CO_2 emissions forced the design team to come up with innovative solutions and push the boundaries to meet the needs of a future aerospace industry with a focus on reducing impact on the environment.

The value for CO_2 emission rate was calculated in Chapter 8.5 as 2.04 kg/km. This value meets the requirement set in Section 2.1. The Learjet 45, a modern business jet with similar payload, has a slightly lower fuel emission rate of 1.766 kg/km [14]. Considering the bigger picture, however, the fact that InVADe provides point to point transportation, reduces not only travel time, but also emissions, since it practically eliminates the need for getting to/from the airport. Therefore, it offers significant advantages in the sustainability aspect, particularly for short flights, which is very often the case for business travel.

Although the noise emissions do not meet the requirement, a brief comparison in Section 5.4 shows that InVADe can be considered a quiet aircraft, when compared to aircraft of similar weight and configuration. Moreover, re-

search suggests that reasonable exposure to noise levels around 80 dB does not cause damage to the human ear [47].

InVADe features a fully electric power transmission. One of the main reasons for selecting this over a conventional mechanical configuration, has to do with sustainability. The current design relies on turboshaft engines, using Jet A fuel, for power generation. The reason for this configuration instead of, for example, simply carrying a battery is that this kind of fuel packs a much higher energy density, the amount of energy that can be stored per kilogram, than a battery can currently store. A comparison of energy density and specific power contained in currently available power systems is given in Figure 11.3. However, with future advances in technology, more sustainable power sources, such as solar power or hydrogen cells, may become a viable means of generating or storing energy on board the aircraft. What makes the InVADe concept appropriate for transportation looking towards a greener future is the fact that its electric power transmission can easily accommodate an alternative, more sustainable electric generator or cells, as long as its energy density is high enough to provide the power required, while being light enough to be carried on board.

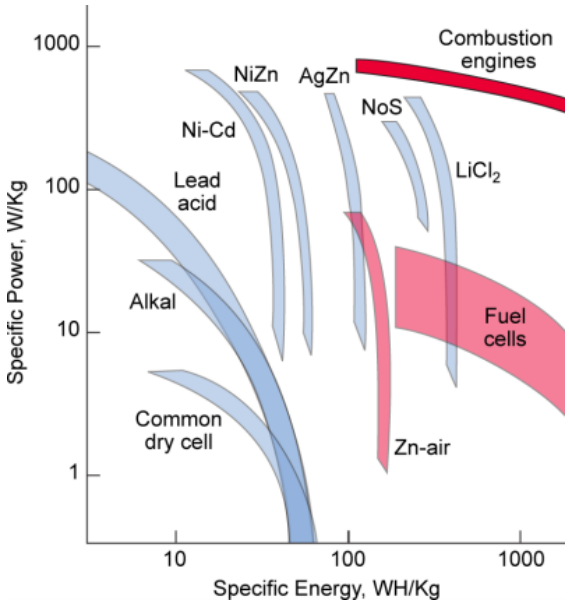

Figure 11.3: Energy density and specific power of currently available power systems [68]

12

REQUIREMENTS COMPLIANCE

In this chapter the requirement compliance will be discussed by using a requirements compliance matrix. This matrix is a table containing the client constraints & technical requirements and team constraints & technical requirements. The Compliance columns are ticked as "Fulfilled", if the requirement was met; "Partially" if the requirement was partially met; and "Not", if the requirement was not met. It also shows the required and achieved values of these requirements. This matrix is shown in Table 12.1 and 12.2. Requirements that were not investigated are marked as NC.

Table 12.1: Compliance matrix of client constraints and technical requirements

Req. ID	**Description**	**Required Value**	**Achieved Value**	**Compliance**		
				Fulfilled	Partially	Not
Ct-cons-01	Range with 1000 kg payload after a VTOL take off from sea level/ ISA+15 °C ambient conditions, including a landing and take-off halfway	2000 km	2000 km	✈		
Ct-cons-02	Payload	10(+2) passengers	10(+2) passengers	✈		
Ct-cons-03	Cockpit crew	1 (2 optional)	1 (2 optional)	✈		
Ct-cons-04	Design cruise speed at 75% power	600 km/h	600 km/h	✈		
Ct-cons-05	Service ceiling	7000 m	7000 m	✈		
Ct-cons-06	Rate of climb	9 m/s	19.8 m/s (See Section [8.1])	✈		
Ct-cons-07	Very low noise levels (urban area operations) within a 100 m distance during take-off and landing	70 dB	80.7 dB (See Section [5.3])			✈
Ct-cons-08	Unit cost	8,000,000 EUR	6,550,000 EUR (See Chapter [10])	✈		
Ct-cons-09	Average unit cost according to the expected production of 500 units over 20 years	-	-	✈		
Ct-cons-10	First flight	2030	2030	✈		
Ct-cons-11	Design flight hours	20,000	20,000	✈		
Ct-cons-12	CO_2 emissions	<2.5 kg/km	2.04 kg/km (See Section [8.5])	✈		
Ct-cons-13	Comply with corresponding CS23 or CS29 (See Section [9.4]) regulations	-	-	✈		
Ct-tech-01	VTOL capability	-	-	✈		
Ct-tech-02	End-of-life disposal plan (See Section [11.3])	-	-	✈		
Ct-tech-03	Investigation into production facilities and their possible locations (See Chapter [9.2])	-	-	✈		

Table 12.2: Compliance matrix of team constraints and technical requirements

Req. ID	**Description**	**Required Value**	**Achieved Value**	**Compliance**		
				Fulfilled	Partially	Not
Tm-cons-01	Take-off and land from helipad	15x15 m	15x15 m	✈		
Tm-cons-02	G-forces	0.6 g - 1.4 g	NC [1]			
Tm-cons-03	Minimum seat pitch and seat width	90x48 cm	90x48 cm	✈		
Tm-cons-04	Minimum cabin height	170 cm	170 cm	✈		
Tm-cons-05	Specific range	1.25 km/kg	1.54 km/kg (See Section [8.8])	✈		
Tm-cons-06	Storage space for 12 times cabin luggage	-	-	✈		
Tm-cons-07	Cabin temperature range	20-24 °C	20-24 °C	✈		
Tm-cons-08	Cabin altitude	2000 m	2000 m	✈		
Tm-cons-09	Operational temperature range	-50 to +90 °C	NC [2]			
Tm-cons-10	Operating cost of less than 1800 EUR per flight hour [19]	<1800 EUR	1,374 EUR	✈		
Tm-cons-11	Dispatch reliability	≥ 98% [24]	NC [3]			
Tm-cons-12	Less than 5.75 days of maintenance downtime per 100 flight hours [25]	-	NC [4]			
Tm-tech-01	Easy to control by pilots and aerodynamically stable during operation (See Section [7])	-	-		✈ [5]	
Tm-tech-02	Accommodate lavatory and partial galley (See Section [3.3])	-	-	✈		
Tm-tech-03	Include state-of-the-art fly-by-wire technology and glass cockpit avionics (See Section [7])	-	-	✈		
Tm-tech-04	Maximise business productivity by providing power sockets and internet connection	-	-	✈		
Tm-tech-05	Comfortable and safe (de)boarding	-	-	✈		

1. Not possible to check at this stage
2. Beyond the scope at this stage
3. Not quantifiable at this stage
4. Not possible to determine at this stage
5. Not necessarily aerodynamically stable during transition and hover

13

CONCLUSIONS

This chapter concludes the preliminary design process of InVADe. The process focussed on designing an aircraft that combines the versatility of a helicopter with the high speed of a business jet. InVADe fulfils both needs by employing VTOL capability and cruising at an airspeed of 600 km/h. Research has shown that a large potential corporate market exists for such an aircraft, and alternative markets may be possible. The resulting design is a quiet, compact 10 passenger aircraft with a wingspan of 13.3 m and a total length of 14 m. This allows the aircraft to land on an average-sized helipad. InVADe is designed to achieve a 2000 km range, including a landing halfway, without refuelling. Its first flight is scheduled to be performed in 2030.

As operations in urban areas are desired, noise emissions must be far below those of comparable aircraft. For that purpose, InVADe is equipped with four ducted fans. Two of these fans are fixed inside the main wing. During cruise flight, these 2.45 m diameter fans are covered to reduce drag and greatly increase the lift force generated by the wing. The other fans provide upward thrust during VTOL and hovering flight. In transition to cruise flight, these fans tilt 90 degrees forward and propel the aircraft to cruise velocity; these fans were sized at a diameter of 1.95 m. Using this configuration, InVADe produces a noise level of 80.7 dB at 100 m distance during take-off and landing.

A pair of GE CT7-derivative engines provide a total 3.5 MW of power to four electric generators, which in turn transmit power, via electric cables, to four electric motors mounted on each duct. The motors then each power individual fans inside the ducts, which, together deliver enough thrust to lift the aircraft vertically off the ground. It was shown that this electric solution is lighter than employing a mechanical drive train, and it allows for a more flexible design.

Current estimates show that the unit cost of the aircraft is about to 6.5 million EUR, whereas operating costs per hour are estimated at 1,374 EUR. This makes InVADe a very affordable aircraft for its class. In addition, an expected CO_2 emission of 2.04 kg/km is reached.

InVADe complies with most key requirements. Although the noise requirement was set at 70 dB for the specified distance, this was found to pay too large a toll on the other aspects of the design, rendering it infeasible. Moreover, as discussed in Section 5.3, a value of 80.7 dB is already a relatively low value when compared to other aircraft. In agreement with the client, it was decided that, considering the aspects mentioned above, this noise value is acceptable. In conclusion, InVADe is expected to offer the business market a fast, reliable and cost effective way of transportation without compromising on comfort and sustainability.

14

FUTURE DEVELOPMENT AND RECOMMENDATIONS

Since the time frame for the DSE project consists of only 10 weeks, the scope of the project is limited to a preliminary design. During this phase only a certain level of detail can be achieved. However, points for further development can already be identified. This section will expose some of these points per department. In terms of future development, a future work flow diagram and a Gantt chart are presented in Appendix A.1.

14.1. AERODYNAMICS

Several uncertainties are still to be solved in the field of aerodynamics. In general, for validation of the theoretical results of aerodynamic parameters, a wind tunnel test must be performed. In addition, the following challenges are still to be tackled.

The fan-in-wing structure in the inner section of the main wing needs to be analysed further to find its influence on the performance. As mentioned in Section 4.8, the outlet air stream of a propulsion system is disturbed with respect to the inlet stream. This has a negative effect on the aerodynamics of the aircraft. Since at this stage of the project it is difficult to predict these effects it is recommended to use CFD program in the next design phase to study these effects in more detail. Next to that, the CFD program is also recommended to be used for investigation of the airflow around the open section of the wing where the ducts are placed. This is because the airflow around the open section is very complicated to analyse analytically.

More resources shall be put on the investigation of the lift generated by the fuselage to get a more precise value. The fuselage takes a significant part in generating lift, as was the case for the Piaggio P.180 Avanti. In the next design phase, resources shall be put on the research of the effect of the fuselage shape on lift generation. This, in order to come with a more exact value of the lift produced by the aircraft's fuselage.

14.2. PROPULSION

In this section, recommendations for the propulsion system are given. These concern mainly noise reduction and considerations for the electrical system.

In the current stage of design, the duct designs are largely based on relatively simple methods and data from the Bell X-22. For further development it is imperative that more a more advanced analysis is done. The front ducts will have to be optimised for cruise flight, which could have a negative impact on take-off noise. Use of CFD is advised.

To achieve the client requirement of 70 dB, further research in noise is to be performed. Additional advanced abatement techniques may further lower produced noise. Techniques proposed for further investigation include the following:

- **Active Noise Control** - This may consist of using microphones and speakers to capture and reproduce the noise profile, but in phase, thus cancelling the original noise. The challenge with this method is that it is sensitive to the position of the observer, and, in some cases will not cancel, but instead add the noise. However, research has been done for its use, particularly in combination with passive noise cancellation techniques, with promising results. One such research was done by Homma. [54]
- **Propeller Lining** - Lining the propeller blades with a Foam Metal Liner (FML) can potentially reduce the noise emission of the fans by a few dB. Although the technique was not applied to the current design, it is recommended for investigation as a possible way of further reducing the noise emissions. The specifics of this technique are described by Sutliff et al. [110].
- **Improving Propeller Efficiency** - Maximum propeller efficiency is directly related to minimum noise. As a general recommendation, any current or future technique that is able to improve propeller efficiency

should be considered as a candidate for a noise abatement technique.

As mentioned in Section 5.4, the aft ducts inserted in the wings, do not provide thorough acoustic shielding for minimising noise. A possible improvement would be to apply, for take off and landing, retractable duct extensions to the aft ducts, so as to more thoroughly damp the noise emitted by the aft fans. This solution was considered by the design team, but ended up being discarded due to the high complexity of such a mechanism, as well as structural and duct-fan clearance concerns. However, if a good solution can be found for these obstacles, and extensions are properly applied, a further reduction of 1-2 dB is expected.
To arrive at a more accurate estimate of the maximum noise level at 100 meters, the interference patterns of the noise sources can be taken into account. In some limited regions, due to interference, it is possible that the total SPL will be either higher or lower than was estimated, depending on constructive or destructive interference Therefore, for more accurate results, this effect should be analysed.

Finally, the effect of lightning strike on the electrical system must be examined as well. If the system cannot be completely shielded, usage of the front fans as ram air turbines (RAT) needs work. With modification of the front motors, it is possible to generate electrical power from the airflow past the fans. Also, proper power routing must be developed, to avoid significant heat losses and electromagnetic interference (EMI) effects on sensitive electrical components. Lastly, an alternative is possible for a battery pack. The possible application of fuel cells to replace this must be investigated. This may result in several benefits. These may include higher energy density and lower ecological impact.

14.3. STRUCTURES & MATERIALS

This section discusses the recommendations regarding the inner structure of the wing. There are a couple of things that could decrease the weight of the wing structure. Further, some areas of potential difficulties should be investigated. As well the production process of the different parts should be kept in mind. Finally, a technology which can decrease the bending loads on the wing will be presented.
For further decreasing the weight one could investigate the influence of putting ribs in the wing box, which should especially be favourable to increase the critical buckling stresses. Additionally, a larger optimisation could be performed with a larger range of thicknesses for the skin and a larger range of stringers and stringer sizes. It was found that during the wing box optimisation that a large amount of stringers with a low cross-sectional area was favourable for weight reduction. However, their is probably a lower limit cross-sectional area for a stringer, after which the stringer not really separates the skin any more. Thus more research is needed regarding the stringers.
Further, rivets are going to be used to attach the stringers to the skins. A wrongly chosen pitch can result in buckling even before the critical buckling stresses. Therefore, more research needs to be done regarding the rivets. Wrongly pitch rivets could cause the wing box to buckle earlier than predicted. However, before testing more research needs to be done regarding the rivets.
Another point of attention are the main spars. At this point the geometry of a spar cross-section is the same along the z-axis, because of the geometry constraints of the aerofoil. Tapering the spar could result in a weight decrease, but one should investigate how the loads from the aerofoil are then transferred from the skin to the spars. Further, the skin of the main spars could perhaps be tapered to further decrease the weight.
Currently, the wing structure has been designed in such a way that it would never fail due to fatigue, because the stress are always under the endurance limit, see Section 6.1.2. Further investigation on the fatigue properties of materials could decrease the weight. For example, if only 10,000 cycles are reached, one should not design for an infinite amount of cycles.
Additional investigation in bending relief due to the weight of the structure and the fuel should be investigated as well, to perhaps further decrease the weight of the wing.
Another important which has not yet been addressed the combination of the vibration of the fans and the other way around. It should be investigated whether or not problems as excessive vibrations or perhaps resonance are going to occur.
Presently, it has only be determined that their are two possible way to connect the wing box and the main spars. First, they could be bolted together, because bolts can cope with higher load than rivets. Further, the joint will have to deal with a lot of vibrations of the wing and the fans and therefore makes the connection fatigue sensitive. Bolts can be pre-loaded to better withstand fatigue. Another convenience of bolts is that they are easy to detach, which easiness the maintenance of the main wing. Further, the joint should be a double but joint, because this does not have any eccentricity which could introduce secondary bending and result in extra stress concentrations. However, the joint should be fail-safe so the double but joint will be more like two single but joints. Thus the bolts do only go to one cover [11]. The size of the joint, the size and number of bolts and the amount of pre-loading should be investigated in more detail.
The second idea is to make the webs and the left and right side of the wing box out of one part. Therefore, no big heavy joint is necessary, only some joints to connect the upper and lower skin to the flanges. Of course it could also be possible that a complete different kind of joint or method will perform better. Thus more research is required.

The buckling coefficients, see Section 6.1.4, were chosen in a conservative way, namely the lowest value was picked. More research on whether or not this is really necessary could be helpful in minimising the weight of the wing structure.
Not only the geometry is important for the characteristic of the wing box, but the way the different parts are manufactured as well. The I-beams could for example be created by welding or by extrusion. Welding is bad for fatigue and is hard to do for thin-walled structures [11]. Therefore welding of the I-beams could be excluded. This is only a small comparison, probably different methods exist as well. However, it is clear that a comparison in manufacturing method for every single part must be done to get the most satisfactory result.
The current wing box has been designed to be placed inside the wing, without using the skin of the wing itself. By using the skin of the wing one could decrease the weight of the total wing. The current method can be adjusted to include aerofoil shaped top and bottom skins. This will increase the moment of inertia as well, because the average distance from the top and bottom skin to the neutral x-axis will increase. When doing this, the top and bottom skin should also cope with the local pressure forces over the skin of the wing.

If the earlier mentioned active winglets, see also Section 4.8, are used in the design these would enable a lighter and smaller structure. Usually winglets increase the bending moment on the wing and cause higher structural loads and a heavier structure. Active winglets however have an extra control surface that uses acceleration sensors to react automatically to loads during flight and reduces these by producing lift in the opposite direction [112]. Test flights with a Cessna Citation performed by Tamarack showed a considerable reduction in bending loads. At a peak gust load of 4.4 g the wing with standard winglets experienced bending loads of 230,000 in-lbs, with the active winglets this was reduced to 170,000 - 180,000 in-lbs [112]. This is a reduction of approximately 24% in bending moment, which would would reduce stresses significantly.

Figure 14.1: Tamarack active winglet with control surface [112]

14.4. STABILITY & CONTROL

Although rigid and promising results have been shown in the Stability & Control chapter, certain areas need further investigation to study the exact behaviour of the aircraft is various flight phases. A list of recommendations is provided below.

At this stage of the design process the canard only exhibits elevators. Since a larger canard surface is mainly important during low speeds, flaps can help to decrease the canard's area and create a smaller wake during cruise flight.

Another method to reduce the canard surface area is to employ the front ducts in generating lift. As they are in front of the c.g. position, they may take a portion of the control force required by the canard to balance the aircraft. In addition, a control force relief may arise from slightly tilting the ducts at slower flights.

Concerning propulsion, InVADe should be able to fly with one front fan inoperative. In terms of control, more investigation is needed to determine the exact thrust distribution between the three remaining fans to remain controllable. Although the tail is sized to account for this, the influence of drag forces acting on the inoperative ducts should be quantified.

During cruise, when the ducts are closed, the inboard part of the wing generates lift. An unused portion of the wing exists at the trailing edge, as no flaps are put there. This space may be usable for additional ailerons, if desired. These may be used for more direct control. However, the need for additional ailerons should be investigated first, as this adds another subsystem to the wing. This increases weight and complexity.

The transition phase is a very complicated phase to analyse. Since the aircraft is partially balancing on the thrust vectors from the fans, and partially relying on the lift generated by the wings and canard, even a qualitative analysis is a complex task. Since a complete analysis of the transition phase is out of the scope of this project, additional research is needed in the further development of InVADe.

Although the principle has been proven on existing quadrotors, the effect of only one plane of symmetry is not clear. Further investigation is needed to precisely define the thrust needed from each fan to roll, yaw and pitch.

14.5. PERFORMANCE

InVADe reaches all its performance requirements and even surpasses some of them. As always though there is room for improvement, some of the options are presented in this subsection.

Increasing the aerodynamic efficiency (the lift to drag ratio) would greatly reduce the power required to reach the cruise speed of 600 km/h which would either result in a smaller power plant or an even higher cruise speed. Moreover a better efficiency would reduce fuel consumption, increase range and increase climb performance.

Increasing the cruise altitude would decrease the drag and again enable the use of a smaller power plant or higher cruise speed. As mentioned before this might cause structural issues and it is also unknown if a higher cruise altitude is really useful for trips of this range.

BIBLIOGRAPHY

[1] R. Abdel-Fadil, A. Eid, and M. Abdel-Salam. "Electrical Distribution Power Systems of Modern Civil Aircrafts". In: *Proceedings of the 2nd International Conference on Energy Systems and Technologies*. Ed. by M. Comsan. 2013.

[2] R. Aboulafia. *Teal Group Bizav Overview (Part 1)*. World Aircraft Sales Magazine. 2009. URL: http://www.avbuyer.com/articles/detail.asp?Id=1483.

[3] AgustaWestland. *Email conversation with Dott. Ing. Luigi U. Ricci Moretti*. 2014.

[4] Airbus. *A318/A319/A320/A321 - Flight deck and systems briefing for pilots - Issue 4*. http://www.a318xp.ucoz.ru/_ld/0/4_A320_Flight_dec.pdf. 2007.

[5] *Airports.de*. Last visited 21/1/2014. URL: http://www.airports.de/.

[6] A. Akturk, A. Shavalikul, and C. Camci. "PIV Measurements and Computational Study of a 5-Inch Ducted Fan for V/STOL UAV Applications". In: *AIAA 2009-332* (2008).

[7] C. Arnold and S. Alston. *Environmental Impact of Composites*. http://www.welshcomposites.co.uk/downloads/environmental20webinar.pdf. Last visited 2013/129.

[8] ATEC. *HPW3000 Engine Brochure*. Last visited 15/1/2014. URL: http://www.pw.utc.com/Content/HPW3000_Engine/pdf/hpw3000_engine_brochure.pdf.

[9] K. Bamberger and T. Carolus. "Optimization Of Axial Fans With Highly Swept Blades With Respect To Losses And Noise Reduction". In: *Noise Control Engineering Journal* 60.6 (2012), pp. 716–725.

[10] Bell Aerospace Company. *X-22A Progress Report No. 73*. Tech. rep. 1969.

[11] O. Bergsma and J. Sinke. *AE2207 Production of Aerospace Systems*. TU Delft, 2013.

[12] A. Bisio, ed. *Energy, Technology and the Environment*. Vol. 1. Wiley and Sons, Inc., 1995, pp. 257–259.

[13] Bombardier Aerospace. *Bombardier Commercial Aircraft Market Forecast 2009-2028*. 2009. URL: http://ir.bombardier.com/var/data/gallery/document/34/24/25/71/13/Bombardier-aerospace-2013-2032-BCA-BBA-Market-Forecast.pdf.

[14] Bombardier Aerospace. *Bombardier Fuel Burn Data*. 2009. URL: https://customer.aero.bombardier.com/webd/bag/BBAD/Custsupp/techinfo/CICOpenDocuments.nsf/vwWebPage/ETS/$FILE/Fuel%20Burn%20Chart_CIC_Production_Models_rev.2.pdf.

[15] Bombardier Aerospace. *Market Forecast 2013-2032*. 2013. URL: http://ir.bombardier.com/var/data/gallery/document/34/24/25/71/13/Bombardier-aerospace-2013-2032-BCA-BBA-Market-Forecast.pdf.

[16] E. Bruhn. *Analysis and Design of Flight Vehicle Structures*. Jacobs Publishing, Inc., 1973.

[17] Bureau of Labor Statistics. *CPI Inflation Calculator*. 2013. URL: http://www.bls.gov/data/inflation_calculator.htm.

[18] Clean Sky. *All-Electric Aircraft*. 2012. URL: http://www.cleansky.eu/content/interview/all-electric-aircraft.

[19] Conklin and de Decker Associates, Inc. *Aircraft Cost Summary*. Last visited 2013/11/27. URL: https://www.conklindd.com/CDALibrary/ACCostSummary.aspx.

[20] G. Cristaldi. *Composites Based on Natural Fibre Fabrics*. http://www.intechopen.com/download/get/type/pdfs/id/12253. http://www.intechopen.com/download/get/type/pdfs/id/12253.

[21] Crompton Greaves. *Low Tension TEFC & SPDP Induction Motors*. URL: http://www.sirus.in/images/crompton-ac-motors.pdf.

[22] D. L. Kohlman. *Introduction to V/STOL airplanes*. Ed. by. Iowa State University Press, Ames, 1981.

[23] J. Dailey et al. *Report of the Panel to Review the V-22 Program*. Tech. rep. Department of Defense, 2001.

[24] B. de Decker. *How Old is too Old?* https://www.conklindd.com/Page.aspx?cid=1070. Last visited 2013/11/26. Conklin & de Decker Associates, Inc.

[25] B. de Decker. *Measuring Reliability and Availability*. https://www.conklindd.com/Page.aspx?hid=1074. Last visited 2013/11/26. Conklin & de Decker Associates, Inc.

[26] B. Donham. *Interference from Electronic Devices*. Boeing Commercial Airplanes Group. 2000.

[27] M. Drela and H. Youngren. *AVL Overview*. http://web.mit.edu/drela/Public/web/avl/. 2012.

[28] DSE Group 7. *Design Synthesis Exercise: Design of a* VTOL *Business Aircraft - Baseline Report*. TU Delft, 2013.

[29] DSE Group 7. *Design Synthesis Exercise: Design of a* VTOL *Business Aircraft - Mid-Term Report*. TU Delft, 2013.

[30] Electric Motors Reference Center. *Induction motors*. Last visited 16/1/2014. URL: http://www.electricmotors.machinedesign.com/guiEdits/Content/bdeee11/bdeee11_7.aspx.

[31] A. Elhafez. *A Review of More Electric Aircraft,* International Conference of Aerospace Science and Aviation Technology. 2009.

[32] Enstroj Susnik Roman s.p. URL: http://www.enstroj.si/images/stories/emrax_dimensions_2013.jpg.

[33] Enstroj Susnik Roman s.p. *Emrax Technical Data*. http://www.enstroj.si/download.php?f=images/stories/technical_data_emrax_228_11_2013.pdf. 2013.

[34] European Aviation Safety Agency. *Certification Specifications for Large Rotorcraft CS-29*. 2012.

[35] European Aviation Safety Agency. *Certification Specifications for Normal, Utility, Aerobatic, and Commuter Category Aeroplanes CS-23*. 2012.

[36] European Aviation Safety Agency. *Type-certificate data sheet General Electric CT7-series engines*. 2013.

[37] *FAR Part 91 - General operating and flight rules - Section 117 - Aircraft Speed*. Federal Aviation Administration.

[38] *FAR Part 91 - General operating and flight rules - Section 151 - Fuel requirements for flight in VFR conditions*. Federal Aviation Administration.

[39] *FAR Part 91 - General operating and flight rules - Section 167 - Fuel requirements for flight in IFR conditions*. Federal Aviation Administration.

[40] FindTheBest. *Compare Jets & Prop Planes*. Last visited 21/1/2014. URL: http://planes.findthebest.com/.

[41] D. G. Fink and H. W. Beaty. *Standard Handbook for Electrical Engineers*. 14th ed. McGraw-Hill, 1999.

[42] Flight International. "Bell X-22A: Analysis of a VTOL research vehicle". In: *Flight International* 200 (1967), pp. 445–449. URL: http://www.flightglobal.com/pdfarchive/view/1967/1967%20-%200453.html.

[43] B. Franklin. *Advice to a Young Tradesman, Written by an Old One*. 1748, pp. 200–202.

[44] A. Garcia et al. *AERONAUTICS AND AIR TRANSPORT: BEYOND VISION 2020*. Tech. rep. Advisory Council for Aeronautics Research in Europe, 2010.

[45] F. George. *Piaggio Aero P180 Avanti II*. Aviationweek. 2007.

[46] M. Giuni. "Formation and early development of wingtip vortices". PhD thesis. University of Glasgow, 2013.

[47] J. Goldstein. *Noise Hazard Evaluation Sound Level Data On Noise Source*. Tech. rep. Army Environmental Hygiene Agency, 1975.

[48] Green Car Congress. *Envia Systems hits 400 Wh/kg target with Li-ion cells; could lower Li-ion cost to* 180/*kW h*. 2012.

[49] S. Gudmundsson. *General Aviation Aircraft Design: Applied Methods and Procedures*. Butterworth-Heinemann, 2013.

[50] H Co., 4/7th Aviation Regiment. URL: http://archive.is/XhLk.

[51] D. Hall. "Assessment of Noise Control Measures for a Model Advanced Ducted Propulsor". In: *Journal of Aircraft* 33 (1996).

[52] Hamilton Sundstrand. *T-62T-46-2 For the V-22 Osprey*. Last visited 14/1/2014. 2000.

[53] R. Hawsey et al. *High Power Density Generator Concepts for Aerospace Electric Power*. Tech. rep. Oak Ridge National Laboratory, 1989.

[54] K. Homma. *Compact Integrated Active-Passive Approach for Axial Fan Noise Control*. Tech. rep. Virginia Polytechnic Institute and State University, 2004.

[55] Honeywell Aerospace. *10th Annual Turbine-Powered Civilian Helicopter Purchase Forecast*. 2008.

[56] Honeywell Aerospace. *15th Annual Turbine-Powered Civilian Helicopter Purchase Forecast*. 2013.

[57] Honeywell Aerospace. *5th Annual Turbine-Powered Civilian Helicopter Purchase Forecast*. 2003.

[58] Hong Kong Port Works Division. *EIA Study for Helipad at Yung Shue Wan, Lamma Island*. Last visited 2014/01/10. BMT.

[59] D. Horwitz. *The End of the Line: Aircraft Recycling Initiatives*. 2007.

[60] IHS Jane's. *All the World's Aircraft*.

[61] *Integrated Aeronautical Information Package*. AIS Netherlands. 2014. URL: http://www.ais-netherlands.nl/aim/2013-11-28-AIRAC/eAIP/html/index-en-GB.html.

[62] D. A. Irwin and N. Pavcnik. "Airbus versus Boeing revisitied: international competition in the aircraft market". In: *Journal of International Economics* 64 (2004), pp. 223–245.

[63] ISO. *ISO 2533:1975 Standard Atmosphere*. 1975.

[64] L. H. H. J. E. Ffowcs Williams. "Aerodynamic Noise Generation by Turbulent Flow in the Vicinity of a Scattering Half Plane". In: *Journal of Fluid Mechanics* 40 (1970).

[65] Jane's Aero-Engines. *General Electric CT7*. IHS Jane's. 2013.

[66] Jane's Aero-Engines. *P&WC PT6B, PT6C, PT6D*. IHS Jane's. 2013.

[67] J. G. Kaufman. *Properties of Aluminum Alloys*. ASM International, 2008.

[68] I. Kroo. *Aircraft Concepts and Technologies for Sustainable Aviation*. Dept. of Aeronautics and Astronautics Stanford University. 2010. URL: http://www.aeronautics.nasa.gov/pdf/23_kroo_green_aviation_summit.pdf.

[69] I. Kroo and J. Alonso. *V-n Diagram*. URL: http://adg.stanford.edu/aa241/structures/vn.html.

[70] G. Kuiper. *New developments around sheet and tip vortex cavitation on ship propellers*. 2001.

[71] G. La Rocca. *AE1201 Aerospace Design and System Engineering Elements I*. TU Delft. 2011.

[72] G. La Rocca. *AE2101 Aerospace Design and System Engineering Elements II*. TU Delft. 2011.

[73] G. La Rocca. *AE3201 System Engineering and Aerospace Design*. TU Delft. 2013.

[74] P. B. Ladkin. *Electromagnetic Interference with Aircraft Systems: why worry?* University of Bielefield. 1997.

[75] C. Lanier Benkard. "A Dynamic Analysis of the Market for Wide-Bodied Commercial Aircraft". In: *Review of Economic Studies* 71 (2004), pp. 581–611.

[76] Lean Enterprise Institute. *What is Lean?* Last visited 20/1/2014. URL: http://www.lean.org/whatslean/.

[77] J. G. Leishman. *Principles of Helicopter Aerodynamics*. Ed. by W. Shyy and M. J. Rycroft. Cambridge University Press, 2006.

[78] X. Liu, Y. Zhou, and S. Ma. "EMI filter design for constant power loads in more electric aircraft power systems". In: *Power Electronics and Motion Control Conference*. 2009.

[79] Lockheed Martin. *Turkish Industry Takes Off In Support Of F-35Turkish Industry Takes Off In Support Of F-35*. Last visited 23/1/2014. URL: www.lockheedmartin.com/us/news/press-releases/2013/may/130508ae_turkish-industry-supports-f-35.html.

[80] X. Luo and D. D. L. Chung. "Electromagnetic interference shielding using continuous carbon-fiber carbon-matrix and polymer-matrix composites". In: *Composites: Part B* 30 (1999), pp. 227–231.

[81] A. Magurno. *Vegetable fibres in automotive interior components*. Die Angew Makromol Chem, 1999, pp. 99–107.

[82] P. Mantle. *Air Cushion Craft Deve*. D.W. Taylor Naval Ship Research and Development Center, 1980.

[83] J. Marte and W. Kurtz. *A Review of Aerodynamic Noise From Propellers, Rotors, and Lift Fans*. http://cafefoundation.org/v2/pdf_tech/Noise.Technologies/NASA.1970.Prop.Noise.Review.pdf. Last visited 2013/12/10.

[84] A. McAlpine, M. Fisher, and B. Tester. ""Buzz-saw" noise: A comparison of measurement with prediction". In: *Journal of Sound and Vibration 290* (2006).

[85] McDonnell Douglas Astronautics Company. *The USAF Stability and Control Digital DATCOM - Volume I*. 1979.

[86] T. Megson. *Aircraft Structures for Enginerring Students*. 4th. Elsevier Science & Technology, 2012.

[87] D. G. Miller. *Test Summary for the ARPA-E Program Envia Systems Prototype Cell*. Tech. rep. Naval Surface Warfare Center, Crane Division, 2012.

[88] J. Mulder et al. *AE3202 Flight Dynamics - Lecture Notes*. TU Delft Blackboard. 2013.

[89] K. Ohtsuta and S. Akishita. *Noise Reduction of Short Ducted Fan by Using Forward Swept and Inclided Blade*. http://www.mb.uni-siegen.de/iftsm/forschung/fan2012_senlis_bamberger.pdf. Last visited 2014/01/09. Mitsubishi Electric Corp.

[90] W Passchier-Vermeer and W. F. Passchier. "Noise exposure and public health". In: *Environmental Health Perspectives* 108 (2000 March), pp. 123–131.

[91] J. Penner et al. *Aviation and the Global Atmosphere*. Tech. rep. IPCC, 1999.

[92] Piaggio Aero Industries S.p.A. *P.1HH HammerHead*. Last visited 21/1/2014. URL: p1hh.piaggioaero.com.

[93] R. Pinker et al. "Prediction of noise generated by fans and compressors in turbojet and turbofan engines, ESDU98008". In: *ESDU International* (2003).

[94] R. W. Prouty. *Helicopter Performance, Stability, and Control*. Robert E. Krieger Publishing Company, 1990.

[95] S. Rajendran. "Design of Parametric Winglets and Wing tip devices A Conceptual Design Approach". PhD thesis. Linkoping studies in Science and Technology, 2013.

[96] D. Raymer. *Aircraft Design: A Conceptual Approach*. American Institute of Aeronautics and Astronautics, Inc., 1992.

[97] T. Rindlisbacher. *Guidance on the Determination of Helicopter Emissions*. Tech. rep. Swiss Federal Department of the Environment, Transport, Energy and Communications, 2009.

[98] R. Rosero et al. *Moving Towards a More Electric Aircraft*. IEEE. 2007.

[99] J. Roskam. *Airplane Design Part I*. Roskam Aviation and Engineering, 1990.

[100] J. Roskam. *Airplane Design Part II*. Roskam Aviation and Engineering, 1985.

[101] J. Roskam. *Airplane Design Part V*. Roskam Aviation and Engineering, 1985.

[102] M. Sadraey. *Aircraft Performance Analysis*. Ed. by D. Mller. VDM Verlag, 2009.

[103] M. H. Sadraey. *Aircraft Design: A Systems Engineering Approach*. WILEY, 2013.

[104] Salary Explorer. *Salary Survey*. Last visited 23/1/2014. URL: www.salaryexplorer.com/salary-survey.php.

[105] K. Sarsfield. *IN FOCUS: Business jet manufacturers turn a corner*. 2012. URL: http://www.flightglobal.com/news/articles/in-focus-business-jet-manufacturers-turn-a-corner-371247/.

[106] *SIA La Reference en Information Aeronautique*. 2014. URL: https://www.sia.aviation-civile.gouv.fr.

[107] C. Sloan. *Inside Boeings 737 Renton Factory and the Successful Next Gen*. 2013. URL: http://www.airlinereporter.com/2013/07/inside-boeings-737-renton-factory-and-the-successful-next-gen/.

[108] D. Soban. *AE3310 Performance lecture notes*. Georgia Institute of Technology.

[109] M. Spelman. *Turkey - Summary of labour market and skills issues*. Tech. rep. accenture, 2012.

[110] D. L. Sutliff et al. *Attenuation of FJ44 Turbofan Engine Noise With a Foam-Metal Liner Installed Over-the-Rotor*. Tech. rep. National Aeronautics and Space Administration, 2009.

[111] A. Thom and K. Duraisamy. "A High Resolution Optimisation of a Turboprop Wing". In: ().

[112] M. Thurber. *Tamarack Active Winglets Offer Weight-saving Aerodynamic Improvements*. Internet. 2012. URL: http://www.ainonline.com/aviation-news/aviation-international-news/2012-11-06/tamarack-active-winglets-offer-weight-saving-aerodynamic-improvements.

[113] E. Torenbeek. *Synthesis of Subsonic Aircraft Design*. Delft University Press, 1982.

[114] G. E. Turney and R. W. Luidens. *Aeronautical Applications of High-Temperature Superconductors*. Tech. rep. AIAA-89-2142. AIAA, 1989.

[115] US Motors. *Induction Generator*. 2013. URL: http://www.usmotors.com/TechDocs/ProFacts/Induction-Generator.aspx.

[116] VanderLande Industries. *Stute Verkehr: Just-In-Time Delivery for Airbus with order fulfilment centres in Bremen and Hamburg*. VanDerLande Industries. 2013. URL: http://www.vanderlande.nl/en/Warehouse-Automation/References/Other-references/Stute.htm.

[117] J. Vanderover and K. Visser. *Analysis of a Contra-Rotating Propeller Driven Transport Aircraft*. ftp://ftp.clarkson.edu/.depts/mae/public_html/papers/vanderover.pdf. Last visited 2014/01/07. Aeroweb.

[118] Vertical Mag. *Teal Group Issues 10-Year Rotorcraft Forecast*. URL: http://www.verticalmag.com/news/article/Teal-Group-issues-10-year-rotorcraft-forecast.

[119] R. Vos and B. Zandbergen. *AE1201 Aerospace Design and Systems Engineering Elements I: The Design of the Landing Gear*. TU Delft, 2011.

[120] M. Voskuijl. *AE2104-11 Flight and Orbital Mechanics Lecture 1&2: Unsteady Climb*. TU Delft, 2011.

[121] M. Voskuijl. *AE2104 Flight Mechanics Lecture 5 - Landing*. TU Delft, 2011.

[122] G. Warwick. *Teams Test More Powerful Engines for U.S. Army Helicopters*. Aerospace Daily & Defense Report. 2013.

[123] G. J. Weden and J. J. Coy. *Summary of Drive-Train Component Technology in Helicopters*. Tech. rep. AVSCOM Research and Technology Laboratories, 1984.

[124] R. Williams. *The Numbers: How do U.S. taxes compare internationally?* 2011. URL: http://www.taxpolicycenter.org/briefing-book/background/numbers/international.cfm.

[125] World Commission on Environment and Development (WCED). *Our Common Future*. Oxford University Press. 1987.

[126] G. E. Wright and F. M. de Piolenc. *Ducted Fan Design, Volume 1*. Ed. by M. Flow. 2001.

[127] H. W. Zhao. "Development of a Dynamic Model of a Ducted Fan VTOL UAV". PhD thesis. School of Aerospace, Mechanical, Manufacturing Engineering; College of Science, Engineering, and Health; RMIT University, 2009.

A

APPENDICES

A.1. PROJECT DESIGN AND DEVELOPMENT LOGIC

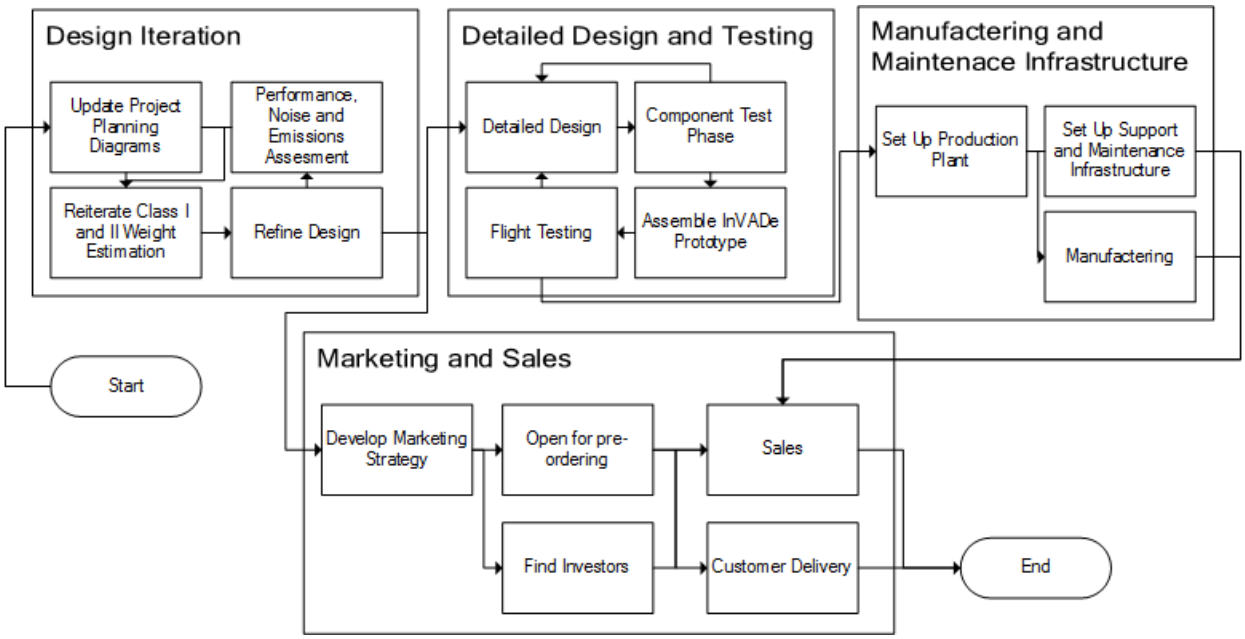

Figure A.1: Future Work Flow Diagram

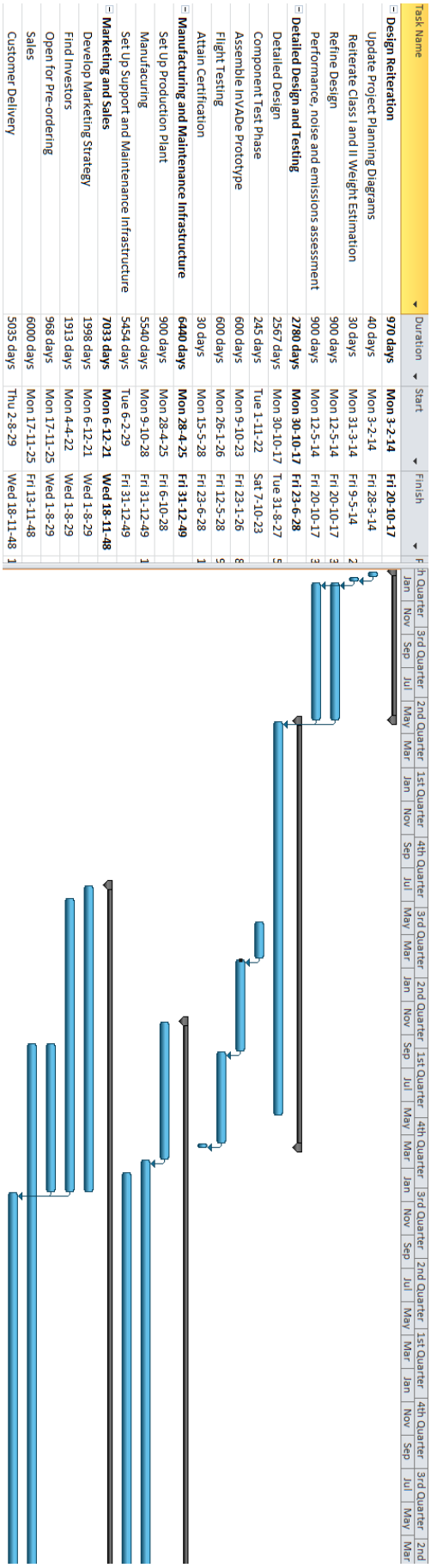

Task Name	Duration	Start	Finish	F
Design Reiteration	**970 days**	**Mon 3-2-14**	**Fri 20-10-17**	
Update Project Planning Diagrams	40 days	Mon 3-2-14	Fri 28-3-14	
Reiterate Class I and II Weight Estimation	30 days	Mon 31-3-14	Fri 9-5-14	2
Refine Design	900 days	Mon 12-5-14	Fri 20-10-17	3
Performance, noise and emissions assessment	900 days	Mon 12-5-14	Fri 20-10-17	3
Detailed Design and Testing	**2780 days**	**Mon 30-10-17**	**Fri 23-6-28**	
Detailed Design	2567 days	Mon 30-10-17	Tue 31-8-27	5
Component Test Phase	245 days	Tue 1-11-22	Sat 7-10-23	
Assemble InVADe Prototype	600 days	Mon 9-10-23	Fri 23-1-26	8
Flight Testing	600 days	Mon 26-1-26	Fri 12-5-28	9
Attain Certification	30 days	Mon 15-5-28	Fri 23-6-28	1
Manufacturing and Maintenance Infrastructure	**6440 days**	**Mon 28-4-25**	**Fri 31-12-49**	
Set Up Production Plant	900 days	Mon 28-4-25	Fri 6-10-28	
Manufacuring	5540 days	Mon 9-10-28	Fri 31-12-49	1
Set Up Support and Maintenance Infrastructure	5454 days	Tue 6-2-29	Fri 31-12-49	
Marketing and Sales	**7033 days**	**Mon 6-12-21**	**Wed 18-11-48**	
Develop Marketing Strategy	1998 days	Mon 6-12-21	Wed 1-8-29	
Find Investors	1913 days	Mon 4-4-22	Wed 1-8-29	
Open for Pre-ordering	968 days	Mon 17-11-25	Wed 1-8-29	
Sales	6000 days	Mon 17-11-25	Fri 13-11-48	
Customer Delivery	5035 days	Thu 2-8-29	Wed 18-11-48	1

Figure A.2: Future Gantt chart

A.2. FUNCTIONAL BREAKDOWN STRUCTURE

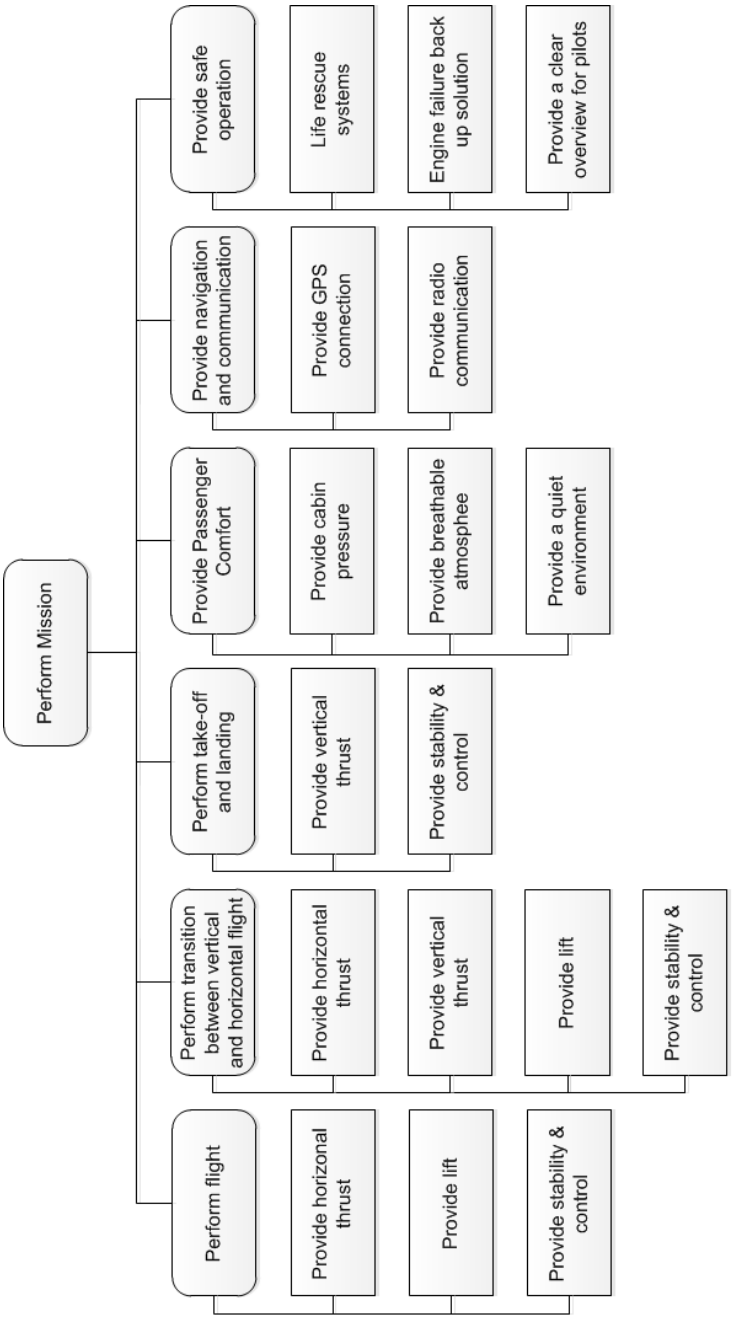

Figure A.3: Functional Breakdown Structure

A.3. FUNCTIONAL FLOW DIAGRAM

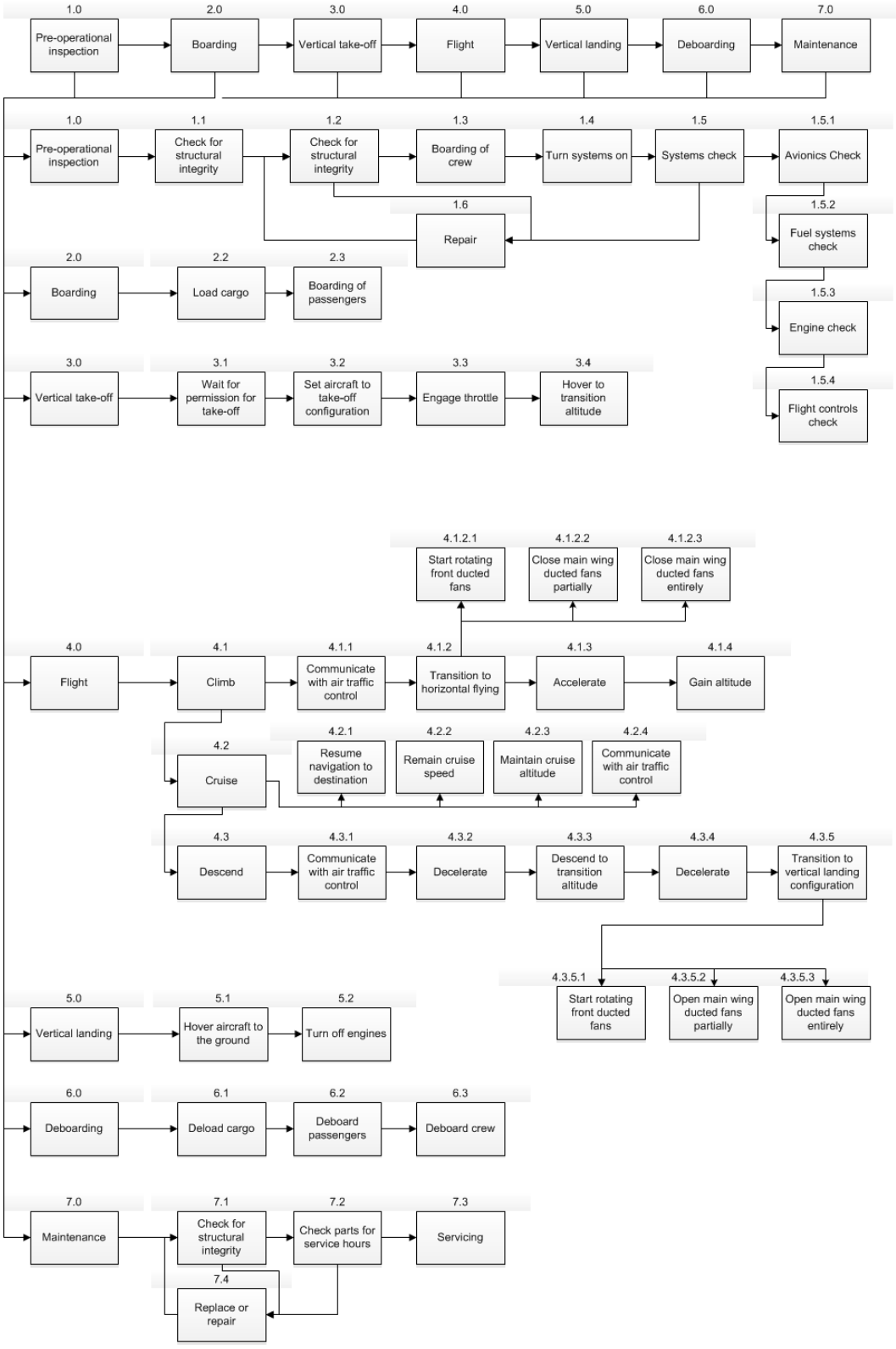

Figure A.4: Functional Flow Diagram

A.4. ELECTRIC BLOCK DIAGRAM

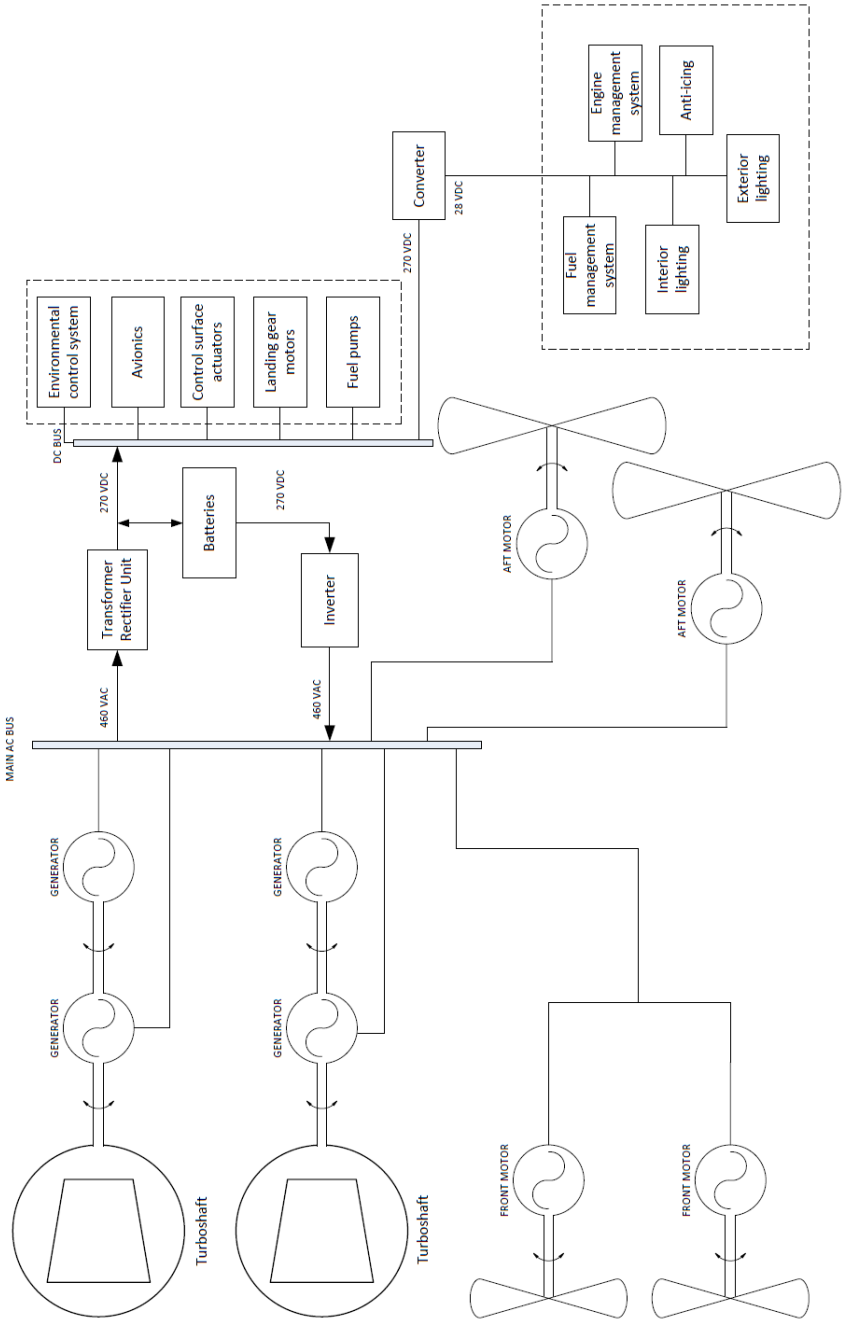

Figure A.5: Electric block diagram. Arrows indicate one-way electrical flow.

A.5. OPERATIONAL FLOW DIAGRAM

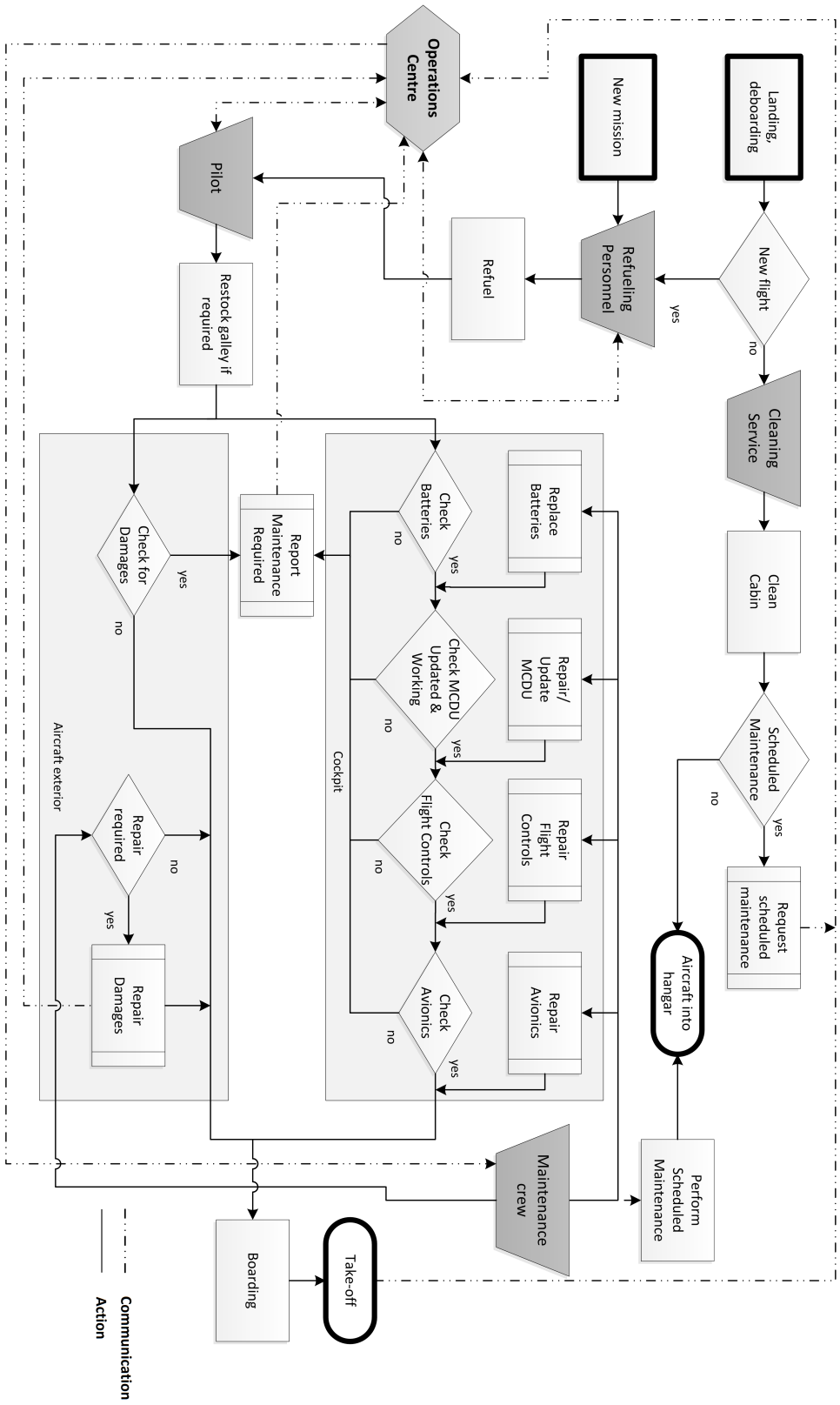

Figure A.6: Operations & Logistics when InVADe is grounded

A.6. COST BREAKDOWN STRUCTURE

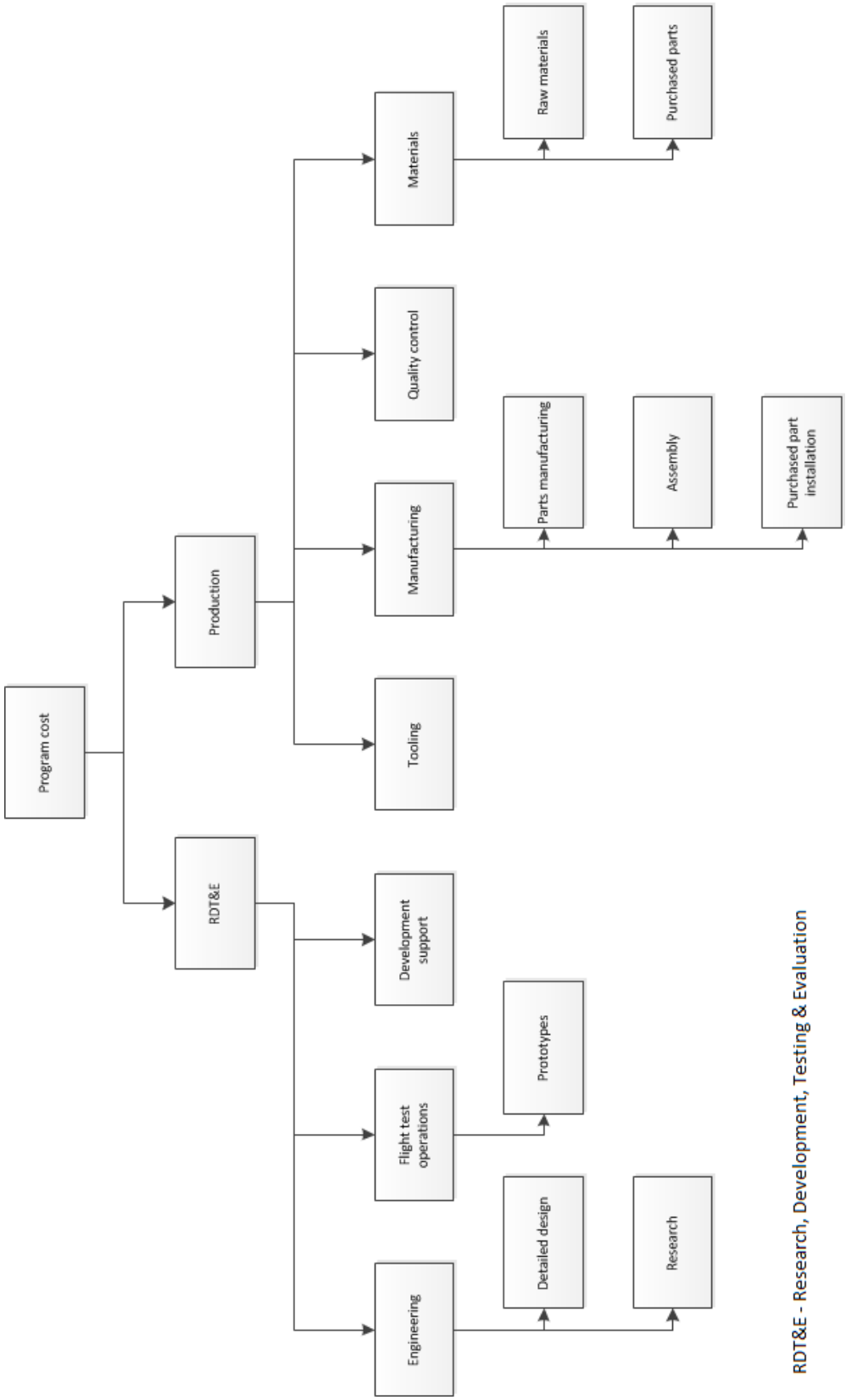

Figure A.7: Cost Breakdown Structure

A.7. RENDERS

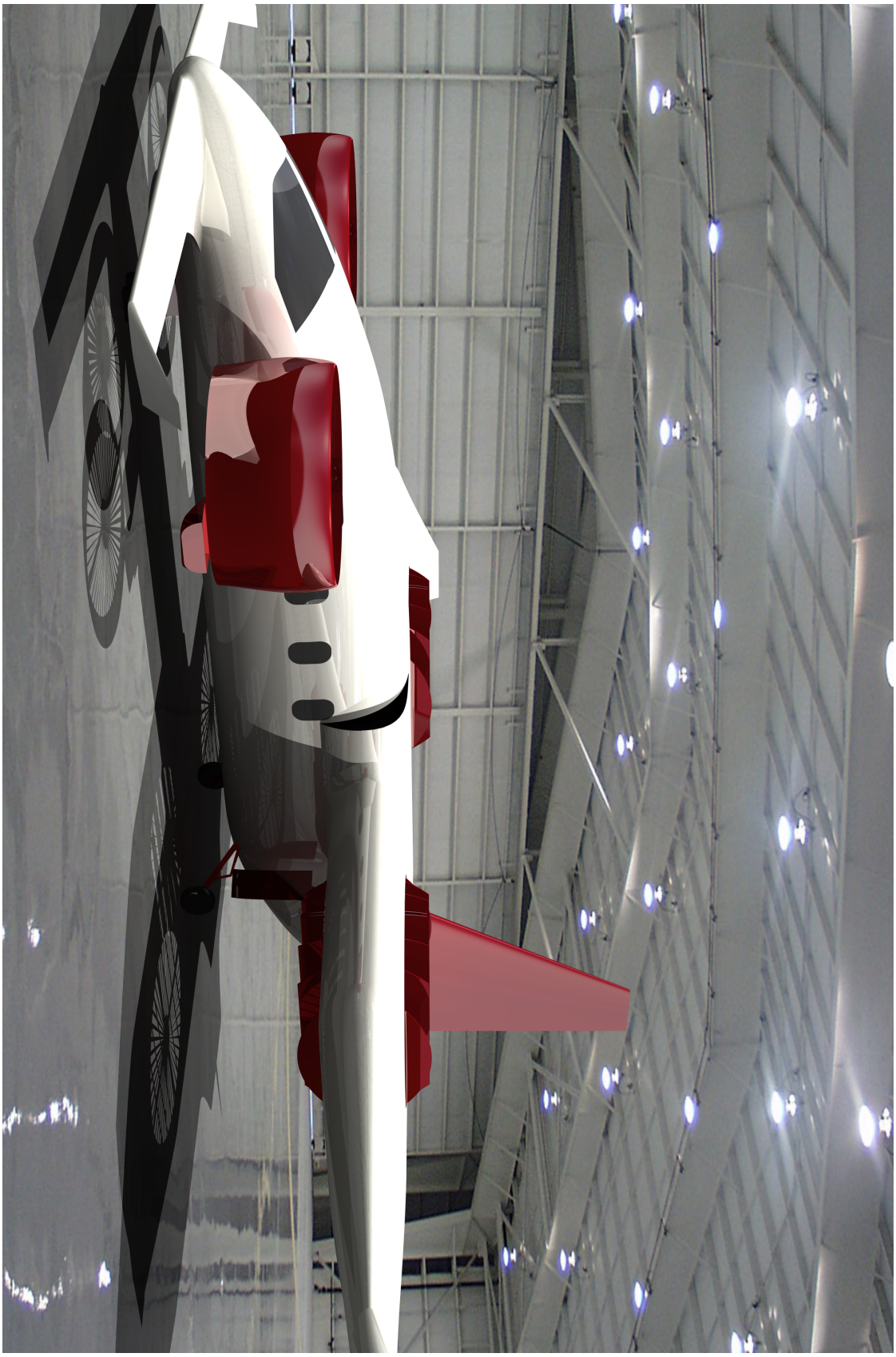

Figure A.8: Render in VTOL configuration

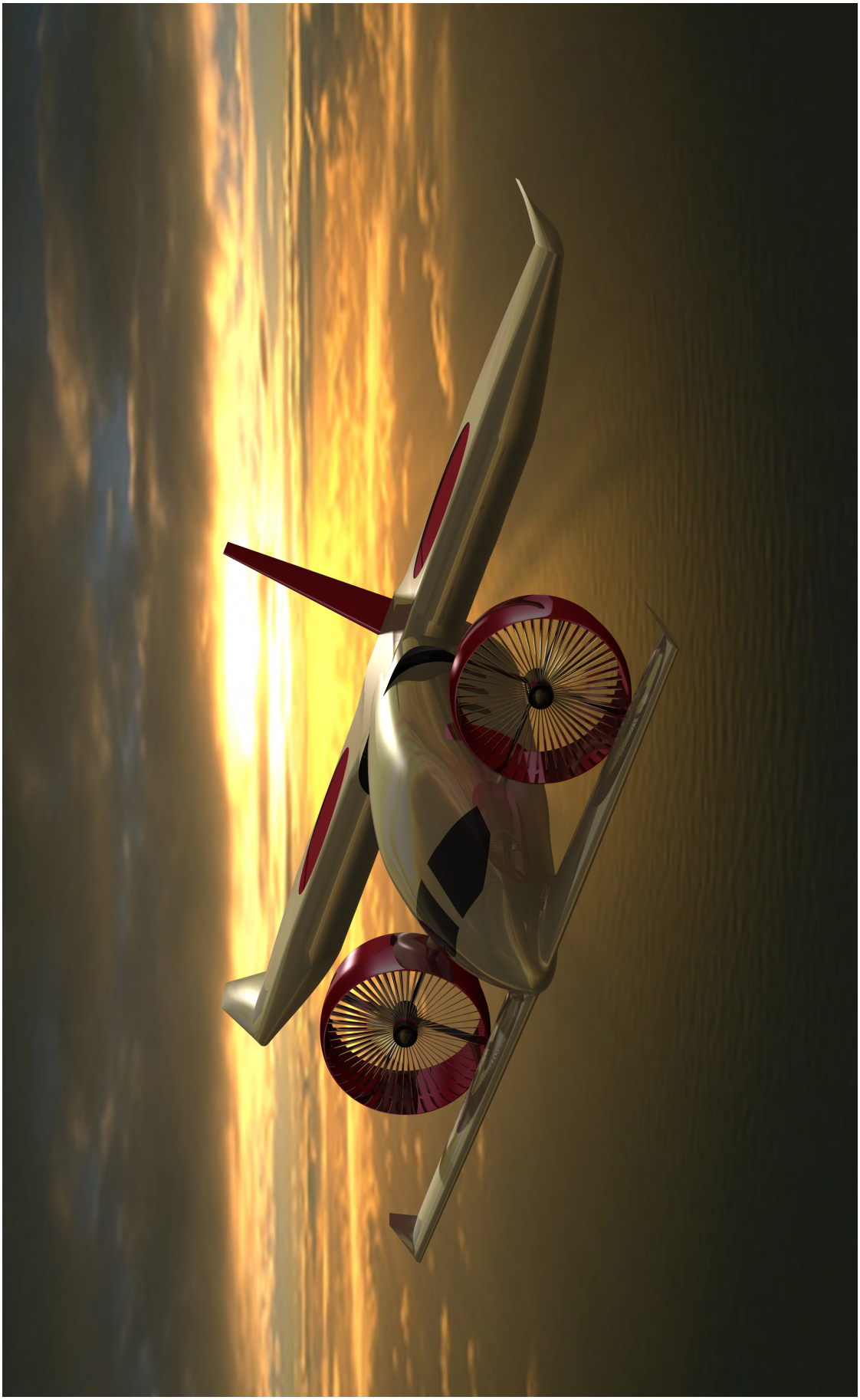

Figure A.9: Render in cruise configuration